frontiers | Research Topics

Assessment of intraoperative image technologies to optimize clinical outcomes in neurosurgical oncology

Edited by
Sergio García, Santiago Cepeda, Julius Höhne and Rafael Martinez-Perez

Published in
Frontiers in Oncology

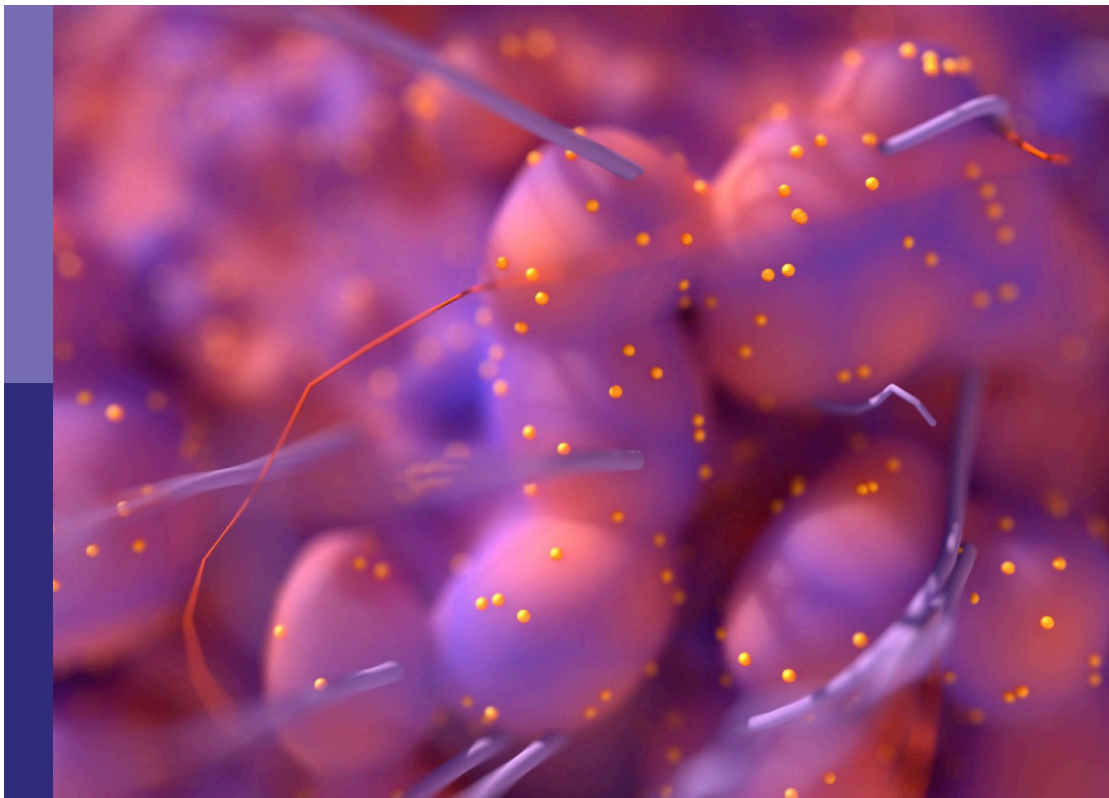

ISSN 1664-8714
ISBN 978-2-8325-2458-9
DOI 10.3389/978-2-8325-2458-9

About Frontiers

Frontiers is more than just an open access publisher of scholarly articles: it is a pioneering approach to the world of academia, radically improving the way scholarly research is managed. The grand vision of Frontiers is a world where all people have an equal opportunity to seek, share and generate knowledge. Frontiers provides immediate and permanent online open access to all its publications, but this alone is not enough to realize our grand goals.

Frontiers journal series

The Frontiers journal series is a multi-tier and interdisciplinary set of open-access, online journals, promising a paradigm shift from the current review, selection and dissemination processes in academic publishing. All Frontiers journals are driven by researchers for researchers; therefore, they constitute a service to the scholarly community. At the same time, the *Frontiers journal series* operates on a revolutionary invention, the tiered publishing system, initially addressing specific communities of scholars, and gradually climbing up to broader public understanding, thus serving the interests of the lay society, too.

Dedication to quality

Each Frontiers article is a landmark of the highest quality, thanks to genuinely collaborative interactions between authors and review editors, who include some of the world's best academicians. Research must be certified by peers before entering a stream of knowledge that may eventually reach the public - and shape society; therefore, Frontiers only applies the most rigorous and unbiased reviews. Frontiers revolutionizes research publishing by freely delivering the most outstanding research, evaluated with no bias from both the academic and social point of view. By applying the most advanced information technologies, Frontiers is catapulting scholarly publishing into a new generation.

What are Frontiers Research Topics?

Frontiers Research Topics are very popular trademarks of the *Frontiers journals series*: they are collections of at least ten articles, all centered on a particular subject. With their unique mix of varied contributions from Original Research to Review Articles, Frontiers Research Topics unify the most influential researchers, the latest key findings and historical advances in a hot research area.

Find out more on how to host your own Frontiers Research Topic or contribute to one as an author by contacting the Frontiers editorial office: frontiersin.org/about/contact

Assessment of intraoperative image technologies to optimize clinical outcomes in neurosurgical oncology

Topic editors

Sergio García — Hospital Universitario Río Hortega, Spain
Santiago Cepeda — Hospital Universitario Río Hortega, Spain
Julius Höhne — University Medical Center Regensburg, Germany
Rafael Martinez-Perez — Geisinger Health System, United States

Citation

García, S., Cepeda, S., Höhne, J., Martinez-Perez, R., eds. (2023). *Assessment of intraoperative image technologies to optimize clinical outcomes in neurosurgical oncology*. Lausanne: Frontiers Media SA. doi: 10.3389/978-2-8325-2458-9

Table of contents

frontiers | Frontiers in Oncology

TYPE Editorial
PUBLISHED 04 May 2023
DOI 10.3389/fonc.2023.1202240

OPEN ACCESS

EDITED AND REVIEWED BY
David D. Eisenstat,
Royal Children's Hospital, Australia

*CORRESPONDENCE
Sergio García-García
iskender_brave@hotmail.com

RECEIVED 07 April 2023
ACCEPTED 28 April 2023
PUBLISHED 04 May 2023

CITATION
García-García S, Höhne J, Martinez-Pérez R and Cepeda S (2023) Editorial: Assessment of intraoperative image technologies to optimize clinical outcomes in neurosurgical oncology. *Front. Oncol.* 13:1202240. doi: 10.3389/fonc.2023.1202240

Editorial: Assessment of intraoperative image technologies to optimize clinical outcomes in neurosurgical oncology

Sergio García-García[1]*, Julius Höhne[2], Rafael Martinez-Pérez[3] and Santiago Cepeda[1]

[1]Neurosurgery Department, Hospital Universitario Río Hortega, Valladolid, Spain, [2]Neurosurgery Department, University Medical Center Regensburg, Regensburg, Germany, [3]Neurosurgery Department, Geisinger Medical Center, Danville, PA, United States

KEYWORDS

intraoperative imaging, neurosurgical oncology, intraoperative magnetic resonance, intraoperative ultrasounds, photodynamic therapy, optical coherence tomography, confocal laser imaging, cost-effectiveness

Editorial on the Research Topic
Assessment of intraoperative image technologies to optimize clinical outcomes in neurosurgical oncology

During the recent decades, neurosurgery and neurosurgical oncology have undergone a significant technological revolution, with new devices and applications being introduced to increase surgical success rates and ensure patient safety. One critical innovation in this field is intraoperative imaging, which has played a paramount role in providing reliable feedback to surgeons during surgeries. From neuronavigation to augmented reality, a broad range of intraoperative imaging techniques are currently available, each promising to overcome the limitations of its predecessors. However, the rapid pace of technological progress has prevented a thorough evaluation of the actual benefits of these new technologies, leading to a lack of robust evidence to support their adoption. Indeed, the economic perspective of these advancements and assumed improvements have been largely disregarded, further hindering the offer of comprehensive recommendations to health systems worldwide.

Increasing the extent of resection in neurosurgical oncology

In neurosurgical oncology, recent research has focused on two main objectives: maximizing the extent of tumor resection while preserving functionality and studying tumoral and peritumoral samples in the intraoperative setting (1, Restelli et al.). This Research Topic highlights the advancements in intraoperative imaging techniques contributing to these essential goals.

In the quest to enhance tumor resection, several studies have explored the use of intraoperative ultrasound (IoUS) and magnetic resonance imaging (ioMRI) (1–7). Wang

et al. demonstrated the effectiveness of IoUS in recurrent glioma surgery, resulting in reduced residual tumor volume, improved postoperative outcomes, and fewer recurrences. Concurrently, Becerra et al. found that 1.5-T high-field ioMRI was a safe and dependable tool in pediatric neuro-oncology surgeries, maximizing tumor resection without increasing neurological deficits or complications.

Integrating diffusion tensor imaging (DTI) tractography with neuronavigation, as explored by Shi et al., has shown promise in preserving visual function during tumor resection in the optic radiation area. Combining these techniques led to better visual outcomes and the identification of clinical factors impacting patients' visual function and quality of life.

A new and burgeoning field in glioma surgery involves the use of 5-ALA, not as a surgical guidance tool to enhance extent of resection but as a therapeutic adjuvant. Ferres et al. observed a significant reduction on glioma recurrence within the first centimeter from the surface of surgical cavity in a cohort of patients undergoing 5-ALA guided surgery compared to those operated without it. Their findings, supported by previous evidence (8, 9), lead authors to recommend intensifying research efforts in this promising field (Ferres et al.).

Intraoperative approach to histological sample analysis

In parallel with the advancements in tumor resection techniques, researchers have also made strides in studying tumoral and peritumoral samples in the intraoperative setting. Restelli et al. conducted a comprehensive review of sodium fluorescein-based confocal laser imaging using the CONVIVO system, highlighting its promising diagnostic performance compared to standard histopathology methods. Nonetheless, further optimization of sodium fluorescein protocols and larger clinical trials are necessary to establish its position in routine clinical practice.

The potential of optical coherence tomography (OCT) for detecting peritumoral white matter damage and residual tumor detection has been investigated by Achkasova et al. and Kuppler et al. Achkasova et al. found that visual assessment of structural OCT images and color-coded maps enabled differentiation of tissue types, with color-coded maps exhibiting higher diagnostic accuracy. Kuppler et al. reported that contactless *in vivo* OCT scanning achieved high accuracy for residual tumor detection, supporting *ex vivo* OCT brain tumor scanning and complementing existing intraoperative techniques.

Intraoperative imaging devices in endoscopic skull base surgery

While advancements in optics, lighting, and imaging displays have greatly improved the field of endoscopic skull base surgery, the adoption of surgical innovations used in open surgery has been limited. Recent advancements in probe sizes and image reconstruction algorithms have increased the use of IoUS in endoscopic skull base surgery (10, 11). End-firing and side-firing probes enhance depth assessment and anatomical real-time guidance during surgery. In this Research Topic, Baker et al. illustrated the utility and potential benefits of side-firing IoUS in endoscopic surgeries for clival chordomas and neuroendocrine pituitary tumors (Baker et al.). Through their research, Baker et al. have demonstrated that the use of IoUS in endoscopic surgery improves surgeon´s judgement of extent of resection. Additionally, this technique demonstrated reduced operative time and the decreased incidence of postoperative endocrine deficits.

Cost effectiveness evidence for intraoperative image technologies

Literature regarding economic evaluation of surgical innovations in neurosurgery is scarce (2, 12). Previous studies have not provided conclusive evidence for a positive correlation between the cost of implementing modern technologies and their clinical benefits. Mosteiro et al. conducted a comparative cost-effectivenes study of intraoperative magnetic resonance (iMR) and IoUS in glioma surgery. Authors found that although iMR might be more expensive and time-consuming, it yielded better clinical outcomes in terms of extent of resection and postoperative performance status. As a result, iMR was found to be cost-effective. However, efforts should be addressed to thoroughly evaluate surgical technological advancements from a clinical and economic perspective, centered on patient care and on the respective social context.

Conclusion

This collection of ten articles offers new insights on surgical innovations applied to neuroncology: new applications of available devices; cutting-edge technologies; clinical series evaluating the benefits of state-of-the-art intraoperative imaging and a necessary study on cost-effectiveness assessment. Moving forward, it will be essential to conduct rigorous clinical trials to validate these techniques and establish standardized protocols for their adoption in settings where their benefit might be optimal. As the field continues to evolve, the insights and findings presented in this collection will serve as an important foundation for further advancements in surgical innovation.

Author contributions

SG-G and SC designed and wrote the draft of this editorial which was posteriorly reviewed by JH and RM-P. All authors approved the final version of the manuscript.

Conflict of interest

The authors declare that the research was conducted in the absence of any commercial or financial relationships that could be construed as a potential conflict of interest.

Publisher's note

References

1. Fountain DM, Bryant A, Barone DG, Waqar M, Hart MG, Bulbeck H, et al. Intraoperative imaging technology to maximise extent of resection for glioma: a network meta-analysis. *Cochrane Database Syst Rev* (2021) 1(1):CD013630. doi: 10.1002/14651858.CD013630.pub2

2. Garcia-Garcia S, Garcia-Lorenzo B, Ramos PR, Gonzalez-Sanchez JJ, Culebras D, Restovic G, et al. Cost-effectiveness of low-field intraoperative magnetic resonance in glioma surgery. *Front Oncol* (2020) 10:586679. doi: 10.3389/fonc.2020.586679

3. Bassaganyas-Vancells C, Roldan P, Gonzalez JJ, Ferres A, Garcia S, Culebras D, et al. Combined use of 5-aminolevulinic acid and intraoperative low-field magnetic resonance imaging in high-grade glioma surgery. *World Neurosurg* (2019). 206–212 doi: 10.1016/j.wneu.2019.06.029

4. Jenkinson MD, Barone DG, Bryant A, Vale L, Bulbeck H, Lawrie TA, et al. Intraoperative imaging technology to maximise extent of resection for glioma. *Cochrane Database Syst Rev* (2018) 1:CD012788. doi: 10.1002/14651858.CD012788.pub2

5. Wu JS, Gong X, Song YY, Zhuang DX, Yao CJ, Qiu TM, et al. 3.0-T intraoperative magnetic resonance imaging-guided resection in cerebral glioma surgery: interim analysis of a prospective, randomized, triple-blind, parallel-controlled trial. *Neurosurgery* (2014) 61(Suppl 1):145–54. doi: 10.1227/NEU.0000000000000372

6. Senft C, Bink A, Heckelmann M, Gasser T, Seifert V. Glioma extent of resection and ultra-low-field iMRI: interim analysis of a prospective randomized trial. *Acta Neurochir Suppl* (2011) 109:49–53. doi: 10.1007/978-3-211-99651-5_8

7. Barone DG, Lawrie TA, Hart MG. Image guided surgery for the resection of brain tumours. *Cochrane Database Syst Rev* (2014) 2014(1):CD009685. doi: 10.1002/14651858.CD009685.pub2

8. Leroy HA, Guerin L, Lecomte F, Baert G, Vignion AS, Mordon S, et al. Is interstitial photodynamic therapy for brain tumors ready for clinical practice? a systematic review. *Photodiagnosis Photodyn Ther* (2021) 36:102492. doi: 10.1016/j.pdpdt.2021.102492

9. Lietke S, Schmutzer M, Schwartz C, Weller J, Siller S, Aumiller M, et al. Interstitial photodynamic therapy using 5-ALA for malignant glioma recurrences. *Cancers (Basel)* (2021) 13(8). doi: 10.3390/cancers13081767

10. Alomari A, Jaspers C, Reinbold WD, Feldkamp J, Knappe UJ. Use of intraoperative intracavitary (direct-contact) ultrasound for resection control in transsphenoidal surgery for pituitary tumors: evaluation of a microsurgical series. *Acta Neurochir (Wien)* (2019) 161(1):109–17. doi: 10.1007/s00701-018-3747-x

11. Marcus HJ, Vercauteren T, Ourselin S, Dorward NL. Intraoperative ultrasound in patients undergoing transsphenoidal surgery for pituitary adenoma: systematic review [corrected]. *World Neurosurg* (2017) 106:680–5. doi: 10.1016/j.wneu.2017.07.054

12. Tan-Torres Edejer T, Baltussen R, Adam T, Hutubessy R, Acharya A, Evans DB, et al. *Making choices in health: WHO guide to cost-effectiveness analysis.: world health organization*. Geneva, Switzerland: World Health Organization. (2003). p. 318.

frontiers | Frontiers in Oncology

TYPE Original Research
PUBLISHED 16 August 2022
DOI 10.3389/fonc.2022.955418

OPEN ACCESS

EDITED BY
Sergio García,
Hospital Universitario Río Hortega, Spain

REVIEWED BY
Santiago Cepeda,
Hospital Universitario Río Hortega, Spain
Hiria Limpo,
University Hospital Fundación Jiménez Díaz, Spain

*CORRESPONDENCE
Yansong Zhang
15805181640@163.com

†These authors have contributed equally to this work and share first authorship

SPECIALTY SECTION
This article was submitted to Neuro-Oncology and Neurosurgical Oncology, a section of the journal Frontiers in Oncology

RECEIVED 28 May 2022
ACCEPTED 29 July 2022
PUBLISHED 16 August 2022

CITATION
Shi J, Lu D, Pan R, Chen H, Teng H, Xu Y, Bo F, Zhou Q and Zhang Y (2022) Applications of diffusion tensor imaging integrated with neuronavigation to prevent visual damage during tumor resection in the optic radiation area.
Front. Oncol. 12:955418.
doi: 10.3389/fonc.2022.955418

Applications of diffusion tensor imaging integrated with neuronavigation to prevent visual damage during tumor resection in the optic radiation area

Jianwei Shi[1†], Dafeng Lu[2†], Ruihan Pan[3†], Hairong Chen[1†], Hong Teng[4†], Yang Xu[1], Fuduo Bo[1], Qi Zhou[1] and Yansong Zhang[1*]

[1]Department of Neurosurgery, The Affiliated Brain Hospital of Nanjing Medical University, Nanjing, China, [2]School of Public Health, Nanjing Medical University, Nanjing, China, [3]Department of Neurosurgery, First Affliated Hospital, Zhejiang Chinese Medical University, Hangzhou, China, [4]Department of Geriatrics , The Affiliated Brain Hospital of Nanjing Medical University, Nanjing, China

Background: Intracranial tumors involving the temporo-occipital lobe often compress or destroy the optic radiation (OpR), resulting in decreased visual function. The aim of this study is to explore the value of diffusion tensor imaging (DTI) tractography integrated with neuronavigation to prevent visual damage when resecting tumors involving the OpR and find potential factors affecting patients' visual function and quality of life (QOL).

Methods: Our study is a cross-sectional study that included 28 patients with intracranial tumors in close morphological relationship with the OpR recruited between January 2020 and February 2022. The surgical incision and approach were preoperatively designed and adjusted according to the DTI tractography results and visual function scores. All patients underwent examinations of visual acuity (VA) and visual field index (VFI) and completed visual function and QOL scales at admission and 2 months after discharge. Logistic regression and linear regression analysis were conducted to evaluate clinical factors potentially affecting pre/postoperative OpR morphology, VA, VFI, visual function, and QOL.

Results: Lesion size was the main factor found to affect visual function (β = -0.74, 95%CI: -1.12~-0.36, P = 0.05), VA (left: β = -0.11, 95%CI: -0.14~-0.08, P < 0.001; right: β = -0.15, 95%CI: -0.17~-0.13, P < 0.001), and VFI (left: β = -0.11, 95%CI: -

0.14~-0.08, P < 0.001; right: β = -0.14, 95%CI: -0.16~-0.12, P < 0.001). Lesion size, edema, and involvement of the lateral ventricle temporal horn were factors affecting OpR morphology and QOL. The 28 patients showed significantly improved VA, VFI, visual function, and QOL results (P < 0.05) 2 months after discharge.

Conclusions: Combining DTI of OpR mapping and microscopic-based neuronavigation aided precise mapping and thus preservation of visual function in patients undergoing tumor resection. Potential clinical factors affecting patients' visual function and QOL scores were identified which are useful for assessing a patient's condition and predicting prognosis.

KEYWORDS

neuronavigation, diffusion tensor imaging, tumor resection, optic radiation, visual function

Introduction

The optic radiation (OpR) begins in the lateral geniculate body and occupies the temporal and parietal lobes in the striatum. Many brain lesions can involve the OpR and cause decreased visual function, visual acuity (VA), and visual field index (VFI). As the most anterior part of the OpR and an important anatomical location in neurosurgery, Meyer's loop projects forward across the superior aspect of the anterior tip of the lateral ventricle's temporal horn. During tumor resection, the protection of Meyer's loop remains challenging, which is responsible for patients' prost-operative visual function and quality of life (QOL) (1). Notably, tractography of the OpR has been shown to limit surgical damage to visual function during tumor resection involving the OpR area (2).

The OpR cannot be distinguished using clinical magnetic resonance imaging (MRI) sequences. Diffusion tensor imaging (DTI) is an advanced MRI technique to evaluate microstructural changes in the brain using water diffusion as the MR contrast and collecting diffusion-weighted (DW) MR images (3). At present, DTI research mainly focuses on tracking neural fiber pathways in the central nervous system. Notably, DTI tractography enables the delineation of the OpR, which can be used to guide the surgeon to prevent visual damage during intracranial tumor resection planning. This surgical strategy can assist with intra-operative planning to decrease the chances of damaging the functional nerves (e.g., OpR, facial nerve, vestibular nerve) and improve patients' QOL following surgery (4–6). DTI integrated with neuronavigation can allow neurosurgeons to evaluate the extent of tumor resection and modify the surgical strategy in real-time, resulting in better surgical results and lowering risks (4, 7).

Intracranial tumor patients with visual impairment are constantly facing challenges in achieving an independent and productive life, so prevention of visual damage during resection is of great value. The primary aim of this study was to examine the potential use of DTI integrated with neuronavigation in surgical planning and intraoperative guidance to predict the anatomical location of the visual pathways and preserve visual function during tumor resection. The secondary aims were to identify clinical factors that may affect OpR morphology, VA, VFI, visual function, and QOL.

Material and methods

Subjects

Twenty-eight patients (13 males; age range: 12–78 years; mean ± standard deviation (SD): 53 ± 21 years) with intracranial tumors touching (the minimum distance between OpR and tumor ≤ 1 cm), pushing, wrapping, or invading the OpR were prospectively recruited to participate in this single-center cross-sectional study at Nanjing Brain Hospital, Nanjing, China, between January 2020 and February 2022. The exclusion criteria were: (1) patients who received craniotomy or radiotherapy before admission; (2) patients with independent ophthalmic diseases or anterior visual pathway dysfunction; (3) patients who refused or did not complete follow-up; and (4) patients who could not cooperate with or complete DTI during MRI scanning.

Demographic data, tumor size, the presence/absence of edema, involvement of the lateral ventricle temporal horn, the extent of resection (EOR), VA, VFI, visual function, and QOL data were collected for all patients. This study was approved by the Nanjing Brain Hospital Ethics Committee and informed written consent was obtained from all patients.

Visual function evaluation

All patients underwent examination of binocular VA and VFI and completed the visual function and QOL scales at admission and 2 months after discharge. The QOL and visual function scales, which were developed by the World Health Organization and American Eye Institute for developing countries, are provided in Supplementary Table 1, 2 (8, 9).

Imaging and fiber tracking

Patients underwent structural MRI and DTI imaging on a 3.0 Tesla MRI scanner (Siemens Magnetom TIM Trio, Erlangen, Germany) before surgery. The lesion size was represented by the product of the maximum diameter of the axial, sagittal, and coronal T1-weighted volumetric acquisition sequence. While including extra- and intra- axial tumors, the minimum distance between the tumor and OpR was measured as well. DTI data were acquired by interlaced echo-planar imaging (IEPI) with 2.0 mm isotropic voxels and 32 directions with a b value of 1,000 s/mm^2 (repetition time (TR) = 6100 ms, echo time (TE) = 106 ms, section thickness = 1.0 mm). All patients underwent a contrast-enhanced MRI one day after surgery, and preoperative MRI was used to evaluate EOR.

The collected MRI data were transferred to a Stealth Station navigation system (Medtronic-Sofamor Danek, USA) and StealthViz ® (Medtronic-Sofamor Danek, USA) software was used to process fiber tractography (fractional anisotropy = 0.2, apparent diffusion coefficient = 0.1). The fiber diameter was 0.2 mm (10). The maximal angle was 45°. After preprocessing (and spatial smoothing, when applied), the lateral geniculate body and occipital cortex, including the calcarine sulcus, were divided into regions of interest (ROIs). The size and direction of the ROIs were adjusted until we found clear fiber bundles passing through the defined ROI using knowledge of each patient's anatomy (Carried out by JS & RP, and then censored by HT). Bundles that could contaminate the optic tracts were eliminated. An OpR morphology score was generated for each patient ranging from 1 to 4, with a higher score indicating greater OpR damage (Carried out by JS & RP, and then censored by YZ) (11).

3D reconstruction of OpR

Cranial® software implemented on a Stealth Station (Medtronic-Sofamor Danek, USA) was used to construct 3D models of the OpR and lesions, and neuronavigation plans were subsequently made. The surgical approach was designed according to the 3D positional relationship between the OpR and the lesion.

Intraoperative neuronavigation and surgery

Targeting was implemented through the guidance of the fiber bundle fusion neuronavigation system. The entry and target points were marked according to the preoperatively designed surgical approach. The distance between the operating position and the OpR was judged in real-time to avoid damage to the OpR. Less aggressive resections given DTI guidance are beneficial. For tumors with complicated locations or invading the OpR, a navigation-guided needle was used to puncture to the boundary between the OpR and the tumor after opening the dura mater. A small piece of methylene blue-colored gelatin sponge was pushed in to help locate the OpR. After reaching the blue-stained area, special attention must be paid. We gently separated and pulled the lesion and peritumoral tissue to the affected side and protected the identified OpR to prevent postoperative visual damage. The use of bipolar electrocoagulation should be reduced and switched to absorbable hemostatic agents such as Surgicel or physical compression hemostasis. If final pathologic results suggest malignant tumors, follow-up radiotherapy and chemotherapy should be given.

The EOR corresponds to the percentage of volume resected with respect to the preoperative volume and was classified as follows: gross total resection, EOR = 100%; near total resection, 95% ≤ EOR < 100%; subtotal resection, 80% ≤ EOR < 95%; partial resection < 80% (12, 13).

Statistical analysis

The paired Student's t-test was used to evaluate the efficacy of surgery by comparing the QOL, visual function, VA, and VFI values between admission and 2 months after discharge with normal distribution. If these variables do not normally distribute, the paired Wilcoxon signed-rank test will be applied. Logistic regression analysis was performed for binary variables. Linear regression was used for continuous variables with a normal distribution and variables that did not conform to the normal distribution were converted to binary variables and then analyzed using logistic regression. Multivariate logistic

regression adopting the backward elimination technique was conducted to evaluate potential risk factors associated with unfavorable results of OpR morphology, VA, VFI, visual function, and QOL. Statistical analyses were performed using R software (version 4.04). All tests were two-tailed and results were considered statistically significant at the 0.05 level unless otherwise specified.

Results

Patient clinical data

Patient demographics and clinical information are listed in Table 1. The results of the visual exam and QOF of 28 patients are presented in Table 2. The most frequent complaint on

TABLE 1 Patient demographics and clinical information.

No.	Sex	Age (years)	Position	Lesion Size	Pathological diagnosis	Edema	Invasion of the temporal horn	OpR Score (s)	Lesion Excision
1	F	21	Right temporal lobe	2.0*2.0*1.5cm	Ganglioglioma	N	Y	1	Gross total resection
2	F	63	Right temporal lobe	5.0*5.0*4.0cm	Meningioma	N	N	2	Gross total resection
3	M	68	Left temporal lobe	2.0*1.5*1.5cm	Glioblastoma	N	N	1	Gross total resection
4	M	78	Left temporal lobe	4.7*3.7*3.9cm	Glioblastoma	Y	Y	4	Near total resection
5	F	74	Left temporal lobe	4.0*3.1*2.1cm	Brain metastasis	Y	N	2	Gross total resection
6	F	65	Left parietal occipital falx	3.5*3.0*3.2cm	Meningioma	N	N	2	Gross total resection
7	M	54	Left temporal lobe	2.0*1.4*1.4cm	Pilocytic astrocytoma	N	N	2	Gross total resection
8	M	61	Left parietal occipital lobe	3.5*3.1*2.5cm	Brain metastasis	Y	N	3	Gross total resection
9	M	70	Right temporal lobe	4.6*2.9*2.2cm	Lymphoma	Y	N	3	Partial resection
10	F	60	Right occipital canopy	2.4*1.5*1.6cm	Meningioma	N	N	1	Gross total resection
11	M	53	Right temporo-parietal occipital lobe	4.8*5.0*3.8cm	Glioblastoma	Y	Y	4	Near total resection
12	F	54	Left temporal insula	2.2*1.7*1.5cm	Glioblastoma	Y	Y	3	Gross total resection
13	M	71	Right temporal lobe	5.8*3.4*3.6cm	Brain metastasis	Y	Y	4	Subtotal resection
14	F	21	Right temporal lobe	1.2*0.8*0.6cm	Cavernous hemangioma	N	N	1	Gross total resection
15	M	67	Left temporo-parietal occipital lobe	5.6*4.5*3.0cm	Glioblastoma	Y	Y	4	Near total resection
16	F	12	Right parietal occipital lobe	3.0*2.0*2.2cm	Astrocytoma	Y	N	2	Gross total resection
17	M	12	Left temporal lobe	1.8*1.2*1.0cm	Cavernous hemangioma	Y	N	1	Gross total resection
18	F	62	Left ventricle and temporal horn	3.0*2.8*2.0cm	Anaplastic astrocytoma	Y	Y	3	Subtotal resection
19	F	15	Right temporal lobe	4.7*3.0*4.5cm	Cavernous hemangioma	Y	N	3	Gross total resection
20	M	56	Left temporal lobe	1.5*1.5*1.2cm	Ganglioglioma	N	Y	1	Gross total resection
21	M	61	Left occipital lobe	1.8*2.2*2.8cm	Cavernous hemangioma	N	N	2	Gross total resection
22	F	20	Left temporal lobe	2.9*2.0*1.7cm	Diffuse glioma	N	N	2	Gross total resection

(Continued)

TABLE 1 Continued

No.	Sex	Age (years)	Position	Lesion Size	Pathological diagnosis	Edema	Invasion of the temporal horn	OpR Score (s)	Lesion Excision
23	F	72	Left ventricle and temporal horn	2.6*1.5*1.3cm	Lymphoma	Y	Y	3	Partial resection
24	M	63	Left temporal insula	4.5*4.6*4.3cm	Anaplastic Glioma	Y	Y	3	Gross total resection
25	M	49	Left temporal lobe	5.0*3.7*4.5cm	Glioblastoma	Y	Y	4	Gross total resection
26	F	68	Left temporal insula	4.0*3.0*2.6cm	Glioblastoma	Y	Y	3	Near total resection
27	F	76	Left temporal lobe	5.8*4.2*3.0cm	Meningioma	Y	N	2	Gross total resection
28	F	41	Left temporo-parietal insula	7.0*5.0*4.8cm	Diffuse glioma	Y	Y	3	Near total resection

(F, female; M, male; Y, yes; N, no; OpR, optic radiation).
*means ×, which is a multiplication sign.

TABLE 2 The results of pre-operative visual exam and QOF compared to post-operative of 28 patients.

No.	Pre-QOL	Post-QOL	Pre-VF	Post-VF	Pre-VA (L)	Post-VA (L)	Pre-VA (R)	Post-VA (R)	Pre-VFI (L)	Post-VFI (L)	Pre-VFI (R)	Post-VFI (R)
1	100.00	100.00	85.67	87.50	0.60	0.60	0.80	0.80	0.99	0.99	0.96	0.96
2	85.43	85.43	54.63	60.18	0.20	0.30	0.50	0.50	0.32	0.33	0.24	0.25
3	100.00	100.00	88.90	88.90	0.80	0.80	1.00	1.00	0.84	0.84	0.91	0.92
4	76.40	76.42	57.42	62.97	0.10	0.10	0.30	0.30	0.21	0.22	0.32	0.34
5	76.40	76.4.0	73.15	78.70	0.50	0.60	0.80	0.80	0.54	0.54	0.47	0.49
6	85.43	88.20	67.60	78.70	0.20	0.20	0.60	0.60	0.47	0.50	0.48	0.48
7	97.23	97.23	87.05	88.90	0.80	0.90	1.00	1.00	0.87	0.87	0.82	0.84
8	86.10	86.10	73.15	73.15	0.50	0.60	0.70	0.70	0.52	0.52	0.49	0.48
9	86.10	86.10	84.27	84.27	0.70	0.70	0.40	0.50	0.36	0.38	0.41	0.42
10	100.00	100.00	88.90	88.90	1.00	1.00	0.80	0.80	0.85	0.88	0.90	0.90
11	70.85	72.93	59.73	65.28	0.40	0.60	0.20	0.30	0.30	0.30	0.25	0.30
12	94.45	97.23	87.50	87.50	0.60	0.80	1.00	1.00	0.77	0.79	0.81	0.83
13	77.78	77.80	70.38	75.93	0.60	0.60	0.20	0.30	0.32	0.32	0.29	0.30
14	100.00	100.00	88.89	88.89	1.20	1.20	1.00	1.00	0.89	0.90	0.91	0.91
15	65.30	65.30	56.03	61.58	0.20	0.20	0.40	0.50	0.36	0.39	0.32	0.32
16	100.00	100.00	88.89	88.89	1.00	1.00	0.80	0.90	0.77	0.80	0.71	0.74
17	100.00	100.00	88.89	88.89	1.00	1.00	1.20	1.20	0.92	0.93	0.95	0.97
18	61.13	63.91	78.70	78.70	0.50	0.60	0.80	0.80	0.54	0.54	0.60	0.61
19	90.98	90.98	78.70	78.70	0.60	0.60	0.40	0.50	0.45	0.48	0.35	0.40
20	97.23	97.36	88.89	88.89	1.00	1.00	1.20	1.20	0.95	0.95	0.94	0.96
21	100.00	100.00	88.89	88.89	0.80	0.80	1.00	1.00	0.95	0.95	0.96	0.96
22	100.00	100.00	87.50	88.89	0.80	0.80	1.00	1.00	0.91	0.93	0.95	0.94
23	81.25	81.25	78.70	84.25	0.60	0.60	0.80	0.80	0.82	0.85	0.79	0.82
24	73.63	76.40	75.93	77.78	0.20	0.30	0.60	0.60	0.26	0.29	0.29	0.30
25	77.78	77.78	73.15	75.93	0.40	0.40	0.50	0.50	0.42	0.43	0.39	0.39
26	77.78	78.70	78.70	78.70	0.30	0.30	0.50	0.60	0.56	0.58	0.56	0.56
27	86.10	88.90	84.27	87.05	0.50	0.60	0.70	0.80	0.67	0.68	0.59	0.60
28	86.10	90.98	78.70	78.70	0.30	0.50	0.60	0.70	0.48	0.49	0.48	0.48

(QOL; quality of life, VF; visual function, VA; visual acuity, VFI; visual field index, L; left, R; right, Pre; preoperative/at admission, Post; postoperative/2 months after admission).

admission was headache and dizziness (n=10, 35.7%), followed by visual deterioration (n=9, 32.1%), seizures (n=6, 21.4%), aphasia (n=2, 7.1%), and numbness (n=1, 3.5%). The mean duration from admission to discharge was 19.8 ± 2.9 days. The lesions included 14 gliomas, 4 meningiomas, 4 cavernous hemangiomas, 3 metastases, and 3 lymphomas. A flowchart of the study design is illustrated in Figure 1. The detailed regression analysis results related to patient characteristics are listed in Supplementary Table 3.

OpR tracking

All 28 patients had normal OpR morphology on the unaffected side. Regarding OpR morphology on the affected side, 6 cases (grade 1, 21.4%) were morphologically normal, 8 cases (grade 2, 28.6%) were squeezed, 9 cases (grade 3, 32.1%) were deformed or partially destroyed, and 5 cases (grade 4, 17.9%) were interrupted. The mean OpR morphology score of the affected side was 2.5 ± 1.0 points. Lesion size (odds ratio, OR = 0.75, 95% confidence interval, 95% CI: 0.634–0.886, P = 0.003), edema (OR = 0.486, 95%CI: 0.281–0.842, P = 0.017), and involvement of the lateral ventricle temporal horn (OR = 0.551, 95% CI: 0.349–0.87, P = 0.018) were the main clinical factors associated with OpR morphological damage (Supplementary Table 3). The minimum distance between the tumor and OpR was only able to be measured in patients with an OpR score of one and was 0.3 cm, 0.7 cm, 1.0 cm, 0.5 cm, 0.3 cm, and 0.4 cm in order.

Analysis of preoperative VA, VFI, visual function, and QOL

Multivariate linear regression analysis was performed for the preoperative variables. Lesion size was identified as more likely factor affecting preoperative visual function (β = -0.74, 95% CI: -1.12~-0.36, P = 0.05), VA (left: β = -0.11, 95%CI: -0.14~-0.08, P < 0.001; right: β = -0.15, 95%CI: -0.17~-0.13, P < 0.001), and VFI (left: β = -0.11, 95%CI: -0.14~-0.08, P < 0.001; right: β = -0.14, 95%CI: -0.16~-0.12, P < 0.001). Advanced age and edema were potential factors for damaged VA and VFI. Advanced age (β = -5.33, 95%CI: -7.01~-3.65, P = 0.004), edema (β = -7.46, 95% CI: -10.83~-4.09, P = 0.037), and involvement of the lateral ventricle temporal horn (β = -7.71, 95%CI: -10.50~-4.92, P = 0.011) were the main risk factors affecting preoperative QOL (Supplementary Table 3).

Analysis of postoperative VA, VFI, visual function, and QOL

Multivariate logistic regression analysis was performed for the postoperative variables. We did not find a significant

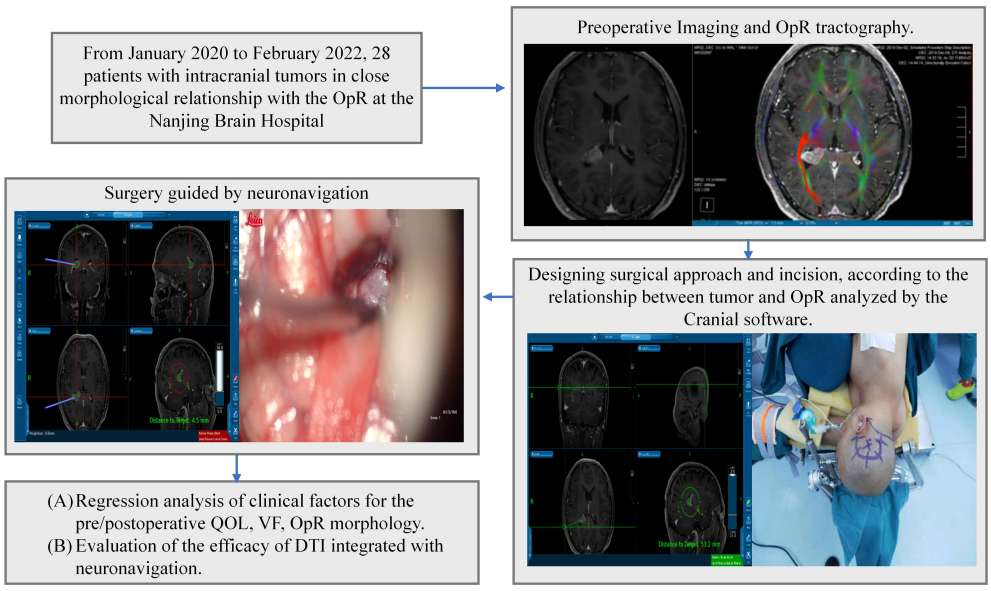

FIGURE 1
Study design. Intraoperative images were acquired following initial dissection and at the end of surgery. OpR, optic radiation, DTI; diffusion tensor imaging, VF; visual function; QOL, quality of life.

association of VA or VFI with sex, age, tumor size, edema, invasion into the temporal horn, the extent of tumor resection, or OpR morphology. In the univariate regression analysis, tumor size (OR = 4.12, 95%CI: 1.75~16.36, P = 0.01) and edema (OR = 1.65, 95%CI: 1.20~2.27, P = 0.01) were significantly related to right VA ($\beta > 0$). However, this result does not mean that larger tumor size and more serious edema result in better VA. Preoperative univariate regression analysis showed that right VA was also significantly associated with tumor size (β = -0.14, 95%CI: -0.16~-0.12, P < 0.001) and edema (β = -0.30, 95%CI: -0.39~-0.21, P = 0.002). Taken together, these results suggest that the impact of tumor size and edema on patients' VA may be recovered after surgery. OpR morphology was the main factor affecting postoperative visual function (OR = 0.203, 95% CI: 0.036–0.731, P = 0.033) while involvement of the lateral ventricle temporal horn (OR = 17.542, 95% CI: 2.678–206.021, P = 0.007) was the main clinical factor affecting postoperative QOL (Supplementary Table 3).

Intraoperative neuronavigation and surgery

According to the preoperative DTI results, 16 patients underwent a surgical approach designed by traditional experience (11 cases employed the trans-cortical approach, 2 cases employed the subtemporal approach, 1 case employed the trans-sylvian approach and 2 cases employed the occipital-transtentorial approach/Poppen approach) and 12 patients underwent a readjusted trans-cortical approach according to the OpR position reconstructed by DTI to avoid damage to the OpR (Figures 2–8). Nineteen cases (68%, 7 gliomas, 4 meningiomas, 4 cavernous hemangiomas, 2 metastases, and 2 lymphomas) underwent gross total resection, 5 cases (18%; 5 gliomas) underwent near total resection, 2 cases (7%; 1 anaplastic astrocytoma, 1 metastasis) underwent subtotal resection, and 2 cases (7%; 2 lymphomas) underwent partial resection.

Efficacy and prognosis

Since the variables did not follow a normal distribution, the paired samples Wilcoxon signed rank test was applied for analysis. Although 7 patients experienced a transient decrease in visual function after surgery caused by brain tissue edema, no patients had worsening VA or VFI two months after discharge. Five patients developed focal impaired awareness autonomic/clonic seizures postoperatively (14). No other discomfort or complications were reported by patients. Two months after discharge, the VA (left, P = 0.002; right, P = 0.002) and VFI (left, P < 0.001; right, P < 0.001) of the included patients had a statistically significant difference relative to the time of admission (Table 2; Supplementary Table 4). Significant differences in visual function (P = 0.001) and QOL (P = 0.002) scores between admission and 2 months after discharge were found for all patients (Supplementary Table 4).

Discussion

Main findings and interpretation

Accurate intraoperative localization of the OpR using tractography has been shown to be effective in neurosurgery (15). At present, three methods can be applied to study the OpR:

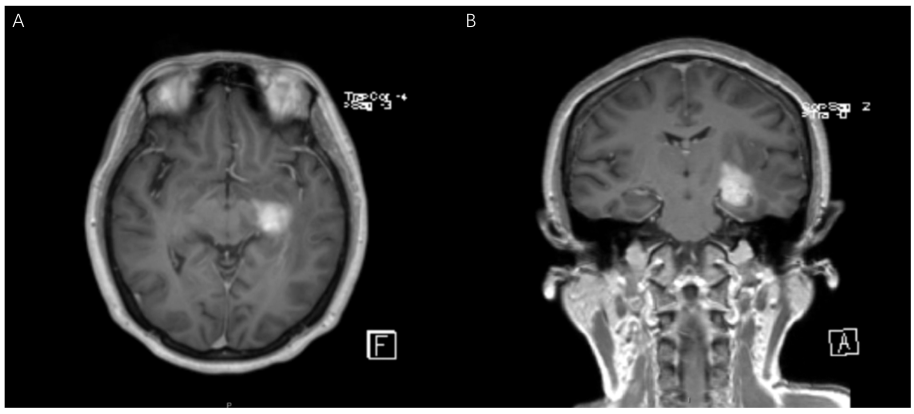

FIGURE 2
Patient No.12 is a 54-year-old female with a main complaint of dizziness. The coronal **(A)** and axial **(B)** MR T1 weighted images showed a 2.2×1.7×1.5cm abnormal signal shadow in the left temporal insula. The initial diagnosis was glioma.

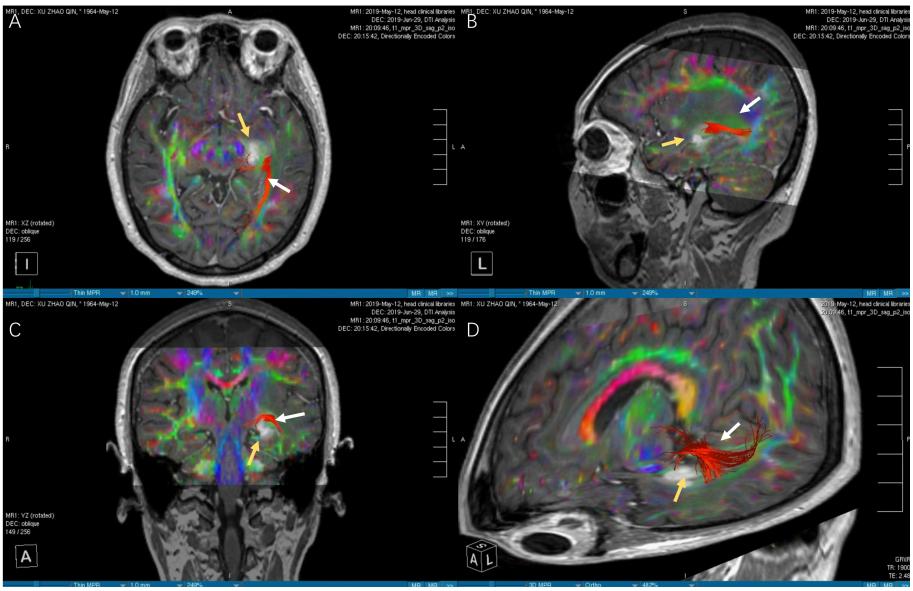

FIGURE 3
The images of DTI tractography of patient No.12 (OpR morphology score = 3). The DTI data was imported into the StealthViz ® software for neuronavigation. The lateral geniculate body and the rectangular sulcus were set as regions of interest to reconstruct the OpR on the affected side. **(A)** The axial image showed partial disruption of left OpR. **(B)** In sagittal view, the OpR on the affected side can be seen behind and above the tumor. **(C)** The coronal image showed that the tumor pushed the starting position of the OpR upward. **(D)** The OpR was partially interrupted (OpR morphology score=3) and was located above and behind the tumor, based on 3D reconstruction. Therefore, the inferior temporal gyrus approach was applied to avoid OpR. The white arrow indicates the OpR and the yellow arrow indicates the tumor. DTI, diffusion tensor imaging, OpR, optic radiation.

(i) determining the relationship between visual field deficits and resected tissue by evaluating the postoperative VA of patients with temporal lobe lesions, which is commonly used in studies of anterior temporal lobectomy for temporal lobe epilepsy (1, 5, 16); (ii) performing anatomical studies using a special fiber separation technique (Klingler's fiber dissection technique) (17); and (iii) DTI and diffusion tensor tractography (DTT) based on DTI (7). StealthViz® is a convenient software application for quick and easy fiber tract imaging that is helpful for neurosurgical planning and navigation (18). Based on anatomy, we adopted the tracking method described by Bertani (19) and Sherbondy (20) to establish ROIs and display the OpR's course. Our results suggest that DTI integrated with neuronavigation is useful and reliable for designing surgical strategies to avoid OpR injury during tumor resection. Potential factors affecting patients' visual function and QOL scores were identified simultaneously.

The most common postoperative complications of surgical treatment for temporo-occipital lobe lesions are decreased VA/VFI, epilepsy, and aphasia (21, 22). Declined visual function and QOL after surgery are very common (23, 24). Prior studies have reported that more than 50% of patients with epilepsy develop visual field deficits after anterior temporal lobectomy (16, 25). There are two main reasons for this risk: (i) direct damage to the OpR and visual cortex through the transcortical approach; (ii) intraoperative damage to arteries supplying the OpR (the blood supply to the anterior OpR is provided by the anterior choroidal artery from the internal carotid artery, the blood supply to the posterior part is provided by the middle and posterior cerebral artery, and the blood supply to the lateral part is provided by the lenticulostriate artery from the middle cerebral artery) (26). Sincoff et al. (27) summarized the three surgical approaches to the OpR area: (i) The trans-cortical approach including the superior, middle, inferior temporal gyrus and the occipital cortex. The effect on the OpR depends on the location of the cortical incision and the amount of cortical resection. The inferior temporal gyrus approach typically leads to fewer injuries to the OpR, due to the anatomical course of the OpR. (ii) The infratemporal approach does not affect the OpR, but the bottom of the temporal lobe often needs to be stretched and the zygomatic arch may need to be removed. (iii) The trans-sylvian approach can avoid the OpR and does not damage the functional language area, but does require the operator to have high anatomical knowledge and superb surgical skills. Meyer's loop mainly projects forward across the superior aspect of the anterior tip of the lateral ventricle's temporal horn. Therefore, the inferior temporal gyrus approach should be considered to protect the OpR, and damage to the supplying artery should be

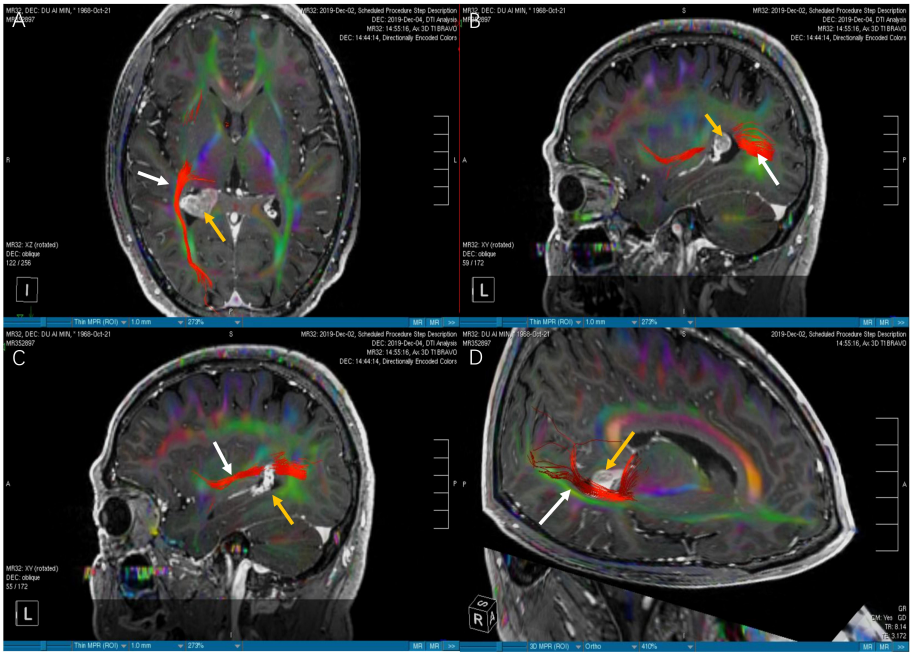

FIGURE 4
The images of DTI tractography of patient No.6 (OpR morphology score = 2). The DTI data was imported into the StealthViz ® software for neuronavigation. The lateral geniculate body and the rectangular sulcus were set as regions of interest to reconstruct the OpR on the affected side. **(A)** Compared with Figure 3A, the axial image showed that the right OpR was normal and healthy. **(B)** In sagittal view, the OpR on the affected side was located at the edge of the lateral ventricular triangle. **(C)** We found that the OpR appeared to be on the lateral of the tumor. But it had the possiblity that the OpR was partially or completely interrupted. **(D)** The 3D reconstruction confirmed that the OpR was just slightly pushed so a OpR morphology score of 2 was given. The white arrow indicates the OpR and the yellow arrow indicates the tumor. DTI; diffusion tensor imaging, OpR; optic radiation.

minimized. In the present study, the 12 patients who were prepared to adopt the preliminary trans-cortical approach were switched to the adjusted inferior temporal gyrus approach according to the reconstructed OpR.

Assessing the visual evoked potential (VEP) remains one of the most common techniques for intraoperative monitoring and protection of the visual pathway. However, many studies have reported that patients' postoperative visual function was

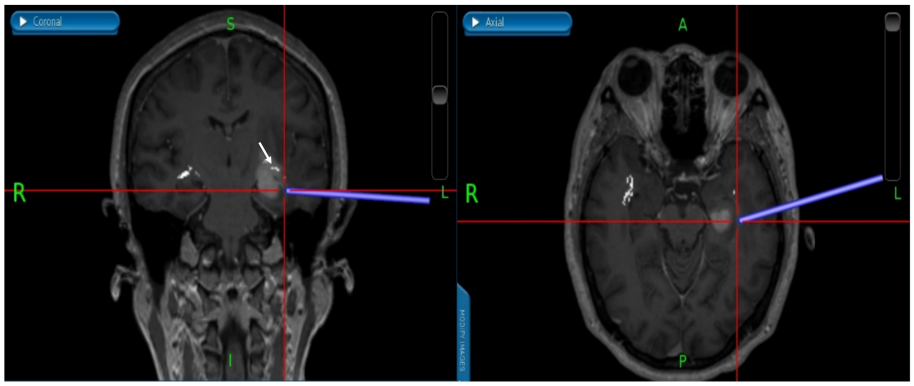

FIGURE 5
(Patient No.12) According to the relationship between tumor and OpR, the surgical approach is adjusted to the inferior temporal gyrus approach. We successfully reached the tumor under the guidance of neuronavigation and avoided OpR damage. The white part indicated by the white arrow is the OpR. OpR, optic radiation.

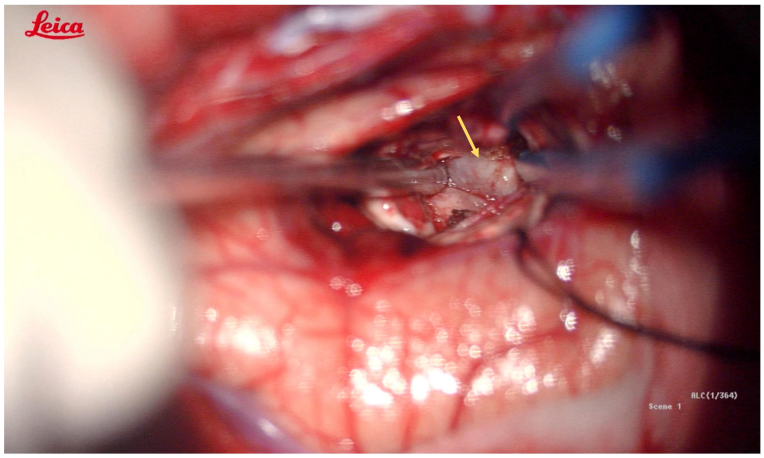

FIGURE 6
(Patient No.12) During the operation, a gray-white tumor with tough texture, unclear boundary and normal blood supply was seen. The rapid pathology suggested an anaplastic glioma (WHO III). The yellow arrow indicates the tumor.

unfavorable despite VEP monitoring during surgery (28). Some reports note that it was not possible to stably monitor VEP during surgery for patients with VA < 0.4 (16). Individual variation in the anatomy of the OpR also increases the risk of damaging the anterior part of the OpR during surgery (29). The application of neuronavigation integrated with DTI can solve this problem. Nine patients in our study with VA < 0.4 on at least one side were well operated on and using multiple ROIs to seed the OpR generated an accurate prediction of OpR anatomy. The application of DTI integrated with neuronavigation can help to precisely locate the lesion and plan the surgical incision and approach. For deep lesions with unclear boundaries, it can also help the operator judge the degree of lesion resection and the relationship between important functional areas and the lesion. Nonetheless, DTI has a significant disadvantage that it is not a "real-time" surgical adjunct. Surgeons must consider changes in the intraoperative anatomy, including midline shift, swelling, relaxation of the cisterns, or anatomical changes during or after tumor resection that may make the DTI inaccurate (30, 31). In our study, 25 patients (89.3%) had a postoperative EOR > 90% and no patient's VA or VFI were worse 2 months after discharge. Furthermore, VA, VFI, visual function, and QOL scores had a statistically significant difference compared to the time of admission ($P < 0.05$). Apart from this application and the aforementioned strategy of intraoperative OpR positioning (under the subtitle 'Intraoperative Neuronavigation and

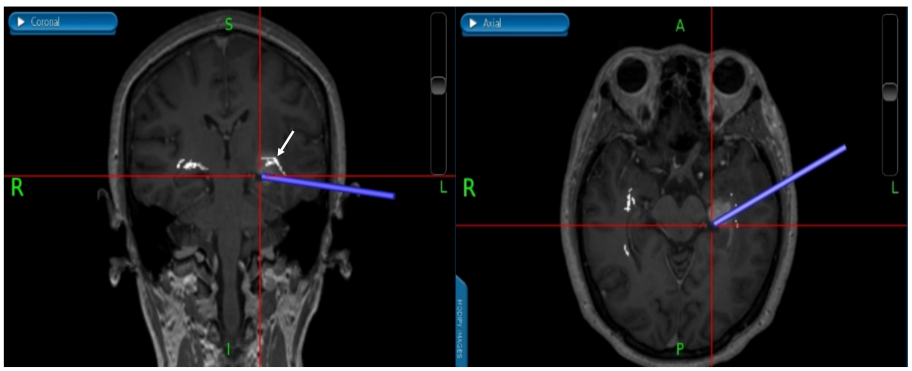

FIGURE 7
(Patient No.12) We used neuronavigation to avoid damage to the brain stem and the real time neuronavigation imaging showed that gross total resection was performed without any injuries of the OpR. The white arrow indicates the OpR. (OpR: optic radiation).

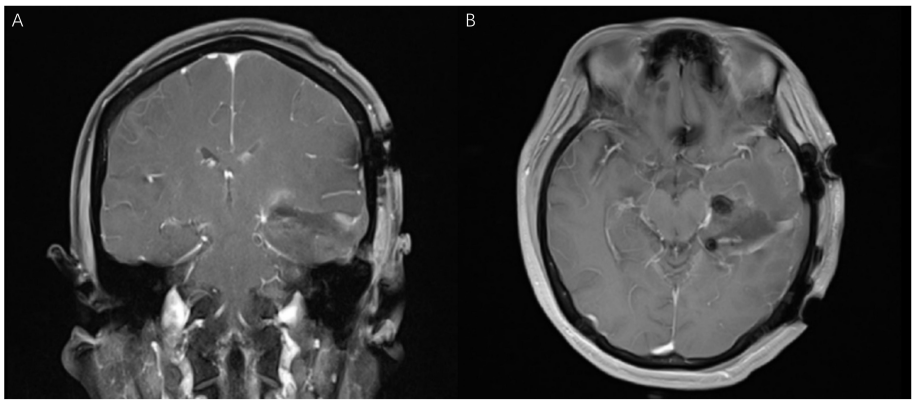

FIGURE 8
(Patient No.12) The coronal **(A)** and axial **(B)** MR T1 weighted images (one day after operation) confirmed the gross total resection of the tumor. The visual functions were well protected.

Surgery'), other possible explanations can be given for this result as follows: (i) With a special focus on visual protection, we tried to preserve the OpR as much as possible based on intraoperative rapid pathology, especially for the patients with an OpR morphology score of 3 or 4. This may not be the best choice for patients with higher levels of malignant tumors. (ii) The follow-up was not long enough to provide a reliable and convincing conclusion and make inevitable causal inferences. This makes the results have the potential to be inflated.

Previous studies have proved that tumor size and tumor-related edema are associated with unfavorable visual outcomes in patients with intracranial tumors (32, 33). The Meyer loop is closely related to the anterior tip of the lateral ventricle and each additional 1 mm of damage to the Meyer loop causes an additional 5% loss of the upper quadrant (34). In our study, lesion size, edema, and involvement of the lateral ventricle temporal horn were closely associated with OpR morphological damage. In addition, we performed regression analysis between preoperative and postoperative VA, VFI, visual function, QOL, and other clinical factors. The preoperative multiple linear regression results suggest that larger tumor size is the most important indicator of poor visual outcomes. Advanced age (β = -5.33, 95%CI: -7.01~-3.65, P = 0.004), edema (β = -7.46, 95%CI: -10.83~-4.09, P = 0.037), and involvement of the lateral ventricle temporal horn (β = -7.71, 95%CI: -10.50~-4.92, P = 0.011) affected patients' preoperative QOL the most.

We did not find significant associations of postoperative VA or VFI with sex, age, tumor size, edema, invasion into the temporal horn, or extent of tumor resection. Preoperative OpR morphology likely played a significant role in the preservation and improvement of postoperative visual function in our study (OR = 0.203, 95% CI: 0.036–0.731, P = 0.033). While the aforementioned factors, including lesion size, edema, and involvement of the lateral ventricle temporal horn, were highly correlated with preoperative OpR morphology, they do not appear to be significantly associated with postoperative OpR morphology. This means that these factors can be partially or entirely resolved during surgery, but can also be due to the small sample size of patients. Severe damage to the OpR, such as deformation or interruption, cannot be reversed. Lastly, involvement of the lateral ventricle temporal horn (OR = 17.542, 95% CI: 2.678–206.021, P = 0.007) was the main clinical factor affecting postoperative QOL.

Strengths and limitations

Our study supports that DTI integrated with neuronavigation is of value for designing surgical strategies to avoid OpR injury in this context and potentially in other pathologies, such as temporal lobe resection for epilepsy. It is supposed to be the first study introducing the application of DTI tractography integrated with neuronavigation in tumor resection with a focus on visual protection to the knowledge of the authors. We extracted as much patient information as possible to conduct a multivariate regression analysis to identify factors related to preoperative and postoperative VA, VFI, visual function and QOL. These findings are useful for assessing a patient's condition and predicting the prognosis in clinical practice.

Although all patients in our study had satisfactory visual function and QOL outcomes, several limitations should be recognized. Firstly, the number of patients was insufficient to achieve robust results, and the histological types were heterogeneous across patients. Consequently, the involvement of the subcortical bundles cannot be compared. Secondly, due to limited time, an insufficient number of patients, and heterogeneity of tumor pathology, we were unable to conduct

a prospective comparative trial. Though similar studies have been discussed, it is difficult to make inevitable causal inferences (35). Thirdly, the follow-up period (2 months) was relatively short, which may cause heterogeneity in the regression results to some extent. Further research needs to be conducted to ensure the applicability and effectiveness of this technology before implementation in routine clinical practice.

Conclusion

Despite advances in surgical technique, visual damage remains common following surgeries performed in the optic radiation area. The application of neuronavigation integrated with diffusion tensor imaging tractography can support effective tumor resection with less injury to the OpR, thereby reducing postoperative visual function decline and improving quality of life. Tumor size was identified as the main reason for poor preoperative visual function. Only severe damage to OpR morphology, whether caused by the disease itself or accidental injury during surgery, can lead to an irreversible decline in postoperative visual function. Further research involving more patients is needed to ensure the applicability and effectiveness of this strategy.

Data availability statement

The original contributions presented in the study are included in the article/Supplementary Material. Further inquiries can be directed to the corresponding author.

Ethics statement

This study was approved by the Nanjing Brain Hospital Ethics Committee and informed written consent was obtained from all patients. Written informed consent to participate in this study was provided by the participants' legal guardian/next of kin.

Author contributions

Author contributions to the study and the manuscript preparation. Conception and design, JS, RP, HC, and YZ. Methodology, JS, DL, and RP; Investigation, JS, RP, HC, FB, QZ, and YZ. Formal Analysis, JS and DL. Writing Original Draft, JS, RP, HC, and HT. Writing - Review and Editing, JS, RP, and YZ. Supervision, JS and HT. Funding Acquisition, YZ and HT. All authors contributed to the article and approved the submitted version.

Funding

This study was supported by the project of Nanjing Medical Youth Talent (No. QRX11010).

Conflict of interest

The authors declare that the research was conducted in the absence of any commercial or financial relationships that could be construed as a potential conflict of interest.

Publisher's note

Supplementary material

The Supplementary Material for this article can be found online at: https://www.frontiersin.org/articles/10.3389/fonc.2022.955418/full#supplementary-material

References

1. Winston GP, Daga P, White MJ, Micallef C, Miserocchi A, Mancini L, et al. Preventing visual field deficits from neurosurgery. *Neurology* (2014) 83(7):604–11. doi: 10.1212/WNL.0000000000000685

2. Vakharia VN, Vos SB, Winston GP, Gutman MJ, Wykes V, McEvoy AW, et al. Intraoperative overlay of optic radiation tractography during anteromesial temporal resection: a prospective validation study. *J Neurosurg* (2022) 136(2):543–52. doi: 10.3171/2020.12.JNS203437

3. Zeineh MM, Holdsworth S, Skare S, Atlas SW, Bammer R. Ultra-high resolution diffusion tensor imaging of the microscopic pathways of the medial temporal lobe. *NeuroImage* (2012) 62(3):2065–82. doi: 10.1016/j.neuroimage.2012.05.065

4. Savardekar AR, Patra DP, Thakur JD, Narayan V, Mohammed N, Bollam P, et al. Preoperative diffusion tensor imaging-fiber tracking for facial nerve identification in vestibular schwannoma: a systematic review on its evolution and current status with a pooled data analysis of surgical concordance rates. *Neurosurg Focus* (2018) 44(3):E5. doi: 10.3171/2017.12.FOCUS17672

5. Chen X, Weigel D, Ganslandt O, Buchfelder M, Nimsky C. Prediction of visual field deficits by diffusion tensor imaging in temporal lobe epilepsy

surgery. *NeuroImage* (2009) 45(2):286–97. doi: 10.1016/j.neuroimage.2008.11.038

6. Henderson F, Abdullah KG, Verma R, Brem S. Tractography and the connectome in neurosurgical treatment of gliomas: the premise, the progress, and the potential. *Neurosurg Focus* (2020) 48(2):E6. doi: 10.3171/2019.11.FOCUS19785

7. Zhang H, Feng Y, Cheng L, Liu J, Li H, Jiang H. Application of diffusion tensor tractography in the surgical treatment of brain tumors located in functional areas. *Oncol Lett* (2020) 19(1):615–22. doi: 10.3892/ol.2019.11167

8. Fletcher AE, Ellwein LB, Selvaraj S, Vijaykumar V, Rahmathullah R, Thulasiraj RD. Measurements of vision function and quality of life in patients with cataracts in southern india. report of instrument development. *Arch Ophthalmol (Chicago Ill 1960)* (1997) 115(6):767–74. doi: 10.1001/archopht.1997.01100150769013

9. Staquet M, Berzon R, Osoba D, Machin D. Guidelines for reporting results of quality of life assessments in clinical trials. *Qual Life Res Int J Qual Life Aspects Treatment Care Rehabil* (1996) 5(5):496–502. doi: 10.1007/BF00540022

10. Borius PY, Roux FE, Valton L, Sol JC, Lotterie JA, Berry I. Can DTI fiber tracking of the optic radiations predict visual deficit after surgery? *Clin Neurol Neurosurg* (2014) 122:87–91. doi: 10.1016/j.clineuro.2014.04.017

11. Lazar M, Alexander AL, Thottakara PJ, Badie B, Field AS. White matter reorganization after surgical resection of brain tumors and vascular malformations. *AJNR Am J Neuroradiol* (2006) 27(6):1258–71.

12. Ruiz-Garcia H, Middlebrooks EH, Trifiletti DM, Chaichana KL, Quinones-Hinojosa A, Sheehan JP. The extent of resection in gliomas-Evidence-Based recommendations on methodological aspects of research design. *World Neurosurg* (2022) 161:382–395.e383. doi: 10.1016/j.wneu.2021.08.140

13. Karschnia P, Vogelbaum MA, van den Bent M, Cahill DP, Bello L, Narita Y, et al. Evidence-based recommendations on categories for extent of resection in diffuse glioma. *Eur J Cancer (Oxford Engl 1990)* (2021) 149:23–33. doi: 10.1016/j.ejca.2021.03.002

14. Falco-Walter JJ, Scheffer IE, Fisher RS. The new definition and classification of seizures and epilepsy. *Epilepsy Res* (2018) 139:73–9. doi: 10.1016/j.eplepsyres.2017.11.015

15. Daga P, Winston G, Modat M, White M, Mancini L, Cardoso MJ, et al. Accurate localization of optic radiation during neurosurgery in an interventional MRI suite. *IEEE Trans Med Imaging* (2012) 31(4):882–91. doi: 10.1109/TMI.2011.2179668

16. Krolak-Salmon P, Guenot M, Tiliket C, Isnard J, Sindou M, Mauguiere F, et al. Anatomy of optic nerve radiations as assessed by static perimetry and MRI after tailored temporal lobectomy. *Br J Ophthalmol* (2000) 84(8):884–9. doi: 10.1136/bjo.84.8.884

17. Koutsarnakis C, Kalyvas AV, Komaitis S, Liakos F, Skandalakis GP, Anagnostopoulos C, et al. Defining the relationship of the optic radiation to the roof and floor of the ventricular atrium: a focused microanatomical study. *J Neurosurg* (2018) 2018:1–12. doi: 10.3171/2017.10.JNS171836

18. Gargiulo P, Árnadóttir I, Gíslason M, Edmunds K, Ólafsson I. New directions in 3D medical modeling: 3D-printing anatomy and functions in neurosurgical planning. *J Healthcare Eng* (2017) 2017. doi: 10.1155/2017/1439643

19. Bertani GA, Bertulli L, Scola E, Di Cristofori A, Zavanone M, Triulzi F, et al. Optic radiation diffusion tensor imaging tractography: An alternative and simple technique for the accurate detection of meyer's loop. *World Neurosurg* (2018) 117:e42–56. doi: 10.1016/j.wneu.2018.05.131

20. Sherbondy AJ, Dougherty RF, Napel S, Wandell BA. Identifying the human optic radiation using diffusion imaging and fiber tractography. *J Vision* (2008) 8(10):12.11–11. doi: 10.1167/8.10.12

21. Jobst BC, Cascino GD. Resective epilepsy surgery for drug-resistant focal epilepsy: a review. *Jama* (2015) 313(3):285–93. doi: 10.1001/jama.2014.17426

22. Grote A, Witt JA, Surges R, von Lehe M, Pieper M, Elger CE, et al. A second chance–reoperation in patients with failed surgery for intractable epilepsy: long-term outcome, neuropsychology and complications. *J Neurol Neurosurg Psychiatry* (2016) 87(4):379–85. doi: 10.1136/jnnp-2015-310322

23. Pathak-Ray V, Ray A, Walters R, Hatfield R. Detection of visual field defects in patients after anterior temporal lobectomy for mesial temporal sclerosis-establishing eligibility to drive. *Eye (London England)* (2002) 16(6):744–8. doi: 10.1038/sj.eye.6700152

24. Jeelani NU, Jindahra P, Tamber MS, Poon TL, Kabasele P, James-Galton M, et al. 'Hemispherical asymmetry in the meyer's loop': a prospective study of visual-field deficits in 105 cases undergoing anterior temporal lobe resection for epilepsy. *J Neurol Neurosurg Psychiatry* (2010) 81(9):985–91. doi: 10.1136/jnnp.2009.182378

25. Hughes TS, Abou-Khalil B, Lavin PJ, Fakhoury T, Blumenkopf B, Donahue SP. Visual field defects after temporal lobe resection: a prospective quantitative analysis. *Neurology* (1999) 53(1):167–72. doi: 10.1212/WNL.53.1.167

26. Helgason C, Caplan LR, Goodwin J, Hedges T3rd. Anterior choroidal artery-territory infarction. report of cases and review. *Arch Neurol* (1986) 43(7):681–6. doi: 10.1001/archneur.1986.00520070039015

27. Sincoff EH, Tan Y, Abdulrauf SI. White matter fiber dissection of the optic radiations of the temporal lobe and implications for surgical approaches to the temporal horn. *J Neurosurg* (2004) 101(5):739–46. doi: 10.3171/jns.2004.101.5.0739

28. Cedzich C, Schramm J, Fahlbusch R. Are flash-evoked visual potentials useful for intraoperative monitoring of visual pathway function? *Neurosurgery* (1987) 21(5):709–15. doi: 10.1227/00006123-198711000-00018

29. Nilsson D, Starck G, Ljungberg M, Ribbelin S, Jönsson L, Malmgren K, et al. Intersubject variability in the anterior extent of the optic radiation assessed by tractography. *Epilepsy Res* (2007) 77(1):11–6. doi: 10.1016/j.eplepsyres.2007.07.012

30. Salama GR, Heier LA, Patel P, Ramakrishna R, Magge R, Tsiouris AJ. Diffusion Weighted/Tensor imaging, functional MRI and perfusion weighted imaging in glioblastoma-foundations and future. *Front Neurol* (2017) 8:660. doi: 10.3389/fneur.2017.00660

31. Choi EB, Jang SH. Diffusion tensor imaging studies on recovery of injured optic radiation: A minireview. *Neural Plasticity* (2020) 2020:8881224. doi: 10.1155/2020/8881224

32. Ju DG, Jeon C, Kim KH, Park KA, Hong SD, Seoul HJ, et al. Clinical significance of tumor-related edema of optic tract affecting visual function in patients with sellar and suprasellar tumors. *World Neurosurg* (2019) 132:e862–8. doi: 10.1016/j.wneu.2019.07.218

33. Leclerc A, Gaberel T, Laville MA, Derrey S, Quintyn JC, Emery E. Predictive factors of favorable visual outcome after surgery of tuberculum sellae meningiomas. a multicenter retrospective cohort study. *World Neurosurg* (2022) S1878-8750(22)00603-9. doi: 10.1016/j.wneu.2022.05.015

34. Winston GP, Daga P, Stretton J, Modat M, Symms MR, McEvoy AW, et al. Optic radiation tractography and vision in anterior temporal lobe resection. *Ann Neurol* (2012) 71(3):334–41. doi: 10.1002/ana.22619

35. Wang X, Cheng Z. Cross-sectional studies: Strengths, weaknesses, and recommendations. *Chest* (2020) 158(1s):S65–s71. doi: 10.1016/j.chest.2020.03.012

frontiers | Frontiers in Oncology

TYPE Review
PUBLISHED 03 October 2022
DOI 10.3389/fonc.2022.998384

OPEN ACCESS

EDITED BY
Santiago Cepeda,
Hospital Universitario Río Hortega, Spain

REVIEWED BY
Liwei Zhang,
Beijing Neurosurgical Institute, Capital Medical University, China
Archya Dasgupta,
Tata Memorial Hospital, India

*CORRESPONDENCE
Francesco Acerbi
francesco.acerbi@istituto-besta.it

†These authors have contributed equally to this work

‡These authors share first authorship

SPECIALTY SECTION
This article was submitted to Neuro-Oncology and Neurosurgical Oncology, a section of the journal Frontiers in Oncology

RECEIVED 19 July 2022
ACCEPTED 08 September 2022
PUBLISHED 03 October 2022

CITATION
Restelli F, Mathis AM, Höhne J, Mazzapicchi E, Acerbi F, Pollo B and Quint K (2022) Confocal laser imaging in neurosurgery: A comprehensive review of sodium fluorescein-based CONVIVO preclinical and clinical applications.
Front. Oncol. 12:998384.
doi: 10.3389/fonc.2022.998384

Confocal laser imaging in neurosurgery: A comprehensive review of sodium fluorescein-based CONVIVO preclinical and clinical applications

Francesco Restelli[1†‡], Andrea Maria Mathis[2†‡], Julius Höhne[3], Elio Mazzapicchi[1], Francesco Acerbi[1*], Bianca Pollo[4] and Karl Quint[5†]

[1]Department of Neurosurgery, Fondazione Istituto di Ricerca e Cura a Carattere Scientifico (IRCCS) Istituto Neurologico Carlo Besta, Milan, Italy, [2]Department of Neurosurgery, Inselspital, Bern University Hospital, University of Bern, Bern, Switzerland, [3]Department of Neurosurgery, Universitätsklinikum, Regensburg, Germany, [4]Department of Neuropathology, Fondazione Istituto di Ricerca e Cura a Carattere Scientifico (IRCCS) Istituto Neurologico Carlo Besta, Milan, Italy, [5]Quint Healthcare, Fürth, Germany

Given the established direct correlation that exists among extent of resection and postoperative survival in brain tumors, obtaining complete resections is of primary importance. Apart from the various technological advancements that have been introduced in current clinical practice, histopathological study still remains the gold-standard for definitive diagnosis. Frozen section analysis still represents the most rapid and used intraoperative histopathological method that allows for an intraoperative differential diagnosis. Nevertheless, such technique owes some intrinsic limitations that limit its overall potential in obtaining real-time diagnosis during surgery. In this context, confocal laser technology has been suggested as a promising method to have near real-time intraoperative histological images in neurosurgery, thanks to the results of various studies performed in other non-neurosurgical fields. Still far to be routinely implemented in current neurosurgical practice, pertinent literature is growing quickly, and various reports have recently demonstrated the utility of this technology in both preclinical and clinical settings in identifying brain tumors, microvasculature, and tumor margins, when coupled to the intravenous administration of sodium fluorescein. Specifically in neurosurgery, among different available devices, the ZEISS CONVIVO system probably boasts the most recent and largest number of experimental studies assessing its usefulness, which has been confirmed for identifying brain tumors, offering a diagnosis and distinguishing between healthy and pathologic tissue, and studying brain vessels. The main objective of this systematic review is to

present a state-of-the-art summary on sodium fluorescein-based preclinical and clinical applications of the ZEISS CONVIVO in neurosurgery.

KEYWORDS

confocal laser endomicroscopy (CLE), confocal imaging, confocal laser microscopy (CLM), *in vivo* imaging, neurosurgery, brain tumors, sodium fluorescein

Introduction

Despite recent therapeutic advances, the prognosis of brain tumors remains poor (1, 2). Surgical resection has a leading role in the treatment of brain tumors, given the results of different clinical trials that have shown that extent of resection (EOR) correlates with better outcomes, especially when combined with adjuvant therapies such as radiotherapy and chemotherapy. Nevertheless, it is well known that Gross Total Removal is not always possible and this aspect is mainly related to the fact that distinction between normal and pathologic tissue is often difficult, especially at the tumor margins (2–5).

Among the several tools and devices that have been implemented in recent years with the objective of increasing EOR, such as intraoperative ultrasound, neuronavigation, and the use of fluorophores, which can improve visualization of tumor tissue during surgery, showing to improve tumor margin identification and lead to more extensive resections (6–9), to date only histopathologic techniques can microscopically identify tumor cells and the actual infiltration at the tumor margins.

Histopathologic analysis remains the gold standard for definitive diagnosis, with frozen section role as the most rapid, used and diffused intraoperative histopathologic method that can offer intraoperative differential diagnosis. Nevertheless, the results obtained with frozen section analysis are often nondiagnostic or, worse, misleading, especially in cases of mechanical tissue destruction by the resection process (10–12). In addition, this method has other significant disadvantages. For instance, tissue sample analysis requires a long time and is usually performed outside of the operating room (OR). Moreover, the accuracy of this technology in determining diagnosis is also questioned due to a well-known diagnostic discrepancy between frozen sections and permanent sections of up to 2.7%, looking at intracranial pathologies (10). Such aspect is further complicated by the inherent heterogeneity of brain tumors. For instance, such tumors (i.e. gliomas) may contain high-grade populations embedded in a low-grade cell population and this aspect would be a significant challenge for the pathologist. For these reasons frozen section analysis still remains an unsatisfactory technology for revealing the histologic features necessary for the final diagnosis, especially if a task of "guiding intraoperative decisions" about EOR is wondered.

In this context, confocal laser technology demonstrated to be a technique that is able to provide real-time microscopic information about tissues and for such reasons it has already been included into common clinical practice in non-neurosurgical fields. Considering the technology, briefly, a laser source is used to deliver light *via* an optical fiber coupler and scanned delivery fiber to a lens system. The lens system that is mounted at the front of the scanner focuses the laser light into the sample to a depth set by a Z depth focusing mechanism integral to the scanner. A fluorescent dye that is in the tissue of interest is excited by the laser light. The fluorescence is collected by the lens system and focused onto the tip of the scanned delivery optical fiber. The optical fiber acts as a confocal pinhole rejecting light other than that from the set Z depth. The fluorescent light is carried to the confocal processor *via* the optical fiber through a fiber based optical coupler and into a detector. The detector synchronously samples the fluorescence providing an electrical representation of the light intensity that is recorded as a digital sample. The digital samples are constructed into an image frame that is sent *via* a digital interface to the integration computer. The integration computer uses custom host software to deliver the image data to a monitor for display and further analysis (Figure 1).

Confocal laser endomicroscopy (CLE) has been implemented with good results in general surgery, or in gastroenterology, urology, and gynecology, where very often a careful examination of pathologic margins is mandatory (13–16). In neurosurgery, CLE is still far from being routinely used, but in recent years it has been proposed in this field. The first studies in mouse glioblastoma (GBM) models were focused on distinguishing normal brain from microvasculature and tumor margins (17–19). After such initial preclinical experiences, the feasibility of CLE in human brain tumors was investigated both in *ex vivo* and *in vivo* studies with promising results (20–23). Second generation CLE systems, such as the ZEISS CONVIVO (Carl Zeiss Meditec AG, Oberkochen, Germany), have been specifically ideated for neurosurgical use and have undergone a deep investigation in recent years. CONVIVO was studied in animal models and in *ex vivo* and *in vivo* experiences, preliminary confirming its ability, when coupled to sodium fluorescein (SF) intravenous injection, in

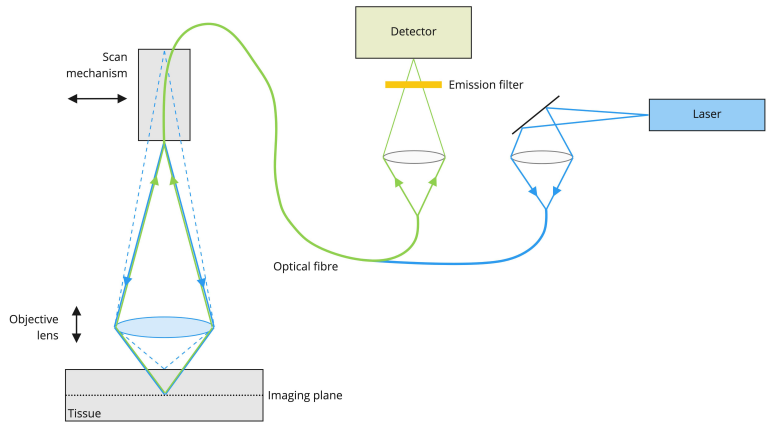

FIGURE 1
CONVIVO system mechanism of action. A laser-beam with a specific wavelength is focused on a point inside the object at a specific Z depth. A fluorescent dye that is in the tissue of interest is excited by the laser light and the fluorescence is collected by the lens system and focused onto the tip of the scanned delivery optical fiber, that acts as a confocal pinhole rejecting light other than that from the set Z depth. Then, the fluorescent light is carried to the confocal processor *via* the optical fiber through a fiber based optical coupler and into a detector, which synchronously samples the fluorescence providing an electrical representation of the light intensity that is recorded as a digital sample. The digital samples are constructed into an image frame that is sent *via* a digital interface to the integration computer. The integration computer uses custom host software to deliver the image data to a monitor for display and further analysis.

intraoperatively providing a large number of optical biopsies with imaging of cells at the microscopic/histologic level, representing the first technique able to provide real-time *in vivo* histopathological data from fresh tissue (24–29). Such aspects also lead to FDA approval of the machine for intracranial neurosurgical procedures in the US (30).

Overall, the neurosurgical literature suggests that this technology is capable of intraoperatively providing information regarding tumor tissue, both for diagnosis and for identifying tumor at periphery. Nevertheless, also due to the paucity of data available, the precise sensitivity, specificity, and accuracy in identifying tumor cells and the actual role this technology could play in neurosurgery soon are still under in-depth investigation.

The main objective of this systematic review is to present an update on the actual SF-based preclinical and clinical applications of the ZEISS CONVIVO in neurosurgery.

Material and methods

Literature search and screening process

A comprehensive literature search was performed in March 2022 and updated in July 2022 to include papers published since. MEDLINE (PubMed), EMBASE and SCOPUS were searched using the following search strings in the "Title/abstract" field: "confocal AND neurosurgery", "confocal AND glioma", "confocal AND brain tumor", "endomicroscopy AND neurosurgery", "endomicroscopy AND brain tumor", "endomicroscopy AND glioma", "confocal imaging AND glioma", "confocal imaging AND brain tumor", "confocal imaging AND neurosurgery", "confocal endomicroscopy AND glioma", "confocal endomicroscopy time limits AND brain tumor", "confocal endomicroscopy AND neurosurgery", "Convivo AND glioma", "Convivo AND brain tumor", "Convivo AND neurosurgery" (published article until July 15th, 2022).

Search was limited to articles in English. All titles and abstracts were checked by two different researchers (F.R. and K.Q.). Frank duplicates were removed. Relevant works were collected, organized, and studied. Furthermore, bibliographies were hand-searched to identify further relevant literature.

If there was a difference in opinion on appropriateness of the works among the researchers, a consensus was reached consulting a third reviewer (A.M.). In order to further broaden the search process for studies that might have been missed through the first search, during this first-phase pure reviews on the topic were not excluded a priori. Given the large differences in patients' cohorts and methodologies used in the different studies analyzed, the literature search did not strictly follow the criteria for a systematic review, therefore trying to identify the highest quality of available evidence for each specific theme.

Eligibility criteria

After the screening process, remaining articles were completely read and analyzed by two authors (F.R. and K.Q.). The authors checked for their relevance and eventual accordance

with our inclusion and exclusion criteria. In particular, only studies concerning *in vivo* or *ex vivo* applications of CONVIVO confocal imaging technology coupled with intravenous SF administration in neurosurgery were analyzed. We decided to include in the review also the clinical results of preclinical works (works with both a preclinical and a clinical experimental part). The following inclusion/exclusion criteria were applied:

Inclusion criteria:

- -Clinical works based on SF-CONVIVO imaging technology applications in neurosurgery;
- -preclinical works with some clinical results related to SF-based CONVIVO confocal imaging technology in neurosurgery;
- -case reports, in which SF-based CONVIVO imaging was performed.

Exclusion criteria: Correspondences, Comments, Letters to the Editor, Proceedings and Conference Papers, purely preclinical studies.

Data extraction

All included studies were extracted and summarized in tables. Authors, year of publication, journal of publication, type of study, CLE system used, fluorophore used, dosage and timing, fluorophore re-administration, number of cases, tumor type(s), study description, main findings and results related to diagnostic performance from each study were reported. Due to the large heterogeneity of the available and identified studies, considering also the limited number of published works, we present the data as a narrative review.

Statistical analysis

Statistical analysis of the data, for the purpose of a meta-analysis, was not possible due to substantial heterogeneity in study design and populations.

Results

A total of 1645 hits were found by the first search among the three Databases (Pubmed 260, EMBASE 435, SCOPUS 950). Among the works we found, 30 works were completely screened reading titles and abstracts, removing duplicates. Finally, 12 full-text articles were considered for eligibility, finding all of them suitable for the final review analysis (Figure 2).

Preclinical studies

The CONVIVO system, designed specifically for neurosurgical use cases, was developed based on a first-generation CLE system designed for gastrointestinal use (Optiscan Pty., Ltd., Mulgrave, Australia). In a rodent glioma model study, Belykh et al. investigated performance improvements of the CONVIVO system (Gen2) compared to

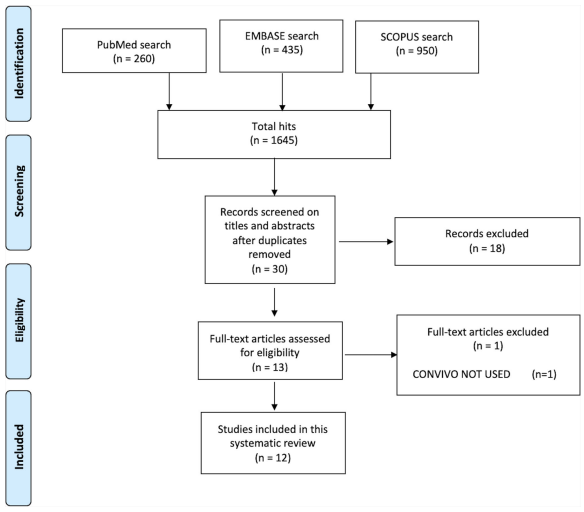

FIGURE 2
The flowchart of search hits and the different Preferred Reporting Items for Systematic reviews and Meta-analyses (PRISMA)-guideline selection phases, from the initial search and the follow-up search (B), resulting in the total 12 included articles.

the Optiscan system (Gen1) (25). Performance in visualization of vessels, normal brain and tumor cells was similar with both systems. Compared to Gen1, Gen2 showed a smaller field of view, but much higher image resolution and better image quality. Further advantages of the Gen2 compared to Gen1 were a more friendly user interface, metadata handling and image transfer process. Gen2 moreover offers a z-stack imaging mode, enabling 3D visualization of tissue areas. In the scope of this study, they administered different concentrations of SF and showed that overall performance is improved when using higher dosages (20 and 40 mg/kg vs. 0.1–8 mg/kg).

In a work from 2018, Belykh et al. investigated the diagnostic accuracy of *in-vivo* CLE in identifying different types of brain tissue (normal brain, injured brain and brain with tumor tissue in a mouse glioma model) (26). Ten female, 10-week old mice were injected with mouse glioma cells to establish a glioma model according to a previously defined protocol (17). Animals were injected with 1 mg/mL (n=3), 0.1 mg/mL (n=4) or no SF (n=3). Using the CONVIVO system (Carl Zeiss Meditec AG) imaging was performed 15 to 60 minutes after SF administration and 10 to 30 minutes after injury to normal brain, at known locations of 1) tumor (n = 60) and 2) injured normal brain (n = 25), in animals administered with SF; and 3) normal brain tissue (n = 5) in control animals (no SF administration). A set of CLE images (n = 40) was given to trained experts for assessing type of tissue (1, 2 or 3). As reference served the diagnosis based on H&E image of correlative specimens. Mean accuracy for correctly differentiating tumor from injured or non-tumor tissue was 85%. Accuracy, specificity, and sensitivity for discriminating tumor from non-tumor tissue was 90%, 86% and 96% respectively.

Ex vivo experiences

In 2018 Belykh and colleagues performed an interesting work where they obtained CLE imaging, Z-stack acquisition, and 3D image rendering of 31 human tumors. In this analysis meningiomas, gliomas, and pituitary adenomas were analyzed *ex vivo*. In this work, for the first time, the CONVIVO system (Carl Zeiss Meditec AG), was used to image human tissue (31). In this specific work, 2-5 mg/kg of SF were administered intravenously 5-60 minutes before imaging in 22 out of the 31 patients in total. Biopsy specimens obtained in the fluorescent tumor areas of patients who received SF intraoperatively were then imaged in the operative room with the help of a stand-alone CLE system within 1–10 minutes after specimen acquisition. No further data on SF protocol of administration were given. Comprehensively, Belykh provided detailed 3D images of different kinds of brain tumors, suggesting that this technology might allow for an increased spatial understanding of tumor cellular architecture, also increasing visualization of surrounding related structures compared with two-dimensional images.

Some years later, the same group used CONVIVO on 47 patients with a total of 122 biopsies analyzed (29 HGGs) (28). The authors were interested in performing a sensibility/specificity study, using a classical SF administration protocol (SF 2 mg/kg for patients with gliomas and meningiomas, SF 5 mg/kg in patients with metastasis). Comprehensively the authors found a positive predictive value of CLE optical biopsies of 97% for all specimens, while a positive predictive value of CLE optical biopsies of 98% for gliomas. Specificity was found to be 90% for all specimens and 94% for gliomas. Furthermore, the authors described improved image quality percentage of accurately diagnosed images (67% vs. 93%) in those cases where a second SF injection was performed during the surgery (after a mean of 2.6 h after the first injection, 5 mg/kg intravenously upon request), suggesting for the first time that a re-administration of SF during the surgical procedure may increase the diagnostic value of the images taken with CONVIVO.

In 2019, the group of Schebesch reviewed their recent experience in a neuro-oncology center, demonstrating the possibility of operating while combining different imaging modalities intraoperatively. They presented three cases with an *ex vivo* analysis by CONVIVO with a 5 mg/kg SF protocol at anesthesia induction (a supratentorial astrocytoma WHO III, a motor area glioblastoma WHO IV and an oligodendroglioma WHO grade III). All these cases were managed combining different visualization modalities, such as high-definition endoscopes, fluorescence-guided surgery and confocal endomicroscopy with CONVIVO. Besides indicating the dosage used, no further details of the imaging procedure were reported (32).

In 2020, the group of Acerbi and colleagues studied the ability of Convivo in offering an intraoperative first-diagnosis during GBM removal *ex vivo*. The authors blindly compared intraoperative CLE and frozen/permanent sections results at both central core and tumor margins of tumors (29). In this specific context, the main objective of the authors was to both check for CONVIVO ability in offering an intraoperative diagnosis and in categorizing morphological patterns (i.e. cellularity, vascularization and necrosis). SF was administered following Acerbi and colleagues recommendations regarding SF usage in neuro-oncological surgery (29). Five mg/kg of SF at anesthesia induction permitted an acceptable identification of tumor tissue during the resections, allowing also to perform CONVIVO analysis. In fact, blindly comparing CONVIVO and frozen sections images a high rate of concordance in both providing a correct diagnosis and categorizing patterns at tumor central core (80 and 93.3%, respectively) and at tumor margins (80% for both objectives) was disclosed. Lower rates of concordance were found if compared to permanent sections (total/partial concordance in 80 and 86.7% for diagnosis and morphological categorization, respectively).

In 2021, Abramov and colleagues investigated the effects of redosing SF on CLE image quality and diagnostic accuracy. They

retrospectively analyzed *ex-vivo*-obtained CLE images from patients resected with SF-based fluorescence guidance (33). SF was administered at anesthesia induction (2 or 5 mg/kg with possibility of redosing in case CLE images brightness was considered inadequate by the neurosurgeon). Three groups of CLE images were analyzed: CLE images acquired from patients after initial dosing (initial-dose group, n = 6), after redosing once (redose group, n = 6), and images from patients without a redosing (single-dose group, n = 9). Images were compared for brightness and contrast, image quality, and qualitative image assessment and diagnostic accuracy by 7 reviewers with different levels of experience. Brightness and contrast of the images were not significantly different when SF was administered at 2 or 5 mg/kg. Across the image groups, brightness and contrast were significantly higher in the redose group vs. initial-dose group and in the initial-dose group vs. the single-dose group ($p < 0.001$ for each). In matched analysis between the initial-dose imaging group vs. the single-dose imaging group, this could be attributed to the timing of the imaging (93.9 ± 50.1 minutes vs. 123.2 ± 35.9 min, $p = 0.002$). A moderate correlation between the timing of imaging and image brightness and contrast of the CLE biopsies was also found (brightness: rho = -0.52, $p < 0.001$; contrast: rho = -0.57, $p < 0.001$), indicating that image acquisition early after SF administration leads to a better image quality. Qualitative image assessment revealed the highest scores in the redose group, followed by the initial-dose and the single-dose groups. Diagnostic accuracy in the redose group, in which images were acquired at a mean of only 6.4 minutes after SF redosing, was 83% regardless of reviewer experience. The time-dependent kinetics and limited signal duration of SF fluorescence resulted in darker images and worse contrast with increasing imaging time, which ranged between 3 and 180 minutes in this *ex-vivo* study.

Belykh and colleagues from the group of Mark Preul undertook a feasibility study for CLE imaging of pituitary adenomas in 2020 (34). In a first feasibility approach, the CONVIVO imaging probe was successfully introduced through the transnasal transsphenoidal corridor in cadaveric specimens and was deemed adequate for imaging of the pituitary area. Secondly, resected human pituitary adenoma tissue samples were imaged *ex-vivo* and compared against standard H&E histology and/or frozen sections. CLE images resembled the tissue and cellular features known from standard histology, showing cells with prominent nuclei, non-organized tissue structure, vascularity, and stroma. There was a heterogeneous uptake of SF that created a nuclear/cytoplasmic contrast along with a contrast between neighboring cells. Depending on the classification used (tissue description or definitive tumor diagnosis), the concordance of the CLE biopsies with either frozen section or permanent histology ranged between 53.8% and 100%. Details of the analysis are described in Supplementary Table 1. Some CLE images were classified as non-diagnostic due to very early (< 1 minute) or late (> 10 minutes) acquisition following SF administration, leading to suboptimal contrasting of the cellular outlines. Other reasons for nondiagnostic images included erythrocyte contamination obstructing the field of view or too small physical samples, which prevented finding an optimal imaging spot.

An interesting case report was published by Belykh and colleagues in 2021 of a patient with an non-enhancing WHO II/III anaplastic oligodendroglioma, predominantly low-grade with high-grade foci of hypercellularity and increased mitotic figures (36). The patient received a single dose of 40 mg/kg of SF at the induction of anesthesia and was subsequently resected using fluorescence-guided surgery using a Yellow 560 filter. CLE images were recorded *ex-vivo*. This dose produced a bright signal and excellent CLE images of extremely clear cellular architecture with mitotic figures, endothelium and axons. A distinct morphologic appearance, not commonly observed with lower-dose SF were observed with the brightness and clarity of the CLE images, especially at the prolonged imaging time of up to 1.5 hours. Besides the typical yellowish skin discoloration, which resolved quickly, no side effects were reported. Besides the higher than usual administered dose of SF, the authors found abnormalities in the preoperative T2/FLAIR signal surrounding the tumor mass, which may be sensitive markers of a damaged blood brain barrier, contributing to an extravasation of SF in this predominantly low-grade oligodendroglioma. In the end, the authors discuss the utility of having a higher dose of SF in those cases where only one dose is planned to be administered at the beginning of an operation and they suggest it as an appropriate approach in those cases where using sensitive imaging such as CLE for discriminating the histoarchitecture of tumor margins may be of help, for instance for LGG tissue that may not be as amenable to 5-ALA fluorescence guidance.

In vivo experiences

To date, three *in vivo* studies have already been performed.

In 2021, Höhne and colleagues published a study on feasibility, safety and potential applications of CLE (35). They performed SF-FGS and CLE-imaging in 12 patients with various CNS malignancies by using 10% SF at a dose of 5 mg/kg. The time between SF-administration and CLE-imaging varied between 10 - 120 minutes. Digital biopsies were taken at the tumor border, tumor center and the perilesional zone, defined as the infiltration/edema zone where the fluorescence signal started to become faint. The digital biopsies were compared against standard H&E histology. The authors reported a seamless integration of CLE-imaging in the surgical flow. As the CLE-probe is similar to other commonly used microsurgical instruments, CLE-imaging could be performed safely without traumatizing healthy tissue. Macroscopic SF-fluorescence was observed and considered helpful guidance in all cases. In CLE-imaging, all tumors (12/12) stained positively for SF at the tumor

border, 11/12 at the tumor center and 7/12 in the perilesional zone. At the weight-adapted dose of 5 mg/kg, a shorter time between SF administration and CLE-imaging resulted in more assessable images. No major side-effects related to the use of SF were observed. The authors concluded CLE to be safe and feasible, and that further prospective trials are needed to confirm its promising potential.

Belykh and colleagues investigated the feasibility of CLE to qualitatively and quantitatively analyze real-time blood flow patterns in brain under normal conditions, after injury and in pathologic brain and spinal cord microvasculature in a large animal model and patient samples (27). In the swine model, SF concentrations ranged from 1 - 5 mg/kg and 0.1% - 0.005%/5 ml. In human patients, 5 ml of 10% SF was administered 5 minutes prior to CLE imaging and a total of >20,000 digital CLE biopsies obtained *in-vivo* or *ex-vivo* were analyzed. Around 8 minutes after SF administration in the animal model, arterial and venous capillaries and vessels between 5 - 250 μm in diameter could be visualized. CLE visualization time extended up to 30 minutes after initial administration and for up to 3 hours when reinjecting SF. They observed a SF-based contrast in the intravascular compartment, in the vessel wall and also in the perivascular parenchyma, when the blood brain barrier was disrupted. This allowed appreciation of vessel wall cellularity, the distinction between arterial and venous vasculature and the vasculature's functional status. They observed that the fluorescence lasted longer than the intravascular contrast visible through the wide-field operation microscope. Both tissue injury, contrast extravasation, and additional injections of SF rendered visualization of the wall of the vessels much easier, rendering the vessel wall clearer at later imaging times. Intravascular events, such as the dynamics of thrombus formation during circulatory arrest, could also be observed. Additionally, lymphatic vessels in the dura could be visualized. In human samples of grade 2 and 3 astrocytomas and oligodendrogliomas and grade 4 glioblastomas, CLE visualized both normal and abnormal microvasculature. Abnormal microvasculature was characterized by disorganized nonlinear appearance and perivascular crowding of cells. Also slow or stagnant flow, perivascular leakage of fluorescent contrast, and cells attached to the inner vascular wall were observed. All such features were clearly visible in CLE images. For clinical considerations, CLE with SF allowed a substantially longer observation of blood flow compared to wide-field ICG or SF. The authors suggested potential use cases for CLE-based SF visualization of vasculature for traumatic brain injury and cerebrovascular lesions (for instance also analyzing the downstream effects of surgical vessel anastomoses or reconstruction), for flow recovery study after stroke, to study perforating vessel competency in vascular cases, studying flow dynamics in moyamoya disease/syndrome, and revealing tumor blood vessel and flow characteristics in oncological cases.

The most recent study by Abramov and colleagues from 2022 aimed to evaluate the *in vivo* safety and feasibility of the ZEISS CONVIVO for intraoperative application in human brain tumor surgery (24). The prospective 30-patient study used 5 mg/kg i.v. of SF given upon the surgeon's request within five minutes prior to imaging. Due to the sufficient quality of the resulting images, no redosing was performed. Entities included 13 gliomas (WHO I, III, and IV), 5 meningiomas (WHO I and II), 6 other primary tumors (all WHO I), 3 metastases (breast, kidney, and lung tumors), and 4 cases with reactive brain tissue following previous resection, chemo- or radiotherapy. CLE images were assessed against frozen sections and permanent histology. Across all samples, the diagnostic accuracy, sensitivity, and specificity reported for CLE vs. frozen section was 94%, 94%, and 100%; for CLE vs. permanent histology 92%, 90%, and 94%, respectively. A neuropathologist could interpret the CLE images in 97% of cases (29/30). Interpretable images were obtained within a mean of 6 images and within the first 5 seconds of imaging. Interpretable image acquisition was positively correlated with study progression, number of cases per surgeon, cumulative length of CLE time, and CLE time per case.

Discussion

In this work we have collected and reviewed the available literature on preclinical and clinical protocols for the application of SF in confocal endomicroscopy (Supplementary Table 1). We have focused on the FDA-approved device ZEISS CONVIVO, which has been designed and dimensioned specifically for use in neurosurgical applications (30). It can record digital *in vivo* and *ex vivo* tissue biopsies in real-time, prior to tissue resection, thus adding an important new tool to the neurosurgeon's and neuropathologist's armamentarium (Figure 3).

Previous studies using CLE in neurosurgery

Starting from the works published on prototype and technically compatible devices to the CONVIVO, such as the devices by OptiScan, may help in comprehending the great interest that such technology is keeping among the neurosurgical community. An initial *ex vivo* clinical study using 0.05% topical acriflavine was performed with a miniaturized confocal laser microscope from OptiScan (37). This study showed a high degree of concordance in histopathologic diagnostic criteria for glioblastoma, such as cell number and density, cell pleomorphism, mitotic figures and rate of mitosis, microvascular proliferation, and pseudopalisading necrosis. Depending on each criterion, the tumors showed various degrees of correspondence between

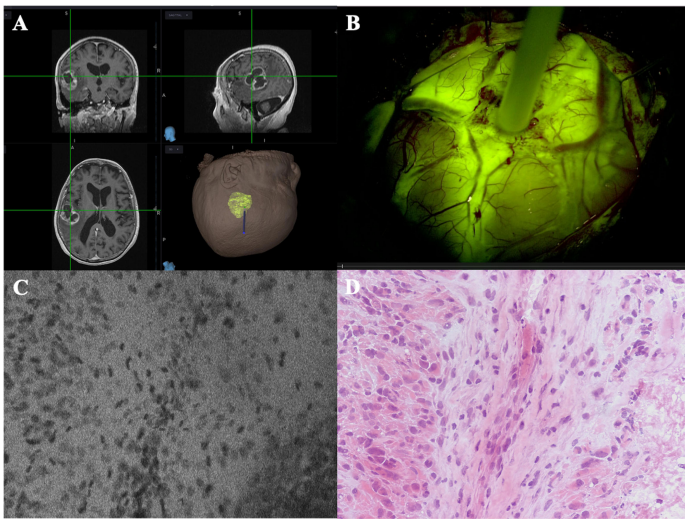

FIGURE 3
Case example of an *in vivo* GBM case analyzed with CONVIVO (courtesy of Dr. Acerbi and Dr. Pollo, Fondazione IRCCS Istituto Neurologico Carlo Besta, Milan, Italy). **(A)** MRI preoperative images of a left parieto-temporal GBM, loaded on Stealth S8 navigation system (Medtronic, Minneapolis, USA). **(B)** CONVIVO stylet placed upon the center of the tumor, on the cerebral surface. As it can be seen, the tumor intensely enhances after intravenous SF administration. **(C, D)** CONVIVO and histological images of the point where the optical biopsy with CONVIVO was obtained. Disordered groups of dark nuclei cells can be seen, along with a stromal component among them. A low fluorescence area on CONVIVO, as it occurs in necrotic parts of the tumor, can be seen in the bottom right of panel **(C)**, with its histological counterpart in the bottom right of panel **(D)**.

confocal imaging and histopathology (cell density and pleomorphism in all 100% of tumors, microvascular proliferation in 44% and mitotic figures and necrosis in 22%). Cell density analyses allowed the authors to differentiate tumor center areas from the infiltration zone on confocal images alone. In just one case, confocal images were perfectly corresponding to histopathology in all five diagnostic aspects. Due to the mutagenic effects observed for acriflavine, subsequent studies were performed with SF due to its standard usage in ophthalmology and its advantageous safety profile.

Among these studies, Eschbacher et al. have used 25 mg/kg of SF administered i.v. at the time of tumor exposure, with *ex vivo* imaging being initiated within two to five minutes and lasting from two to ten minutes (38). The study design allowed direct comparison of CLE images with standard histology. The CLE biopsies correlated well with the traditional histological findings across a variety of tumor types. Pathognomonic cytoarchitectural features could be visualized by CLE as well. Overall, 92.9% (26/28) of lesions were correctly diagnosed by CLE alone in a blinded analysis, well within the range of diagnostic accuracy between 92% and 99.7% reported for frozen sections and standard histology (10–12, 39, 40). This seminal work of Eschbacher et al., in particular, describes in detail the morphological appearance of meningiomas, schwannomas, low- and high-grade gliomas, ependymomas and hemangioblastomas, and prepared the ground for tumor-specific criteria for CLE image interpretation.

Clinical use and potential applications of new-generation CLE technology in neurosurgery

Second generation CLE systems, such as the ZEISS CONVIVO, have been specifically ideated for neurosurgical use and have undergone a deep investigation in recent years, preliminarily confirming their ability, when coupled to SF intravenous injection, in intraoperatively providing many optical biopsies with histological resolution, representing the first technique able to provide near real-time *in vivo* histopathological data from fresh tissue. Such a new-generation system has undergone a deep investigation in recent years, as anticipated above, due to multiple reasons. Intraoperatively, the time until a neuropathological diagnosis is received could be greatly shortened. The sensitivity and quickness in having an answer of such a system could influence neurosurgical decision making, particularly at the presumed margins of a tumor resection cavity. Real-time *in vivo* histology could contribute to a better and quicker visualization of the tumor border at the microscopic level, inspecting eloquent tissue for tumor invasion, and possibly augmenting current standard fluorescence-guided surgery practices. Mistakes and incorrectness related to sampling procedures are common issue during frozen-section analysis. These aspects could be lessened with real-time examination of specimens. *In vivo* confocal microscopy could also favor the

selection of areas characterized by highly cellular tissue, facilitating histological diagnosis, molecular testing and eventual tissue banking for downstream diagnostic workflows. Also common confounding factors, such as frozen-section artifact and cautery artifacts may also be avoided when applied in lieu of frozen-section. Moreover, because all data are digitally acquired and stored, electronic transmission of images to remotely located neuropathologists could enable a real-time telepathology with benchside diagnosis. Lastly, the readily available digital images can be used for advanced image analysis using artificial intelligence, known in radiology as radiomics or radiogenomics. Exemplarily, using MRI imaging data and convolutional neural networks, a review of fourteen studies reported a sensitivity of 94% and specificity of 87% for classifying the IDH status, and 90% sensitivity and 89% specificity for assessing the 1p19q codeletion status in WHO grade II/III tumors. Whether a similar approach can be achieved using digital histologic imaging remains to be investigated. CLE technology could be a door opener to such advanced diagnostic approaches.

Safety profile of sodium fluorescein

As anticipated, the technology that resides under the possibility of looking at a cellular level with the ZEISS CONVIVO is based on SF administration. Looking at SF, as anticipated, this dye recently gained great interest in the neurosurgical community for oncological and neurovascular applications. In particular, its ability to accumulate in cerebral areas where a damage to the BBB has occurred allows the dye to concentrate at tumor sites, rendering tumor tissue more visible, particularly if a dedicated filter on the surgical microscope is equipped (41). One of the main reasons for the widespread use of SF is, besides its proven ability to increase GTR rates and a very affordable low cost (around 5 Euros per vial), its well described safety profile, as confirmed by several years of application in general surgery, gastroenterology, and especially in ophthalmology (42). Looking at the safety profile, most reports of allergic reactions due to SF are related to angiographies for vitreo-retinal pathologies. These sporadic patients are generally affected by mild allergic reactions, like nausea and vomiting, sneezing and pruritus, rather than severe, life-threatening ones, like laryngeal edema, seizures or circulatory shock. This aspect was confirmed in the previous years by various works (42, 43). In neurosurgical literature, we couldn't find structured reports of side effects other than isolated severe ARs reports (44–47). This aspect may be due to unidentified cases but also to unreported events. Nevertheless, almost every study where SF was used in neurosurgery, either for oncological or neurovascular cases, has always underlined the totally safe profile of this dye, even for high doses, also considering that in recent years the development of specific filters for surgical microscopes (Pentero with YELLOW560 filter, Carl Zeiss Meditec AG) allowed a reduction in SF doses necessary to enhance tumor tissue during oncological surgeries from 10-15 mg/kg to dosages around 5 mg/kg (48). As expected, such safety data have been confirmed by the articles we reviewed. No serious adverse events were encountered in the published CONVIVO series, apart from yellow-colored urine and, in some patients, yellow tinging of the skin that usually resolved in all series within 24 to 48 hours. This aspect remained true even when considering those works, in which SF was administered at 40 mg/kg (36), or in which SF was voluntarily re-administered (33). In fact, starting from this point, some authors suggested studies with higher SF doses due to this established safety profile.

Sodium fluorescein clinical protocols in neurosurgery and in CLE imaging

Looking at the possible use that SF may have in neurosurgery, researchers have studied multiple uses of SF, in particular to demarcate tumor borders and to help in achieving gross total resection (41). Starting from the early experiences of Shinoda and colleagues in 2003, where high doses of SF (up to 20 mg/kg) were used, due to the lack of special filters equipped on surgical microscopes (49), the current trend consists in lower dosages (around 5 mg/kg), due to the progressive availability of microscopes equipped with special filters specific to the wavelengths required for SF. Various reports of SF use in vascular surgery include examination of flow dynamics in arteriovenous malformations before and after exclusion of arterial feeders, pre and postoperative study of intracranial aneurysms, cortical microcirculation imaging, assessing of anastomotic patency in revascularization procedures, and analyzing flow in perforating arteries in proximity to aneurysms. Such aspects are usually studied with different administration protocols, that range around the administration of a bolus type of injection, on demand, of around 500 mg of SF (50).

Different points regarding administration protocols should be raised when it comes to SF protocols in CLE. In fact, the difference should be underlined between a correct SF administration timing for a neuro-oncological purpose (i.e. to increase EOR) versus the best timing for obtaining clear CLE images. Regarding the first point, the group of Acerbi and colleagues already pointed out that time of injection is a fundamental aspect to allow an optimal discrimination between tumor and peri-tumoral areas. In particular, it was suggested to implement a low-dose (5 mg/kg) i.v. administration of SF at the end of patient intubation (i.e. around 1 h before dural opening). In fact, with this timing of injection a good discrimination of fluorescent and non-fluorescent tissue may be obtained, with consequent high rate of GTR for HGGs (41). In fact, one of the issues of injecting SF in an acute way (for

instance, on demand during neurovascular surgeries) is that this methodology leads to an intense fluorescence uptake, even by normal brain tissue, because of the passage of SF throughout small capillary vessels (50). This type of bolus injection has therefore been advocated only for vascular indications, as for aneurysms or arteriovenous malformation surgery (see above), similarly to what is carried out, normally, for indocyanine green injection, with good results (51).

Looking at SF protocols of administration in CONVIVO imaging, it must be said that most of the authors are keeping a somewhat similar protocol of administration, with SF being given at patient intubation, following neuro-oncological purposes (Figure 4). Acerbi and colleagues studied 15 GBM cases in 2020 using the well-established 5 mg/kg protocol at anesthesia induction, and no re-administration. In this specific case, time from SF injection to CONVIVO scanning was higher, up to a mean of 137.96 min. for biopsies taken at the tumor core and 130.76 min. for biopsies taken at tumor margin with a mean value of 134 ± 31 minutes (122–214 min), taken together (29). In Höhne and colleagues' *in vivo* experience, a weight-adapted dose of 5 mg/kg of SF was administered intravenously prior to imaging and the timing varied between patients. It was observed that a shorter elapsed time correlated to more readable and assessable images (35). In both *ex vivo* works of Belykh from 2018 and 2020, a 2-5 mg/kg of SF administration around one hour before imaging was executed with good results in terms of tumor visualization (26, 28). In particular, in the 2020 work, the authors noticed that, in many cases, biopsy acquisition occurred more than 90 minutes after the first SF administration, which resulted in suboptimal contrast in CLE images, and such decrease in image quality was also found for biopsies when the SF was injected 1 to 5 minutes before imaging (28). Nevertheless, when considering the analysis of all biopsies, as well as the glioma-only biopsies obtained at different time points after SF injection, no correlation between the timing of SF administration and image quality was shown (20). Interestingly, when 40 mg/kg were administered to a patient, CLE demonstrated high-quality images with excellent contrast in visualizing tumor cells, supporting the idea of higher doses or re-administration during surgery. A confirmation of this aspect was then given in two subsequent and recent works from Abramov and Belykh in 2021 (33, 36). In the first work, the administration of 40 mg/kg of SF at anesthesia induction in a low-grade glioma patient improved CLE visualization of tumor cellularity, while in the second work a retrospective comparison was performed between *ex vivo* images acquired after SF redosing, images from the same patients acquired after the initial SF dose (initial-dose imaging group), and images from patients in whom redosing was not used. Interestingly, the authors found that the brightest and most contrasting images were taken in the redosing group if compared to the initial-dose and single-dose groups ($p < 0.001$). The decay of SF signal resulted to be negatively correlated with brightness and contrast. It was also found that as the mean timing of imaging increased, the percentage of accurately diagnosed images decreased ($p = 0.03$).

Considering all the works together, apart from their *ex vivo* or *in vivo* nature, and apart from the time from SF to surgical resection that could be necessary following the "neuro-oncological purpose" specified above, it seems that clearer CLE images can be obtained when shorter times between SF administration and CLE imaging and higher doses of SF are taken into consideration, but the exact timing seems to be dependent on the specific tumor type. Nevertheless, at the present time, we feel it is too early to state if there is a "best option" for each case. As mentioned before, giving higher SF dosages may increase readability of CLE images, but, in turn, rendering tumor removal more difficult due to the lack of

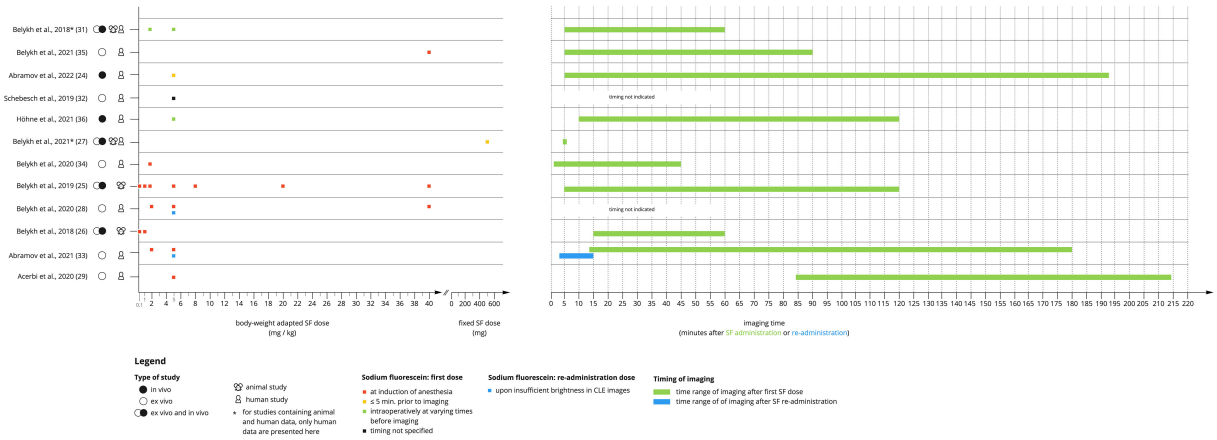

FIGURE 4
Graphical visualization of SF dosing protocols and timing of imaging in the different studies analyzed.

tumor specificity of SF. On the contrary, keeping lower SF dosage protocols may improve this aspect at the expense of CLE image quality. Further research is needed to highlight pros and cons of the different approaches, trying to find an algorithm that may help surgeons in choosing the correct dosage for each specific case.

Looking at the only available CONVIVO vascular experience by Belykh and colleagues from 2021, patients received 5 ml of 10% SF i.v. 5 minutes prior to CLE imaging (27). The earliest visualization of the vessel wall was 8 minutes after SF injection, with visualization being more common at approximately 30 minutes after injection. As expected, tissue injury, contrast extravasation, and higher dosages (i.e., additional injections of SF) resulted to be directly correlated with easier vessel wall visualization. After intravenous injection of SF, fluorescence intensity was strong enough for CLE intravascular imaging for at least 20-30 minutes and adequate for longer imaging after subsequent SF injections. Lastly, blood flow could be visualized continuously within a total time of more than three hours of imaging when reinjecting SF (27).

As a further step, we performed a brief online survey among the clinical users of the CONVIVO around the world, regarding their experiences in appropriate dosage and timing of SF for CLE, of which we report just a narrative recap.

We found each center currently using SF dosages that strictly follow local institutional guidelines for vascular or neuro-oncological use (max. 500 mg). High regulatory burdens hamper the evaluation of higher dosages in clinical trials. The timing of the i.v. injection however varies among centers. For instance, most centers usually inject a single dose at the time of skin incision or dural opening and a few others administer a single dose 5 - 15 minutes before the intended imaging time. These differences result in time delays from injection to imaging of about 5 to 60 minutes. All investigators reported good quality images with their protocols, which suggests that timing does not completely correlate with image quality at this specific point, reflecting the findings of some authors (31, 51), but at the same time raising questions on the possibility and necessity of creating a "standard" injection protocol with standard doses and timing of injections. Probably, most of the reasons for these questions find an answer in the necessity of following a clear clinical question (such as: need to identify the tumor border?; need to make a diagnosis?; need for increased contrast in a lower grade tumor)?. As a matter of fact, one of the hot topics that still needs to be better studied and defined is the appropriate SF injection protocol, especially considering its timing when looking for a tumor margin. While for fluorescence-guided resection early administration of SF is recommended to achieve proper demarcation of tumor versus non-tumor tissue by the degree of SF extravasation, as stated above, late SF administration with CLE enables demarcation based on the cytoarchitectural structure, which seems to be prioritized among the community of pathologists. Whether this is widely applicable in practice remains to be clarified and results shall be regarded when defining the SF administration protocols. In this context, the question of the potential of CLE for non-contrast-enhancing tumors has been raised additionally. Non-contrast-enhancing tumors show an intact blood brain barrier and therefore no or very little extravasation of SF into the tumor nor the brain parenchyma, thus not suitable for CLE. With injection of SF after brain incision, CLE may pave the way to identify tumor margins in tumor entities showing intact BBB. Investigations thereof are currently ongoing.

Another issue raised by the community is a proper reading and understanding of the cytoarchitectural characteristics of the CLE images. Hereby, a better understanding of the underlying pharmacodynamics of SF in different types of tissue or tumor types would be beneficial and further comparison with conventional histological methods is needed. Work is ongoing in cross-correlating CLE images with classical H&E images. Parallels and differences are widely discussed and analyzed among the pathologists of the user community.

Validation of CLE against other modalities like magnetic resonance imaging-based navigation or diffusion tensor imaging fiber tracking, which all lose accuracy during surgery, or even the potential of CLE to enable re-calibration of the navigation, are subjects of further investigations raised by the community. Moreover, CLE for vessel formations, although addressed by some authors (27), needs further validation. Other aspects that the community raised are that the system could potentially contribute to an improved selection of specimens for cyto- or histological examination ("sampling quality control") and that SF extravasation and uptake patterns could potentially improve understanding of the tumor environment *in vivo* or serve as a biomarker to support intraoperative diagnosis.

In conclusion, considering also the possible future applications that this machine may demonstrate in neurosurgery, the analyzed publications show promising diagnostic performance of CONVIVO compared to standard methods in histopathology. Nevertheless, the multitude of used SF protocols and the conditions investigated still warrant a better understanding of the method and its application in neuro-oncology and a further optimization of SF protocols for CLE, and we feel that this is one of the main points that future investigations may have as a main objective. At this time, three centers are running larger clinical trials (a multicenter trial in Germany: INVIVO, NCT04597801 (52); a trial in Berne, Switzerland: CLEBT, NCT04280952 (53); a trial in Milano, Italy: Besta Institute Review Board, verbal n. 72/2020), focusing on the concordance of CLE with definitive histopathological analysis. Their results will help to further improve SF protocols in the various tumor entities investigated. Non-inferiority when comparing CLE with current diagnostic standards, such as frozen section, is a further criterion required prior to positioning the method in routine clinical practice. Data from similar *in vivo* trials performed with the CONVIVO already show promising

results (24) and more clinical data are expected from the three ongoing trials. Moreover, further data from studies analyzing "vascular" applications of CONVIVO are still lacking, as we feel that CONVIVO might have potentiality in assessing qualitatively and quantitatively blood flow in a specific vessel of interest, rendering the technology of high interest also during neurovascular procedures such as clipping of aneurysms, removal of arteriovenous malformations and performing bypasses. Looking at the oncological purposes, once appropriate protocols for the different use cases will be determined and the proof of accuracy provided, also with the possible help of Big Data technology (54), specific classification systems will need to be defined to ensure standardized diagnostic criteria and to establish a common language among the clinical users, favoring the system to enter routine clinical practice.

Author contributions

Conceptualization, FR, AM, KQ and FA, methodology, FR and KQ, investigation, FR, AM, JH, EM, KQ, BP and FA, data curation, FR, KQ, EM, writing, original draft preparation, FR, AM, KQ writing, review and editing, FR, AM, KQ, EM, JH, BP, FA, supervision, FA All authors contributed to the article and approved the submitted version.

Funding

This research is partially funded by Carl Zeiss Meditec AG, Oberkochen, Germany.This work was partially supported by the Associazione Paolo Zorzi per le Neuroscienze Onlus and by the Italian Ministry of Health (RRC).

Conflict of interest

KQ receives fees for coordinating the community of researchers and clinicians working with the ZEISS CONVIVO device.

The remaining authors declare that the research was conducted in the absence of any commercial or financial relationships that could be construed as a potential conflict of interest.

Publisher's note

Supplementary material

The Supplementary Material for this article can be found online at: https://www.frontiersin.org/articles/10.3389/fonc.2022.998384/full#supplementary-material

References

1. Brown TJ, Brennan MC, Li M, Church EW, Brandmeir NJ, Rakszawski KL, et al. Association of the extent of resection with survival in glioblastoma. *JAMA Oncol* (2016) 2:1460–0. doi: 10.1001/jamaoncol.2016.1373

2. Keles GE, Chang EF, Lamborn KR, Tihan T, Chang C-J, Chang SM, et al. Volumetric extent of resection and residual contrast enhancement on initial surgery as predictors of outcome in adult patients with hemispheric anaplastic astrocytoma. *J Neurosurg* (2006) 105:34–40. doi: 10.3171/jns.2006.105.1.34

3. Sanai N, Berger MS. Glioma extent of resection and its impact on patient outcome. *Neurosurgery* (2008) 62:753–64. doi: 10.1227/01.neu.0000318159.21731.cf

4. Sanai N, Polley M-Y, McDermott MW, Parsa AT, Berger MS. An extent of resection threshold for newly diagnosed glioblastomas. *J Neurosurg* (2011) 115:3–8. doi: 10.3171/2011.2.jns10998

5. Kuhnt D, Becker A, Ganslandt O, Bauer M, Buchfelder M, Nimsky C. Correlation of the extent of tumor volume resection and patient survival in surgery of glioblastoma multiforme with high-field intraoperative MRI guidance. *Neuro-Oncol* (2011) 13:1339–48. doi: 10.1093/neuonc/nor133

6. Upadhyay UM, Golby AJ. Role of pre- and intraoperative imaging and neuronavigation in neurosurgery. *Expert Rev Med Device* (2008) 5:65–73. doi: 10.1586/17434440.5.1.65

7. Hollon T, Stummer W, Orringer D, Suero Molina E. Surgical adjuncts to increase the extent of resection: Intraoperative MRI, fluorescence, and raman histology. *Neurosurg Clin N Am* (2019) 30:65–74. doi: 10.1016/j.nec.2018.08.012

8. Janson M, Michael K, Berg J, Anderson JC. The role of intraoperative sonography in neurosurgery. *J Diagn Med Sonogr* (2005) 21:148–51. doi: 10.1177/8756479305274454

9. Lara-Velazquez M, Al-Kharboosh R, Jeanneret S, Vazquez-Ramos C, Mahato D, Tavanaiepour D, et al. Advances in brain tumor surgery for glioblastoma in adults. *Brain Sci* (2017) 7:166–6. doi: 10.3390/brainsci7120166

10. Plesec TP, Prayson RA. Frozen section discrepancy in the evaluation of central nervous system tumors. *Arch Pathol Lab Med* (2007) 131:1532–40. doi: 10.5858/2007-131-1532-FSDITE

11. Mat Zin AA, Zulkarnain S. Diagnostic accuracy of cytology smear and frozen section in glioma. *Asian Pac J Cancer Prev APJCP* (2019) 20:321–5. doi: 10.31557/APJCP.2019.20.2.321

12. Obeidat FN, Awad HA, Mansour AT, Hajeer MH, Al-Jalabi MA, Abudalu LE. Accuracy of frozen-section diagnosis of brain tumors: An 11-year experience from a tertiary care center. *Turk Neurosurg* (2019) 29:242–6. doi: 10.5137/1019-5149.JTN.23220-18.2

13. Neumann H, Langner C, Neurath MF, Vieth M. Confocal laser endomicroscopy for diagnosis of barrett's esophagus. *Front Oncol* (2012) 2:42. doi: 10.3389/fonc.2012.00042

14. Kiesslich R, Gossner L, Goetz M, Dahlmann A, Vieth M, Stolte M, et al. *In vivo* histology of barrett's esophagus and associated neoplasia by confocal laser endomicroscopy. *Clin Gastroenterol Hepatol Off Clin Pract J Am Gastroenterol Assoc* (2006) 4:979–87. doi: 10.1016/j.cgh.2006.05.010

15. Kiesslich R, Burg J, Vieth M, Gnaendiger J, Enders M, Delaney P, et al. Confocal laser endoscopy for diagnosing intraepithelial neoplasias and colorectal cancer *in vivo*. *Gastroenterology* (2004) 127:706–13. doi: 10.1053/j.gastro.2004.06.050

16. Tan J, Quinn MA, Pyman JM, Delaney PM, McLaren WJ. Detection of cervical intraepithelial neoplasia *in vivo* using confocal endomicroscopy. *BJOG* (2009) 116:1663–70. doi: 10.1111/j.1471-0528.2009.02261.x

17. Martirosyan NL, Georges J, Eschbacher JM, Cavalcanti DD, Elhadi AM, Abdelwahab MG, et al. Potential application of a handheld confocal endomicroscope imaging system using a variety of fluorophores in experimental gliomas and normal brain. *Neurosurg Focus* (2014) 36:E16. doi: 10.3171/2013.11.FOCUS13486

18. Martirosyan NL, Georges J, Kalani MYS, Nakaji P, Spetzler RF, Feuerstein BG, et al. Handheld confocal laser endomicroscopic imaging utilizing tumor-specific fluorescent labeling to identify experimental glioma cells *in vivo*. *Surg Neurol Int* (2016) 7:S995–S1003. doi: 10.4103/2152-7806.195577

19. Sankar T, Delaney PM, Ryan RW, Eschbacher J, Abdelwahab M, Nakaji P, et al. Miniaturized handheld confocal microscopy for neurosurgery: Results in an experimental glioblastoma model. *Neurosurgery* (2010) 66:410–7. doi: 10.1227/01.NEU.0000365772.66324.6F

20. Martirosyan NL, Eschbacher JM, Kalani MYS, Turner JD, Belykh E, Spetzler RF, et al. Prospective evaluation of the utility of intraoperative confocal laser Endomicroscopy in patients with brain neoplasms using fluorescein sodium: experience with 74 cases. *Neurosurg Focus* (2016) 40:E11. doi: 10.3171/2016.1.FOCUS15559

21. Pavlov V, Meyronet D, Meyer-Bisch V, Armoiry X, Pikul B, Dumot C, et al. Intraoperative probe-based confocal laser endomicroscopy in surgery and stereotactic biopsy of low-grade and high-grade gliomas: A feasibility study in humans. *Neurosurgery* (2016) 79:604–12. doi: 10.1227/NEU.0000000000001365

22. Charalampaki P, Javed M, Daali S, Heiroth H-J, Igressa A, Weber F. Confocal laser endomicroscopy for real-time histomorphological diagnosis: Our clinical experience with 150 brain and spinal tumor cases. *Neurosurgery* (2015) 62 Suppl 1:171–6. doi: 10.1227/NEU.0000000000000805

23. Breuskin D, Szczygielski J, Urbschat S, Kim Y-J, Oertel J. Confocal laser endomicroscopy in neurosurgery-an alternative to instantaneous sections? *World Neurosurg* (2017) 100:180–5. doi: 10.1016/j.wneu.2016.12.128

24. Abramov I, Park MT, Belykh E, Dru AB, Xu Y, Gooldy TC, et al. Intraoperative confocal laser endomicroscopy: Prospective *in vivo* feasibility study of a clinical-grade system for brain tumors. *J Neurosurg* (2022) 1:1–11. doi: 10.3171/2022.5.JNS2282

25. Belykh E, Miller EJ, Carotenuto A, Patel AA, Cavallo C, Martirosyan NL, et al. Progress in confocal laser endomicroscopy for neurosurgery and technical nuances for brain tumor imaging with fluorescein. *Front Oncol* (2019) 9:554. doi: 10.3389/fonc.2019.00554

26. Belykh E, Miller EJ, Patel AA, Yazdanabadi MI, Martirosyan NL, Yağmurlu K, et al. Diagnostic accuracy of a confocal laser endomicroscope for *in vivo* differentiation between normal injured and tumor tissue during fluorescein-guided glioma resection: Laboratory investigation. *World Neurosurg* (2018) 115:e337–48. doi: 10.1016/j.wneu.2018.04.048

27. Belykh E, Zhao X, Ngo B, Farhadi DS, Kindelin A, Ahmad S, et al. Visualization of brain microvasculature and blood flow *in vivo*: Feasibility study using confocal laser endomicroscopy. *Microcirc N Y N 1994* (2021) 28:e12678. doi: 10.1111/micc.12678

28. Belykh E, Zhao X, Ngo B, Farhadi DS, Byvaltsev VA, Eschbacher JM, et al. Intraoperative confocal laser endomicroscopy *ex vivo* examination of tissue microstructure during fluorescence-guided brain tumor surgery. *Front Oncol* (2020) 10:599250. doi: 10.3389/fonc.2020.599250

29. Acerbi F, Pollo B, De Laurentis C, Restelli F, Falco J, Vetrano IG, et al. *Ex vivo* fluorescein-assisted confocal laser endomicroscopy (CONVIVO® system) in patients with glioblastoma: Results from a prospective study. *Front Oncol* (2020) 10:606574. doi: 10.3389/fonc.2020.606574

30. US Food & Drug Administration. *Approval letter to Carl zeiss meditec AG. 510(k) premarket notification* . Available at: https://www.accessdata.fda.gov/scripts/cdrh/cfdocs/cfpmn/pmn.cfm?ID=K181116 (Accessed July 11, 2022).

31. Belykh E, Patel AA, Miller EJ, Bozkurt B, Yağmurlu K, Woolf EC, et al. Probe-based three-dimensional confocal laser endomicroscopy of brain tumors: Technical note. *Cancer Manag Res* (2018) Volume 10:3109–23. doi: 10.2147/CMAR.S165980

32. Schebesch K-M, Rosengarth K, Brawanski A, Proescholdt M, Wendl C, Höhne J, et al. Clinical benefits of combining different visualization modalities in neurosurgery. *Front Surg* (2019) 6:56. doi: 10.3389/fsurg.2019.00056

33. Abramov I, Dru AB, Belykh E, Park MT, Bardonova L, Preul MC. Redosing of fluorescein sodium improves image interpretation during intraoperative *ex vivo* confocal laser endomicroscopy of brain tumors. *Front Oncol* (2021) 11:668661. doi: 10.3389/fonc.2021.668661

34. Belykh E, Ngo B, Farhadi DS, Zhao X, Mooney MA, White WL, et al. Confocal laser endomicroscopy assessment of pituitary tumor microstructure: A feasibility study. *J Clin Med* (2020) 9:E3146. doi: 10.3390/jcm9103146

35. Höhne J, Schebesch K-M, Zoubaa S, Proescholdt M, Riemenschneider MJ, Schmidt NO. Intraoperative imaging of brain tumors with fluorescein: Confocal laser endomicroscopy in neurosurgery. clinical and user experience. *Neurosurg Focus* (2021) 50:E19. doi: 10.3171/2020.11.FOCUS20783

36. Belykh E, Onaka NR, Zhao X, Abramov I, Eschbacher JM, Nakaji P, et al. High-dose fluorescein reveals unusual confocal endomicroscope imaging of low-grade glioma. *Front Neurol* (2021) 12:668656. doi: 10.3389/fneur.2021.668656

37. Schlosser H-G, Suess O, Vajkoczy P, van Landeghem FKH, Zeitz M, Bojarski C. Confocal neurolasermicroscopy in human brain – perspectives for neurosurgery on a cellular level (including additional comments to this article). *Cent Eur Neurosurg* (2010) 71:13–9. doi: 10.1055/s-0029-1237735

38. Eschbacher J, Martirosyan NL, Nakaji P, Sanai N, Preul MC, Smith KA, et al. *In vivo* intraoperative confocal microscopy for real-time histopathological imaging of brain tumors. *J Neurosurg* (2012) 116:854–60. doi: 10.3171/2011.12.JNS11696

39. Rao S, Rajkumar A, Ehtesham MD, Duvuru P. Challenges in neurosurgical intraoperative consultation. *Neurol India* (2009) 57:464–8. doi: 10.4103/0028-3886.55598

40. Roessler K, Dietrich W, Kitz K. High diagnostic accuracy of cytologic smears of central nervous system tumors. A 15-year experience based on 4,172 patients. *Acta Cytol* (2002) 46:667–74. doi: 10.1159/000326973

41. Acerbi F, Broggi M, Schebesch K-M, Höhne J, Cavallo C, De Laurentis C, et al. Fluorescein-guided surgery for resection of high-grade gliomas: A multicentric prospective phase II study (FLUOGLIO). *Clin Cancer Res Off J Am Assoc Cancer Res* (2018) 24:52–61. doi: 10.1158/1078-0432.CCR-17-1184

42. Yannuzzi LA, Rohrer KT, Tindel LJ, Sobel RS, Costanza MA, Shields W, et al. Fluorescein angiography complication survey. *Ophthalmology* (1986) 93:611–7. doi: 10.1016/S0161-6420(86)33697-2

43. Kwan AS, Barry C, McAllister IL, Constable I. Fluorescein angiography and adverse drug reactions revisited: The lions eye experience. *Clin Exp Ophthalmol* (2006) 34:33–8. doi: 10.1111/j.1442-9071.2006.01136.x

44. Tanahashi S, Lida H, Dohi S. An anaphylactoid reaction after administration of fluorescein sodium during neurosurgery. *Anesth Analg* (2006) 103:503. doi: 10.1213/01.ANE.0000227205.37935.10

45. Dilek O, Ihsan A, Tulay H. Anaphylactic reaction after fluorescein sodium administration during intracranial surgery. *J Clin Neurosci Off J Neurosurg Soc Australas* (2011) 18:430–1. doi: 10.1016/j.jocn.2010.06.012

46. Dallapiazza R, Bond AE, Grober Y, Louis RG, Payne SC, Oldfield EH, et al. Retrospective analysis of a concurrent series of microscopic versus endoscopic transsphenoidal surgeries for knosp grades 0–2 nonfunctioning pituitary macroadenomas at a single institution: Clinical article. *J Neurosurg* (2014) 121:511–7. doi: 10.3171/2014.6.JNS131321

47. Francaviglia N, Iacopino DG, Costantino G, Villa A, Impallaria P, Meli F, et al. Fluorescein for resection of high-grade gliomas: A safety study control in a single center and review of the literature. *Surg Neurol Int* (2017) 8:145. doi: 10.4103/sni.sni_89_17

48. Acerbi F, Broggi M, Eoli M, Anghileri E, Cuppini L, Pollo B, et al. Fluorescein-guided surgery for grade IV gliomas with a dedicated filter on the surgical microscope: Preliminary results in 12 cases. *Acta Neurochir (Wien)* (2013) 155:1277–86. doi: 10.1007/s00701-013-1734-9

49. Shinoda J, Yano H, Yoshimura S-I, Okumura A, Kaku Y, Iwama T, et al. Fluorescence-guided resection of glioblastoma multiforme by using high-dose fluorescein sodium. *Tech note J Neurosurg* (2003) 99:597–603. doi: 10.3171/jns.2003.99.3.0597

50. Zhao X, Belykh E, Cavallo C, Valli D, Gandhi S, Preul MC, et al. Application of fluorescein fluorescence in vascular neurosurgery. *Front Surg* (2019) 6:52. doi: 10.3389/fsurg.2019.00052

51. Acerbi F, Broggi M, Broggi G, Ferroli P. What is the best timing for fluorescein injection during surgical removal of high-grade gliomas? *Acta Neurochir (Wien)* (2015) 157:1377–8. doi: 10.1007/s00701-015-2455-z

52. *Technische universität münchen. comparison of fluorescein-INtra-VItal microscopy versus conventional frozen section diagnosis for intraOperative histopathological evaluation (INVIVO)* (2022). Available at: https://clinicaltrials.gov/ct2/show/NCT04597801 (Accessed July 7, 2022).

53. *University hospital inselspital, berne. confocal laser endomicroscopy for brain tumors* (2022). Available at: https://clinicaltrials.gov/ct2/show/NCT04280952 (Accessed July 7, 2022).

54. Izadyyazdanabadi M, Belykh E, Mooney MA, Eschbacher JM, Nakaji P, Yang Y, et al. Prospects for theranostics in neurosurgical imaging: Empowering confocal laser endomicroscopy diagnostics *via* deep learning. *Front Oncol* (2018) 8:240. doi: 10.3389/fonc.2018.00240

frontiers | Frontiers in Oncology

TYPE Original Research
PUBLISHED 28 October 2022
DOI 10.3389/fonc.2022.1016264

OPEN ACCESS

EDITED BY
Sergio García,
Hospital Universitario Río Hortega, Spain

REVIEWED BY
Xiangyi Kong,
Chinese Academy of Medical Sciences and Peking Union Medical College, China
Angel Horcajadas Almansa,
Hospital Virgen de las Nieves, Spain

*CORRESPONDENCE
Alejandra Mosteiro
mosteiro@clinic.cat

SPECIALTY SECTION
This article was submitted to Neuro-Oncology and Neurosurgical Oncology, a section of the journal Frontiers in Oncology

RECEIVED 11 August 2022
ACCEPTED 05 October 2022
PUBLISHED 28 October 2022

CITATION
Mosteiro A, Di Somma A, Ramos PR, Ferrés A, De Rosa A, González-Ortiz S, Enseñat J and González JJ (2022) Is intraoperative ultrasound more efficient than magnetic resonance in neurosurgical oncology? An exploratory cost-effectiveness analysis. *Front. Oncol.* 12:1016264. doi: 10.3389/fonc.2022.1016264

Is intraoperative ultrasound more efficient than magnetic resonance in neurosurgical oncology? An exploratory cost-effectiveness analysis

Alejandra Mosteiro[1,2*], Alberto Di Somma[1,2], Pedro Roldán Ramos[1,2], Abel Ferrés[1], Andrea De Rosa[3], Sofía González-Ortiz[3], Joaquim Enseñat[1,2] and Jose Juan González[1,2]

[1]Department of Neurosurgery, Hospital Clínic de Barcelona, Barcelona, Spain, [2]Facultad de Medicina, Universitat de Barcelona, Barcelona, Spain, [3]Division of Neurosurgery, Università degli Studi di Napoli "Federico II", Naples, Italy, [4]Department of Radiology, Hospital Clínic de Barcelona, Barcelona, Spain

Objective: Intraoperative imaging is a chief asset in neurosurgical oncology, it improves the extent of resection and postoperative outcomes. Imaging devices have evolved considerably, in particular ultrasound (iUS) and magnetic resonance (iMR). Although iUS is regarded as a more economically convenient and yet effective asset, no formal comparison between the efficiency of iUS and iMR in neurosurgical oncology has been performed.

Methods: A cost-effectiveness analysis comparing two single-center prospectively collected surgical cohorts, classified according to the intraoperative imaging used. iMR (2013-2016) and iUS (2021-2022) groups comprised low- and high-grade gliomas, with a maximal safe resection intention. Units of health gain were gross total resection and equal or increased Karnofsky performance status. Surgical and health costs were considered for analysis. The incremental cost-effectiveness ratio (ICER) was calculated for the two intervention alternatives. The cost-utility graphic and the evolution of surgical duration with the gained experience were also analyzed.

Results: 50 patients followed an iMR-assisted operation, while 17 underwent an iUS-guided surgery. Gross total resection was achieved in 70% with iMR and in 60% with iUS. Median postoperative Karnofsky was similar in both group (KPS 90). Health costs were € 3,220 higher with iMR, and so were surgical-related costs (€ 1,976 higher). The ICER was € 322 per complete resection obtained with iMR, and € 644 per KPS gained or maintained with iMR. When only surgical-related costs were analyzed, ICER was € 198 per complete resection with iMR and € 395 per KPS gained or maintained.

Conclusion: This is an unprecedented but preliminary cost-effectiveness analysis of the two most common intraoperative imaging devices in neurosurgical oncology. iMR, although being costlier and time-consuming, seems cost-effective in terms of complete resection rates and postoperative performance status. However, the differences between both techniques are small. Possibly, iMR and iUS are complementary aids during the resection: iUS real-time images assist while advancing towards the tumor limits, informing about the distance to relevant landmarks and correcting neuronavigation inaccuracy due to brain shift. Yet, at the end of resection, it is the iMR that reliably corroborates whether residual tumor remains.

KEYWORDS

intraoperative magnetic resonance, intraoperative ultrasound, neurosurgical oncology, glioma, cost-effectiveness

Introduction

Intraoperative imaging is a major asset in modern neurosurgical oncology which helps the surgeon delineating tumor boundaries and identifying remnants (1–3). It ultimately improves the extent of resection (EoR), a major prognostic factor in both high (4, 5) and low-grade gliomas (6, 7), as well as in brain metastasis (8).

Imaging devices have evolved during the last decades, becoming more precise, versatile and accessible. Still, each modality has its own strengths and shortcomings (3). Intraoperative ultrasound (iUS) is convenient in terms of costs, maneuverability and it provides real-time representations of the operative field. However, it is an operator dependent technique and it has restricted resolution for tissue differentiation (9). In contrast, intraoperative magnetic resonance (iMR) is considered the prime study for brain assessment, with high accuracy in tissue definition and reliable for achieving gross total resection of brain tumors (10, 11). But iMR requires specific infrastructure and high initial investment (12). Moreover, its long acquisition times and the particular workflow required increase the operative duration.

Following the differential features of intraoperative imaging devices, tertiary neurosurgical centers have been choosing between modalities according to their preferences and prospects. However, a formal comparison of the efficiency between iUS and iMR in the neurosurgical oncology setting has not been performed yet. Hereby, we have evaluated the cost-effectiveness of iUS and iMR for brain tumor resection. Comparing the economic costs and health benefits of these two alternative interventions will provide objective data for decision makers and future investments.

Methods

Population of reference

The patients included in this retrospective analysis were part of two prospectively collected clinical registries. One cohort was composed of consecutive patients treated from high and low grade gliomas, with a maximal safe resection intention, with the assistance of a low field-iMR (PoleStar N-20, Odin Medical Technologies, Yokneam, Israel and Medtronic, Louisville, CO, USA). These patients were recruited between June 2013, date of the installation of the device, and June 2016. The data corresponding to this cohort has already been published in this same journal by our group (13).

The second cohort consisted of patients treated for high- and low-grade gliomas, with a maximal safe resection intention, with the aid of an iUS (bk5000 neurosurgical system, BK Medical, Burlington, Massachusetts, USA) and a specific neurosurgical probe (bk Craniotomy Transducer N13C5). No other iUS appliances were used, neither 3D reconstructions nor co-registration with the neuronavigation system. Intraoperative contrast agents were not applied. These patients were operated between October 2021, date of acquisition of the device, and May 2022.

Neurophysiologic monitoring was implemented in both cohorts, whenever the surgical team considered it appropriate. In cases with initial suspicion of high-grade glioma, intraoperative fluoresce with 5-aminolevulinic acid (Gliolan ®) was additionally used to guide the resection. In all the cases, neuronavigation was employed to tailor the craniotomy and to aid with the resection. Patients in which both intraoperative

devices were used were excluded from the analysis; they belong to the intermediate time period (2016-2021).

The study research was approved by the institutional review board (HCB/2013/8782 and HCB/2022/0651). Patients signed an informed consent before surgery (agreeing the use of the low field-iMR and for the academic and scientific use of their anonymized data). The study complies with national legislation in the field of biomedical research, the protection of personal data (15/1999) and the standards of Good Clinical Practice, as well as with the Helsinki Declaration (1975 and 1983 revisions). Patient records were anonymized before analysis.

Surgical technique and outcome measurements

Patients within the iMR and iUS cohorts were operated with conventional microsurgical techniques, including an ultrasonic aspirator and standard neuronavigation. In both groups, neurophysiologic monitoring was employed when the location of the lesion required motor cortical or subcortical mapping. Awake surgery was chosen for language mapping in suitable candidates. Functional criteria for stopping the resection remained unchanged across the duration of the whole study. To reduce the bias inherent to the variable degree of surgeons' expertise with iUS operation, all interventions were performed by only two surgeons specialized in neurosurgical oncology.

The primary outcome was EoR, defined as Gross Total Resection (GTR) if at least 90% of the mass was removed; Near Total Resection (NTR) if at least 80% of the mass was removed; or Partial Resection (PR) if less than 80% of the mass was removed (14). In high grade gliomas and metastasis, the tumor mass corresponded to the contrast-enhancing lesion. In low grade gliomas, the lesion consisted of T2/FLAIR hyperintense infiltrative area. The secondary outcomes were the presence of surgical-related complications and the performance status at discharge (assessed by the Karnosfky Performance Status, KPS).

Postoperative complications included hemorrhage (epidural, subdural or intraparenchymal), wound infection, new neurological deficits, hydrocephalus, and venous thromboembolic disease. Other variables of interest were demographic (age and gender) and clinical variables (preoperative KPS), histopathological diagnosis, need of re-intervention within the first year, surgical duration, need for intensive care and total hospital length of stay.

Economic analysis

Economic evaluation consisted of a cost-effectiveness analysis where the two intraoperative imaging techniques were compared, namely the low-field iMR with the iUS. The cost-effectiveness equation explored the incremental cost per unit of health gained with a given device. The effectiveness measures used were maintained or increased postoperative KPS and the EoR, expressed as a dichotomous variable, considering whether GTR was achieved or not achieved. The incremental effectiveness was expressed as the mean difference in the postoperative KPS and as the difference in the percentage of GTR achieved with each technique.

Health-related costs included health related variables [stay in the intensive care unit (days), hospital length of stay (days), type and number of radiological images performed before and after the intervention] and surgical-related variables, namely the operating time (in minutes), the use of prosthesis (dural substitutes, miniplates, hemostatic materials, etc.) and the use of neuronavigation system, the surgical pack and the intraoperative image device. The cost of the imaging device imputed to each patient was inferred as the cost per patient according to all the indications in which iMR or iUS are currently applied to, for the total lifespan of the device. Indications for iMR are intrinsic and extrinsic brain lesions, cavernomas, pituitary macroadenomas and epilepsy surgery, which comprises about 120 surgeries per year in our institution. Indications for iUS include intrinsic and extrinsic brain lesions, hydrocephalus and neurovascular interventions. These account for about 150 surgeries per year. The life cycle of both devices was set at 10 years. Although other health-related costs were described, they did not compute for the cost-effectiveness analysis (stay in the intensive care unit [days], hospital length of stay [days], type and number of radiological images performed before and after the intervention). Prices were extracted from our institution's budget and cost of health credits. The same unitary prices were apply to both cohorts, even when they differ in eight years, so as to obtain comparable expenses (euro 2018). Therefore, no discount rates were applied. Costs were expressed as mean cost per patient.

The mean incremental cost and mean incremental effectiveness were calculated for each modality. The cost-effectiveness ratio (ICER) was defined as the ratio between the incremental cost and the incremental effectiveness of the two intervention alternatives, as follows:

$$ICER = \frac{Cost\ \ of\ \ iMR - Cost\ \ of\ \ iUS}{GTR\ \ with\ \ iMR - GTR\ \ with\ \ iUS}$$

The ICER values of the two intraoperative imaging variants were represented in a cost-utility plane. In this graphic, the north-east corner indicates a more expensive and more effective intervention, whereas the south-east corner indicated a less costly but more effective intervention. Finally, a graphical representation of the evolution of surgical times with the sequentially acquired experience of the surgical team was obtained for both techniques.

Calculations were performed using Microsoft Excel XPTM and SPSS (IBM version 23.0). The present analysis followed the

Health Economic Evaluation Reporting Standards (CHEERS) guidelines for communicating economic evaluations of health interventions. No statistical tests were conducted as neither hypothesis testing, nor the level of statistical significance were relevant to our analysis.

Brief literature review

To contextualize our results in terms of efficacy and efficiency, we ran a succinct literature review of the main trials and observational studies reporting the outcomes of the use of iMR and/or iUS for glioma resection. Concretely, we conducted a PubMed search with the words "intraoperative ultrasound" and/or "intraoperative magnetic resonance" and "glioma surgery". Only studies reporting the rates of gross total resection were included. Small series or series older than 2005 were excluded. Results of the search were summarized in an informative table, along with our own current results, specifying the year of publication, the type of intraoperative imaging device used, the study design, the tumor type included, the sample size, the rates of gross tumor resection and the surgical duration (if available). No statistical analysis was performed to compare between the different studies.

Results

A total of 67 patients were included for the analysis: 50 had an iMR assisted surgery and 17 had an iUS guided intervention. Patients in which iUS was only used to obtain a biopsy were excluded from the analysis. A detailed description of the iMR results and cost-effectiveness analysis has already been published by our group (13). The results regarding iUS and the comparison between the two techniques in terms of cost-effectiveness are original and had not been previously reported.

Both cohorts had a male preponderance, a mean age of 50-60 years and an overall good performance status preoperatively (median KPS 90). In both groups, the predominant tumor type was high grade glioma (62% in iMR vs 70% in iUS) (Table 1).

Clinical outcomes

Surgical resection of tumors assisted with iMR, compared to iUS, provided higher rates of complete resection and lower incidence of postoperative complications (Table 2). The potential benefit related to iMR is regarded as an observational trend, since no statistical comparison was performed, as this falls outside the objectives of this study. With iMR gross total resection was achieved in 70% of cases, with acceptable postoperative morbidity (median KPS 80, complication rate of 14% with 8% needing reintervention). Complications in the iMR group included three symptomatic hematomas, one CSF fistula, two cerebral focal ischemia and one new-onset epilepsy.

Conversely, with iUS complete resection was obtained in 60% of cases. Postoperative outcomes were similar in terms of performance status (mean KPS 80), yet morbidity was higher with iUS than with iMR. With iUS there was a 20% complication rate, which included two epidural hematomas, one surgical-cavity hematoma and one surgical-site infection. 11% of iUS-guided cases needed a reintervention due to surgical-related complications (Table 2).

Health related costs

Mean cost per operation was higher if iMR had been used, ascending to € 5,162, compared to € 3,186 with the iUS. The number of patients requiring ICU and the mean length of hospital stay were also higher in the iMR setting (patients requiring ICU in iMR 34% vs 24% in iUS; mean LoS in

TABLE 1 Socio-demographic and clinical variables.

	iMR (n = 50)	iUS (n = 17)	p
Gender, female [n (%)]	20 (40)	5 (30)	0.160
Age [median (range)]	53 (21-82)	57 (47-74)	0.566
Preoperative KPS [median (range)]	90 (70-100)	90 (40-100)	0.232
Low grade glioma [n (%)]	19 (38)	5 (30)	0.156
High grade glioma [n (%)]	31 (62)	12 (70)	0.154

iMR, intraoperative magnetic resonance; iUS, intraoperative ultrasound; KPS, Karnofsky performance status.

TABLE 2 Clinical outcomes and total cost per intervention type.

	iMR (n = 50)	iUS (n = 17)	Differential (iMR-iUS)
Gross total resection, n (%)	35 (70)	10 (60)	10
Complications, n (%)	7 (14)	4 (20)	- 6
Reintervention, n (%)	4 (8)	2 (11)	- 3
Postoperative KPS [median (range)]	80 (60-100)	80 (60-100)	0
Postoperative KPS equal or increased [n (%)]	37 (70)	11 (65)	5
Total cost per intervention	10,893	7,673	3,220
OR	5,162	3,186	1,976
ICU	472	326	146
Hospitalization	4,177	2,358	1,819
Diagnostic images	1,082	739	343

ICU, Intensive care unit; iMR, intraoperative magnetic resonance; iUS, intraoperative ultrasound; KPS, Karnofsky performance status; OR, operating room.

hospital with iMR 10 days vs 6 days with iUS). Therefore, the total health-related costs for each intervention were higher with iMR assisted-surgery (€ 10,893) than with iUS guided-surgery (€7,673) (Table 3).

Surgical duration was more than double when iMR was used than when iUS was chosen, with an average of 241 minutes more per intervention. Interestingly, the sequential evolution of surgical times was different for the two techniques: While iMR-surgery tended to become nimbler with time, a flat evolution of the iUS-surgery was observed (Figure 1).

Cost-effectiveness analysis

The costs of iMR-assisted surgery were higher than with iUS (incremental cost per intervention of € 3,220). Meanwhile, the iMR seems more effective at achieving gross total removal of the tumor (mean percentage difference of 10 points). Still, postoperative performance status was similar with both techniques, but iMR showed slightly higher rates of equal or increased postoperative KPS (incremental benefit of 5 percentage points).

The results of the cost-effectiveness analysis (Table 4) reveal that, in terms of health-related costs, iMR seems cost-effective when compared to iUS in terms of complete tumor removal (ICER € 322 per GTR achievement) and postoperative performance status (ICER € 644 per KPS gained or maintained with iMR). These lines of results are maintained when only surgical-related costs are concerned, with and ICER of € 198 per GTR and an ICER of € 395 per KPS gained with iMR.

In the cost-effectiveness plane representing the results of iUS compared to the iMR, nearly half of the replicates fall within the north-east corner, indicating a costlier and more effective intervention (Figure 2).

Examples of the intraoperative images used during the interventions can be seen in Figure 3.

Discussion

This is an unprecedented but preliminary cost-effectiveness analysis comparing the two most commonly used intraoperative imaging devices in oncologic neurosurgery. Our results suggest that iMR, although being costlier and time-consuming, seems to be cost-effective comparing to iUS in terms of surgical resection rates, with an ICER of € 322 per GTR attained. A similar conclusion is obtained when only surgical-related costs are regarded, with and ICER of € 198 per GTR. On the other hand, when KPS was taken as the unit of health gain, slight differences were found among the two techniques; still, iMR seemed to be cost-effective to the iUS counterpart. Whether the apparent profitability of the iMR is worth the high initial investments required and the longer surgical duration times will depend on the willingness-to-pay threshold of each local healthcare system and the logistics policy of each institution.

Our economic analysis was performed under two different economic perspectives: one accounted only for the surgical-related costs, and the other one including all the total costs incurred during hospitalization. This strategy was intended to reduce the bias related to the differences in those costs not directly related to the intraoperative image of choice, such as systemic complications and length of stay. For instance, the higher rates of postoperative complications within the iUS-guided group might not be directly related to the imaging devise *per se* (potential selection bias). Meanwhile, a slightly poorer postoperative KPS within the iUS group might be the consequence of a more ambitious approach to resection, by which trying to achieve higher GTR rates there is collateral damage in the form of new neurological deficits (due to small vessel violation or grey/white matter disruption).

In both series, the intention of the surgeries was maximal safe resection. In cases of tumors located near eloquent cortical or subcortical structures, neurophysiological monitoring was performed. In both iUS and iMR cohorts there were cases in

TABLE 3 Resources used and computed unit costs.

	iMR (n = 50)	iUS (n = 17)	Unit cost (€)
OR			
Time (min) [mean (SD)]	450 (70)	209 (47)	5
Surgical pack [% (n)]	100 (50)	100 (17)	1,150
Prosthesis [% (n)]	88 (44)	24 (4)	272
Navigation system [% (n)]	100 (50)	100 (17)	862
LF-iMR [% (n)]	100 (50)	0	833*
LF-iUS [% (n)]	0	100 (17)	67**
ICU [% (n)]	34 (17)	24 (4)	555
Hospitalization [mean LoS in days (SD)]	10 (5)	6 (2)	422
Preoperative images [mean (SD)]			
MR	1.35 (1.3)	1.18 (0.6)	170
PET	0.1 (0.3)	0.12 (0.3)	566
X-Ray	1.1 (1.2)	1.18 (0.5)	15
portable X-Ray	0.1 (0.5)	0	32
CT	0.4 (0.6)	0.47 (0.6)	72
Postoperative images [mean (SD)]			
MR	2.8 (1.65)	1.65 (0.7)	170
PET	0	0.06 (0.23)	566
SPECT	0.1 (0.3)	0	166
X-Ray	1.7 (3.5)	1.5 (0.8)	15
portable X-Ray	0.3 (0.9)	0.3 (0.2)	32
CT	0.7 (1.4)	1.12 (1.3)	72
TOTAL UNIT COST (€)	10,893	7,673	

ICU, Intensive care unit; iMR, intraoperative magnetic resonance; iUS, intraoperative ultrasound; LoS, Length of Stay; OR, operating room.
*Cost per intervention using iMR based on the life cycle (10 years) and the potential number of annual patients (n = 120) who benefit from the iMR device.
**Cost per intervention using iUS based on the life cycle (10 years) and the potential number of annual patients (n = 150) who benefit from the iUS device.

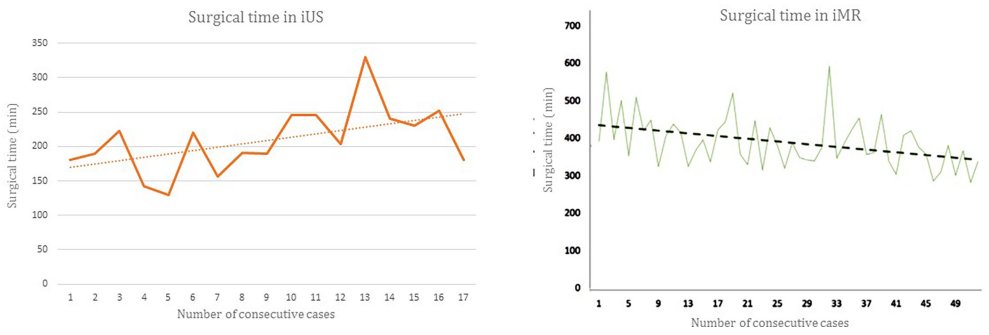

FIGURE 1
Surgical time per patient according to the intraoperative imaging device. The graphics illustrate the sequential evolution of surgical times required for each patient. The superimposed line demonstrates the trend of intraoperative duration as the experience increases with each imaging technology. *Left*, intraoperative ultrasound (iUS) and *Right*, intraoperative magnetic resonance (iMR). Reprinted with permission of García-García et al., 2020 (13).

10.3389/fonc.2022.1016264

TABLE 4 Cost-effectiveness analysis.

	iMR	iUS	Difference	ICERSurgery-related	ICERHealth-related
Health-related cost (€)	10,893	7,673	3,220		
Surgical-related cost (€)	5,162	3,186	1,976		
Effectiveness measure (postoperative KPS equal or increased), %	70	65	5	395	644
Effectiveness measure (Gross total resection, % cases)	70	60	10	198	322

ICER, Incremental Cost-Effectiveness Ratio; iMR, intraoperative Magnetic Resonance; iUS, intraoperative UltraSound; KPS, Karnofsky Performance Status.

which resection was halted prematurely due to the proximity of functional areas. However, a plausible explanation for the difference (10%) in GTR between both techniques is a mismatched distribution in the functionally limiting tumor excisions. In fact, in our institution, iMR is used in well-selected candidates, in whom total tumor resection is pursued as a primary goal and in whom the total removal of the tumor seems feasible according to the preoperative planning. On the contrary, iUS is now used as a regular aid for tumor resection, even in cases where a complete removal was only sought up to some extent (potential selection bias).

Regarding surgical duration, the use of iMR increased operating times to near double those with iUS, a similar magnitude to what had been previously reported (15). Interestingly, duration seems to decrease with cumulative cases in the iMR device, but not so with the use of iUS. Perhaps, the workflow required for iMR involves the whole surgical team (surgeons, anesthesiologist and nurses), who progressively become more confident and agile with patient preparation and device mobilization. Conversely, iUS relies directly on the surgeon's ability to acquire the desired projections and to correctly interpret the images. Consequently, the learning curve might be slower, and the number of interventions needed to decrease surgical times might exceed the contemplated 17 cases. Indeed, the interpretation of iUS results could become better with time and experience, and so would the resection rates.

Although the limited experience with iUS was also concerning at the beginning, the results obtained by our group are in line with previously reported series, Table 5 summarizes the results so far reported about the efficacy of iUS guided glioma surgery (10, 16–19, 21-42). In this regard, a common obstacle for identifying residual tumor was the acoustic enhancement artifact, due to the liquefied surgical cavity. Some authors have suggested that serial iUS acquisitions during the resection may help differentiate between artifact and tumor at the end of the procedure (31); meanwhile, specific software is also becoming available (29). Another strategy is the use of sonographic contrast agents; even if the experience with these is limited, they seem to enhance the lesion borders compared with the standard B-mode iUS. Moreover, contrast-guided evaluation provides information about the tumor perfusion pattern, which could also facilitate the surgical procedure (32).

Arguably, iMR provides better image resolution, tissue differentiation and wider field of view. These intrinsic

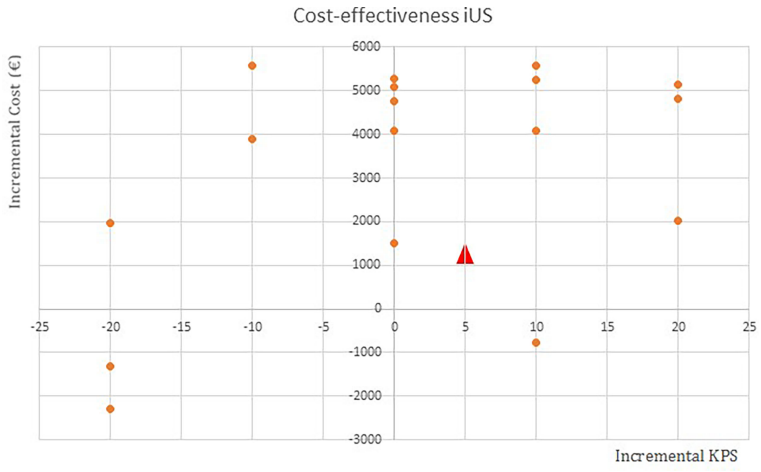

FIGURE 2
Cost-effectiveness plane of intraoperative ultrasound (iUS) compared to the intraoperative magnetic resonance imaging device. Each blue point represents a replicated case. The red triangle is the average of all the cases. X-axis, Effectiveness measure (KPS); Y-axis, Cost in euros.

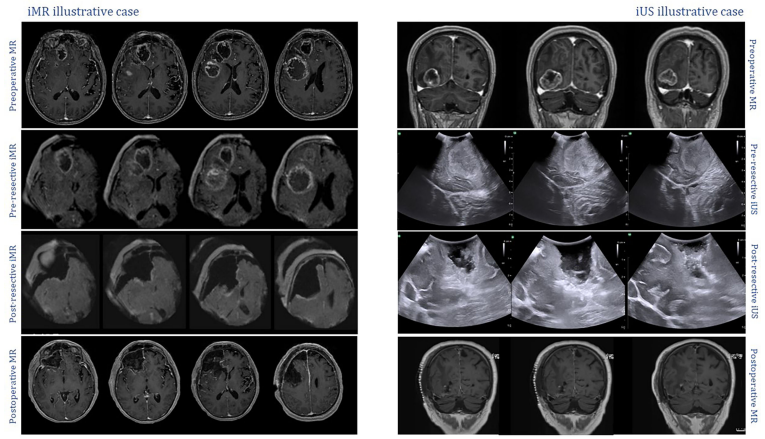

FIGURE 3
Intraoperative captures displaying examples of the imaging techniques undertaken during the study. *Left*, low-field iMR illustrative case. All images correspond to axial sections of T1 sequences after gadolinium administration. On the top row, preoperative MR study showing a right frontal lesion corresponding to a high-grade glioma; on the second row, initial iMR acquisition; on the third row, iMR control image obtained after resection, no residual disease can be seen around the surgical cavity; on the last row, postoperative MR confirming complete resection of the tumor. *Right*, iUS illustrative case. On the top row, preoperative MR T1+gadolinium coronal sections showing a right occipital high-grade lesion; on the second row, initial iUS exploration with a coronal view of the occipital lesion adjacent to the tentorium cerebelli; on the third row, iUS control exploration after surgical resection, with no apparent residual disease; on the last row, postoperative MR T1+gadolinium confirming complete resection of the tumor.

characteristics are conceivably responsible for the greater tumor resection rates (33). Notwithstanding, iUS is a currently evolving field, with advances like elastography (34), the use of contrast agents (32), integration with preoperative MR navigation (35, 36), along with the increased experience in the neurosurgical ground. Thus, iUS might soon proof effective to increase resection rates to as close as those obtained with iMR. In such a case, iUS would become more cost-effective and certainly more attainable for the general public, given the lower initial investment required.

Possibly, iMR and iUS are complementary aids in surgical neuroncology. During the resection, iUS provides real-time information while the surgeon is advancing towards the tumor limits, informing about the distance to relevant landmarks, such are the ventricles or blood vessels, and correcting neuronavigation inaccuracy due to brain shift and deformation (28, 37). Yet, at the end of the resection, it is the iMR that would reliably corroborate whether residual tumor has been left (38).

Limitations

Limitations of the present study include the time lapse between the collection of iMR series and iUS series of patients and the heterogeneity of both cohorts. Even when the general management of oncologic patients has not significantly changed over the last decade, advances in neuronavigation and improved experience in neurophysiologic mapping might have acted as bias when comparing the primary and secondary clinical outcomes between the two series. Probably, another source cofounding is the use of gross total resection as the unit of health gain; even when this parameter is of great clinical relevance, its achievement is not only related to the ability of detecting residual tumor. In fact, the surgical aim in this study was a maximal safe resection, and thus safety (e.g., neurophysiological alert, closeness to critical areas like the ventricles, the main vessels, the brainstem, etc.) might preclude the cautious surgeon from total resection. To add to this variability, it should be noted that provided the iUS is a highly operator-dependent technique, particularly compared to iMR, the reliability of the results regarding surgical duration and quality of resection are strictly linked to the surgeon's experience and expertise.

Finally, certain aspects of the study design should be addressed. The limited sample size, particularly in the iUS group, could be a source of deviation of the global results; however, this study was not intended to prove the superiority of one intraoperative technique over the other. Conversely, this economic evaluation is meant to help in health-related decision making during the set-up of novel operative armamentarium. In fact, the decision process underlying a cost-effectiveness analysis should be based only on the mean net benefits of each intervention irrespective of whether the difference between them is statistically significant (39, 40). Certainly, cost-effectiveness studies are typically performed within or after efficacy trials; nonetheless, no randomized trials are currently

TABLE 5 Summary of the main trials and observational studies evaluating intraoperative ultrasound and magnetic resonance imaging for the resection of high and/or low-grade gliomas.

Author	Intraoperative image	Study type	Tumor type	Sample size (imaging)	Rates of gross total resection	Surgical duration (min), mean
Senft et al., 2011 (10)	iMR, ultra-low-field	Randomized trial	Glioma grade 4	24	96%	250
Kubben et al., 2014 (16)	iMR, ultra-low-field	Randomized trial	Glioma grade 4	6	50%	90-120 more than control
Wu et al., 2014 (17)	iMR, high-field	Randomized trial	Glioma grades 2-4	44	91% high-grade 82% low-grade	Not reported
Bai et al., 2015 (18)	iMR, high-field	Prospective controlled trial	Glioma grades 2-4. Language area	112	95%	Not reported
Incekara et al., 2015 (19)	iMR, high-field	Retrospective cohort study	Glioma grades 1-2.	29	93%	Not reported
Rorder et al., 2013 (20)	iMR, high-field	Retrospective cohort study	Glioma grade 4	27	74%	354
Schatlo et al., 2015 (21)	iMR, ultra-low-field	Retrospective cohort study	Glioma grade 4	55	45%	Not reported
Familiari et al., 2018 (22)	iMR, high-field	Retrospective cohort study	Glioma grades 3-4	64	67%	Not reported
Bassaganyas-Vancells et al. 2019 (23)	iMR, ultra-low-field	Retrospective cohort study	Glioma grades 3-4	58	72%	188
Fujii et al., 2022 (24)	iMR, low-field	Retrospective cohort study	Glioma grades 2-4	11	73%	466
Current study (Present study data)	iMR, low-field	Retrospective cohort study	Glioma grades 2-4	50	70%	450
Renner et al., 2005 (25)	iUS	Prospective series	Glioma grade 4 and metastasis	22	58%	Not reported
Moiyadi et al., 2013 (26)	iUS, navigated	Retrospective cohort study	Glioma grade 3-4	51	47%	264
Solheim et al., 2010 (27)	iUS	Retrospective cohort study	Glioma grade 4	142	37%	Not reported
Shetty et al., 2021 (28)	iUS, navigated	Retrospective series	Glioma grades 2-4	210	75%	Not reported
Current study (Present study data)	iUS	Retrospective cohort study	Glioma grade 2-4	17	60%	209

In studies where two groups are compared, the sample size refers to the group exposed to the intraoperative imaging.

available comparing iMR and iUS in neurosurgical oncology. On the other hand, economic evaluation is not typically concerned with hypothesis testing, is rather more an estimation, and thus could still provide useful information even when under-powered.

Conclusion

In intracranial oncological procedures, iMR and iUS seem to afford similar results in terms of extent of resection and postoperative performance status; still, the outcomes slightly favor iMR although at a higher relative cost and with longer surgical times. Surgical duration decreases with cumulative experience with iMR, but not so much with the use of iUS, reflecting the obvious differences in the intraoperative workflows between both techniques; while iMR involves the whole surgical team becoming familiarized with patient preparation and device mobilization, iUS relies directly on the surgeon's ability to simultaneously acquire and interpret the examination images. Possibly, iMR and iUS are complementary aids in neurosurgical oncology: Whilst iUS assists the surgeon with real-time captures while advancing towards the tumor limits, informing about the distance to relevant landmarks and correcting neuronavigation inaccuracy due to brain shift; at the end of the resection, it is the iMR that reliably corroborates whether residual tumor remains.

Data availability statement

The raw data supporting the conclusions of this article will be made available by the authors, without undue reservation.

Ethics statement

The studies involving human participants were reviewed and approved by Comité de Etica de Investigación Clínica, Hospital Clínic de Barcelona, Spain. Written informed consent for participation was not required for this study in accordance with the national legislation and the institutional requirements.

Author contributions

AM, AS, and JG designed and led the present study. JG, AS, and PR developed the theory and performed the computations. AM, AF, and AR collected the clinical and economic data. AM, AS, SG-O, and JG performed the analytical methods and interpreted them. AM drafted the manuscript. JG, AS, and PR critically revised the manuscript. JE gave institutional, material, and logistic support. All authors contributed to the article and approved the submitted version.

Conflict of interest

The authors declare that the research was conducted in the absence of any commercial or financial relationships that could be construed as a potential conflict of interest.

Publisher's note

All claims expressed in this article are solely those of the authors and do not necessarily represent those of their affiliated organizations, or those of the publisher, the editors and the reviewers. Any product that may be evaluated in this article, or claim that may be made by its manufacturer, is not guaranteed or endorsed by the publisher.

References

1. Fountain DM, Bryant A, Barone DG, Waqar M, Hart MG, Bulbeck H, et al. Intraoperative imaging technology to maximise extent of resection for glioma: a network meta-analysis. *Cochrane Database Syst Rev* (2021) 1(1):CD013630. doi: 10.1002/14651858.CD013630.pub2

2. Verburg N, de Witt Hamer PC. State-of-the-art imaging for glioma surgery. *Neurosurg Rev* (2021) 44(3):1331–43. doi: 10.1007/s10143-020-01337-9

3. Noh T, Mustroph M, Golby AJ. Intraoperative imaging for high-grade glioma surgery. *Neurosurg Clin N Am* (2021) 32(1):47–54. doi: 10.1016/j.nec.2020.09.003

4. Sanai N, Polley MY, McDermott MW, Parsa AT, Berger MS. An extent of resection threshold for newly diagnosed glioblastomas. *J Neurosurg* (2011) 115 (1):3–8. doi: 10.3171/2011.2.jns10998

5. Li YM, Suki D, Hess K, Sawaya R. The influence of maximum safe resection of glioblastoma on survival in 1229 patients: Can we do better than gross-total resection? *J Neurosurg* (2016) 124(4):977–88. doi: 10.3171/2015.5.JNS142087

6. McGirt MJ, Chaichana KL, Attenello FJ, Weingart JD, Than K, Burger PC, et al. Extent of surgical resection is independently associated with survival in patients with hemispheric infiltrating low-grade gliomas. *Neurosurgery.* (2008) 63 (4):700–7. doi: 10.1227/01.NEU.0000325729.41085.73

7. Smith JS, Chang EF, Lamborn KR, Chang SM, Prados MD, Cha S, et al. Role of extent of resection in the long-term outcome of low-grade hemispheric gliomas. *J Clin Oncol* (2008) 26(8):1338–45. doi: 10.1200/JCO.2007.13.9337

8. Lee CH, Kim DG, Kim JW, Han JH, Kim YH, Park CK, et al. The role of surgical resection in the management of brain metastasis: a 17-year longitudinal study. *Acta Neurochir (Wien).* (2013) 155(3):389–97. doi: 10.1007/s00701-013-1619-y

9. Moiyadi A, Shetty P. Objective assessment of utility of intraoperative ultrasound in resection of central nervous system tumors: A cost-effective tool for intraoperative navigation in neurosurgery. *J Neurosci Rural Pract* (2011) 2(1):4–11. doi: 10.4103/0976-3147.80077

10. Senft C, Bink A, Franz K, Vatter H, Gasser T, Seifert V. Intraoperative MRI guidance and extent of resection in glioma surgery: a randomised, controlled trial. *Lancet Oncol* (2011) 12(11):997–1003. doi: 10.1016/S1470-2045(11)70196-6

11. Mohammadi AM, Sullivan TB, Barnett GH, Recinos V, Angelov L, Kamian K, et al. Use of high-field intraoperative magnetic resonance imaging to enhance the extent of resection of enhancing and nonenhancing gliomas. *Neurosurgery.* (2014) 74(4):339–48. doi: 10.1227/NEU.0000000000000278

12. Makary M, Chiocca EA, Erminy N, Antor M, Bergese SD, Abdel-Rasoul M, et al. Clinical and economic outcomes of low-field intraoperative MRI-guided tumor resection neurosurgery. *J Magn Reson Imaging.* (2011) 34(5):1022–30. doi: 10.1002/jmri.22739

13. Garcia-Garcia S, García-Lorenzo B, Ramos PR, Gonzalez-Sanchez JJ, Culebras D, Restovic G, et al. Cost-effectiveness of low-field intraoperative magnetic resonance in glioma surgery. *Front Oncol* (2020) 10:586679. doi: 10.3389/fonc.2020.586679

14. Karschnia P, Vogelbaum MA, van den Bent M, Cahill DP, Bello L, Narita Y, et al. Evidence-based recommendations on categories for extent of resection in diffuse glioma. *Eur J Cancer.* (2021) 149:23–33. doi: 10.1016/j.ejca.2021.03.002

15. Ginat DT, Swearingen B, Curry W, Cahill D, Madsen J, Schaefer PW. 3 Tesla intraoperative MRI for brain tumor surgery. *J Magn Reson Imaging.* (2014) 39 (6):1357–65. doi: 10.1002/jmri.24380

16. Kubben PL, Scholtes F, Schijns OE, Ter Laak-Poort MP, Teernstra OP, Kessels AG, et al. Intraoperative magnetic resonance imaging versus standard neuronavigation for the neurosurgical treatment of glioblastoma: A randomized controlled trial. *Surg Neurol Int* (2014) 5:70. doi: 10.4103/2152-7806.132572

17. Wu JS, Gong X, Song YY, Zhuang DX, Yao CJ, Qiu TM, et al. 3.0-T intraoperative magnetic resonance imaging-guided resection in cerebral glioma surgery: interim analysis of a prospective, randomized, triple-blind, parallel-controlled trial. *Neurosurgery* (2014) 61 Suppl 1:145–54. doi: 10.1227/NEU.0000000000000372

18. Bai SC, Xu BN, Wei SH, Geng JF, Wu DD, Yu XG, et al. Intraoperative high-field magnetic resonance imaging combined with functional neuronavigation in resection of low-grade temporal lobe tumors. *World J Surg Oncol* (2015), 13:286. doi: 10.1186/s12957-015-0690-7

19. Incekara F, Olubiyi O, Ozdemir A, Lee T, Rigolo L, Golby A. The value of pre- and intraoperative adjuncts on the extent of resection of hemispheric low-grade gliomas: A retrospective analysis. *J Neurol Surg A Cent Eur Neurosurg* (2016) 77(2):79–87. doi: 10.1055/s-0035-1551830

20. Roder C, Bisdas S, Ebner FH, Honegger J, Naegele T, Ernemann U, et al. Maximizing the extent of resection and survival benefit of patients in glioblastoma

surgery: high-field iMRI versus conventional and 5-ALA-assisted surgery. *Eur J Surg Oncol* (2014) 40(3):297–304. doi: 10.1016/j.ejso.2013.11.022

21. Schatlo B, Fandino J, Smoll NR, Wetzel O, Remonda L, Marbacher S, et al. Outcomes after combined use of intraoperative MRI and 5-aminolevulinic acid in high-grade glioma surgery. *Neuro Oncol* (2015) 17(12):1560–7. doi: 10.1093/neuonc/nov049

22. Familiari P, Frati A, Pesce A, Miscusi M, Cimatti M, Raco A. Real impact of intraoperative magnetic resonance imaging in newly diagnosed glioblastoma multiforme resection: An observational analytic cohort study from a single surgeon experience. *World Neurosurg* (2018) 116:e9–e17. doi: 10.1016/j.wneu.2017.12.176

23. Bassaganyas-Vancells C, Roldán P, González JJ, Ferrés A, García S, Culebras D, et al. Combined use of 5-aminolevulinic acid and intraoperative low-field magnetic resonance imaging in high-grade glioma surgery. *World Neurosurg* (2019) 130:e206–12. doi: 10.1016/j.wneu.2019.06.029

24. Fujii Y, Ogiwara T, Watanabe G, Hanaoka Y, Goto T, Hongo K, et al. Intraoperative low-field magnetic resonance imaging-guided tumor resection in glioma surgery: Pros and cons. *J Nippon Med Sch.* (2022) 89(3):269–76. doi: 10.1272/jnms.JNMS.2022_89-301

25. Renner C, Lindner D, Schneider JP, Meixensberger J. Evaluation of intraoperative ultrasound imaging in brain tumor resection: a prospective study. *Neurol Res* (2005) 27(4):351–7. doi: 10.1179/016164105X40039

26. Moiyadi AV, Shetty PM, Mahajan A, Udare A, Sridhar E. Usefulness of three-dimensional navigable intraoperative ultrasound in resection of brain tumors with a special emphasis on malignant gliomas. *Acta Neurochir (Wien).* (2013) 155(12):2217–25. doi: 10.1007/s00701-013-1881-z

27. Solheim O, Selbekk T, Jakola AS, Unsgård G. Ultrasound-guided operations in unselected high-grade gliomas–overall results, impact of image quality and patient selection. *Acta Neurochir (Wien).* (2010) 152(11):1873–86. doi: 10.1007/s00701-010-0731-5

28. Shetty P, Yeole U, Singh V, Moiyadi A. Navigated ultrasound-based image guidance during resection of gliomas: practical utility in intraoperative decision-making and outcomes. *Neurosurg Focus.* (2021) 50(1):E14. doi: 10.3171/2020.10.FOCUS20550

29. Unsgård G, Sagberg LM, Müller S, Selbekk T. A new acoustic coupling fluid with ability to reduce ultrasound imaging artefacts in brain tumour surgery-a phase I study. *Acta Neurochir (Wien).* (2019) 161(7):1475–86. doi: 10.1007/s00701-019-03945-x

30. Bø HK, Solheim O, Kvistad KA, Berntsen EM, Torp SH, Skjulsvik AJ, et al. Intraoperative 3D ultrasound-guided resection of diffuse low-grade gliomas: radiological and clinical results. *J Neurosurg* (2019) 132(2):518–29. doi: 10.3171/2018.10.JNS181290

31. Unsgård G, Lindseth F. 3D ultrasound-guided resection of low-grade gliomas: principles and clinical examples. *Neurosurg Focus.* (2019) 47(6):E9. doi: 10.3171/2019.9.FOCUS19605

32. Prada F, Perin A, Martegani A, Aiani L, Solbiati L, Lamperti M, et al. Intraoperative contrast-enhanced ultrasound for brain tumor surgery. *Neurosurgery.* (2014) 74(5):542–52. doi: 10.1227/NEU.0000000000000301

33. Tronnier VM, Bonsanto MM, Staubert A, Knauth M, Kunze S, Wirtz CR. Comparison of intraoperative MR imaging and 3D-navigated ultrasonography in the detection and resection control of lesions. *Neurosurg Focus.* (2001) 10(2):E3. doi: 10.3171/foc.2001.10.2.4

34. Cepeda S, García-García S, Arrese I, Velasco-Casares M, Sarabia R. Advantages and limitations of intraoperative ultrasound strain elastography applied in brain tumor surgery: A single-center experience. *Oper Neurosurg (Hagerstown).* (2022) 22(5):305–14. doi: 10.1227/ons.0000000000000122

35. Prada F, Del Bene M, Mattei L, Casali C, Filippini A, Legnani F, et al. Fusion imaging for intra-operative ultrasound-based navigation in neurosurgery. *J Ultrasound.* (2014) 17(3):243–51. doi: 10.1007/s40477-014-0111-8

36. Berntsen EM, Gulati S, Solheim O, Kvistad KA, Torp SH, Selbekk T, et al. Functional magnetic resonance imaging and diffusion tensor tractography incorporated into an intraoperative 3-dimensional ultrasound-based neuronavigation system: impact on therapeutic strategies, extent of resection, and clinical outcome. *Neurosurgery.* (2010) 67(2):251–64. doi: 10.1227/01.NEU.0000371731.20246.AC

37. Dohrmann GJ, Rubin JM. History of intraoperative ultrasound in neurosurgery. *Neurosurg Clinics N Am* (2001) 12(1):155–66. doi: 10.1016/s1042-3680(18)30074-3

38. Bastos DCA, Juvekar P, Tie Y, Jowkar N, Pieper S, Wells WM, et al. Challenges and opportunities of intraoperative 3D ultrasound with neuronavigation in relation to intraoperative MRI. *Front Oncol* (2021) 11:656519. doi: 10.3389/fonc.2021.656519

39. Claxton K. The irrelevance of inference: a decision-making approach to the stochastic evaluation of health care technologies. *J Health Econ* (1999) 18(3):341–64. doi: 10.1016/s0167-6296(98)00039-3

40. Bader C, Cossin S, Maillard A, Bénard A. A new approach for sample size calculation in cost-effectiveness studies based on value of information. *BMC Med Res Methodol* (2018) 18(1):113. doi: 10.1186/s12874-018-0571-1

41. Mahboob S, McPhillips R, Qiu Z, Jiang Y, Meggs C, Schiavone G, et al. Intraoperative ultrasound-guided resection of gliomas: A meta-analysis and review of the literature. *World Neurosurg* (2016) 92:255–63. doi: 10.1016/j.wneu.2016.05.007

42. Zhang J, Chen X, Zhao Y, Wang F, Li F, Xu B. Impact of intraoperative magnetic resonance imaging and functional neuronavigation on surgical outcome in patients with gliomas involving language areas. *Neurosurg Rev* (2015) 38(2):319–30. doi: 10.1007/s10143-014-0585-z

frontiers | Frontiers in Oncology

TYPE Original Research
PUBLISHED 30 November 2022
DOI 10.3389/fonc.2022.1043697

OPEN ACCESS

EDITED BY
Julius Höhne,
University Medical Center Regensburg, Germany

REVIEWED BY
Bharat Guthikonda,
Louisiana State University Health Shreveport, United States
Maryam Jalessi,
Iran University of Medical Sciences, Iran

*CORRESPONDENCE
Marcus A. Zachariah
mzachariah@umc.edu

†These authors have contributed equally to this work and share first authorship

SPECIALTY SECTION
This article was submitted to Neuro-Oncology and Neurosurgical Oncology, a section of the journal Frontiers in Oncology

RECEIVED 13 September 2022
ACCEPTED 08 November 2022
PUBLISHED 30 November 2022

CITATION
Baker KE, Robbins AC, Wasson RG, McCandless MG, Lirette ST, Kimball RJ, Washington CW, Luzardo GD, Stringer SP and Zachariah MA (2022) Side-firing intraoperative ultrasound applied to resection of pituitary macroadenomas and giant adenomas: A single-center retrospective case-control study.
Front. Oncol. 12:1043697.
doi: 10.3389/fonc.2022.1043697

Side-firing intraoperative ultrasound applied to resection of pituitary macroadenomas and giant adenomas: A single-center retrospective case-control study

Katherine E. Baker[1†], Austin C. Robbins[1†], Robert G. Wasson[1], Martin G. McCandless[1], Seth T. Lirette[2], Rebekah J. Kimball[1], Chad W. Washington[1], Gustavo D. Luzardo[1], Scott P. Stringer[3] and Marcus A. Zachariah[1*]

[1]Department of Neurosurgery, The University of Mississippi Medical Center, Jackson, MS, United States, [2]Department of Data Science, The University of Mississippi Medical Center, Jackson, MS, United States, [3]Department of Otolaryngology, The University of Mississippi Medical Center, Jackson, MS, United States

Introduction: Multiple intraoperative navigation and imaging modalities are currently available as an adjunct to endoscopic transsphenoidal resection of pituitary adenomas, including intraoperative CT and MRI, fluorescence guidance, and neuronavigation. However, these imaging techniques have several limitations, including intraoperative tissue shift, lack of availability in some centers, and the increased cost and time associated with their use. The side-firing intraoperative ultrasound (IOUS) probe is a relatively new technology in endoscopic endonasal surgery that may help overcome these obstacles.

Methods: A retrospective analysis was performed on patients admitted for resection of pituitary adenomas by a single surgeon at the University of Mississippi Medical Center. The control (non-ultrasound) group consisted of twelve (n=12) patients who received surgery without IOUS guidance, and the IOUS group was composed of fifteen (n=15) patients who underwent IOUS-guided surgery. Outcome measures used to assess the side-firing IOUS were the extent of tumor resection, postoperative complications, length of hospital stay (LOS) in days, operative time, and self-reported surgeon confidence in estimating the extent of resection intraoperatively.

Results: Preoperative data analysis showed no significant differences in patient demographics or presenting symptoms between the two groups. Postoperative data revealed no significant difference in the rate of gross total

resection between the groups (p = 0.716). Compared to the non-US group, surgeon confidence was significantly higher (p < *0.001)*, and operative time was significantly lower for the US group in univariate analysis (p = 0.011). Multivariate analysis accounting for tumor size, surgeon confidence, and operative time confirmed these findings. Interestingly, we noted a trend for a lower incidence of postoperative diabetes insipidus in the US group, although this did not quite reach our threshold for statistical significance.

Conclusion: Incorporating IOUS as an aid for endonasal resection of pituitary adenomas provides real-time image guidance that increases surgeon confidence in intraoperative assessment of the extent of resection and decreases operative time without posing additional risk to the patient. Additionally, we identified a trend for reduced diabetes insipidus with IOUS.

KEYWORDS

adenoma, skull base, ultrasound, endoscopic, imaging, sella, tumor, neurosurgery

Introduction

Pituitary adenomas comprise a group of tumors differing in cell origin, response to treatment, and function. Common symptoms include hormonal dysfunction, vision changes, and headaches (1). Maximal resection is associated with prolonged progression-free survival, improvement of neurological deficits, and an increased likelihood of hormonal remission (2–4). Several technologies are currently employed to aid in the resection of pituitary adenomas. Intraoperative neuronavigation may confirm visual identification of anatomy; however, its effectiveness may be limited by intraoperative tissue shift, especially during the resection of larger tumors. Intraoperative MRI (iMRI), intraoperative CT (iCT), and fluorescence guidance may also be used to maximize safe resection (5). However, these techniques are not always available and may substantially increase the time, cost, and complexity of pituitary surgery.

Intraoperative ultrasound (IOUS) has not commonly been used in pituitary adenoma resection but has recently become more prevalent (6–10). Both end-firing and side-firing probes are available, each suited for specific applications. End-firing probes are helpful for depth assessment, while side-firing probes enhance awareness of anatomy adjacent to the probe tip and potentially beyond the endoscopic field of view. Early generation end-firing ultrasound probes were larger, which limited the effectiveness of these models. In some cases, the size of these probes prevented the advancement of the probe tip into the sella turcica, restricting use to the sphenoid sinus (11). Recent models of both end-firing and side-firing probes have been designed specifically for use in transsphenoidal surgery. We have previously reported the potential benefits of end-firing IOUS technology in the resection of a clival chordoma (12).

The development of relatively low-cost, minimally invasive, side-firing probes has allowed surgeons to use IOUS within the sella turcica for optimal imaging of the cavernous carotids and parasellar region. Side-firing IOUS may improve the surgeon's ability to estimate the extent of resection while avoiding injury to nearby anatomy and perhaps improving the safety of endoscopic transsphenoidal resection of pituitary adenomas. These newer probes have proved helpful for identifying vascular structures, such as the internal carotid artery and branches of the Circle of Willis, in addition to other vital structures, such as the optic chiasm and diaphragm sellae (13) (Figure 1). The surgeon may also use other features of the IOUS to guide their resection. For example, measurements are easily obtained intraoperatively and can provide perspective on the size of the residual tumor and the distance to nearby structures (Figure 1D). Clear identification of these structures allows the surgeon to accurately assess their location and tailor the resection accordingly, thus preventing CSF leaks caused by violation of the diaphragm or damage to other nearby structures. Previous studies in the literature report the implementation of new imaging techniques in surgical settings and their effects on self-reported surgeon confidence when identifying key structures (14–20). However, the effects of IOUS guidance on surgeon confidence are not well described. Our study compares surgeon confidence with and without the use of side-firing IOUS and shows that side-firing IOUS guidance increases surgeon confidence.

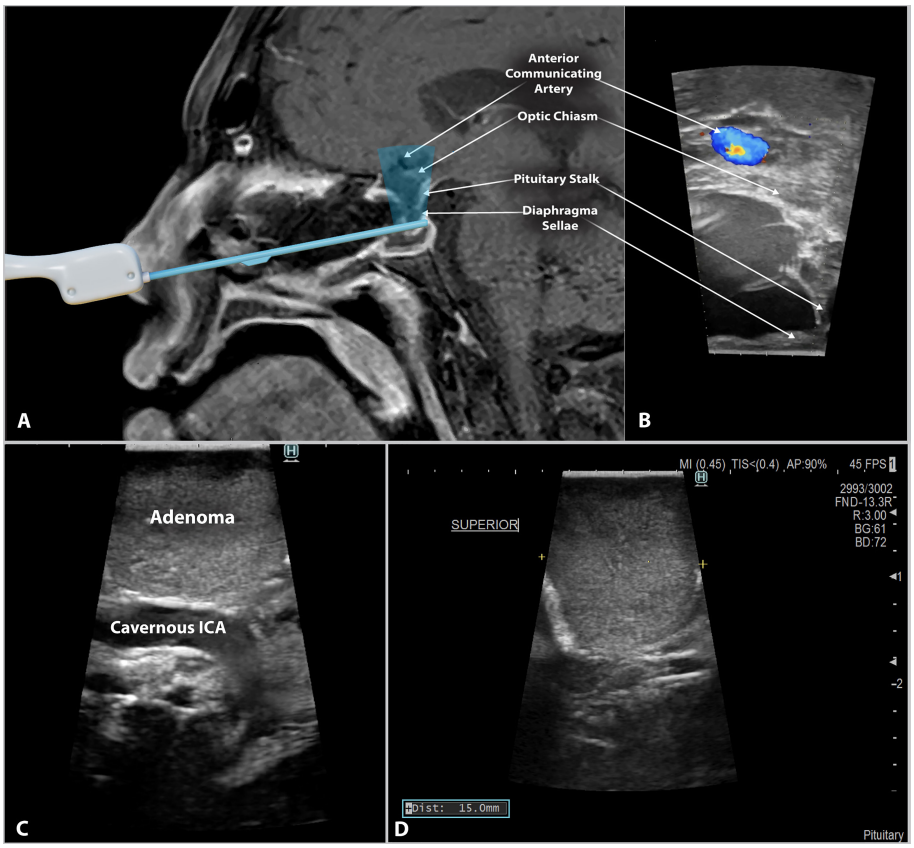

FIGURE 1
Side-firing intraoperative ultrasound in endoscopic endonasal pituitary surgery. **(A)** Schematic image depicting the scanning window of the side-firing ultrasound transducer. A digital ultrasound probe model is superimposed onto a T1 post-gadolinium MRI. **(B)** Intraoperative ultrasound image from the same patient showing intraoperative imaging of the surrounding parasellar anatomy. During image acquisition, the probe tip was abutted to the inferior surface of the diaphragma sellae, as demonstrated in Figure 1A. **(C)** Side-firing IOUS image showing pituitary adenoma tissue and the location of the cavernous segment of the Internal Carotid artery (cavernous ICA). The IOUS probe is directed laterally within the sella turcica. This image demonstrates the ability to identify critical structures and their relationship to the tumor tissue. **(D)** IOUS can be used to obtain tumor size data intraoperatively. The yellow symbols (+) in the above image indicate the location of the measurement, with the results displayed in the bottom left corner.

Methods

Study design

A retrospective analysis was conducted on all patients admitted for elective endonasal transsphenoidal resection of pituitary adenomas by a single surgeon at the University of Mississippi Medical Center (UMMC) from 10/7/2020 to 2/23/2022. The study focused on the following data: patient demographics (age, sex, race), preoperative findings (presenting symptoms, tumor size, and Knosp grade), intraoperative findings (surgeon confidence, operative time, and complications), and postoperative findings (gross total resection, subtotal resection, complications, and length of stay). Patients underwent preoperative MRI with and without gadolinium contrast and preoperative hormone evaluations. Surgery for the non-US control group consisted of twelve (n = 12) patients who received surgery before implementing IOUS for pituitary macroadenoma resection at our institution on 7/13/2021. Following this date, all subsequent surgeries (n = 15) were guided by the Fujifilm/Hitachi side-firing pituitary guidance ultrasound transducer and neuronavigation.

Surgical approach

An endoscopic endonasal transsphenoidal approach was performed on all patients in this study. The initial portion of the procedure and follow-up appointments were conducted in collaboration with Otolaryngology. The procedure was handed off to neurosurgery after entry into the sphenoid sinus, and the

remainder of the surgery was performed following standard endoscopic techniques.

Intraoperative ultrasound

The IOUS probe used in this study is the Fujifilm/Hitachi pituitary guidance transducer. The Fujifilm ultrasound probe is a commercially available, side-firing linear array transducer with a 60˚ trapezoidal scanning window and a maximum diameter of 2.87 mm. The probe fires at a 90-degree angle from the axis of insertion. The scanning window is tilted as the surgeon rotates the probe, and images are acquired perpendicular to the probe axis. This capability allows the surgeon to sweep through the surrounding anatomy and creates a large field of view that is particularly useful when working in the surgical corridor of endoscopic endonasal surgery (Figure 1). For the US group, the surgeon used IOUS several times as the case progressed to estimate the extent of resection and identify residual tumor. Additionally, color flow Doppler imaging was used to quickly assess proximity to intracranial vasculature (Figure 1).

Outcome measures

Outcome measures used to assess the effectiveness of side-firing IOUS were the extent of tumor resection, postoperative complications, length of hospital stay (LOS) in days, operative time, and self-reported surgeon confidence in assessing the extent of resection intraoperatively. To measure surgeon confidence, the surgeon was asked at the end of each case to rate his confidence in the intraoperative assessment of the extent of resection. This measure is subjective and scored on a scale of 1-10, with 10 being the highest confidence and 1 being the lowest confidence. The extent of resection was determined based on the interpretation of each patient's three-month postoperative MRI. GTR was defined by the absence of visible tumor tissue on three-month postoperative MRI as determined by a neuroradiologist blinded to the study.

Data collection and analysis

UMMC's institutional review board approved this study, and informed consent was obtained from all patients (IRB File # 2021-1012). Patient data were collected from the electronic medical record and managed using REDCap (Research Electronic Data Capture) electronic data capture tools hosted at the University of Mississippi Medical Center (19, 20). Data manipulation and visualization were performed using GraphPad Prism.

Statistical analysis

Patient characteristics were analyzed with standard summary statistics. An alpha of 0.05 was selected as the threshold of significance for all analyses, and significant p values are denoted with an asterisk (*) in the figures. A X^2-test or independent t-test was used to assess significance where appropriate, and Fisher's Exact Test was used to assess significance in smaller subpopulations. Potential correlations were examined using linear regression and multilinear analysis to assess the multivariate interactions of surgeon confidence, tumor size, and operative time. Data is presented in this paper as mean ± standard deviation or percent of patients when appropriate.

Results

Demographic data

The case-control study included two groups of patients with pituitary adenomas. The first group underwent tumor resection without IOUS guidance (n = 12), and the second with IOUS guidance (n = 15). The non-US group consisted of 67% males and 33% females, 60% African American and 40% Caucasian, with an average age of (47.4 ± 16.9) years. The US group included 69% men, 31% women, 69% African American, and 31% Caucasian, with an average age of (57.3 ± 7.4) years. There were no significant differences in patient demographics (age, sex, race) between the two groups (Table 1).

Preoperative tumor characterization

Tumors were characterized preoperatively for both groups and classified as microadenoma (<1 cm), macroadenoma (1 cm-4 cm), or giant adenoma (> 4 cm). None of the patients had microadenomas, 78% had macroadenomas, and the remainder were giant adenomas (22%). There was no significant difference in tumor size between the non-US group (3.43 ± 1.5 cm) and the US group (2.89 ± 1.5 cm), although the US group had a greater proportion of macroadenomas (93%) than the non-US group (54%) (p = 0.029). The difference in tumor size between groups was controlled for in subsequent analyses of operative time, surgeon confidence, and tumor size presented below. There was no significant difference in preoperative Knosp Grade, as shown in Figure 2. Patients in both groups had similar presenting symptoms, with the most common being vision loss (non-US: 100%, US: 73%), followed by headache (non-US: 54%, US: 47%), and hormonal dysfunction (non-US: 39%, US: 20%) (Figure 2).

TABLE 1 Baseline Characteristics and Presenting Symptoms.

Characteristics	US, n=15	Non-US, n=13	P-Value
Age at surgery (years)			0.067
Mean ± SD	57.3 ± 7.4	47.4 ± 16.9	
Range	42-66	19-74	
95% CI	53.3-61.4	37.2-57.6	
M/F (% Female) *	10/5 (33%)	9/4 (31%)	>0.99
AA/C (% AA) *	9/6 (40%)	9/4 (31%)	0.705

AA, African American; C, Caucasian; LOS, Length of Stay.
X^2-test and independent t-test were performed.
*Fisher Exact Test was performed.
Bold text indicates P < 0.05.

Postoperative results

IOUS use did not affect the extent of resection; gross total resection was achieved in 53% of US patients and 46% of non-US patients (p = 0.716). Within the subset of patients with subtotal resection, the postoperative Knosp grades showed no difference, as shown in Figure 3 (p = 0.343). There was no difference in total postoperative complications between the two groups (non-US: 46%, US: 33%) (p = 0.488). However, there was a trend toward fewer diabetes insipidus complications in the US group (7%) compared to the non-US group (39%) (p = 0.069), although this did not reach our threshold for statistical significance. More data will need to be collected to confirm this trend. There was no difference in postoperative length of hospital stay between the non-US group (7.08 ± 9.3 days) and US group (3.13 ± 1.3 days) (p = 0.155).

Operative time was significantly lower in the US group (201 ± 48 minutes) than in the non-US group (280 ± 93 minutes) (p = 0.011). Linear regression showed that the operative time remained lower in the US group than the non-US group when adjusted for tumor size (Slope p = 0.9844, Intercept p = 0.02) (Figure 4), suggesting that IOUS results in shorter operative time for all tumor sizes.

In our study, surgeon confidence is a self-reported measure that we defined as how confident the surgeon feels in the accurate intraoperative assessment of extent of resection. The US group had a significantly higher average surgeon confidence level (6.9 ± 1.4) than the non-US group (4.9 ± 1.2) (p < 0.001).

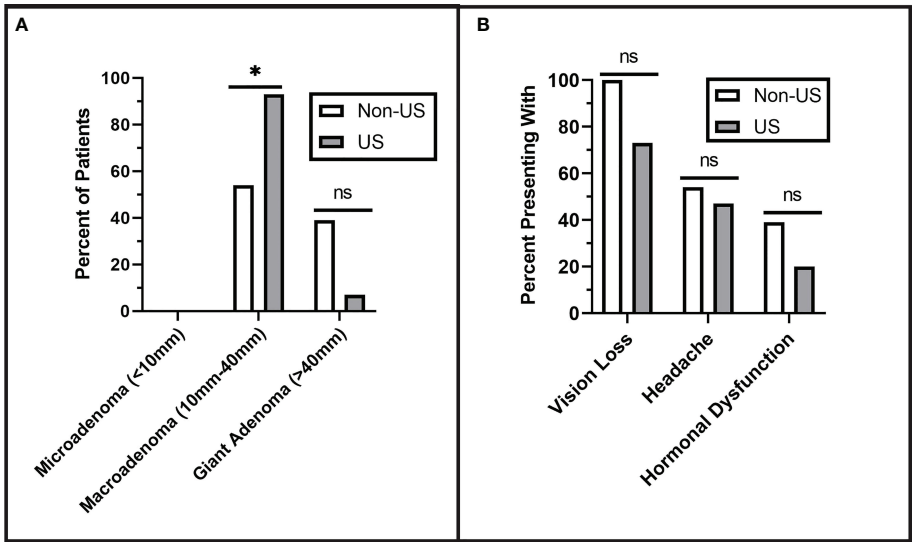

FIGURE 2
Preoperative Tumor Characterization. **(A)** Pituitary adenomas were classified by size. No microadenomas were observed in either group. The US group had significantly more macroadenomas than the non-US group (p = 0.029). **(B)** There were no significant differences in the rates of presenting symptoms including vision loss (p = 0.102), headache (p = 0.705), and hormonal dysfunction (p = 0.410). Asterisks (*) indicate significance of p < 0.05. Values that did not reach the threshold for significance (p= <0.05) were labeled as non-significant (ns).

10.3389/fonc.2022.1043697

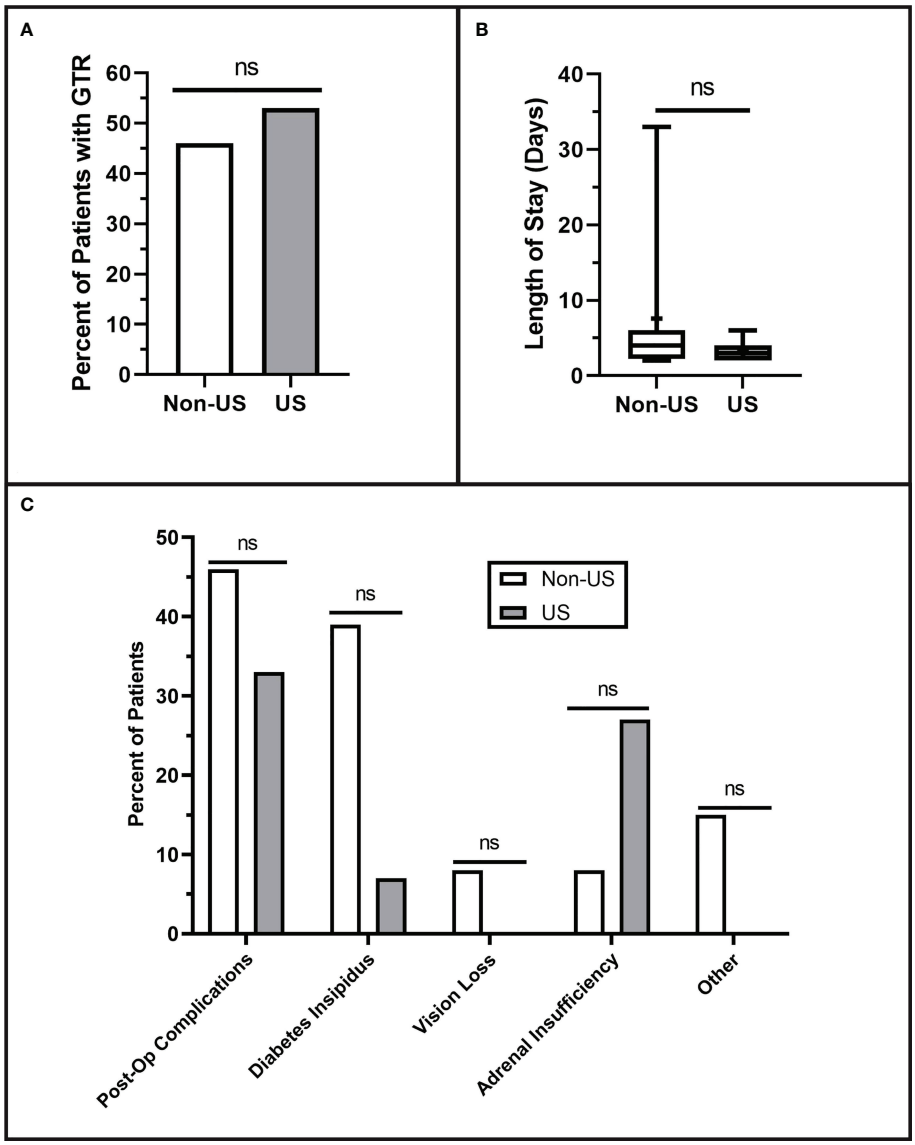

FIGURE 3
Postoperative Resection Results. **(A)** Qualitative extent of tumor resection was classified as either gross total (GTR) or subtotal. The extent of resection was determined based on the interpretation of each patient's three-month postoperative MRI. No differences were observed in qualitative extent of resection (p = 0.716). **(B)** Length of hospital stay showed no difference between the groups (p = 0.155). **(C)** There were no significant differences in the numbers of postoperative complications (p = 0.488) including diabetes insipidus (p = 0.069), vision loss (p = 0.464), adrenal insufficiency (p = 0.333), or other complications (P = 0.206). Values that did not reach the threshold for significance (p= <0.05) were labeled as non-significant (ns).

Surgeon confidence remained significantly greater in the US group than in the non-US group when adjusted for tumor size (Slope p = 0.7991, Intercept p < 0.0001) (Figure 5), indicating that IOUS use increased surgeon confidence regardless of tumor size.

Without IOUS, operative time dramatically increased as surgeon confidence declined (R = -0.867); however, IOUS use did not show a significant increase in operative time associated with lower confidence (R = -0.223). IOUS use significantly reduced the increase in operative time associated with lower surgeon confidence in the non-US group (Slope p = 0.0168) (Figure 6), suggesting that IOUS speeds up operative times even when surgeon confidence levels are lower.

Discussion

Intraoperative imaging technologies are implemented to provide guidance for a safer and more complete resection. Conventional intraoperative imaging techniques, such as

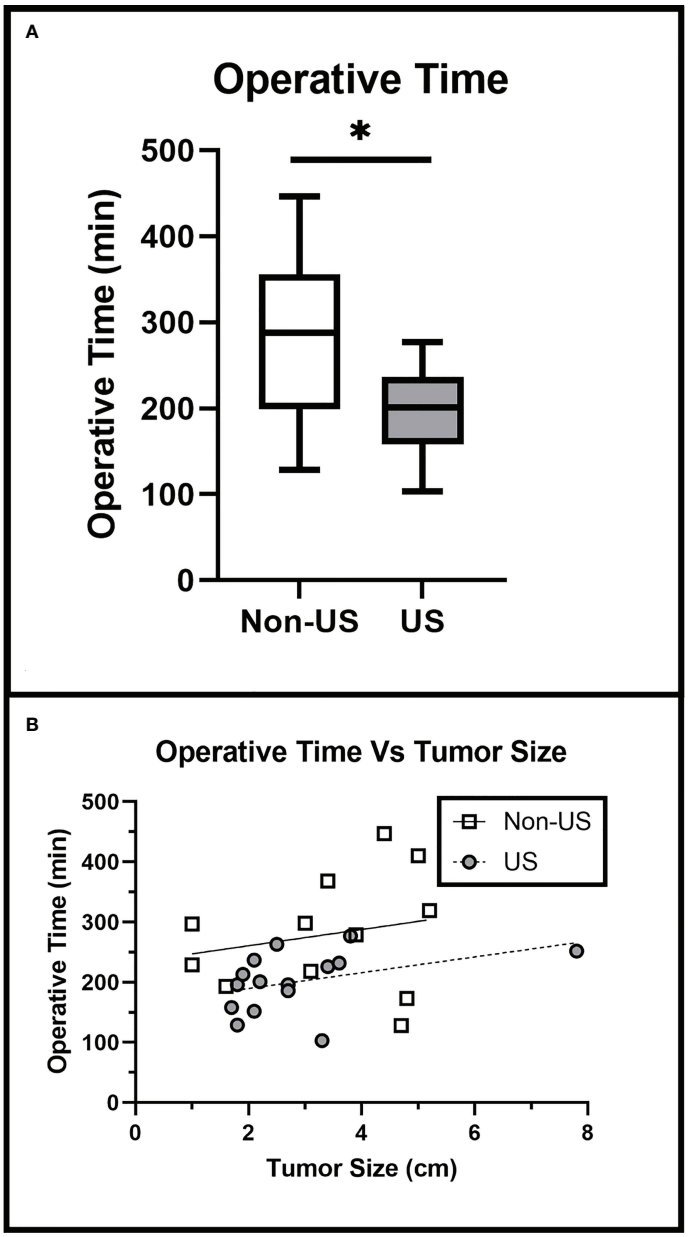

FIGURE 4
Operative Time is Reduced with the Use of IOUS: **(A)** IOUS significantly reduced procedure duration (p = 0.011). **(B)** IOUS reduced operative time when adjusted for tumor size (Slope p = 0.7991, Intercept p < 0.0001). Asterisks (*) indicate a significance of p < 0.05. Crosses (+) indicate mean values.

neuronavigation and iMRI, may help optimize the resection of pituitary adenomas, although these modalities often have limitations (5, 7, 14, 18, 21, 22).

Neuronavigation is frequently utilized for preoperative planning and evaluation of the patient's anatomy. However, as resection proceeds, intraoperative tissue shift may alter the anatomy of the surgical field and render preoperatively identified landmarks inaccurate. In the case of large and giant pituitary adenomas, the diaphragma sellae is often displaced from its usual location as the tumor expands superiorly. As resection proceeds, the diaphragma sellae descends from its preoperative location and can no longer be accurately localized on intraoperative imaging. Undetected tissue shift increases the risk of incomplete resection and the risk of injury to critical structures. To address this concern, iMRI has become increasingly widespread; however, iMRI is costly, time-intensive, may require modification of the operating room layout to accommodate the equipment, and has been

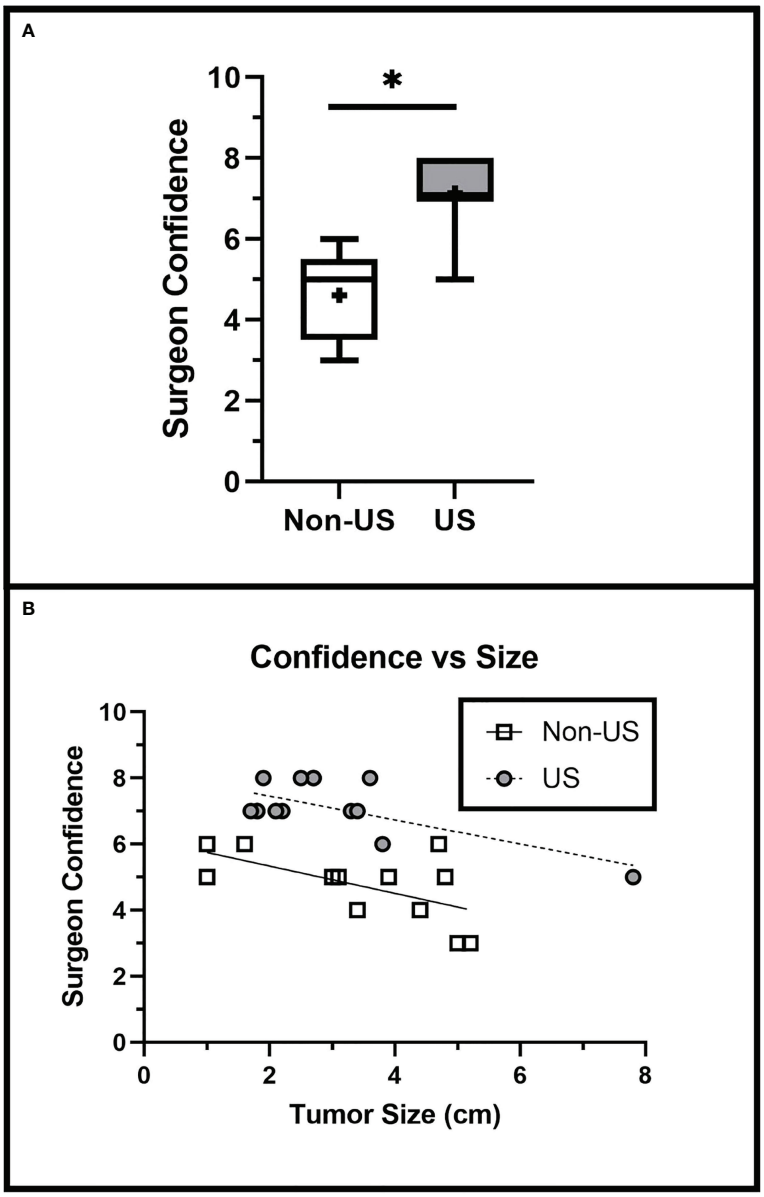

FIGURE 5
Surgeon Confidence is Increased with IOUS Use. **(A)** IOUS improved surgeon confidence in assessing the extent of tumor resection intraoperatively ($p < 0.001$). **(B)** Surgeon confidence was greater in the US group when adjusted for tumor size (Slope $p = 0.7991$, Intercept $p = 0.02$). Asterisks (*) indicate significance of $p < 0.05$. Crosses (+) indicate mean values.

associated with increased rates of false-positive identification of tumor tissue (5, 21). iMRI, in particular, substantially prolongs overall procedural time because of the time associated with operation of the iMRI machine and image acquisition (23–26). Additionally, fluid accumulation in and around the parasellar region may complicate the interpretation of MR images during resection (7).

iCT is well-described in both adult and pediatric neurosurgery. iCT is associated with increased operative times, although it is considerably faster than iMRI (26). iCT provides high-quality images that can be beneficial in specific pathologies but does not provide the soft tissue imaging resolution afforded by iMRI. Further, iCT may increase radiation exposure to patients and operating room staff (27, 28).

Fluorescent label-based guidance may improve resection by selectively causing tumor tissue to fluoresce, assisting visualization and resection. Studies have shown conflicting results among the available fluorescent agents (19, 29). Sodium

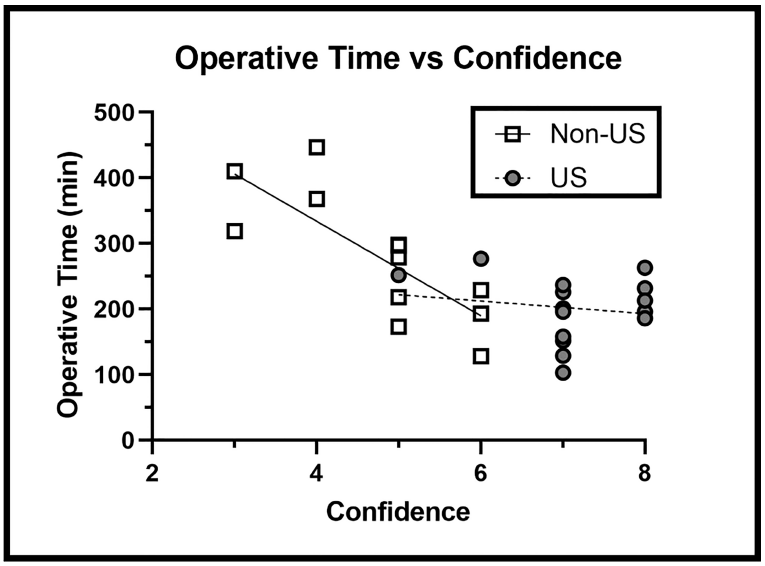

FIGURE 6
Operative Time versus Surgeon Confidence Findings: IOUS use prevented the increase in operative time associated with lower levels of surgeon confidence (p = 0.0168).

fluorescein (FNa) and 5-ALA with laser-based optical biopsy are two agents that have been shown to selectively fluoresce adenomatous tissue; however, these results are not consistent across all studies (29). In a study specific to endoscopic endonasal skull base surgery, 5-ALA was ineffective for the identification of neoplastic pituitary adenoma tissue (19). Another selective fluorescent agent, OTL38, exhibits promise in non-functioning pituitary adenomas. Newer agents, such as OTL38, are near-infrared region (NIR) fluorophores, while older agents, such as 5-ALA, are visible-light fluorophores. OTL38 binds to folate-expressing cells of non-functional adenomas and has greater photon tissue penetration than visible light fluorophores, allowing clearer demarcation between normal and neoplastic tissue (30). Although, this agent is still under investigation and more evidence is necessary to distinguish these agents as effective selective fluorescent agents to guide the resection of pituitary adenomas (29, 30).

IOUS has previously been used as an adjunct technology in endonasal pituitary surgery; however, the large size of older probes and limited availability have prevented widespread use in pituitary surgery. Recent probe advancements, particularly those designed specifically to suit the endoscopic endonasal approach, have allowed IOUS to become a much more effective tool in the transsphenoidal resection of pituitary adenomas. IOUS provides high-resolution real-time feedback to the surgeon without exposing the patient to additional radiation.

The side-firing IOUS enables the surgeon to quickly identify structures such as the diaphragma sellae, suprachiasmatic cistern, and cavernous carotids (Figure 1C). The surgeon may also utilize the intraoperative measuring capability of the probe to provide perspective on the size of the residual tumor and the distance to nearby structures (Figure 1D). Detection of critical structures with IOUS allows the surgeon to assess their location and limit their resection accordingly to prevent disruption of the nearby anatomy. For example, CSF leaks may be provoked by violating the diaphragma sellae during the transsphenoidal resection of pituitary adenomas.

Previous studies of IOUS have reported decreased incidence of intraoperative complications and intraoperative bleeding (8, 9). Interestingly, our results demonstrated a trend toward decreased postoperative diabetes insipidus with IOUS, which was not noted in previous studies of side-firing IOUS. These results are likely due to the increased confidence in identifying normal pituitary tissue with the IOUS probe and the ability to avoid disruption of the posterior pituitary gland and/or pituitary stalk, similar to the previous example of the diaphragma sellae. Additionally, pituitary adenomas may contain intratumoral membranes or cystic components, which may be mistaken for the diaphragma sellae. IOUS may be used to prevent this misidentification and ensure appropriate resection of tumor tissue concealed behind the membrane or cyst wall.

This study attempts to perform an initial quantification of the benefits of side-firing IOUS in pituitary surgery in a controlled manner. According to our data, IOUS has no negative impact on patient outcomes and is associated with

similar resection fraction, complications, and length of stay compared to control. Additionally, IOUS shortens the operative time and increases surgeon confidence. These results indicate that IOUS is a safe, effective, and efficient adjunct to endoscopic endonasal resection of pituitary adenomas.

However, there are limitations to IOUS use in endoscopic endonasal surgery. Some neurosurgeons have little experience using ultrasound in the operating room, so they must undergo IOUS training which takes time and practice to develop confidence when interpreting US images intraoperatively (6). The US machine occupies space in the operating room and may require repositioning other equipment and alteration of the workflow. However, the IOUS machine requires far less space than iCT or iMRI machines. Another drawback to IOUS use is the cost of the specialized probe, IOUS machine, and necessary training (16). While this study demonstrates the benefits of a side-firing US probe for transsphenoidal resection of large macroadenomas in the parasellar region, end-firing probes may be more appropriate in some circumstances. In the case of tumors that displace the normal pituitary posteriorly, an end-firing probe would be better indicated to properly visualize the posteriorly displaced pituitary gland to avoid its injury. If the pituitary is translated superiorly, a side-firing probe is more beneficial. This case typically reveals a diaphragm with a thickened appearance on IOUS due to the superior displacement of the normal pituitary gland, which adheres the gland to the diaphragm. Other surgeons have reported success using the end-firing probe to find small microadenomas within normal pituitary (4, 11, 31). One limitation of the study is the higher percentage of giant adenomas in the non-US group, although there was no significant difference in GTR between the groups. As tumor size and pattern of extension are key factors in achieving GTR, future studies between giant adenomas with similar patterns of extension and tumor characteristics are needed to resolve this limitation.

Despite these limitations, this study demonstrated that IOUS is associated with reduced operative time and increased surgeon confidence in assessing the extent of resection intraoperatively. Because surgeon confidence is subjective, the results may differ between surgeons. Additional studies are needed to explore how side-firing IOUS guidance impacts surgeon confidence among a larger group of surgeons. IOUS may enhance understanding of the intraoperative normal and tumor anatomy, allowing the surgeon to feel more confident as they make surgical decisions. The surgeon can employ the IOUS probe before proceeding with resection to confirm surgical orientation and location of critical structures. Before completion of the procedure, the probe may be used to verify that all tumor has been resected.

Conclusion

Existing adjunct technologies face limitations in resection of large and giant pituitary adenomas. This case-control study demonstrated that IOUS decreased operative time and increased surgeon confidence without any negative impact on patient outcomes. Additionally, our data suggested a nonsignificant trend towards decreased incidence of postoperative diabetes insipidus, which may potentially result from increased confidence in identifying normal pituitary tissue and avoiding injury to the posterior pituitary. In further studies, a change in surgical outcomes may be observed with larger sample sizes. Our findings suggest that IOUS is a valuable adjunct to guide resection of large and giant pituitary adenomas.

Data availability statement

The raw data supporting the conclusions of this article will be made available by the authors, without undue reservation.

Ethics statement

The studies involving human participants were reviewed and approved by University of Mississippi Institutional Review Board. The patients/participants provided their written informed consent to participate in this study.

Author contributions

KB drafted the manuscript, prepared figures and figure legends, operated ultrasound machine during resection, collected intraoperative ultrasound images and conducted chart review/data collection. AR provided writing assistance, assisted/operated ultrasound machine during resection, collected intraoperative ultrasound images, and conducted chart review/data collection. RW drafted the manuscript, conducted statistical analyses, prepared figures and figure legends. MM conducted statistical analyses and provided direction, SL provided guidance for statistical analysis, RK provided writing assistance and direction. SS collaborated with MZ to perform the endoscopic endonasal surgery. MZ provided care to the patient, collected intraoperative ultrasound images, and provided important critical feedback on intellectual content. All authors read and approved the manuscript. All authors contributed to the article and approved the submitted version.

Funding

This work was supported by research grants from Fujifilm and from the Mississippi Center for Translational and Clinical Research (U54GM115428).

Conflict of interest

Author MZ owns stock in Exelixis and Zinnia Healthcare, for whom he has also consulted. He has participated in prior research projects that were supported by BK Medical. He also has research support from the University of Mississippi Medical Center for clinical and translational research.

The remaining authors declare that the research was conducted in the absence of any commercial or financial relationships that could be construed as a potential conflict of interest.

Publisher's note

All claims expressed in this article are solely those of the authors and do not necessarily represent those of their affiliated organizations, or those of the publisher, the editors and the reviewers. Any product that may be evaluated in this article, or claim that may be made by its manufacturer, is not guaranteed or endorsed by the publisher.

References

1. Mindermann T, Wilson CB. Thyrotropin-producing pituitary adenomas. *J Neurosurg* (1993) 79(4):521–7. doi: 10.3171/jns.1993.79.4.0521

2. Sylvester PT, Evans JA, Zipfel GJ, Chole RA, Uppaluri R, Haughey BH, et al. Combined high-field intraoperative magnetic resonance imaging and endoscopy increase extent of resection and progression-free survival for pituitary adenomas. *Pituitary* (2014) 18(1):72–85.

3. Torres A, Sanmillan JL, Lau R, Gabarros A. Final outcome in growth hormone–secreting adenomas after combination of maximal tumor resection and medical treatment. *World Neurosurg* (2021) 154:e292–301. doi: 10.1016/j.wneu.2021.07.018

4. Watson JC, Shawker TH, Nieman LK, DeVroom HL, Doppman JL, Oldfield EH. Localization of pituitary adenomas by using intraoperative ultrasoound pituitary in patients with cushing's disease and no demonstrable tumor on magnetic resonance imaging. *J Neurosurg* (1998) 89(6):927–32. doi: 10.3171/jns.1998.89.6.0927

5. Buchfelder M, Schlaffer SM, Zhao Y. The optimal surgical techniques for pituitary tumors. *Best Pract Res Clin Endocrinol Metab* (2019) 33(2):101299. doi: 10.1016/j.beem.2019.101299

6. Marcus HJ, Vercauteren T, Ourselin S, Dorward NL. Intraoperative ultrasound in patients undergoing transsphenoidal surgery for pituitary adenoma: Systematic review. *World Neurosurg* (2017) 106:680–5. doi: 10.1016/j.wneu.2017.07.054

7. Mortini P, Albano L, Barzaghi LR, Losa M. Pituitary surgery. *La Presse Médicale* (2021) 50(4):104079. doi: 10.1016/j.lpm.2021.104079

8. Alshareef M, Lowe S, Park Y, Frankel B. Utility of intraoperative ultrasonography for resection of pituitary adenomas: a comparative retrospective study. *Acta Neurochirurgica* (2021) 163(6):1725–34. doi: 10.1007/s00701-020-04674-2

9. Domino JS, Gattozzi DA, Jack M, Carroll M, Harn N, Beahm DD, et al. Outcomes of intraoperative ultrasound for endoscopic endonasal transsphenoidal pituitary surgery in adenomas with parasellar extension. *Interdiscip Neurosurg* (2021) 25:101225. doi: 10.1016/j.inat.2021.101225

10. Alomari A, Jaspers C, Reinbold W-D, Feldkamp J, Knappe UJ. Use of intraoperative intracavitary (direct-contact) ultrasound for resection control in transsphenoidal surgery for pituitary tumors: Evaluation of a microsurgical series. *Acta Neurochirurgica* (2018) 161(1):109–17.

11. Ram Z, Shawker TH, Bradford MH, Doppman JL, Oldfield EH. Intraoperative ultrasound-directed resection of pituitary tumors. *J Neurosurg* (1995) 83(2):225–30. doi: 10.3171/jns.1995.83.2.0225

12. Zachariah MA, Robbins A, Geisler R, Martinez-Perez R, Prevedello DM. Endoscopic endonasal resection of clival chordoma assisted by a novel minimally invasive ultrasound technology: 2-dimensional operative video. *Oper Neurosurg* (2022) 23(3). doi: 10.1227/ons.0000000000000279

13. Robbins AC, Winter KA, Smalley ZP, Godil S, Luzardo G, Washington C, et al. *Side-firing intraoperative ultrasound for resection of Large and giant pituitary adenomas*. Jackson, MS (2022).

14. Itayem DA, Anzalone CL, White JR, Pallanch JF, O'Brien EK. Increased accuracy, confidence, and efficiency in anterior ethmoidal artery identification with segmented image guidance. *Otolaryngol–Head Neck Surg* (2019) 160(5):818–21. doi: 10.1177/0194599818825454

15. Hyde ER, Berger LU, Ramachandran N, Hughes-Hallett A, Pavithran NP, Tran MGB, et al. Interactive virtual 3D models of renal cancer patient anatomies alter partial nephrectomy surgical planning decisions and increase surgeon confidence compared to volume-rendered images. *Int J Comput Assist Radiol Surg* (2019) 14(4):723–32. doi: 10.1007/s11548-019-01913-5

16. Walker TLJ, Bamford R, Finch-Jones M. Intraoperative ultrasound for the colorectal surgeon: Current trends and barriers. *ANZ J Surg* (2017) 87(9):671–6. doi: 10.1111/ans.14124

17. Bhakhri K, Hyde ER, Mak SM, Berger LU, Ourselin S, Routledge T, et al. Surgeon knowledge of the pulmonary arterial system and surgical plan confidence is improved by interactive virtual 3D-CT models of lung cancer patient anatomies. *Front Surg* (2021) 8.

18. Goren O, Monteith SJ, Hadani M, Bakon M, Harnof S. Modern intraoperative imaging modalities for the vascular neurosurgeon treating intracerebral hemorrhage. *Neurosurg Focus* (2013) 34(5):E2.

19. Chang SW, Donoho DA, Zada G. Use of optical fluorescence agents during surgery for pituitary adenomas: Current state of the field. *J Neuro-Oncol* (2018) 141(3):585–93.

20. Pushparajah K, Chu KYK, Deng S, Wheeler G, Gomez A, Kabir S, et al. Virtual reality three-dimensional echocardiographic imaging for planning surgical atrioventricular valve repair. *JTCVS Tech* (2021) 7:269–77.

21. Buchfelder M, Schlaffer S-M. Intraoperative magnetic resonance imaging for pituitary adenomas. *Imaging Endocr Disord* (2016) 45:121–32. doi: 10.1159/000442328

22. Knosp E, Steiner E, Kitz K, Matula C. Pituitary adenomas with invasion of the cavernous sinus space. *Neurosurgery* (1993) 33(4):610–8. doi: 10.1227/00006123-199310000-00008

23. Bernatowicz R, Peereboom D. Lessons learned: Clinical trials and other interventions for glioblastoma. *Glioblastoma* (2016), 279–90. doi: 10.1016/B978-0-323-47660-7.00024-0

24. Archer DP, Cowan RAM, Falkenstein RJ, Sutherland GR. Intraoperative mobile magnetic resonance imaging for craniotomy lengthens the procedure but does not increase morbidity. *Can J Anesth* (2002) 49(4):420–6. doi: 10.1007/BF03017334

25. Ginat DT, Swearingen B, Curry W, Cahill D, Madsen J, Schaefer PW. 3 Tesla intraoperative MRI for brain tumor surgery. *J Magnet Reson Imaging* (2013) 39(6):1357–65. doi: 10.1002/jmri.24380

26. Noh T, Mustroph M, Golby AJ. Intraoperative imaging for high-grade glioma surgery. *Neurosurg Clin North Am* (2021) 32(1):47–54. doi: 10.1016/j.nec.2020.09.003

27. Klingler J-H, Naseri Y, Reinacher PC, Hoedlmoser H, Urbach H, Hohenhaus M. Patient radiation exposure from intraoperative computed tomography in spinal surgery. *Spine J* (2022) 22(9):1576–8. doi: 10.1016/j.spinee.2022.03.008

28. Jenkins NW, Parrish JM, Sheha ED, Singh K. Intraoperative risks of radiation exposure for the surgeon and patient. *Ann Trans Med* (2021) 9(1):84–4. doi: 10.21037/atm-20-1052

29. Vergeer RA, Theunissen REP, van Elk T, Schmidt I, Postma MR, Tamasi K, et al. Fluorescence-guided detection of pituitary neuroendocrine tumor (PitNET) tissue during endoscopic transsphenoidal surgery available agents, their potential, and technical aspects. *Rev Endocr Metab Disord* (2022) 23(3):647–57. doi: 10.1007/s11154-022-09718-9

30. Cho SS, Jeon J, Buch L, Nag S, Nasrallah M, Low PS, et al. Intraoperative near-infrared imaging with receptor-specific versus passive delivery of fluorescent agents in pituitary adenomas. *J Neurosurg* (2019) 131(6):1974–84. doi: 10.3171/2018.7.JNS181642

31. Knappe UJ, Engelbach M, Konz K, Lakomek HJ, Saeger W, Schönmayr R, et al. Ultrasound-assisted microsurgery for cushing's disease. *Exp Clin Endocrinol Diabetes*. (2011) 119(4):191–200. doi: 10.1055/s-0029-1241207

frontiers | Frontiers in Oncology

TYPE Original Research
PUBLISHED 02 December 2022
DOI 10.3389/fonc.2022.1080685

OPEN ACCESS

EDITED BY
Sergio García,
Hospital Universitario Río Hortega, Spain

REVIEWED BY
David Aebisher,
University of Rzeszow, Poland
Nathan Simmons,
Dartmouth Hitchcock Medical Center, United States

*CORRESPONDENCE
Abel Ferrés
abferres@clinic.cat

SPECIALTY SECTION
This article was submitted to Neuro-Oncology and Neurosurgical Oncology, a section of the journal Frontiers in Oncology

RECEIVED 26 October 2022
ACCEPTED 18 November 2022
PUBLISHED 02 December 2022

CITATION
Ferrés A, Di Somma A, Mosteiro A, Topczewski TE, Roldán P, Pedrosa L, Diao D, Pineda E, Sierra A, Enseñat J and González-Sánchez JJ (2022) Photodynamic therapy in glioblastoma: Detection of intraoperative inadvertent 5-ALA mediated photodynamic therapeutical effect after gross total resection. *Front. Oncol.* 12:1080685. doi: 10.3389/fonc.2022.1080685

Photodynamic therapy in glioblastoma: Detection of intraoperative inadvertent 5-ALA mediated photodynamic therapeutical effect after gross total resection

Abel Ferrés[1]*, Alberto Di Somma[1,2], Alejandra Mosteiro[1], Thomaz Eduardo Topczewski[1], Pedro Roldán[1,2], Leire Pedrosa[3], Diouldé Diao[3], Estela Pineda[2,4], Àngels Sierra[5], Joaquim Enseñat[1,2] and José Juan González-Sánchez[1,2]

[1]Department of Neurosurgery, Clínic Institute of Neurosciences, Hospital Clínic of Barcelona, Barcelona, Spain, [2]Faculty of Medicine and Health Sciences, University of Barcelona, Barcelona, Spain, [3]Department of Biomedicine, Faculty of Medicine, August Pi i Sunyer Biomedical Research Institute (IDIBAPS), Barcelona, Spain, [4]Servicio de Oncología Médica, Clinical Institute of Hematological and Oncological Diseases, Hospital Clinic of Barcelona, Barcelona, Spain, [5]Department of Medicine and Life Sciences, Facultad de Ciencias de la Salud y de la Vida, Universidad Pompeu Fabra, Barcelona, Spain

Introduction: Glioblastoma (GBM) remains the most frequent and lethal primary brain tumor in adults, despite advancements in surgical resection techniques and adjuvant chemo- and radiotherapy. The most frequent recurrence pattern (75-90%) occurs in the form of continuous growth from the border of the surgical cavity, thus emphasizing the need for locoregional tumor control. Fluorescence-guided surgical resection using 5-ALA has been widely implemented in surgical protocols for such tumors. Recent literature also highlights the applicability of 5-ALA-mediated photodynamic therapy to obtain locoregional tumor control further. This study aims to identify if 5-ALA mediated photodynamic therapeutic effect after gross total glioblastoma resection has inadvertently occurred due to the exposition of protoporphyrin IX charged peripheral tumoral cells to operative room light sources.

Methods: Of 146 patients who were intervened from glioblastoma between 2015 and 2020, 33 were included in the present study. Strict gross total resection (without supralocal resection) had been accomplished, and adjuvant chemoradiotherapy protocol was administered. Two comparison groups were created regarding the location of the recurrence (group A: up to 1 centimeter from the surgical cavity, and group B: beyond 1 centimeter from the surgical cavity). The cutoff point was determined to be 1 centimeter because of the visible light penetrance to the normal brain tissue.

Results: In univariate analysis, both groups only differed regarding 5-ALA administration, which was significantly related to a minor relative risk of presenting the recurrence within the first centimeter from the surgical cavity **(Relative Risk = 0,655 (95% CI 0,442-0,970), p-value=0,046)**. Results obtained in univariate analysis were corroborated posteriorly in multivariate analysis **(RR=0,730 (95% CI 0,340-0,980), p=0,017)**.

Discussion: In the present study, a probable inadvertent 5-ALA photodynamic therapeutical effect has been detected in vivo. This finding widely opens the door for further research on this promising theragnostic tool.

KEYWORDS

photodynamic therapy, 5-aminolevulinic acid, glioblastoma, neurosurgical oncology, locorregional adjuvant therapy

Introduction

Glioblastoma (GBM) (1) remains the most frequent (incidence of about 4-5 cases per 100000 inhabitants per year) and lethal (median overall survival time of 15 months) primary brain tumor in adults (2), despite the best surgical resection techniques and adjuvant chemo-radiotherapy (3, 4). Its highly infiltrating nature and tendency to recurrence primarily limits locoregional disease control and impedes cure, thus resulting in low survival rates (5, 6). Therefore, there is a need to identify and develop new treatments to increase locoregional disease control following surgical resection.

In this direction, locoregional photodynamic therapy has been progressively studied, especially *in vitro*. It has shown promising results in selective tumoral cell death, thus sparing normal brain parenchyma (7–14). Photodynamic therapy (PhT) is a two-step treatment that involves the administration of a photosensitizer agent (5-aminolevulinic acid; 5-ALA), which produces intracellular Protoporphyrin IX (PPIX) accumulation. PPIX is a fluorophore metabolite whose activation at a specific light wavelength (600-800 nm) generates oxidative stress and consequent cell death (10, 15–17).

It is well known that GBM cells can be found up to 4 centimeters beyond the border of radiologically or histologically identifiable tumor (18), and the most frequent recurrence pattern (75-90%) occurs in the form of continuous growth from the border of the surgical cavity (19–23). In association, visible white light (380-700 nm) penetrance in cerebral tissue may reach 1-centimeter depth (especially at 600 nm and favored in cases of low residual cell density in the surgical field (24)), and part of its spectrum is superposed for PPIX activation (25–28) resulting in its therapeutic effect.

Based on the previous statements, a minor recurrence rate within the first centimeter from the surgical cavity border may be hypothesized in patients affected by GBM after gross total resection (100% of the contrast-enhancing lesion) when 5-ALA has been administrated in conjunction with visible light exposure to the surgical field during the surgery.

The present study aims to determine if locoregional photodynamic therapy has been inadvertently produced *in vivo*, thus encouraging further investigation in humans.

Materials and methods

Study population

The central nervous system (CNS) tumor database of the Hospital Clínic de Barcelona, Spain, was queried to identify all patients treated for glioblastoma between 2015 and 2020. A total of 146 patients were initially identified. Patients finally included in the present study were those whose gross total resection of the contrast-enhancing lesion was achieved, resulting in 33 individuals. Supratotal resection (contrast-enhancing lesion plus 100% of hyperintense area in T2-weighted FLAIR) was not obtained. Variables included in the study were demographic characteristics, initial symptoms, initial functional status, tumor location, preoperative tumor volumetry, tumor superficiality classification (29), leptomeningeal dissemination, ependymal disease, 5-aminolevulinic acid administration (5-ALA), intraoperative adjuvants (neurophysiologic monitoring and intraoperative magnetic resonance imaging (MRI), surgical time, light exposure time, supratotal resection, adjuvant treatment (chemotherapy and radiotherapy protocols), location of the recurrence with respective to the surgical field (up to 1 cm vs. beyond 1 cm), and complications. Two comparison groups were created according to the location of the recurrence (Group A: up

to 1 cm from the surgical field, and Group B: beyond 1 cm from the surgical field). Differences between groups have been initially evaluated through univariate analysis, focusing on differences regarding 5-ALA administration. After that, the differences encountered were corroborated using multivariate analysis. This study involving human participants was reviewed and approved by Barcelona's Clínic hospital ethical board. According to legislation, participant informed consent was not necessary to be obtained because of the study's retrospective nature, anonymized recorded clinical data, and the impossibility of identifying participants directly or through identifiers in study results.

Location of the recurrence

The study's principal objective was to evaluate if there are differences regarding the location of the recurrence concerning the surgical field in patients whose 5-ALA was administrated versus patients whose 5-ALA was not administrated and if an unnoticed photodynamic therapeutical effect could explain these differences after controlling for possible confounding variables.

The initial and residual tumors were measured onto volumetric MRI acquired through a 1,5 T scanner (Siemens) within the first 48 hours from the surgery, through a semiautomatic region of interest (ROI) analysis with Iplan cranial v.3.0 software (Brainlab®, Feldkirchen, Germany). T1-weighted gadolinium-enhanced and T2-weighted FLAIR sequences were used to define preoperative enhancing tumor volume and infiltrative volume outside the enhanced areas, respectively. Residual tumor volume was measured in postoperative MRI performed up to 48 hours from the surgery and co-registered with the preoperative dataset. Only patients presenting gross total resection of the contrast-enhancing lesion were included. A variable amount of infiltrating non-contrast enhancing tumor (hyperintense in T2-weighted FLAIR sequence) may have been resected. Still, in any of the included participants, FLAIR area resection reached 100%, thus not considered supratotal resection. For these patients, the follow-up MRI when recurrence after first-line treatment was detected was posteriorly evaluated. Radiologic tumor recurrence was defined according to the response assessment in neuro-oncology (RANO-HGG) 2010 criteria (30). The location of the recurrence from the surgical field was calculated using the nearest distance between the previous surgical field to the recurrent lesion (if solitaire) or the nearer recurrent lesion (if multiple) using the ruler tool of the radiological imaging software RAIM server DICOM viewer® (UDIAT S.A., Sabadell, Barcelona). Patients were then categorized into the two groups previously described in the study population. An example is provided in Figure 1.

Light exposure time

The retrospective nature of this study focused on evaluating a possible inadvertent 5-ALA photodynamic therapeutic effect in patients affected by GBM impeded a protocolized light delivery to the surgical field in terms of homogenous distribution, intensity, and time duration. Thus, the light was progressively delivered to the surgical cavity during tumor resection and

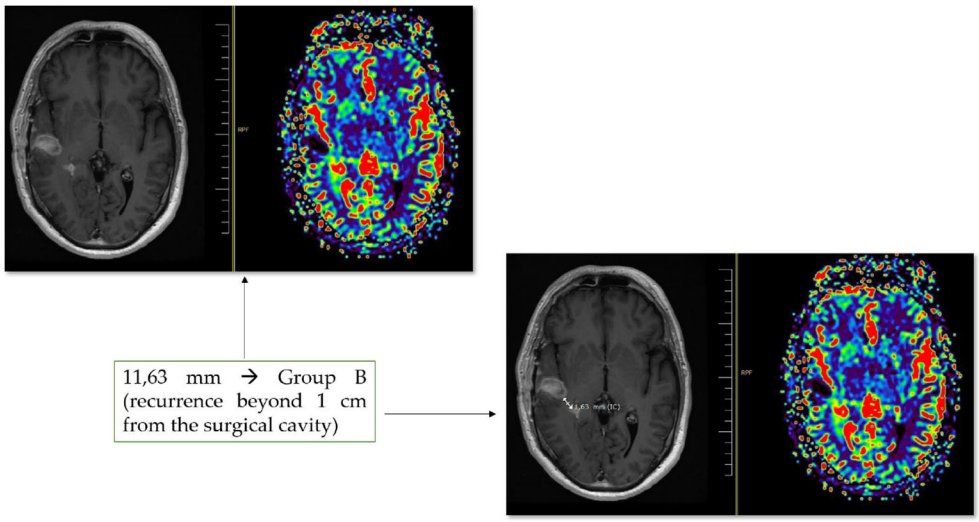

FIGURE 1
An example of the location of recurrence evaluation is provided. In this figure, a unique recurrence is detected at 11,63 mm from the surgical cavity. It allows us to classify the patient in group B MRI perfusion sequences may help both detect the recurrence and discard pathological gadolinium uptake at the margins of the surgical cavity.

hemostasis. In our study and being aware of this previously mentioned heterogenicity in light delivery, we considered light exposure time as the result of the duration between corticotomy and dural closure. This information was retrospectively obtained from surgical and anesthesia reports.

Statistical analysis

Descriptive analysis was realized for both comparison groups. Continuous variables were described using median and range, and categoric variables were defined using absolute and relative frequencies. Comparative analysis was realized after that. For univariate analysis, differences between groups for continuous variables were evaluated using the Mann-Whitney U test and presented with the p-value. Differences between groups for categoric variables were assessed using the Chi-square test and given *via* relative risk (RR) and p-value. Multivariate analysis was calculated using logistic regression, and differences were presented with the p-value and RR.

Results

Thirty-three patients from 146 initially identified to be treated for glioblastoma were finally included in the statistical analysis. Gross total resection (without supratotal resection) was achieved, and complete adjuvant therapy (chemo- and radiotherapy) was administered, thus homogenizing the sample.

The median age was 63,5 and 63 years for groups A and B, respectively, with male predominance in group A (11; 61,1%) and slight female predominance in group B (8; 53,3%). Initial symptoms were more frequent behavioral changes in group A and seizures in group B, without significant differences in initial functional status (median Karnofsky Performance Scale (KPS) of 95 and 90 for each group, respectively). Tumors were more frequently located in the temporal lobe (9; 50%) in group A and frontal (5; 33,3%) and parietal (4; 26,3%) lobes in group B, principally cortical positioned in both groups, without significant differences. Median preoperative volumetry was slightly different between groups: 25,43cc for group A and 30,64cc for group B, without reaching statistical significance. In most cases, neither leptomeningeal dissemination nor ependymal disease was detected. For group B, intraoperative MRI and neuromonitoring were more frequently needed as intraoperative adjuvants without reaching statistical significance. No significant differences were related to the tumor's molecular characteristics (MGMT, IDH, ATRX, EGFR, TP53, and Ki67). All patients received adjuvant chemo- and radiotherapy without significant differences in the treatment protocol. Regarding chemotherapy, temozolomide was the first choice in both groups (94,4% and 100% for groups A and B, respectively). Regarding radiotherapy, hyperfractioned protocol was also the first option in both groups (90,4% and 86,7% for groups A and B, respectively). After treatment of the tumor, no significant differences were found between groups regarding hospital length of stay, complications, and functional status. Group's characteristics are summarized in Table 1.

TABLE 1 Basal characteristics.

Variable		Group A (n=18)	Group B (n=15)	p-value
Age		63,5 (41-87)	63 (49-88)	0,2
Sex	Male	11 (61,1%)	7 (46,7%)	0,494
	Female	7 (38,9%)	8 (53,3%)	
Initial symptoms	Headache	1 (5,6%)	3 (20%)	0,153
	Seizure	2 (11,1%)	4 (26,7%)	
	Hemiparesis/hemiplegia	2 (11,1%)	3 (20%)	
	Behavioral changes	9 (50%)	3 (20%)	
	Hemihypoesthesia/anesthesia	2 (11,1%)	0	
	Aphasia	0	1 (6,7%)	
	Facial paralysis	0	1 (6,7%)	
	Mutism	2 (11,1%)	0	
Initial KPS		95 (80-100)	90 (70-100)	0,539
Tumor location	Frontal	2 (11,1%)	5 (33,3%)	0,223
	Temporal	9 (50%)	2 (13,3%)	
	Parietal	5 (27,8%)	4 (26,3%)	
	Occipital	1 (5,6%)	2 (13,3%)	
	Frontoparietal	0	1 (6,7%)	
	Parietooccipital	1 (5,6%)	1 (6,7%)	

(Continued)

10.3389/fonc.2022.1080685

TABLE 1 Continued

Variable			Group A (n=18)	Group B (n=15)	p-value
Superficiality	Subventricular zone		0	0	0,641
	Cortex		14 (77,8%)	12 (80%)	
	Subventricular zone and cortex		3 (16,7%)	3 (30%)	
	None (white substance)		1 (5,6%)	0	
Preoperative tumor volumetry			25,43cc (15,65-45,86)	30,64 (20,79-47,76)	0,776
Leptomeningeal dissemination	Yes		2 (11,1%)	2 (13,3%)	0,622
	No		15 (83,3%)	12 (80%)	
Ependymal disease	Yes		0	1 (6,7%)	0,437
	No		18 (100%)	13 (86,7%)	
5-ALA (5-aminolevulinic acid)	Yes		11 (61,1%)	14 (93,3%)	**0,046**
	No		7 (38,9%)	1 (6,7%)	
Light exposure time (min)			135 (15-207)	84 (27-252)	0,166
Intraoperative adjuvants	iMRI		3 (16,7%)	8 (53,3%)	0,223
	Neuromonitoring		0	4 (26,7%)	
	Awake		2 (11,1%)	0	
MGMT	Methylated		10 (55,6%)	11 (73,3%)	0,704
	No methylated		6 (33,3%)	4 (26,7%)	
IDH	Mutated		0	0	0,255
	Wild type		18 (100%)	15 (100%)	
ATRX	ATRX +		0	1 (6,7%)	1
	ATRX -		4 (22,2%)	8 (53,3%)	
TP53	Mutated		5 (27,8%)	8 (53,3%)	0,238
	No mutated		9 (50%)	4 (26,7%)	
EGFR	Mutated		5 (27,8%)	10 (66,7%)	0,262
	Wild type		3 (16,7%)	1 (6,7%)	
Ki67			30% (20-70%)	25% (5-40%)	0,112
Chemotherapy	Temozolomide		17 (94,4%)	15 (100%)	0,232
	Bevacizumab		1 (5,6%)	0	
Radiotherapy	Hyperfractioned		17 (90,4%)	13 (86,7%)	0,193
	WBRT		1 (5,6%)	0	
	Hypofractionated		0	2 (13,3%)	
Postoperative complications	Immediate (first 24 hours)	Hematoma	1 (5,6%)	0	0,209
	Early (from first 24h up to 6th month)	Subacute hydrocephalus	0	1 (6,7%)	0,1
		Surgical wound infection	0	1 (6,7%)	
		Hematoma	1 (5,6%)	0	
	Late (beyond 6th month)	Hydrocephalus	1 (5,6%)	1 (6,7%)	0,282
Hospital length of stay			6 (4-21)	6,5 (3-25)	0,543
Early KPS (up to 6th month)			90 (50-100)	90 (70-100)	0,654
Late KPS (after 6th month)			80 (50-100)	70 (40-90)	0,235

Statistically significative values in bold.

When evaluating the relation between 5-ALA administration and the location of the recurrence, significant differences were found in the univariate analysis. 5-ALA administration was significantly related to a minor relative risk of presenting the recurrence within the first centimeter from the surgical cavity (0,655 95% CI 0,442-0,970; p=0,046) (Table 2). Afterward, the authors analyzed if light exposure time may be related to the location of the recurrence for the 5-ALA subgroup, and no significant differences were found (p=0,166) (Table 3).

The relation initially found between 5-ALA administration and minor relative risk to present the recurrence within the first centimeter from the surgical field was posteriorly evaluated in conjunction with other possible confounding variables in the multivariate analysis. Items included in the statistical analysis, different from 5-ALA administration, were superficiality

TABLE 2 Univariate analysis.

Variable		5-ALA		RELATIVE RISK	p-Value
		Yes	No		
Recurrence location	Recurrence up to 1 cm from the surgical cavity	11 (61,1%)	7 (38,9%)	**0,655 (0,442-0,970)**	**0,046**
	Recurrence beyond 1 cm from surgical cavity	14 (93,3%)	1 (6,7%)	5,833 (0,805-42,253)	

Evaluation of the relationship between 5-ALA exposure and recurrence location.
Statistically significative values in bold.

classification, radiotherapy protocol administered, chemotherapy protocol administered, ependymal disease, leptomeningeal dissemination, and light exposure time. Again, only the relation between 5-ALA administration and negligible risk for the location of the recurrence up to the first centimeter from the surgical cavity reached statistical significance (0,730 95% CI 0,340-0,980); p=0,017) (Table 4).

Discussion

Because the most frequent recurrence pattern in patients affected by HGG occurs in the form of continuous growth from the border of the surgical cavity, 5-ALA metabolites (protoporphyrin IX) can be activated at the visible light wavelength (380-700 nm), and its penetrance in cerebral tissue may reach up to 1 cm depth, the apparent 5-ALA photodynamic therapeutical effect may have been inadvertently produced on operated patients affected from glioblastoma when 5-ALA has been administered preoperatively, and tumoral intracellular protoporphyrin IX intraoperatively activated through operative room light sources. The present study aimed to analyze if this hypothesized 5-ALA photodynamic effect has been inadvertently produced in a cohort of patients affected by glioblastoma.

Considering the previously exposed statements, the authors hypothesized that the recurrence of patients with 5-ALA that was administrated preoperatively would be less probable located within the first centimeter from the surgical cavity. To accurately evaluate this hypothesis, confusion control is of utmost importance. Restrictive inclusion criteria, group comparativeness evaluation, and multivariate analysis were used. Our results have shown that recurrences were significantly less frequent within the first centimeter from the surgical cavity in the 5-ALA group, thus increasing the possibility of having detected an inadvertent *in vivo* 5-ALA photodynamic therapeutical effect in patients affected by GBM IDH wild-type. The presented results may have been facilitated, at least partially, due to the superficial location (cortical) of the tumors in most of the individuals included in the study. This location eases light exposure in the hole surgical cavity and promotes photodynamic reactions in patients in the 5-ALA group.

In addition to the principal analysis, differences regarding the location of the recurrence were evaluated concerning light exposure times only for the subgroup of patients whose 5-ALA was administered preoperatively. Paradoxically to what we would expect, the median light exposure time was minor in patients whose 5-ALA was administered and recurrence located beyond 1 cm from the surgical field, without reaching statistical significance. It is described in the literature that the dose of light delivered is essential to obtain maximum photobleaching of photosensitizer, thus resulting in optimal effectivity of the therapy. Advanced photobleaching is the fluence rate that causes more than 95% photobleaching of photosensitizer and is related to better results. For 5-ALA photodynamic therapy, advanced photobleaching is achieved at 4 mm from the surface of a light diffuser emitting power of 200 mW/cm for 1 hour (31–34). In the present study, median light exposure time surpasses 60 minutes in both groups; nevertheless, the power of the light

TABLE 3 Univariate analysis.

Variable		Light exposure time (median)	p-Value
Recurrence location	Up to 1 cm from the surgical cavity	136	0,166
	Beyond 1 cm from the surgical cavity	81	

Evaluation of the relationship between light exposure time and recurrence location in the 5-ALA group.

TABLE 4 Multivariate analysis.

Variable	Recurrence location (up to 1 cm from surgical cavity vs. Beyond 1 cm)
5-ALA	**0,017 (RR=0,540; 95% CI 0,453-0,872) (a)**
Superficiality classification	0,299
Radiotherapy protocol	0,107
Chemotherapy protocol	0,283
Ependymal disease	0,169
Leptomeningeal dissemination	0,332

(a) relation between recurrence location beyond 1 cm from the surgical cavity and 5-ALA administration.
Statistically significative values in bold.

source and surgical field exposure may not be constant and/or homogeneous between groups or individuals in the same group. Uncontrolled differences in reaching advanced photobleaching of the photosensitizer between groups may explain, at least partially, the paradoxical trend in results obtained.

In the literature, few studies have reported their preliminary experience with 5-ALA photodynamic therapy in patients affected by high-grade gliomas. Regarding its efficacy as a surgical adjuvant, one group combined fluorescence-guided surgery (FGS) and postoperative photodynamic therapy; 5-ALA photodynamic therapy was performed with an implanted catheter in patients with primary GBM on the day of FGS. Photodynamic therapy was then realized at 24-hour intervals for five sessions, and the results were compared with the control group (conventional surgical resection). Delayed mean tumor progression (8.6 vs. 4.8 months) and increased mean survival (52.8 vs. 24.6 weeks) were observed in the group that received both FGS and photodynamic therapy when compared with the control group (35). Another group combined 5-ALA FGS in patients affected by recurrent GBM and intracavitary 5-ALA photodynamic therapy through lase diffusers strategically positioned inside the resection cavity. They reported median progression-free survival of 6 months without an increase in surgical morbidity and postoperative complications (36). Regarding its efficacy as a sole rescue treatment for GBM recurrences, two groups report their experience. One of them evaluated the efficacy of this therapy in 10 patients affected by small (maximum diameter < 3 cm) circumscribed recurrent malignant gliomas. The 1-year survival rate was 60%, with a median survival of 15 months. The other group also evaluated the efficacy of this therapy in 15 patients affected by small newly diagnosed (maximum diameter < 4 cm). It was compared to GBM patients who underwent tumor resection alone. The interstitial photodynamic therapy group demonstrated a significantly longer median progression-free survival of 16 vs. 10.2 months and a 3-years survival of 56 vs. 21% (33, 37).

The two most extensive clinical studies have been recently published: On the one hand, Leroy et al., in 2021, described a series of 251 patients who underwent interstitial 5-ALA photodynamic therapy. Overall mortality was 1%, and transient and persistent morbidity was 5%. Tumor response after photodynamic therapy was 92%, progression-free survival was 14,5 months for *de novo* lesions and 14 months for recurrent ones, respectively, and overall survival was 19 months and eight months for the same groups, respectively (38). On the other hand, Lietke et al., in 2021, described 44 retrospectively evaluated patients after being also treated with interstitial photodynamic therapy. The median time to failure was 7.1 months, and the median progression-free survival was 13 months (39).

Although the publications are increasing on such attractive novel therapy, more studies are needed to further evaluate the efficacy, effectiveness, and safety of the 5-ALA photodynamic therapy for treating patients affected by GBM. The authors consider that the previously presented literature, in conjunction with the results mentioned in the present study, may justify efforts to investigate such a promising adjuvant and/or rescue therapy for the treatment of GBM. Our efforts have been primarily oriented toward evaluating its intraoperative efficacy because a lack of publications is evident in this specific treatment modality. In this direction, recently published preliminary results of the INDYGO trial postulated that 5-ALA photodynamic therapy delivered immediately after resection as adjuvant therapy for GBM is safe and may help to decrease the recurrence risk by targeting residual tumor cells in the resection cavity (40).

Study limitations

Although necessary to provide the most reliable results, restrictive inclusion criteria limit its generalization. In addition, the study's retrospective nature carries inherent bias despite efforts to control it as much as possible. Also, as mentioned previously in the methodology section, heterogenicity regarding light exposure time must be considered when analyzing related results. Nevertheless, despite this heterogenic light exposure, recurrence was less frequent within the first centimeter from the surgical cavity when 5-ALA was administered, and gross total resection was accomplished. Finally, although supramarginal resections have been excluded, smaller tumors located in non-eloquent areas may allow for a more aggressive resection, thus resulting in partial excision of the surrounding tissue. In the present study, achieving more significant resection of the peritumoral brain parenchyma may overestimate the photodynamic therapy's effect due to the smaller amount of pathologic tissue (hyperintense in MRI FLAIR sequence) surrounding the surgical cavity.

Conclusion

A possible inadvertent 5-ALA photodynamic therapeutical effect may have been detected in patients affected by GBM after gross total resection. These results, in conjunction with favorable data published in the literature and previously presented in the present study, encourage further investigation of this promising therapy as a surgical add-on after primary GBM resection or recurrence or as a sole rescue treatment in non-resectable or recurrent cases of this primary brain cancer.

Data availability statement

The raw data supporting the conclusions of this article will be made available by the authors, without undue reservation.

Ethics statement

This study involving human participants was reviewed and Photodynamic therapy in glioblastoma approved by Barcelona's Clínic hospital ethical board. According to legislation, participant informed consent was not necessary to be obtained because of the study's retrospective nature, anonymized recorded clinical data, and the impossibility of identifying participants directly or through identifiers in study results.

Author contributions

AF and JG-S designed and led the present study. AF and AM developed the theory and performed the computations. AF and AM collected the clinical and economic data. AF, AM, AD, TT, PR, LP, DD, AS, and JG-S performed the analytical methods and interpreted them. AF drafted the manuscript. JG-S, AD, PR, AS, and JE critically revised the manuscript. JE gave institutional, material, and logistic support. All authors contributed to the article and approved the submitted version.

Conflict of interest

The authors declare that the research was conducted in the absence of any commercial or financial relationships that could be construed as a potential conflict of interest.

Publisher's note

References

1. Louis DN, Perry A, Wesseling P, Brat DJ, Cree IA, Figarella-Branger D, et al. The 2021 WHO classification of tumors of the central nervous system: a summary. *Neuro Oncol* (2021) 23(8):1231–51. doi: 10.1093/neuonc/noab106

2. Thakkar JP, Dolecek TA, Horbinski C, Ostrom QT, Lightner DD, Barnholtz-Sloan JS, et al. Epidemiologic and molecular prognostic review of glioblastoma. *Cancer Epidemiol Biomarkers Prev* (2014) 23(10):1985–96. doi: 10.1158/1055-9965.EPI-14-0275

3. Stupp R, Hegi ME, Mason WP, van den Bent MJ, Taphoorn MJ, Janzer RC, et al. Effects of radiotherapy with concomitant and adjuvant temozolomide versus radiotherapy alone on survival in glioblastoma in a randomised phase III study: 5-year analysis of the EORTC-NCIC trial. *Lancet Oncol* (2009) 10(5):459–66. doi: 10.1016/S1470-2045(09)70025-7

4. Stupp R, Mason WP, van den Bent MJ, Weller M, Fisher B, Taphoorn MJB, et al. Radiotherapy plus concomitant and adjuvant temozolomide for glioblastoma. *N Engl J Med* (2005) 352(10):987–96. doi: 10.1056/NEJMoa043330

5. Sahm F, Capper D, Jeibmann A, Habel A, Paulus W, Troost D, et al. Addressing diffuse glioma as a systemic brain disease with single-cell analysis. *Arch Neurol* (2012) 69(4):523–6. doi: 10.1001/archneurol.2011.2910

6. Claes A, Idema AJ, Wesseling P. Diffuse glioma growth: a guerilla war. *Acta Neuropathol* (2007) 114(5):443–58. doi: 10.1007/s00401-007-0293-7

7. Tetard MC, Vermandel M, Leroy HA, Leroux B, Maurage CA, Lejeune JP, et al. Interstitial 5-ALA photodynamic therapy and glioblastoma: Preclinical model development and preliminary results. *Photodiagnosis Photodyn Ther* (2016) 13:218–24. doi: 10.1016/j.pdpdt.2015.07.169

8. Hirschberg H, Sørensen DR, Angell-Petersen E, Peng Q, Tromberg B, Sun CH, et al. Repetitive photodynamic therapy of malignant brain tumors. *J Environ Pathol Toxicol Oncol* (2006) 25(1–2):261–79. doi: 10.1615/JEnvironPatholToxicolOncol.v25.i1-2.170

9. Olzowy B, Hundt CS, Stocker S, Bise K, Reulen HJ, Stummer W. Photoirradiation therapy of experimental malignant glioma with 5-aminolevulinic acid. *J Neurosurg* (2002) 97(4):970–6. doi: 10.3171/jns.2002.97.4.0970

10. Hirschberg H, Berg K, Peng Q. Photodynamic therapy mediated immune therapy of brain tumors. *Neuroimmunol Neuroinflamm* (2018) 5(7):27. doi: 10.20517/2347-8659.2018.31

11. Busch TM, Xing X, Yu G, Yodh A, Wileyto EP, Wang HW, et al. Fluence rate-dependent intratumor heterogeneity in physiologic and cytotoxic responses to photofrin photodynamic therapy. *Photochem Photobiol Sci* (2009) 8(12):1683–93. doi: 10.1039/b9pp00004f

12. Madsen SJ, Sun CH, Tromberg BJ, Hirschberg H. Development of a novel indwelling balloon applicator for optimizing light delivery in photodynamic therapy. *Lasers Surg Med* (2001) 29(5):406–12. doi: 10.1002/lsm.10005

13. Tsai J-C, Hsiao Y-Y, Teng L-J, Chen C-T, Kao M-C. Comparative study on the ALA photodynamic effects of human glioma and meningioma cells. *Lasers Surg Med* (1999) 24(4):296–305. doi: 10.1002/(sici)1096-9101(1999)24:4<296::aid-lsm7>3.0.co;2-f

14. Stummer W, Stocker S, Novotny A, Heimann A, Sauer O, Kempski O, et al. *In vitro* and *in vivo* porphyrin accumulation by C6 glioma cells after exposure to 5-aminolevulinic acid. *J Photochem Photobiol B* (1998) 45(2–3):160–9. doi: 10.1016/S1011-1344(98)00176-6

15. Ewelt C, Nemes A, Senner V, Wölfer J, Brokinkel B, Stummer W, et al. Fluorescence in neurosurgery: Its diagnostic and therapeutic use. review of the literature. *J Photochem Photobiol B* (2015) 148:302–9. doi: 10.1016/j.jphotobiol.2015.05.002

16. Mahmoudi K, Garvey KL, Bouras A, Cramer G, Stepp H, Jesu Raj JG, et al. 5-aminolevulinic acid photodynamic therapy for the treatment of high-grade gliomas. *J Neurooncol* (2019) 141(3):595–607. doi: 10.1007/s11060-019-03103-4

17. Kaneko S, Fujimoto S, Yamaguchi H, Yamauchi T, Yoshimoto T, Tokuda K. Photodynamic therapy of malignant gliomas. *Prog Neurol Surg* (2018) 32:1–13. doi: 10.1159/000469675

18. Silbergeld DL, Chicoine MR. Isolation and characterization of human malignant glioma cells from histologically normal brain. *J Neurosurg* (1997) 86(3):525–31. doi: 10.3171/jns.1997.86.3.0525

19. Lee SW, Fraass BA, Marsh LH, Herbort K, Gebarski SS, Martel MK, et al. Patterns of failure following high-dose 3-d conformal radiotherapy for high-grade astrocytomas: a quantitative dosimetric study. *Int J Radiat Oncol Biol Phys* (1999) 43(1):79–88. doi: 10.1016/S0360-3016(98)00266-1

20. Loeffler J, Alexander E, Hochberg FH, Wen PY, Morris JH, Schoene WC, et al. Clinical patterns of failure following stereotactic interstitial irradiation for malignant gliomas. *Int J Radiat Oncol Biol Phys* (1990) 19(6):1455–62. doi: 10.1016/0360-3016(90)90358-Q

21. Halperin EC, Burger PC, Bullard DE. The fallacy of the localized supratentorial malignant glioma. *Int J Radiat Oncol Biol Phys* (1988) 15(2):505–9. doi: 10.1016/S0360-3016(98)90036-0

22. Gaspar LE, Fisher BJ, Macdonald DR, Leber DV, Halperin EC, Schold SC, et al. Supratentorial malignant glioma: patterns of recurrence and implications for external beam local treatment. *Int J Radiat Oncol Biol Phys* (1992) 24(1):55–7. doi: 10.1016/0360-3016(92)91021-E

23. Petrecca K, Guiot MC, Panet-Raymond V, Souhami L. Failure pattern following complete resection plus radiotherapy and temozolomide is at the resection margin in patients with glioblastoma. *J Neurooncol* (2013) 111(1):19–23. doi: 10.1007/s11060-012-0983-4

24. Genina EA, Genina EA, Bashkatov AN, Bashkatov AN, Tuchina DK, Tuchina DK, et al. Optical properties of brain tissues at the different stages of glioma development in rats: pilot study. *BioMed Opt Express* (2019) 10(10):5182–97. doi: 10.1364/BOE.10.005182

25. Quirk BJ, Brandal G, Donlon S, Vera JC, Mang TS, Foy AB, et al. Photodynamic therapy (PDT) for malignant brain tumors–where do we stand? *Photodiagnosis Photodyn Ther* (2015) 12(3):530–44. doi: 10.1016/j.pdpdt.2015.04.009

26. Wang H-W, Zhu TC, Putt ME, Solonenko M, Metz J, Dimofte A, et al. Broadband reflectance measurements of light penetration, blood oxygenation, hemoglobin concentration, and drug concentration in human intraperitoneal tissues before and after photodynamic therapy. *J BioMed Opt* (2005) 10 (1):014004. doi: 10.1117/1.1854679

27. Stables GI, Ash DV. Photodynamic therapy. *Cancer Treat Rev* (1995) 21 (4):311–23. doi: 10.1016/0305-7372(95)90035-7

28. Plaetzer K, Krammer B, Berlanda J, Berr F, Kiesslich T. Photophysics and photochemistry of photodynamic therapy: fundamental aspects. *Lasers Med Sci* (2009) 24(2):259–68. doi: 10.1007/s10103-008-0539-1

29. Lim DA, Cha S, Mayo MC, Chen MH, Keles E, Vandenberg S, et al. Relationship of glioblastoma multiforme to neural stem cell regions predicts invasive and multifocal tumor phenotype. *Neuro Oncol* (2007) 9(4):424–9. doi: 10.1215/15228517-2007-023

30. Wen PY, Macdonald DR, Reardon DA, Cloughesy TF, Sorensen AG, Galanis E, et al. Updated response assessment criteria for high-grade gliomas: response assessment in neuro-oncology working group. *J Clin Oncol* (2010) 28 (11):1963–72. doi: 10.1200/JCO.2009.26.3541

31. Johansson A, Faber F, Kniebühler G, Stepp H, Sroka R, Egensperger R, et al. Protoporphyrin IX fluorescence and photobleaching during interstitial photodynamic therapy of malignant gliomas for early treatment prognosis. *Lasers Surg Med* (2013) 45(4):225–34. doi: 10.1002/lsm.22126

32. Johansson A, Palte G, Schnell O, Tonn JC, Herms J, Stepp H. 5-aminolevulinic acid-induced protoporphyrin IX levels in tissue of human malignant brain tumors. *Photochem Photobiol* (2010) 86(6):1373–8. doi: 10.1111/j.1751-1097.2010.00799.x

33. Beck TJ, Kreth FW, Beyer W, Mehrkens JH, Obermeier A, Stepp H, et al. Interstitial photodynamic therapy of nonresectable malignant glioma recurrences using 5-aminolevulinic acid induced protoporphyrin IX. *Lasers Surg Med* (2007) 39 (5):386–93. doi: 10.1002/lsm.20507

34. Stepp H, Stummer W. 5-ALA in the management of malignant glioma. *Lasers Surg Med* (2018) 50(5):399–419. doi: 10.1002/lsm.22933

35. Eljamel MS, Goodman C, Moseley H. ALA and photofrin fluorescence-guided resection and repetitive PDT in glioblastoma multiforme: a single centre phase III randomised controlled trial. *Lasers Med Sci* (2008) 23(4):361–7. doi: 10.1007/s10103-007-0494-2

36. Schipmann S, Müther M, Stögbauer L, Zimmer S, Brokinkel B, Holling M, et al. Combination of ALA-induced fluorescence-guided resection and intraoperative open photodynamic therapy for recurrent glioblastoma: case series on a promising dual strategy for local tumor control. *J Neurosurg* (2020) 134 (2):426–36. doi: 10.3171/2019.11.JNS192443

37. Schwartz C, Rühm A, Tonn J-C, Kreth S, Kreth F-W. SURG-25INTERSTITIAL PHOTODYNAMIC THERAPY OF *DE-NOVO* GLIOBLASTOMA MULTIFORME WHO IV. *Neuro Oncol* (2015) 17(Suppl 5): v219. doi: 10.1093/neuonc/nov235.25

38. Leroy HA, Guérin L, Lecomte F, Baert G, Vignion AS, Mordon S, et al. Is interstitial photodynamic therapy for brain tumors ready for clinical practice? a systematic review. *Photodiagnosis Photodyn Ther* (2021) 36:102492. doi: 10.1016/j.pdpdt.2021.102492

39. Lietke S, Schmutzer M, Schwartz C, Weller J, Siller S, Aumiller M, et al. Interstitial photodynamic therapy using 5-ALA for malignant glioma recurrences. *Cancers (Basel)* (2021) 13(8):1767. doi: 10.3390/cancers13081767

40. Vermandel M, Dupont C, Lecomte F, Leroy HA, Tuleasca C, Mordon S, et al. Standardized intraoperative 5-ALA photodynamic therapy for newly diagnosed glioblastoma patients: a preliminary analysis of the INDYGO clinical trial. *J Neurooncol* (2021) 152(3):501–14. doi: 10.1007/s11060-021-03718-6

frontiers | Frontiers in Oncology

TYPE Methods
PUBLISHED 04 January 2023
DOI 10.3389/fonc.2022.1021335

OPEN ACCESS

EDITED BY
Sergio García,
Hospital Universitario Río Hortega, Spain

REVIEWED BY
Shivaram Avula,
Alder Hey Children's NHS Foundation Trust, United Kingdom
Francesco Acerbi,
IRCCS Carlo Besta Neurological Institute Foundation, Italy

*CORRESPONDENCE
Victoria Becerra
mariavictoria.becerra@sjd.es

†These authors have contributed equally to this work and share first authorship

This article was submitted to Neuro-Oncology and Neurosurgical Oncology, a section of the journal Frontiers in Oncology

SPECIALTY SECTION
RECEIVED 17 August 2022
ACCEPTED 05 December 2022
PUBLISHED 04 January 2023

CITATION
Becerra V, Hinojosa J, Candela S, Culebras D, Alamar M, Armero G, Echaniz G, Artés D, Munuera J and Muchart J (2023) The impact of 1.5-T intraoperative magnetic resonance imaging in pediatric tumor surgery: Safety, utility, and challenges. *Front. Oncol.* 12:1021335. doi: 10.3389/fonc.2022.1021335

The impact of 1.5-T intraoperative magnetic resonance imaging in pediatric tumor surgery: Safety, utility, and challenges

Victoria Becerra[1*†], José Hinojosa[1†], Santiago Candela[1], Diego Culebras[1], Mariana Alamar[1], Georgina Armero[2], Gastón Echaniz[3], David Artés[3], Josep Munuera[4,5] and Jordi Muchart[4,5]

[1]Department of Neurosurgery, Hospital Sant Joan de Déu, Esplugues de Llobregat (Cataluña), Spain, [2]Department of Pediatrics, Hospital Sant Joan de Déu, Esplugues de Llobregat (Cataluña), Spain, [3]Department of Anesthesiology, Hospital Sant Joan de Déu, Esplugues de Llobregat (Cataluña), Spain, [4]Diagnostic Imaging Department, Hospital Sant Joan de Déu, Esplugues de Llobregat (Cataluña), Spain, [5]Diagnostic and Therapeutic Imaging, Institut de Recerca Sant Joan de Déu, Esplugues de Llobregat (Cataluña), Spain

Objective: In this study, we present our experience with 1.5-T high-field intraoperative magnetic resonance imaging (ioMRI) for different neuro-oncological procedures in a pediatric population, and we discuss the safety, utility, and challenges of this intraoperative imaging technology.

Methods: A pediatric consecutive-case series of neuro-oncological surgeries performed between February 2020 and May 2022 was analyzed from a prospective ioMRI registry. Patients were divided into four groups according to the surgical procedure: intracranial tumors (group 1), intraspinal tumors (group 2), stereotactic biopsy for unresectable tumors (group 3), and catheter placement for cystic tumors (group 4). The goal of surgery, the volume of residual tumor, preoperative and discharge neurological status, and postoperative complications related to ioMRI were evaluated.

Results: A total of 146 procedures with ioMRI were performed during this period. Of these, 62 were oncology surgeries: 45 in group 1, two in group 2, 10 in group 3, and five in group 4. The mean age of our patients was 8.91 years, with the youngest being 12 months. ioMRI identified residual tumors and prompted further resection in 14% of the cases. The mean time for intraoperative image processing was 54 ± 6 min. There were no intra- or postoperative security incidents related to the use of ioMRI. The reoperation rate in the early postoperative period was 0%.

Conclusion: ioMRI in pediatric neuro-oncology surgery is a safe and reliable tool. Its routine use maximized the extent of tumor resection and did not result

in increased neurological deficits or complications in our series. The main limitations included the need for strict safety protocols in a highly complex surgical environment as well as the inherent limitations on certain patient positions with available MR-compatible headrests.

KEYWORDS

intraoperative magnetic resonance imaging, pediatric brain tumors, neurooncological surgery, residual tumor, oncology

Introduction

The use of intraoperative magnetic resonance imaging (ioMRI) has proven to be a relevant technological innovation in the surgical treatment of intracranial tumors. The first publications on intraoperative low-field MRI date back to the mid-1990s (1–3). Since then, with the advent of high-field systems, the development of surgical protocols and MRI has become increasingly recognized as a useful neurosurgical tool in everyday practice (4–6).

Currently, ioMRI is a well-established imaging system that provides maximum safety for tumor resection in adults, since it allows neuronavigational information to be updated with intraoperative images and compensates for changes that occur during surgery in the geometry of the brain relative to neuronavigational instrumentation for the preservation of the neurological functions (3, 7–9).

For malignant intracranial neoplasms in the pediatric population, the extent of surgical tumor removal constitutes the factor most strongly associated with longer life expectancy prior to initiation of radiotherapy or adjuvant chemotherapy/immunotherapy (10–12). Similarly, the complete removal of benign intracranial tumors may be curative (13, 14). So, the identification of an unsuspected residual tumor tissue that is potentially resectable on intraoperative imaging can eliminate the indication of a second-look surgery, achieving the surgical goal with less guesswork.

ioMRI has been shown to be useful in other nonresectable surgical procedures such as biopsies of unresectable intracranial tumors and the placement of a reservoir into a cystic tumor (15).

The purpose of this report was to (1) present our experience with high-field ioMRI for different neuro-oncological surgeries in a pediatric population, (2) discuss the safety, utility, and challenges of this tool during these neurosurgical procedures, and (3) examine our medium/long-term patients' outcomes.

Abbreviations: ioMRI, intraoperative magnetic resonance imaging; GTR, gross total resection; STR, subtotal resection; PR, partial resection; DBS, deep brain stimulation; GPi, globus pallidus internus; SEEG, stereoelectroencephalography; LITT, laser interstitial thermotherapy; NOS, not otherwise specified; EOR, extent of resection.

Methods

Patients

Since the inception of the ioMRI-guided surgery program in February 2020 at our institution, clinical data records have been entered into a prospective database with institutional review board approval. All procedures were performed between February 2020 and May 2022. Data collection for this project continues. All patients under 18 years old were included in the present study.

Data were collected from medical records regarding the patient's history, type of surgical procedure, surgical issues (aim of surgery, approach, degree of extent of tumor resection), preoperative and discharge neurological status, and postoperative complications.

We categorized our pediatric population treated with ioMRI into four groups according to the surgical procedure (Table 1). Group 1 encompassed a series of patients who underwent procedures for the resection of intracranial tumors. Group 2 included patients who underwent operations for resection of spinal disease. Group 3 consisted of patients who underwent a percutaneous procedure for an unresectable tumor biopsy using VarioGuide system (BrainLab, Germany). Group 4 comprised patients for the placement of catheters in cystic tumoral lesions.

Operating theater setup

In 2020, our neurosurgical department acquired a high-field 1.5-Tesla ioMRI suite (Philips Ingenia; Philips Healthcare, Cleveland, Ohio, USA). Our ioMRI setup is based on a two-room concept in which the patient is transported between the operating theater and a static MR scanner, both spaces being separated by sliding double doors.

At the weekly surgical scheduling meeting, each elective neurosurgical procedure that involves the application of ioMRI

TABLE 1 All surgical procedures performed with ioMRI between February 2020 and May 2022.

Pathology Group	No of surgical procedures
Oncology	**62**
Supratentorial tumors	24
Infratentorial tumors	21
Intraspinal tumors	2
Stereotactic biopsy for unresectable tumors	10
Ommaya catheter placement for cystic tumors	5
Epilepsy surgery	**28**
Depth electrode placement	**22**
Dystonia-Deep brain stimulation (DBS) in bilateral globus pallidus internus (GPi)	9
Stereoelectroencephalography (SEEG)	11
Others	2
Laser interstitial thermotherapy (LITT)	**24**
Hypothalamic hamartoma	10
Disconnective surgery completion	10
Brain tumors or dysplasias	4
Vascular pathology	**2**
Cavernous malformations	2
Hydrocepahlus	**5**
Preoperative marking of the lesion	**2**
Diastematomyelia	1
Dorsal arachnoid cyst	1
Investigation	**2**
Total	**147**

is pointed out; the date of surgery is reserved; and the estimated time slot required for the ioMRI is simultaneously booked for the same day. Likewise, the neuroanesthesia, neuroradiology, and neurophysiology teams are informed that the surgery is planned with ioRMI. From an anesthesia point of view, it is important to have prepared MRI-compatible monitoring devices for ioMRI. When ioMRI is not scheduled, the MRI scanner is available for in-patients.

A safety protocol is performed at specific time points throughout the surgical procedure. There are three time points for the ioMRI security checklist to ensure an out-of-danger workflow: the first one is in-patient positioning, that is, prior to sterile drape placement and antisepsis; the second one takes place before transferring the patient to the ioMRI room; and the last check is on the return to the operating theater after the acquisition of intraoperative images. Our safety checklist is based on the experience of other groups (4–6), and we include specific surgical and anesthetic checks that should be considered in pediatric patients. This protocol has been agreed upon by different specialists involved in neurosurgical procedures: neurosurgeons, anesthetists, nurses, radiologists, imaging technicians, and neurophysiologists. Prior to its implementation, a simulation session was carried out, making it possible to optimize and validate this security checklist (Figure 1) (16).

Cranial immobilization was performed with different systems. Two head holders were available for ioRMI enhancement: the NORAS OR Head Holder Flexibility and Head Coil Set 1.5 T Philips Scanner (Noras MRI products GmbH, Hoecherg, Germany) and the DORO LUCENT® ioMRI cranial stabilization system TRUMPF (Black Forest Medical Group, Freiburg, Germany). A standard cranial stabilization system using the MAYFIELD® Skull Clamps or MAYFIELD® Pediatric Horseshoe Headrest (Integra, Princeton, NJ, USA) is also used when the MR was scheduled only as a final check and withdrawn before entering the MR suite. The choice

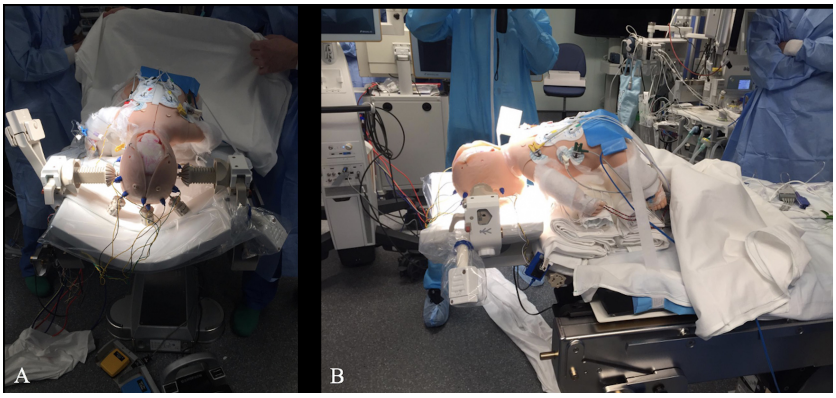

FIGURE 1
(A, B) Images of one of the pediatric models used in the simulation session for the validation of the ioMRI checklist carried out by the different teams involved in this workflow.

of the head clamp system was conditioned by the age of the patient, the surgical positioning, and the preference of the neurosurgeon.

Indication of ioMRI

Before the surgical procedure, we defined the utility of the ioMRI according to different issues depending on the type of surgery.

In groups 1 and 2 (pediatric brain and spinal tumors, respectively), intraoperative images were acquired either as a final control of the degree of tumor resection or to rule out complications associated with the surgical procedure. In cases where a tumor remnant that could be further resected was suspected (e.g., in large tumors where anatomy has shifted or the orientation was complicated), the patient went back to the operating theater, and an update of the navigation system was indicated.

For the other two groups, ioMRI was used to provide image control immediately after the surgical procedure and to check if the surgical objective had been achieved or if any complication occurred.

Imaging protocol

An MRI was performed before and during surgery in each oncology case. For intraoperative imaging, with minor changes regarding specific tumor types, radiological sequences were the same as those used in a preoperative imaging protocol following the SIOPE Brain Tumor Group guidelines [3D T1, axial T2 fast spin echo (FSE), coronal T2 FSE, axial diffusion-weighted imaging (DWI), susceptibility weighted imaging (SWI), contrast administration, and 3D T1 turbo field echo (TFE) and 3D FLAIR]. Two additional planes of FSE= fast spin echo; T2-weighted imaging were acquired for posterior fossa tumors (17). In intracranial tumors, volumetric assessment by manual segmentation was performed using Elements software (BrainLab, Germany). Volume measurement was based on preoperative and intraoperative gadolinium-enhancement (contrast-enhancing tumors) or T2-weighted/FLAIR (noncontrast-enhancing or poorly contrast-enhancing tumors) MR images to determine the extent of tumor resection. In order to avoid air artifacts, filling the surgical cavity with serum and the use of TSE DWI=diffusion-weighted imaging can be of great help.

All intraoperative MRI were judged along with a neuroradiologist regarding the decision of whether a residual tumor was detected and intraoperative complications related to the surgical procedure.

In cases in which the surgeon's decision implied continuing with the removal of the tumor, a postoperative MRI was performed, usually within the first 48 h.

Results

During the timeline of the study, between February 2020 and May 2022, ioMRI was used in 147 surgical procedures, as shown in Table 1. Of all these surgeries, 62 were oncological, and they were divided according to the condition treated, as indicated in Table 2. The median age at the time of surgery was 8.91 years (range 1–18). There were 27 female patients and 31 male patients.

10.3389/fonc.2022.1021335

TABLE 2 The four groups of oncological patients treated using ioMRI.

Group and Tumor Histology	No of surgical procedures
Group 1: Intracranial tumors	**45**
A. Supratentorial tumor	24
Pilocytic astrocytoma	1
Ganglioglioma	3
Low-grade glioma NOS	1
Adamantinomatous craniopharyngioma	2
Subependymal giant cell astrocytoma	1
Choroid plexus papilloma	1
Choroid plexus xanthogranuloma	1
Pituitary adenoma/PitNET	4
Desmoplastic infantile ganglioglioma	1
Glioblastoma (hemispheric glioma)	1
Diffuse midline glioma, H3K27M-altered	1
Infant-type hemispheric glioma	2
Ewing sarcoma	1
Metastases (Neuroblastoma)	2
Atypical teratoid/rhabdoid tumor	1
Supratentorial ependymoma, ZFTA fusion-positive	1
B. Infratentorial tumors	21
Medulloblastoma	7
Posterior fossa ependymoma, group PFA	3
Diffuse midline glioma, H3K27M-altered	1
Embryonal tumor with multilayered rosettes	1
Metastases (Neuroblastoma)	1
Pilocytic astrocytoma	8
Group 2: Intraspinal lesions	**2**
Aneurysmal bone cyst	1
Pilocytic astrocytoma	1
Group 3: Stereotactic biopsy for unresectable tumors	**10**
Diffuse midline glioma, H3K27M-altered	7
Diffuse low-grade glioma, MAPK pathway-altered	1
Ganglioglioma	2
Group 4: Catheter placement for cystic tumors	**5**
Focal brainstem pilocytic astrocytoma	3
Hypothalamic chiasmatic pilocytic astrocytoma	1
Pilocytic astrocytoma (of floor of the fouth ventricule)	1

10.3389/fonc.2022.1021335

Group 1: Intracranial tumors

As shown in Table 2, 45 surgical procedures for the removal of brain tumors were performed, with 24 supratentorial and 21 infratentorial lesions.

Out of seven patients that were previously treated at another institution, four underwent partial tumor debulking, and in three cases, a biopsy sample of the lesion was obtained (Table 3).

The most common symptom on preoperative neurological examination was intracranial hypertension (37.8%), followed by visual impairment (26%) and coordination disturbance (22.2%). Cranial nerve deficit (11%), hypophyseal-hypothalamic dysfunction (11%), seizures (8.9%), torticollis (6.7%), macrocephaly (4.4%), and motor deficit (4.4%) were less frequent. In one case, there was an incidental diagnosis of a brain tumor after an extension examination justified by Li–Fraumeni syndrome. In another eight patients (one on two occasions), tumor recurrence was an unexpected finding in a routine MRI control.

Surgery was performed for newly diagnosed tumors in 27 cases, for the removal of a remnant disease in seven cases, and for tumor recurrence in 11 cases. In three cases, the surgical intention was to perform an extended biopsy of the tumor: a pterional approach for a chiasmatic hypothalamic tumor, a far lateral cerebellar approach for a focal midline tumor, and a retrosigmoid approach for a diffuse midline glioma with a large bulbar exophytic component, respectively.

TABLE 3 Clinical and radiological aspects of group 1.

Parameters	Intracranial tumors
No. of procedures	**45**
At the time of surgery	
Newly diagnosed tumors	27
Recurrent tumors	11
Remnant disease after prior recent surgery	7
Location	
Supratentorial tumors	24
Infratentorial tumors	21
Volumetric assessment	
Median preoperative tumor volume (cm^3)	**28.77**
Range	0.15–308
Median intraoperative tumor volume (cm^3)	**0.43**
Range	0.0–9.73
Median extent of resection (EoR) (%)	**96.61**
Range	31–100

The mean extent of tumor resection in all patients was 96.61% (range 31%–100%) after comparing tumor volumes between preoperative and intraoperative MR images. The median preoperative tumor volume was 28.77 cm^3 (range 0.15–308 cm^3), and the median intraoperative residual tumor volume was 0.43 cm^3 (range 0–9.73 cm^3).

The surgical goal *a priori* was gross-total resection (GTR) (≥98% of tumor volume) in 33 cases, subtotal resection (STR) (≥90% of tumor volume) in six, and partial resection (PR) (<90% of tumor volume) in three cases (Figure 2). ioMRI confirmed GTR in 32 cases, STR in seven, and PR in three.

In 27 out of 33 cases, GTR was confirmed after the first ioMRI (Figure 3). In one case of suprasellar craniopharyngioma, macroscopical resection was not completed, and a small remnant of the tumor was intentionally left attached to the carotid artery. In the other five cases, ioMRI revealed some residual tumors. In one case, the intraoperative finding corresponded to a small blood clot with no evidence of an additional tumor, and in the other four, there was a clear remnant lesion that went unnoticed during surgery. In these cases, the mean intraoperative tumor volume was 3.0 cm^3. If an intraoperative MRI had not been performed, tumor removal would have been 84%, 75%, 92%, 97%, and 51.5% instead of 100%.

In a patient who was planned for STR due to a tumor location in a nearby functional area, the use of ioMRI made it possible to improve the degree of resection and turn a PR into an STR (which was the preoperative goal). After evaluation of the intraoperative images, the surgeon considered it feasible to proceed with further removal of the tumor without compromising functional structures. A second MRI study was performed, and the surgical outcome was verified.

There were only three patients who underwent PR. In all cases, the indication for surgery was partial debulking due to histology, involvement of eloquent structures, and the possibility of medical treatment. These cases included an optic pathway/hypothalamic glioma (EOR = 64%), a focal brainstem glioma (*KIAA1549-BRAF* fusion pilocytic astrocytoma) (EOR = 78%), and a diffuse midline glioma with H3K27M alterations (EOR = 31%).

In one patient, the intraoperative images showed an artifact that prevented an adequate evaluation of the study due to damage to the coil. The surgeon's impression was that a complete removal had been achieved, although immediate postoperative control revealed a small tumor remnant. Fortunately, the patient did not require a second-look surgery due to the histological type (medulloblastoma type 3/4) and the size of the residual tumor.

In summary, additional resection of residual tumor was performed after ioMRI in 14% of oncological cases.

Intracranial surgeries were performed by rigid immobilization of the patient's head using the different cranial systems. Of the six patients who required a return to the OR, NORAS had been used in four and a horseshoe headrest in two.

There was a 27.4% complication rate in the entire series, all of them transient and successfully resolved. There were no intraoperative safety incidents related to the use of ioMRI.

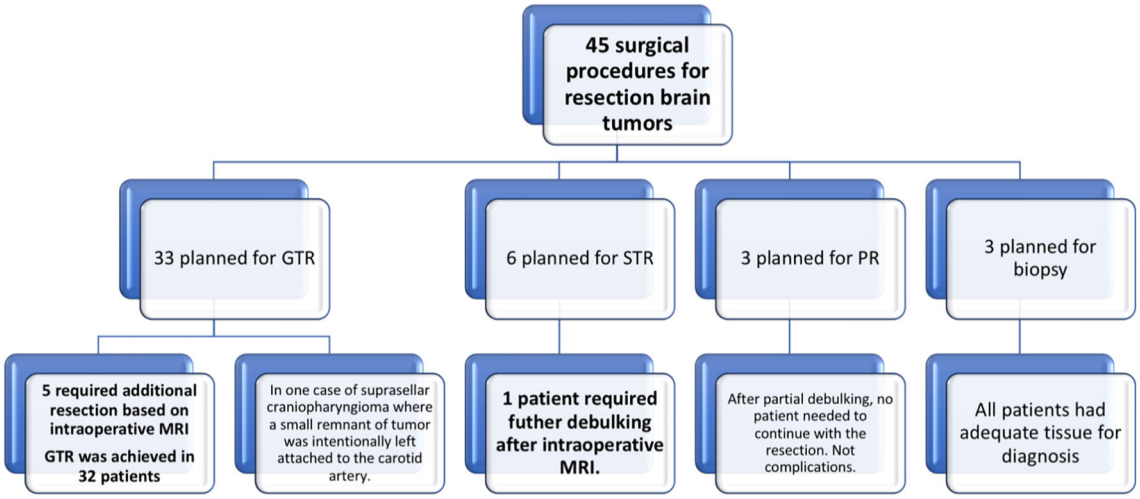

FIGURE 2
Summary flowchart of all operated intracranial tumor cases (Group 1).

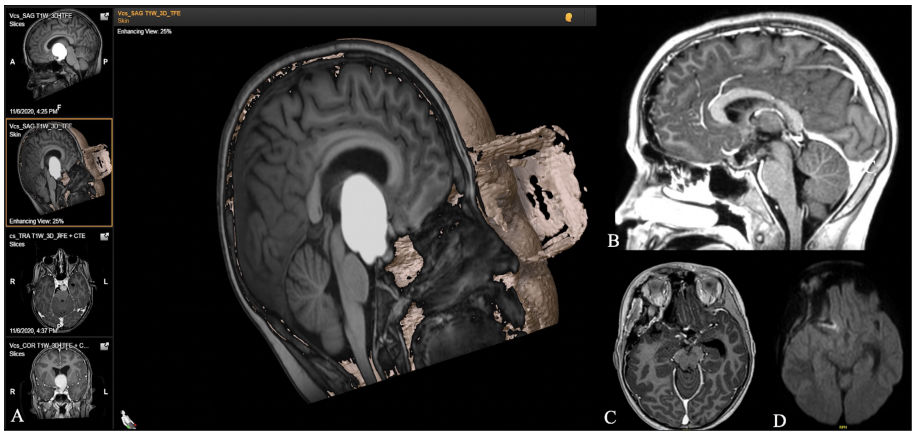

FIGURE 3
(A) 3D coronal T1-weighted reconstruction and axial coronal T1-weighted contrast-enhanced MR images of a 12-year-old boy diagnosed with a large craniopharyngioma. Sagittal **(B)** and axial **(C)** T1-weighted, contrast-enhanced and diffusion-weighted **(D)** intraoperative images after pterional resection, demonstrating a radical excision without complications. Note the integrity of the pituitary stalk and both the hypothalamic and mammillary bodies.

Postoperatively, four patients developed a pseudomeningocele: one was managed with temporary lumbar drainage, and three were successfully treated with a compressive dressing. Another patient was readmitted 5 days after discharge due to *Escherichia coli* meningitis in the context of a CSF fistula; she was successfully treated with intravenous antibiotic therapy and suture reinforcement. Postoperative hydrocephalus with CSF fistula occurred in one patient, which was resolved with the placement of a permanent shunt. Among the systemic complications, there were two urinary tract infections, two electrolyte imbalances, and two cases of transitory central hyperthermia. Worsening in neurological status occurred in four patients: two of them developed a transient postoperative cerebellar mutism syndrome with VII and VI cranial nerve deficits; another patient with a focal brainstem tumor had hemihypoesthesia and partial involvement of the third cranial nerve; and a fourth one developed a transient psychiatric disorder due to a levetiracetam intoxication. All of them improved during the hospital stay.

The Mayfield clamp was damaged during the surgery, resulting in a depressed skull fracture. The headrest was

changed to a horseshoe headrest. ioMRI was especially helpful in detecting a suspected depressed skull fracture under a Mayfield clamp, ruling out the presence of other intracranial complications.

Group 2: Intraspinal tumors

Spinal tumor resection was performed in two patients. The first was diagnosed with a D12 aneurysmal bone cyst, while the other second was diagnosed with a D8–D10 intramedullary pilocytic astrocytoma. In both cases, a GTR was achieved without any complication.

Group 3: Stereotactic biopsy for unresectable tumors

In 10 patients, a stereotactic biopsy procedure was performed, as shown in Table 2.

In all of them, ioMRI was obtained at the end of the surgery, and the track of the biopsy needle within the preoperative plan was confirmed (Figure 4). In one case, intraoperative images revealed a small hematoma within the tumor that did not require surgical management. Another patient with DIPG suffered transient diplopia and numbness of the hand but recovered completely in the first postoperative days.

Group 4: Catheter placement for cystic tumors

In four patients, for a total of five procedures, surgery involved the placement of a catheter inside a cystic tumor (Figure 5). In one patient, an Ommaya reservoir catheter was placed in the cyst of a hypothalamic chiasmatic tumor. Three other patients were treated for cystic brainstem focal tumors. One of them needed a second procedure to treat a catheter obstruction.

In all surgeries, an MRI showed the optimal location of the catheters and ruled out complications without any safety issues.

Discussion

In this study, we present our experience with ioMRI-assisted treatment in neuro-oncological surgery at the Sant Joan de Déu Hospital. We elected to use ioMRI for tumor excision surgeries and percutaneous procedures either as a final or intraoperative control. We analyzed the impact of ioMRI on these patients and documented the utility and safety of this technique.

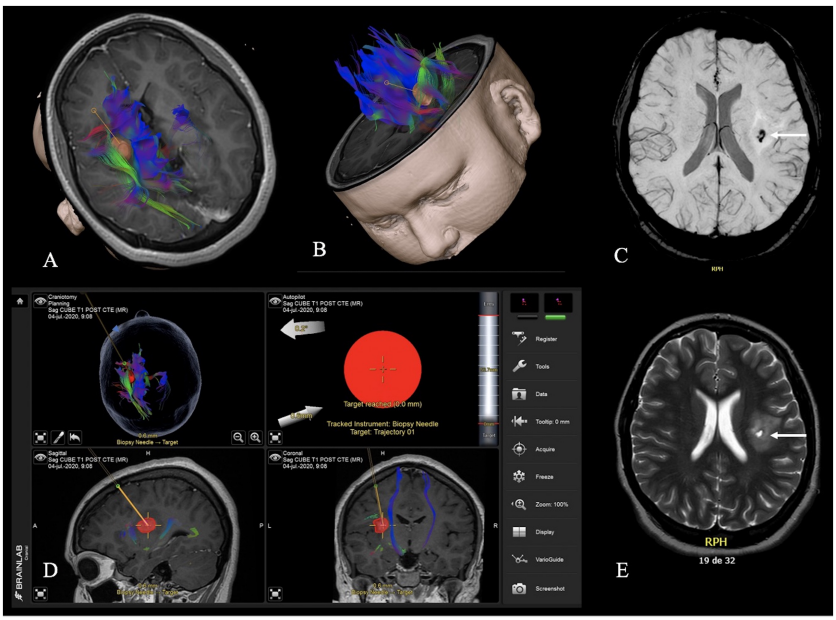

FIGURE 4
3D reconstruction showing a left insular tumor, its relationship with the motor bundle and the arcuate fasciculus, and the biopsy trajectory **(A, B)**. Screenshot of the planned biopsy tract to the target **(D)**. Intraoperative MRI with a T2-weighted **(E)** and SWI **(C)** as a final control to verify the location of the tumor samples indicated by the arrows and to rule out complications related to the procedure.

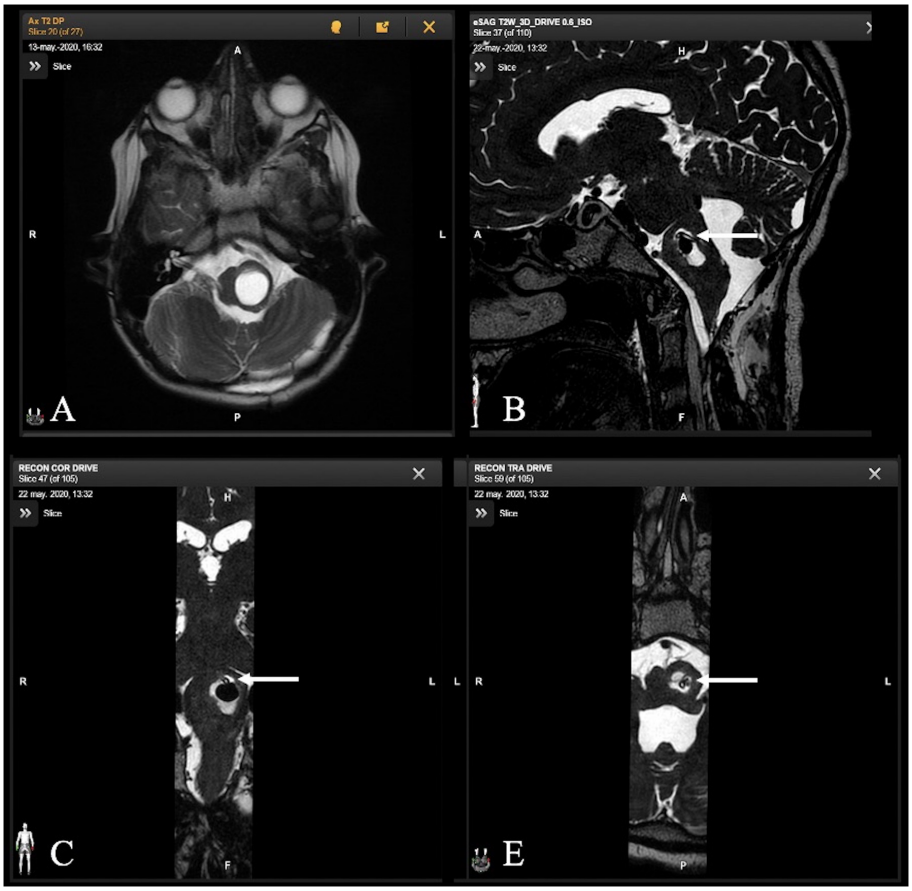

FIGURE 5
Axial T2-weighted MR image of a 13-year-old child with a focal brainstem tumor and a large cyst **(A)**. Acquisition of intraoperative MR images as final controls with sagittal, axial, and coronal T2-weighted images shows correct placement of the catheter, indicated by the white arrow, within the tumor cyst component **(B–D)**.

Currently, ioMRI is a significant advance in the neurosurgical care of adult patients with intracranial pathology. The ioMRI has proven to be reliable and safe, and there is evidence of its benefits in further tumor volume reduction without increasing postoperative neurological morbidity (18–22).

For pediatric intracranial neoplasms, surgery constitutes a cornerstone in their management, despite the development of new therapeutic modalities. However, radical or maximally safe resection must be well-balanced against the risk of new neurological sequelae to achieve high rates of overall survival and disease control along with the success rate of chemotherapy and/or radiation therapy (23). Shah and colleagues reported that ioMRI-guided resections for tumors reduced the need for early re-reoperation with postoperative comparable deficits versus conventional pediatric resections (24). Other published reports have concluded that ioMRI proved to be useful in reducing the final tumor volume with additional resection (range, 17%–60%) without intraoperative complications and avoiding the cost and operative risk associated with a later reoperation (24–34). Our results showed that in 14% of the intracranial tumor surgeries, the ioMRI provided valuable information that allowed the surgeon to proceed with further resection of remnants. In five cases of intracranial tumors in which a complete tumor resection had been planned, the intraoperative image revealed a tumor remnant despite the subjective impression of the neurosurgeon being that of radical excision. In all cases, the surgeon returned to the operating room to complete the surgery in order to achieve the established preoperative goal and avoid a reoperation days later. The same reasoning was applied to patients in whom the goal was subtotal removal of the tumor because eloquent areas were involved.

It should be noted that in one case, the intraoperative finding corresponded to a small blood clot. This situation constitutes a false positive, that is, a suspicious area with contrast enhancement that is actually due to rapid gadolinium extravasation in vessels with partial hemostasis at the margins of the resection cavity. Prior intraoperative MRI studies described this phenomenon. An exhaustive comparison with the preoperative image is recommended, since contrast

enhancement in an area where there was previously no tumor would have to be interpreted with caution and, obviously, be reviewed in the operating room (35).

In our experience, we observed that patients diagnosed with large-volume tumors could particularly benefit from ioMRI to avoid leaving hidden tumor remains in a situation where orientation is complicated and anatomy has shifted, resulting in a loss of navigational dependability. Most often, complete resection is required, as it could be curative or improve the prognosis of the disease. Likewise, ioMRI was deemed useful in the removal of deep-seated tumors or in proximity to eloquent areas (motor and/or speech, brainstem) or major fiber bundles (i.e., corticospinal tract) as it provided the possibility of redefining anatomical relationships, verifying the existence of residual disease, and, if necessary, allowed the neurosurgeon to continue with the surgery with greater confidence and security.

Furthermore, in 15 surgical procedures in groups 1 and 2 (15%), ioMRI was useful because it provided a final radiological control, saving these pediatric patients additional anesthesia or sedation for routine postoperative imaging.

In current guidelines, it is only accepted if it has been done on a 3-T scanner, but in our experience, our image quality is good enough to use the final ioMRI at 1.5 T as a baseline examination for future follow-up, although more studies are needed in this area (17, 36).

The reoperation rate during the early postoperative period was 0%. Other groups corroborated these outcomes, Choudhri et al. showed a tumor-related early reoperation rate from 6% to 0% and at 30 days, from 7% to 1% (29). A significant reduction in the number of reoperations was also reported by Avula et al., who showed higher early reoperation rates (within 6 months) in the conventional group in contrast with the ioMRI group (14 *vs.* 0%; $p = 0.003$) (37). Giordano et al., in 82 surgical intracranial procedures performed using ioMRI, reported the absence of early reintervention (31). All the authors of the cited literature agreed that the use of ioMRI makes it possible to reduce the necessity for repeat surgery in the immediate postoperative days. This involvement translates not only into clinical and economic advantages but also into benefits in the emotional and psychological sphere for the patient and their families since it eliminates the stress of facing an early reoperation.

In our series of pediatric patients, no incidents or adverse events related to the use of ioMRI have been recorded. Likewise, our data did not reveal that ioMRI-guided surgery resulted in an accumulated risk of neurological sequelae or complications in order to achieve the maximum degree of surgical resection. In fact, it should be pointed out that in one case in which the cranial fixation system was damaged, making it necessary to replace it with another one during surgery, ioMRI enabled the detection of a sinking skull fracture, ruled out other complications, and verified the surgical goal.

So, we believe that ioMRI is truly beneficial in pediatric pathology for several reasons. It allows the neurosurgeon's subjective impression that the surgical objective has been achieved and the complications associated with the surgery to be confirmed. It can also be used to identify and delimit suspicious remains and/or update neuronavigation, compensate for inaccuracies due to brain changes, and save anesthesia for postoperative MRI control in younger patients.

On the contrary, this technology may raise a number of concerns. One of them is the prolongation of surgical time; however, keeping an efficient and smooth workflow was possible with trained and coordinated team building. Another one is whether the increased operative time increases the risk of infection. Among the infectious complications, only *Escherichia coli* meningitis occurred after CSF fistula in the immediate postoperative period. These data are within the reported 0%–2.5% risk cited in other pediatric ioMRI imaging series (15, 26, 29, 32, 38–41), which did not differ from others in which ioMRI was not used (42, 43). Regarding safety, the high-strength magnetic field generates a complex and hazardous environment; mitigation of risks related to accidents caused by ferromagnetic instruments in order to guarantee the safety of both the patient and the staff could be carried out by applying a strict safety checklist, as other groups have also reported (4–6). The average duration required for completing the safety guideline and intraoperative image process was 54 ± 6 min. This value was similar to that mentioned by Matsumae, who reported 47 min after 3 years of experience with intraoperative MRI (4), and Ahmadi et al., 57 min from skin to skin in 516 tumors performed with intraoperative MRI scan (44). The checklist did not take more than 2 or 3 min, as reported by the Zurich group, or a little more than 8 min, as reported by Matsumae and colleagues (4, 6).

Finally, the technical aspects of positioning the pediatric patient with the use of ioMRI are mostly related to the configuration of the surgical table. Our table does not have independent segments that can be adjusted separately. Placements were limited to supine and prone positioning. The sitting position was not used; in our department, posterior fossa tumors were operated on in the prone position. In the lateral position, which we mostly use for cerebellopontine angle tumors, MRI-compatible headrests were not used due to their configuration and the difficulty for the patient's head and neck to be well flexed. Moreover, the prone position was the most difficult to achieve in younger patients due to the configuration of the table and the limited range of motion of the adapter between the table and the compatible MRI head immobilization device. Adequate flexion of the head to accomplish a correct surgical approach made it necessary to place supplemental padding under the patient and, thus, to be able to solve the limitation in the movement of the head downwards. In very young patients, in whom a headrest along with the spike headrest was necessary to maintain stability, compatible MRI headrests were not used. These limitations have also been reported by other groups (31, 45).

The limitations of the study are the sample size and the heterogeneity of the patients. Although our results are consistent with those of other series published in the literature and mentioned in this article.

Conclusion

We have evaluated a consecutive series of ioMRI neuro-oncological procedures carried out at our institution over a period of 27 months. Despite the heterogeneity of our patients, we found that this imaging tool has proven to be safe and reliable in our pediatric population. There are no complications or safety accidents related to its use. Also, it was effective in increasing the extent of tumor resection without increasing neurological morbidity or complications. The disadvantage of intraoperative imaging is that it is a time-consuming technique, so proper case selection and an experienced team are essential. It is important to consider the uniqueness of the positioning of the pediatric patient, which is influenced by the configuration of the surgical table and cranial immobilization systems.

Data availability statement

The original contributions presented in the study are included in the article/supplementary material. Further inquiries can be directed to the corresponding author.

Author contributions

Conception and design: VB and JH. Acquisition of data: VB. Analysis and interpretation of data: VB and JH. Drafting the article: VB and JH. Critical revision of the article: all of the authors. Reviewed submitted version of manuscript: all of the authors. Approved the final version of the manuscript on behalf of both authors: VB and JH. Study supervision: VB and JH. All authors contributed to the article and approved the submitted version.

Acknowledgments

We would like to thank our radiology technologist—Mr. Manuel Gómez Ponce—for performing iMRIs and our scrub nurse team—Ms. Sonia Acero, Ms. Miriam Álamo, Ms. Rosa Aguilar, Mr. Fernando Borreguero, and Ms. Otilia Martín. The authors thank Ms. Nuria Palau and Mr. Carlos J. García for their professionalism.

Conflict of interest

The authors confirm that the research was conducted in the absence of any commercial or financial relationships that could be construed as a potential conflict of interest.

Publisher's note

References

1. Black PM, Moriarty T, Alexander E3rd, Stieg P, Gleason PL, Martin CH, et al. Development and implementation of intraoperative magnetic resonance imaging and its neurosurgical applications. *Neurosurgery* (1997) 41:831–45. doi: 10.1097/00006123-199710000-00013

2. Steinmeier R, Fahlbusch R, Ganslandt O, Nimsky C, Buchfelder M, Kaus M, et al. Intraoperative magnetic resonance imaging with the magnetom open scanner: concepts, neurosurgical indications, and procedures: a preliminary report. *Neurosurgery* (1998) 43(4):739–49. doi: 10.1097/00006123-199810000-00005

3. Knauth M, Wirtz CR, Tronnier VM, Aras N, Kunze S, Sartor K. Intraoperative MR imaging increases the extent of tumor resection in patients with high-grade gliomas. *AJNR Am J Neuroradiol* (1999) 20(9):1642–6. Available at: http://www.ajnr.org/content/20/9/1642.long

4. Matsumae M, Nakajima Y, Morikawa E, Nishiyama J, Atsumi H, Tominaga J, et al. Improving patient safety in the intra-operative MRI suite using an on-duty safety nurse, safety manual and checklist. *Acta Neurochir Suppl* (2011) 109:219–22. doi: 10.1007/978-3-211-99651-5_34

5. Rahmathulla G, Recinos PF, Traul DE, Avitsian R, Yunak M, Harper NT, et al. Surgical briefings, checklists, and the creation of an environment of safety in the neurosurgical intraoperative magnetic resonance imaging suite. *Neurosurg Focus* (2012) 33(5):E12. doi: 10.3171/2012.9.FOCUS12260

6. Steinen MN, Fierstra J, Pangalu A, Regli L, Bozinov O. The Zurich checklist for safety in the intraoperative magnetic resonance imaging suite: technical note. *Oper Neurosurg (Hagerstown)* (2018) 16(6):756–65. doi: 10.1093/ons/opy205

7. Nimsky C, Ganslandt O, Cerny S, Hastreiter P, Greiner G, Fahlbusch R. Quantification of, visualization of, and compensation for brain shift using intraoperative magnetic resonance imaging. *Neurosurgery* (2000) 47:1070–80. doi: 10.1097/00006123-200011000-00008

8. Gessler F, Foster MT, Duetzmann S, Mittelbronn M, Hattingen E, Franz K, et al. Combination of intraoperative magnetic resonance imaging and intraoperative fluorescence to enhance the resection of contrast enhancing gliomas. *Neurosurgery* (2015) 77(1):16–22. doi: 10.1227/NEU.0000000000000729

9. Nickel K, Renovanz M, Koünig J, Stöckelmaier L, Hickmann AK, Nadji-Ohl M, et al. The patients' view: impact of the extent of resection, intraoperative imaging, and awake surgery on health-related quality of life in high-grade glioma patients-results of a multicenter cross-sectional study. *Neurosurg Rev* (2018) 41(1):207–19. doi: 10.1007/s10143-017-0836-x

10. Wisoff JH, Boyett JM, Berger MD, Brant C, Li H, Yates AJ, et al. Current neurosurgical management and the impact of the extent of resection in the treatment of malignant gliomas of childhood: a report of the children's cancer group trial no. CCG-945. *J Neurosurg* (1998) 89(1):52–9. doi: 10.3171/jns.1998.89.1.0052

11. Rodríguez D, Cheung MC, Housri N, Quiñones-Hinojosa A, Camphausen K, Koniaris LG. Outcomes of malignant CNS ependymomas: An examination of 2408 cases through the surveillance, epidemiology, and end results (SEER) database (1973-2005). *J Surg Res* (2009) 156(2):340–51. doi: 10.1016/j.jss.2009.04.024

12. Cage TN, Clark AJ, Aranda D, Gupta N, Sun PP, Parsa AT, et al. A systematic review of treatment outcomes in pediatric patients with intracranial ependymomas. *J Neurosurg Pediatr* (2013) 11(6):673–81. doi: 10.3171/2013.2.PEDS12345

13. Gajjar A, Sanford RA, Heideman R, Jenkins JJ, Walter A, Li Y, et al. Low-grade astrocytoma: a decade of experience at st. Jude children's research hospital. *J Clin Oncol* (1997) 15(8):2792–9. doi: 10.1200/JCO.1997.15.8.2792

14. Lee RP, Foster KA, Lillard JC, Klimo P, Ellison DW, Orr B, et al. Surgical and molecular considerations in the treatment of pediatric thalamopeduncular tumors. *J Neurosurg Pediatr* (2017) 20(3):247–55. doi: 10.3171/2017.4.PEDS16668

15. Hall WA, Martin AJ, Liu H, Pozza CH, Casey SO, Michel E, et al. High-field strength interventional magnetic resonance imaging for pediatric neurosurgery. *Pediatr Neurosurg* (1998) 29:253–9. doi: 10.1159/000028732

16. Candela Cantó S, Alamar M, Aláez C, Muchart J, Forero C, Gala C, et al. Highly realistic simulation for robot-assisted hypothalamic hamartoma real-time MRI-guided laser interstitial thermal therapy (LITT). *Childs Nerv Syst* (2020) 36 (6):1131–42. doi: 10.1007/s00381-020-04563-0

17. Avula S, Peet A, Morana G, Morgan P, Warmuth-Metz M, Jaspan T. European Society for paediatric oncology (SIOPE) MRI guidelines for imaging patients with central nervous system tumours. *Childs Nerv Syst* (2021) 37(8):2497–508. doi: 10.1007/s00381-021-05199-4

18. Hatiboglu MA, Weinberg JS, Suki D, Rao G, Prabhu S, Shah K, et al. Impact of intraoperative high-field magnetic resonance imaging guidance on glioma surgery: a prospec- tive volumetric analysis. *Neurosurgery* (2009) 64:1073–81. doi: 10.1227/01.NEU.0000345647.58219.07

19. Hofmann BM, Nimsky C, Fahlbusch R. Benefit of 1.5-T intraoperative MR imaging in the surgical treatment of craniopharyngiomas. *Acta Neurochir (Wien)* (2011) 153:1377–90. doi: 10.1007/s00701-011-0973-x

20. Coburger J, Hagel V, Wirtz CR, Köning R. Surgery for glioblastoma: impact of the combined use of 5-aminolevulinic acid and intraoperative MRI on extent of resection and survival. *PloS One* (2015) 10(6):e0131872. doi: 10.1371/journal.pone.0131872

21. Scherer M, Jungk C, Younsi A, Kickingereder P, Müller S, Unterberger A. Factors triggering an additional resection and determining residual tumor volume on intraoperative MRI: analysis from a prospective single-center registry of supratentorial gliomas. *Neurosurg Focus* (2016) 40(3):E4. doi: 10.3171/2015.11.FOCUS15542

22. Jones PS, Swearingen B. Intraoperative MRI for pituitary adenomas. *Neurosurg Clin N Am* (2019) 30:413–20. doi: 10.1016/j.nec.2019.05.003

23. Pollack IF. Multidisciplinary management of childhood brain tumors: a review of outcomes, recent advances, and challenges. *J Neurosurg Pediatr* (2011) 8:135–48. doi: 10.3171/2011.5.PEDS1178

24. Shah MN, Leonard JR, Inder G, Gao F, Geske M, Haydon DH, et al. Intraoperative magnetic resonance imaging to reduce the rate of early reoperation for lesion resection in pediatric neurosurgery. *J Neurosurg Pediatr* (2012) 9:259–64. doi: 10.3171/2011.12.PEDS11227

25. Kremer P, Tronnier V, Steiner HH, Metzner R, Ebinger F, Rating D, et al. Intraoperative MRI for interventional neurosurgical procedures and tumor resection control in children. *Childs Nerv Syst* (2006) 22:674–8. doi: 10.1007/s00381-005-0030-2

26. Levy R, Cox RG, Hader WJ, Myles T, Sutherland GR, Hamilton MG. Application of intraoperative high-field magnetic resonance imaging in pediatric neurosurgery. *J Neurosurg Pediatr* (2009) 4:467–74. doi: 10.3171/2009.4.PEDS08464

27. Yousaf J, Avula S, Abernethy LJ, Mallucci CL. Importance of intraoperative magnetic resonance imaging for pediatric brain tumor surgery. *Surg Neurol Int* (2012) 3(suppl 2):S65–72. doi: 10.4103/2152-7806.95417

28. Kubben PL, van Santbrink H, ter Laak-Poort M, Weber JW, Vles JSH, Granzen B, et al. Implementation of a mobile 0.15-T intraoperative MR system in pediatric neuro-oncological surgery: feasibility and correlation with early postoperative high-field strength MRI. *Childs Nerv Syst* (2012) 28:1171–80. doi: 10.1007/s00381-012-1815-8

29. Choudhri AF, Klimo PJr, Auschwitz TS, Whitehead MT, Boop FA. 3 T intraoperative MRI for management of pediatric CNS neo- plasms. *AJNR Am J Neuroradiol* (2014) 35:2382–7. doi: 10.3174/ajnr.A4040

30. Roder C, Breitkopf M, Bisdas S, Da Silva Freitas R, Dimostheni A, Ebinger M, et al. Beneficial impact of high-field intraoperative magnetic resonance imaging on the efficacy of pediatric low-grade glioma surgery. *Neurosurg Focus* (2016) 40: E13. doi: 10.3171/2015.11.FOCUS15530

31. Giordano M, Samii A, Lawson Mclean ACL, Bertalanffy H, Fahlbusch R, Samii M, et al. Intraoperative magnetic resonance imaging in pediatric neurosurgery: safety and utility. *J Neurosurg Pediatr* (2017) 19:77–84. doi: 10.3171/2016.8.PEDS15708

32. Tejada S, Avula S, Pettorini B, Henningan D, Abernethy L, Mallucci C. The impact of intraoperative magnetic resonance in routine pediatric neurosurgical practice: a 6-year appraisal. *Childs Nerv Syst* (2018) 34:617–26. doi: 10.1007/s00381-018-3751-8

33. Day EL, Scott M. The utility of intraoperative MRI during pediatric brain tumor surgery: a single-surgeon case series. *J Neurosurg Pediatr* (2019) 24:577–83. doi: 10.3171/2019.6.PEDS1998

34. Low SYY, Lim EHL, Loh LEL, Mok YH, Siow YN, Ping L, et al. Use of an offsite intraoperative MRI operating theater for pediatric brain tumor surgery: Experience from a Singapore children's hospital. *World Neurosurg* (2020) 135:e28–35. doi: 10.1016/j.wneu.2019.10.083

35. Wirtz CR, Bonsanto MM, Knauth M, Tronnier VM, Albert FK, Staubert A, et al. Intraoperative magnetic resonance imaging to update interactive navigation in neurosurgery: method and preliminary experience. *Comput Aided Surg* (1997) 2 (3-4):172–9. doi: 10.3109/10929089709148110

36. Avula S, Jaspan T, Pizer B, Pettorini B, Garlick D, Hennigan D, et al. Comparison of intraoperative and post-operative 3-T MRI performed at 24-72 h following brain tumour resection in children. *Neuroradiology* (2021) 63(8):1367–76. doi: 10.1007/s00234-021-02671-5

37. Avula S, Pettorini B, Abernethy L, Pizer B, Williams D, Mallucci C. High field strength magnetic resonance imaging in paediatric brain tumour surgery–its role in prevention of early repeat resections. *Childs Nerv Syst* (2013) 29:1843–50. doi: 10.1007/s00381-013-2106-8

38. Lam C, Hall WA, Truwit CL, Liu H. Intra-operative MRI-guided approaches to the pediatric posterior fossa tumors. *Pediatr Neurosurg* (2001) 34:295–300. doi: 10.1159/000056041

39. Nimsky C, Gansladt O, Gralla J, Buchfelder M, Fahlbusch R. Intraoperative low-field magnetic resonance imaging in pediatric neurosurgery. *Pediatr Neurosurg* (2003) 38:83–9. doi: 10.1159/000068046

40. Samdani A, Schulder M, Catrambone J, Carmel P. Use of a compact intraoperative low-field magnetic imager in pediatric neurosurgery. *Childs Nerv Syst* (2005) 21:108–13. doi: 10.1007/s00381-004-1008-1

41. Roth J, Beni L, Biyani N, Constantini S. Intraoperative portable 0.12-Tesla MRI in pediatric neurosurgery. *Pediatr Neurosurg* (2006) 42:74–80. doi: 10.1159/000090459

42. Lassen B, Helseth E, Egge A, Due-Tonnessen BJ, Ronning P, Meling TR. Surgical mortality and selected complications in 273 consecutive craniotomies for intracranial tumors in pediatric patients. *Neurosurgery* (2012) 70:936–43. doi: 10.1227/NEU.0b013e31823bcc61

43. Foster MT, Hennigan D, Grayston R, Van Baarsen K, Sunderland G, Millward C, et al. Reporting morbidity associated with pediatric brain tumor surgery: are the available scoring systems sufficient? *J Neurosurg Pediatr* (2021) 27:556–65. doi: 10.3171/2020.9.PEDS20556

44. Ahmadi R, Campos B, Haux D, Rieke J, Beigel B, Unterberg A. Assessing perioperative complications associated with use of intraoperative magnetic resonance imaging during glioma surgery – a single centre experience with 516 cases. *Br J Neurosurg* (2016) 30(4):397–00. doi: 10.3109/02688697.2016.1161726

45. Boop FA, Bate B, Choudhri AF, Burkholder B, Klimo PJr. Preliminary experience with an intraoperative MRI- compatible infant headholder: technical note. *J Neurosurg Pediatr* (2015) 15:539–43. doi: 10.3171/2014.10.PEDS14447

frontiers | Frontiers in Oncology

TYPE Case Report
PUBLISHED 01 March 2023
DOI 10.3389/fonc.2023.1039159

OPEN ACCESS

EDITED BY
Sergio García,
Hospital Universitario Río Hortega, Spain

REVIEWED BY
Jose L. Sanmillan,
Bellvitge University Hospital, Spain
Kumar Abhinav,
University of Bristol, United Kingdom

*CORRESPONDENCE
Marcus A. Zachariah
mzachariah@umc.edu

SPECIALTY SECTION
This article was submitted to Neuro-Oncology and Neurosurgical Oncology, a section of the journal Frontiers in Oncology

RECEIVED 07 September 2022
ACCEPTED 20 February 2023
PUBLISHED 01 March 2023

CITATION
Baker KE, Robbins AC, Kumm ZT, Ziemke MK, Washington CW, Luzardo GD, Taylor CS, Stringer SP and Zachariah MA (2023) Case report: Side-firing intraoperative ultrasound guided endoscopic endonasal resection of a clival chordoma.
Front. Oncol. 13:1039159.
doi: 10.3389/fonc.2023.1039159

Case report: Side-firing intraoperative ultrasound guided endoscopic endonasal resection of a clival chordoma

Katherine E. Baker[1], Austin C. Robbins[1], Zeynep T. Kumm[2], Michael K. Ziemke[1], Chad W. Washington[1], Gustavo D. Luzardo[1], Charlotte S. Taylor[3], Scott P. Stringer[4] and Marcus A. Zachariah[1]*

[1]Department of Neurosurgery, The University of Mississippi Medical Center, Jackson, MS, United States, [2]Department of Pathology, The Ohio State University, Columbus, OH, United States, [3]Department of Radiology, The University of Mississippi Medical Center, Jackson, MS, United States, [4]Department of Otolaryngology, The University of Mississippi Medical Center, Jackson, MS, United States

Clival chordomas are locally invasive midline skull base tumors arising from remnants of the primitive notochord. Intracranial vasculature and cranial nerve involvement of tumors in the paraclival region necessitates image guidance that provides accurate real-time feedback during resection. Several intraoperative image guidance modalities have been introduced as adjuncts to endoscopic endonasal surgery, including stereotactic neuronavigation, intraoperative ultrasound, intraoperative MRI, and intraoperative CT. Gross total resection of chordomas is associated with a lower recurrence rate; therefore, intraoperative imaging may improve long-term outcomes by enhancing the extent of resection. However, among these options, effectiveness and accessibility vary between institutions. We previously published the first use of an end-firing probe in the resection of a clival chordoma. End-firing probes provide a single field of view, primarily limited to depth estimation. In this case report, we discuss the benefits of employing a novel minimally invasive side-firing ultrasound probe as a cost-effective and time-efficient option to navigate the anatomy of the paraclival region and guide endoscopic endonasal resection of a large complex clival chordoma.

KEYWORDS

chordoma, skull base, ultrasound, endoscopic, imaging, clivus, tumor, neurosurgery

Introduction

Clival chordomas are complex midline skull base tumors with high recurrence rates. Gross total resection of these lesions is important, as it is associated with improved long-term outcomes (1). However, the invasive nature of chordomas and the close relationship of clival tumors to the brainstem and other critical deep structures complicates resection.

Several image guidance adjuncts are available for endoscopic endonasal resection of chordomas, including stereotactic neuronavigation, intraoperative ultrasound, intraoperative MRI, and intraoperative CT (2, 3). Intraoperative MRI and CT increase the accuracy of resection through real-time imaging. Although, these devices may not be available in every center, extend the duration of surgery, and have been associated with increased rates of false-positive identification of neoplastic tissue (4–6).

Alternatively, intraoperative ultrasound (IOUS) presents a fast, cost-effective, and recently widely available option. IOUS provides real-time visualization of nearby anatomy, allowing the surgeon to estimate the extent of resection and the location of critical structures with greater confidence (7, 8). Both end-firing and side-firing ultrasound probes are available for the endoscopic endonasal approach, but side-firing ultrasound may be favorable for the purpose of navigating the surrounding anatomy of the paraclival region. End-firing probes are limited mainly to depth assessment, while side-firing probes enhance understanding of anatomy adjacent to the probe tip and potentially beyond the endoscopic field of view (9). Side-firing IOUS is a safe and effective adjunct to endoscopic endonasal surgery that can reduce operative time and increase the surgeon's confidence in the extent of resection (8). We previously published the results of a case-control study demonstrating the utility of side-firing IOUS in the resection of large and giant pituitary adenomas (8). In this report, we describe the first use of a minimally invasive side-firing IOUS probe in the resection of a large complex clival chordoma. This case report follows Care Guidelines.

Patient information

The patient is a 63-year-old female who initially presented to otolaryngology in 2021 with a six-month history of intermittent hoarseness and difficulty swallowing. She stated that she first became aware of the hoarseness after contracting COVID-19 one year earlier, though her symptoms have become more significant within the past six months. Additionally, she reported a six-month history of difficulty swallowing solid and liquid foods, thick nasal drainage, globus sensation, and a constant urge to clear her throat. The patient mentioned that she works as a daycare director, which occasionally requires significant vocal strain, and often carries a "spit cup" due to difficulty swallowing saliva throughout the day.

Her past medical history includes hypertension and gastroesophageal reflux disease. She has no history of stroke or intubation and no surgical history. She has a 40-pack-year history of cigarette smoking and currently smokes one-half pack of cigarettes daily. There is no relevant family history. At presentation, the patient denied dyspnea, otalgia, unintentional weight loss, hemoptysis, or throat pain (Supplementary Figure 1).

Clinical findings and diagnostic assessment

The initial physical exam revealed vocal cord paralysis, diminished palate elevation, and tongue deviation. Laryngoscopy was performed, and it was noted that the left vocal cord was paralyzed in the paramedian position resulting in impaired mobility, incomplete glottic closure, and pooling of saliva. Diagnoses of complete left vocal cord paralysis and oropharyngeal dysphagia were made, and a CT of the neck was obtained for further evaluation of the patient's presenting symptoms.

CT imaging revealed a left posterior fossa mass and the patient was referred to neurosurgery. Subsequent magnetic resonance imaging demonstrated a well-defined, enhancing mass of the left skull base and posterior fossa with significant mass effect on the brainstem. There was associated lytic erosion of the clivus, left sphenoid sinus, petrous apex, and occipital condyle, extending into the left hypoglossal canal and jugular foramen (Figure 1).

Differential diagnoses included chondrosarcoma, schwannoma, chordoma, or other metastatic lesions. Indications for surgery included multiple cranial neuropathies, House-Brackman 2 facial droop, hearing loss, swallowing dysfunction, tongue deviation, hoarseness, and gait instability likely due to brainstem compression.

Therapeutic intervention

After discussing the risks and benefits with the patient and presenting the case to a multidisciplinary tumor board, surgery was offered to the patient. Due to the significant lateral extension, cranial nerve involvement, and bony invasion of the tumor, it was determined that a multistage approach would be most appropriate for this patient.

The patient underwent endoscopic endonasal transclival resection of the large clival chordoma guided by a Fujifilm/Hitachi side-firing pituitary guidance ultrasound transducer (Figure 2A) and neuronavigation. The goal of the initial endoscopic endonasal stage was to biopsy and resect the portion of the tumor medial to the hypoglossal canal to relieve pressure on the brainstem. The expanded endoscopic endonasal approach was considered a reasonable approach to resect the portion of the tumor medial to cranial nerves III, VI, and XII, and a second stage far-lateral approach was planned to resect the lateral extension of the tumor that was not accessible *via* the midline endoscopic endonasal approach (10–12). The risks, benefits, and alternatives were discussed with the patient, who wished to proceed. Prior to surgery, the patient developed House-Brackmann 2 left facial paralysis, left-sided hearing loss to finger rub, and difficulty walking.

Side-firing intraoperative ultrasound

The Fujifilm ultrasound probe is a single-use, side-firing linear array transducer with a 60° trapezoidal scanning window and a maximum diameter of 2.87 mm, ideal for endonasal surgical approaches. The scanning window is tilted as the surgeon rotates the probe, and images are acquired perpendicular to the probe axis. This capability allows the surgeon to sweep through the surrounding anatomy with minimal manipulation of the probe and creates a large field of view that is particularly useful when

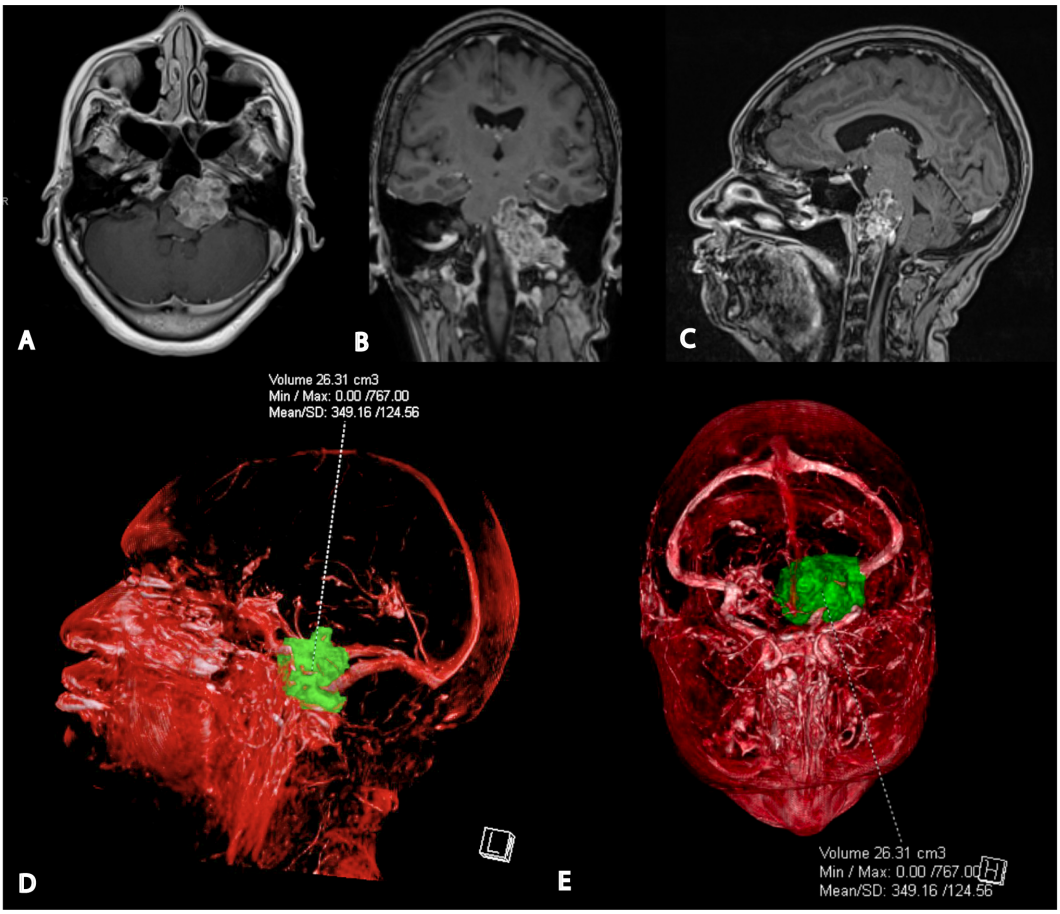

FIGURE 1
Preoperative magnetic resonance imaging and 3D tumor segmentation. **(A)** Axial T1-weighted post-gadolinium MRI shows the tumor's proximity to the left vertebral artery, proximal basilar artery, and internal carotid artery. **(B)** Coronal T1-weighted post-gadolinium MRI indicates the involvement of the left occipital condyle, jugular foramen, and hypoglossal canal. **(C)** Sagittal post-gadolinium T1 weighted MRI demonstrating significant mass effect on pons and medulla. **(D)** Lateral view of the 3D segmented tumor volume from the patient's left side. **(E)** Superior view of the 3D segmented tumor volume.

working in the narrow surgical corridor of endoscopic endonasal surgery.

The detection depth of the side-firing IOUS probe is adjustable; in our experience, images are easily obtained 1-2cm from the probe's tip. Longer trajectories may be possible with fine adjustments to gain and detection depth. Color flow imaging enables the surgeon to quickly assess the proximity of vital structures, such as the vertebrobasilar complex, in real-time (Figure 2). Smaller arterial branches, such as the anterior cerebral artery, anterior communicating artery, and meningohypophyseal trunk, can also be identified. IOUS was used throughout the case to estimate the extent of resection and the location of residual tumor (Figure 3).

Clival chordomas are often well-circumscribed lesions that do not require adjunctive intraoperative imaging. The expanded endoscopic endonasal approach allows for greater surgical maneuverability and direct tumor visualization. Therefore, IOUS guidance is not always necessary for a safe and complete resection. However, in some cases, particularly large and invasive chordomas such as this, we consider the side-firing IOUS a helpful adjunct because it allows the surgeon to assess the proximity of nearby critical structures, particularly those that may be encased in tumor tissue (Supplementary Video).

Effective use of IOUS requires a thorough understanding of skull base anatomy, and there is an initial learning curve. In our experience, identifying vasculature using doppler is the best place to begin learning. Next, the surgeon can proceed to more easily identified structures, such as the pituitary gland and the diaphragma sellae, before progressing to more complex tumors.

Surgical approach

Otolaryngology performed the initial steps of the expanded endoscopic endonasal surgery by harvesting a right pedicled nasoseptal flap which was temporarily placed inferiorly into the nasopharynx for later closure. A bilateral sphenoidotomy, left ethmoidectomy, and left maxillary mega antrostomy were performed with additional bone removal from the

10.3389/fonc.2023.1039159

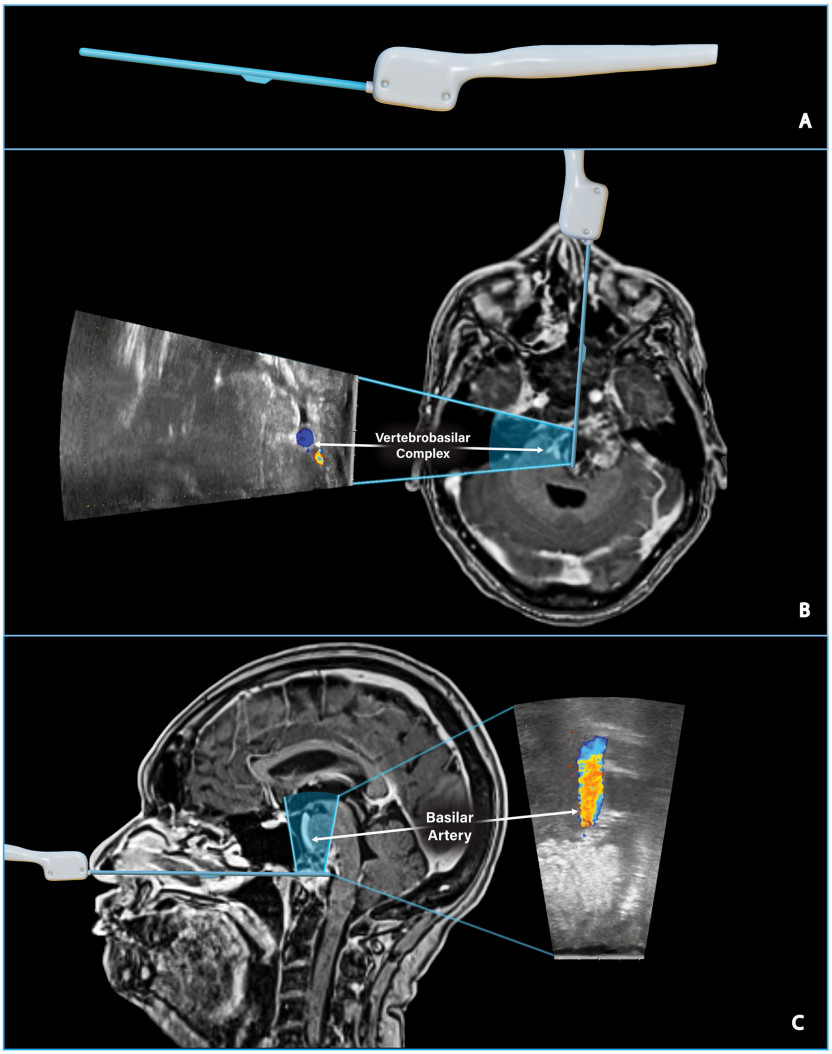

FIGURE 2
Assessing the location of critical vascular structures. **(A)** Digitally sculpted side-firing ultrasound transducer model. **(B)** Preoperative T1 post-gadolinium MRI and ultrasound model illustrate the side-firing ultrasound scanning window in an axial plane. The ultrasound image taken intraoperatively shows the left and right vertebral arteries just proximal to the vertebrobasilar junction. The IOUS image can be directly compared to the location of the vertebrobasilar junction on preoperative MRI. **(C)** Preoperative T1 post-gadolinium MRI and ultrasound model illustrate the side-firing ultrasound scanning window in a sagittal plane. IOUS image confirms hyperechoic tumor tissue directly above the ultrasound probe and the nearby basilar artery as seen on preoperative MRI.

posterior wall of the maxillary sinus to allow wide access to the pterygopalatine fossa.

After entering the sphenoid sinus, the procedure was turned over to neurosurgery. The sphenoidotomy was widened, and the pterygoid wedge was drilled until access lateral and inferior to the left carotid was obtained. Given the tumor's inferior and left lateral extension, this wide exposure was necessary to increase surgical maneuverability.

The tumor was exposed from its superior to inferior limit and as far laterally as possible, approximately 4 cm lateral of the midline. The thick tumor capsule was opened with Kerrison rongeurs, and the tumor was resected using a two-suction technique. Curved suction was utilized to reach further laterally and inferiorly, while IOUS and neuronavigation were used to guide resection and avoid vascular injury. Resection continued until the presence of mobile tissue suggested we had reached the posterior wall of the tumor capsule. IOUS was used to confirm that resection had reached the tumor capsule's posterior wall and verified the location of the vertebrobasilar complex (Figure 2).

After resecting the bulk of the tumor and reaching the lateral limit of safe dissection, IOUS was used to inspect the paraclival region once more before completing the case. Based on the real-time ultrasound imaging, it was determined that a complete resection had been performed superiorly and to the right. However, there was residual tumor extending to the left side, beyond the reach of the expanded endoscopic endonasal approach (Figure 3). Residual tumor was anticipated as part of the preoperative plan and discussed with the patient. Postoperative imaging was consistent with the findings observed on IOUS and confirmed that the central area of the mass was resected entirely, while some residual tumor remained lateral to the hypoglossal canal (the lateral limit of the endoscopic endonasal approach) (Figure 4). A diagnosis of chordoma was confirmed on pathology.

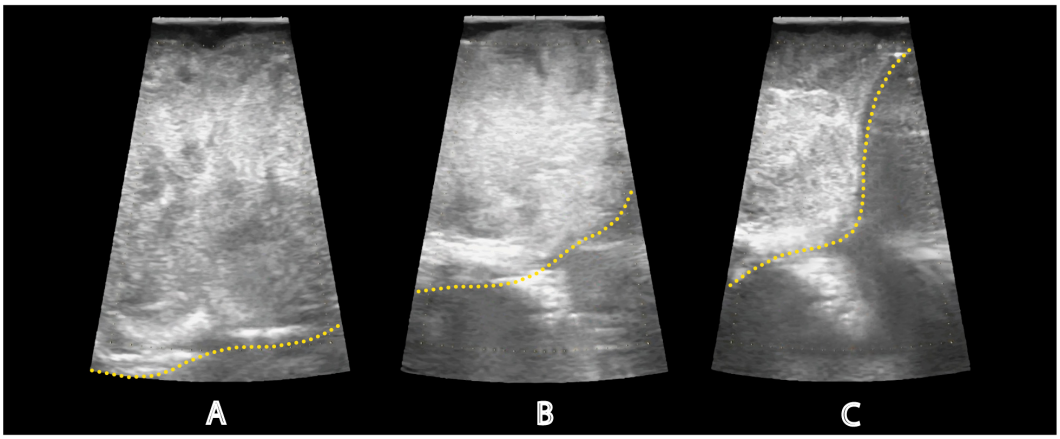

FIGURE 3
Assessing the extent of tumor resection. Intraoperative ultrasound images show the progressive reduction of remaining tumor tissue throughout resection. The probe is located in the lower clival region and directed toward the patient's left side. The yellow dotted line denotes the shifting tumor margin. **(A)** IOUS from the beginning of resection showed a large amount of tumor tissue. IOUS images were taken after twenty **(B)** and forty-five **(C)** minutes to assess the extent of resection. IOUS at the end of resection revealed a significant reduction in tumor volume; however, residual tumor was noted laterally and could not be reached endoscopically. The doppler channel was removed in these images for clarity.

Histopathological features and immunohistochemistry

Morphologically, the tumor was arranged into lobules separated by fibrous septae. The cytoarchitecture between the lobules showed cells forming cords, epitheloid sheets or single cells admixed within a myxoid matrix. Physaliphorous cells were abundant in the cords and showed clear/eosinophilic cytoplasm with vacuolated-bubbly appearance. Prominent nuclei or mitotic figures were scarce. The immunohistochemical study showed that tumor cells were positive for cytokeratin AE1/AE3, S-100 and INI-1 (Figures 4D–G).

Follow-up and outcomes

Following surgery, the patient was transferred to the intensive care unit, where she was closely monitored. Her pain was well controlled and there were no postoperative complications. The postoperative MRI revealed expected post-surgical changes, with residual tumor remaining lateral to the hypoglossal canal (Figure 4).

The patient was accompanied by her family to the one-month follow-up appointment, where the chordoma diagnosis was discussed, and the family expressed concern about the possibility of recurrence after surgery. Her case was presented again at the multidisciplinary tumor board meeting the following week, and the patient's family was informed of the plan for the second stage far-lateral craniotomy. A subsequent preoperative MRI showed tumor progression and invasion of the previously clear resection bed.

Postoperative imaging demonstrated significant improvements following the completion of the far-lateral craniotomy. After surgery, the patient recovered well, and her family reported that she is alert, walking more, and her swallowing dysfunction has improved. She is currently undergoing proton beam radiotherapy for adjuvant treatment of residual tumor.

Discussion

Side-firing ultrasound probes allow detection of tumor beyond the field of view during an endoscopic endonasal approach. The enhanced detection ability facilitates the identification of associated vasculature and potential residual tumor, particularly the lateral aspects of the tumor located behind the carotid arteries. Typically, clival chordomas are associated with non-variable anatomical landmarks, and intraoperative imaging may not be necessary for resection. In this case, an expanded endoscopic endonasal approach was performed for widened direct access and visualization of the tumor. Despite the widened surgical corridor of this approach, IOUS guidance was beneficial due to the close association and encasement of nearby critical structures such as the vertebrobasilar complex, lower cranial nerves, and dura.

The use of side-firing IOUS enables careful identification of critical structures encased in tumor tissue before proceeding with resection. CSF leaks, for example, can be caused by damage to the dura, which is often closely associated with the tumor capsule. In cases such as this, IOUS is advantageous because it can be used quickly and repeatedly throughout the surgery to avoid harm to critical structures while not extending the overall duration of the surgery.

While this report demonstrates the benefits of a side-firing US probe for transclival resection of a clival chordoma, end-firing probes may be more appropriate in some circumstances, such as resection of pituitary microadenomas (13–15). However, within the narrow surgical corridor, significant manipulation is required to obtain images of the surrounding paraclival region, limiting the utility of end-firing probes to depth estimation (9).

There are limitations to using IOUS in endoscopic endonasal surgery. Some neurosurgeons have little operating-room experience with ultrasound and must undergo IOUS training, which takes time and practice to develop confidence while interpreting US images intraoperatively (16, 17). The US machine takes up space in the

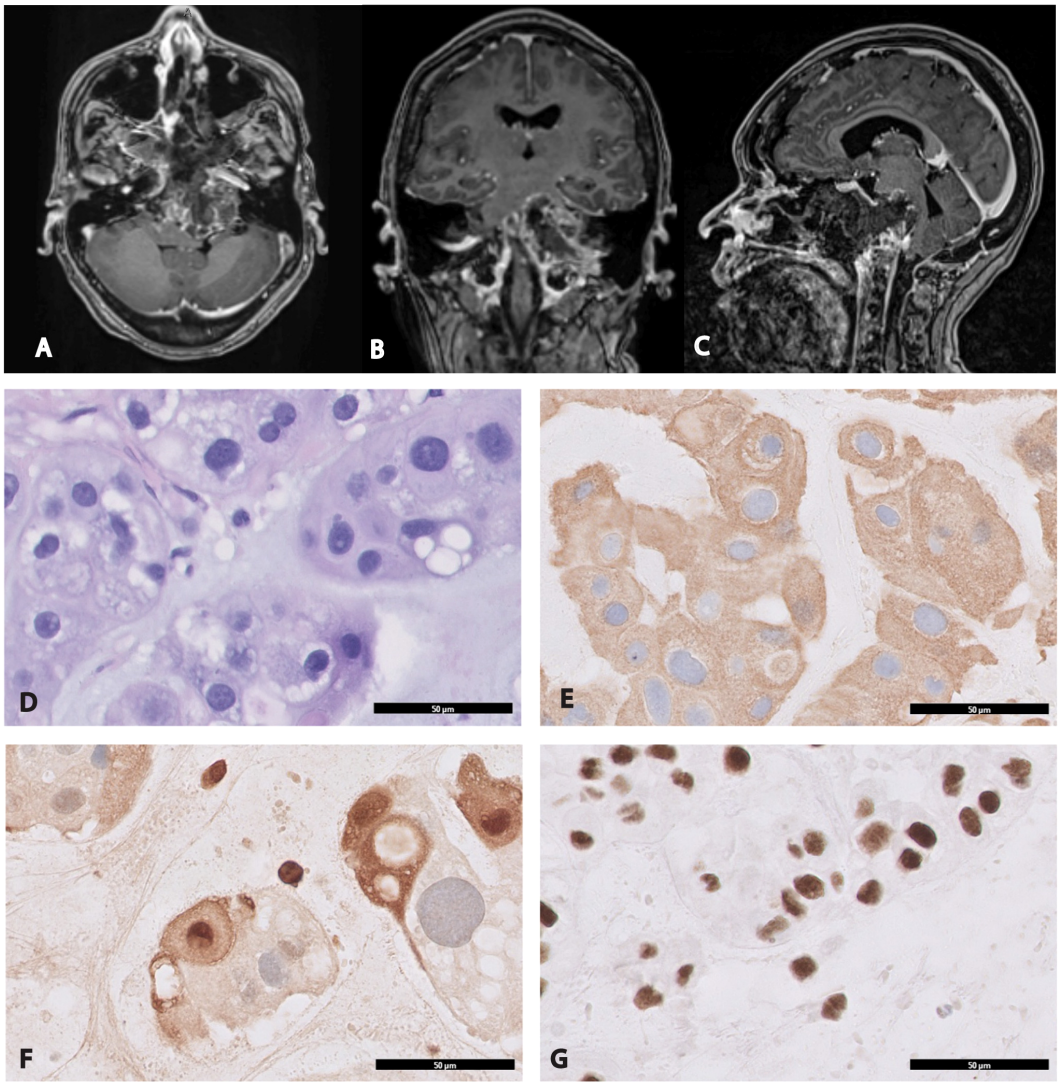

FIGURE 4
Postoperative magnetic resonance imaging and histological examination of chordoma. Immediate postoperative imaging confirmed the presence of residual neoplastic tissue that was detected on intraoperative ultrasound (Figure 3). The residual tumor is located primarily around the left occipital condyle and left petrous canal beyond the reach of the endoscopic endonasal approach. **(A)** Axial T1-weighted post-gadolinium MRI. **(B)** Coronal T1-weighted post-gadolinium MRI. **(C)** Sagittal T1-weighted post-gadolinium MRI. **(D)** H&E stain cytologically atypical cells of chordoma characterized by clear/vacuolated cytoplasm arranged in cords and sheets, x400. Immunohistochemical evaluation demonstrates that the tumor cells are strongly positive for **(E)** cytokeratin AE1/AE3, x400 **(F)** S-100, x400 and **(G)** INI-1, x400.

operating room and may require the repositioning of other equipment and changes to the workflow; however, the IOUS machine takes up far less space than iCT or iMRI machines. Another disadvantage of using IOUS is the cost of the probe, the IOUS machine, and the training (16).

Side-firing IOUS can serve as a helpful adjunct to endoscopic resection of large paraclival lesions by enhancing tumor identification and confirming the location of nearby structures vulnerable to injury. In the resection of pituitary adenomas, side-firing ultrasound has been shown to be safe and associated with reduced operative time (8, 18, 19). We previously performed a larger-scale case-control analysis demonstrating the utility of side-firing IOUS in the resection of pituitary macroadenomas (8). IOUS may improve understanding of intraoperative normal and tumor anatomy, allowing the surgeon to make more confident surgical decisions. The surgeon can employ the IOUS probe before proceeding with resection to confirm surgical orientation and the location of critical structures. Before completion of the procedure, the probe may be used to verify that all tumor has been resected.

Conclusion

Clival chordomas are relatively rare, aggressive tumors that tend to recur after surgical resection. Gross total resection is associated with improved progression-free survival. Therefore, intraoperative image guidance may enhance tumor resection while helping avoid injury to critical structures, particularly in the case of large complex

chordomas such as this. The use of IOUS as an adjunct to surgical resection of these lesions is safe, fast, and allows the surgeon to identify tumor outside of the working area or hidden behind other structures such as the carotid artery.

Patient perspective

From the patient's perspective, she is pleased with the overall outcome and felt happy that she had no worsening cranial nerve deficits following surgery. Although she and her family were initially nervous about the diagnosis of chordoma, they have remained positive, and the patient is amenable to further procedures or radiation if necessary. Her only complaint was that she did not enjoy remaining intubated for one day following her second surgery. Her quality of life has improved, and she is currently undergoing proton beam radiotherapy with the support of her family.

Data availability statement

The raw data supporting the conclusions of this article will be made available by the authors, without undue reservation.

Ethics statement

Written informed consent was obtained from the individual(s) for the publication of any potentially identifiable images or data included in this article.

Author contributions

KB drafted the manuscript, created the ultrasound model, and prepared operative video, figures and figure legends. CT approved radiological images, provided guidance, created 3D reconstructions of preoperative imaging. AR provided writing assistance and direction. ZK provided pathology images and descriptions. SS collaborated with MZ to perform the endoscopic endonasal surgery. MZ provided care to the patient, collected intraoperative ultrasound images, and provided important critical feedback on intellectual content. All authors contributed to the article and approved the submitted version.

Funding

This work was supported by research grants from Fujifilm and from the Mississippi Center for Translational and Clinical Research (U54GM115428).

Acknowledgments

The authors would like to thank Gary Randall Sanders of the Department of Radiology for processing and creating the 3D tumor reconstruction images included in this case report. We also thank Dr. Jose Otero for kindly facilitating the histopathological analysis by introducing us to Dr. Zeynep T. Kumm.

Conflict of interest

MZ owns stock in Exelixis and Zinnia Healthcare, for whom he has also consulted. He has participated in prior research projects that were supported by BK Medical. He also has research support from the University of Mississippi Medical Center for clinical and translational research.

The remaining authors declare that the research was conducted in the absence of any commercial or financial relationships that could be constructed as a potential conflict of interest.

Publisher's note

Supplementary material

The Supplementary Material for this article can be found online at: https://www.frontiersin.org/articles/10.3389/fonc.2023.1039159/full#supplementary-material

References

1. Bai J, Li M, Shi J, Jing L, Zhai Y, Zhang S, et al. Mid-term follow-up surgical results in 284 cases of clival chordomas: The risk factors for outcome and tumor recurrence. *Neurosurg Rev* (2021) 45(2):1451–62. doi: 10.1007/s10143-021-01576-4

2. Gulsuna B, Karaaslan B, Kaymaz M, Emmez H, Cindil E, Sahin MM, et al. Intraoperative magnetic resonance imaging assisted endoscopic endonasal resection of clival chordomas. *Front Oncol* (2022) 11:733088. doi: 10.3389/fonc.2021.733088

3. Vitaz TW, Inkabi KE, Carrubba CJ. Intraoperative MRI for transphenoidal procedures: Short-term outcome for 100 consecutive cases. *Clin Neurol Neurosurg* (2011) 113(9):731–5. doi: 10.1016/j.clineuro.2011.07.025

4. Buchfelder M, Schlaffer SM, Zhao Y. The optimal surgical techniques for pituitary tumors. *Best Pract Res Clin Endocrinol Metab* (2019) 33(2):101299. doi: 10.1016/j.beem.2019.101299

5. Buchfelder M, Schlaffer S-M. Intraoperative magnetic resonance imaging for pituitary adenomas. *Imaging Endocr Disord* (2016) 45:121–32. doi: 10.1159/000442328

6. Mortini P, Albano L, Barzaghi LR, Losa M. Pituitary surgery. *La Presse Médicale* (2021) 50(4):104079. doi: 10.1016/j.lpm.2021.104079

7. Giurintano JP, Gurrola J, Theodosopoulos PV, El-Sayed IH. Use of ultrasound for navigating the internal carotid artery in revision endoscopic endonasal skull base surgery. *Cureus* (2021) 13(2):e13547. doi: 10.7759/cureus.13547

8. Baker KE, Robbins AC, Wasson RG, McCandless MG, Lirette ST, Kimball RJ, et al. Side-firing intraoperative ultrasound applied to resection of pituitary macroadenomas and giant adenomas: A single-center retrospective case-control study. *Front Oncol* (2022) 12:1043697. doi: 10.3389/fonc.2022.1043697

9. Zachariah MA, Robbins A, Geisler R, Martinez-Perez R, Prevedello DM. Endoscopic endonasal resection of clival chordoma assisted by a novel minimally invasive ultrasound technology: 2-dimensional operative video. *Oper Neurosurg* (2022) 23(3). doi: 10.1227/ons.0000000000000279

10. Kassam AB, Gardner P, Snyderman C, Mintz A, Carrau R. Expanded endonasal approach: fully endoscopic, completely transnasal approach to the middle third of the clivus, petrous bone, middle cranial fossa, and infratemporal fossa. *Neurosurg Focus* (2005) 19(1):1–10. doi: 10.3171/foc.2005.19.1.7

11. Kassam A, Snyderman CH, Mintz A, Gardner P, Carrau RL. Expanded endonasal approach: The rostrocaudal axis. part II. posterior clinoids to the foramen magnum. *Neurosurg Focus* (2005) 19(1):1–7. doi: 10.3171/foc.2005.19.1.5

12. Vaz-Guimaraes Filho F, Wang EW, Snyderman CH, Gardner PA, Fernandez-Miranda JC. Endoscopic endonasal "far-medial" transclival approach: Surgical anatomy and technique. *Oper Tech Otolaryngology-Head Neck Surg* (2013) 24 (4):222–8. doi: 10.1016/j.otot.2013.09.003

13. Knappe UJ, Engelbach M, Konz K, Lakomek H-J, Saeger W, Schönmayr R, et al. Ultrasound-assisted microsurgery for Cushing's disease. *Exp Clin Endocrinol Diabetes* (2011) 119(4):191–200. doi: 10.1055/s-0029-1241207

14. Ram Z, Shawker TH, Bradford MH, Doppman JL, Oldfield EH. Intraoperative ultrasound-directed resection of pituitary tumors. *J Neurosurg* (1995) 83(2):225–30. doi: 10.3171/jns.1995.83.2.0225

15. Watson JC, Shawker TH, Nieman LK, DeVroom HL, Doppman JL, Oldfield EH. Localization of pituitary adenomas by using intraoperative ultrasoound pituitary in patients with cushing's disease and no demonstrable tumor on magnetic resonance imaging. *J Neurosurg* (1998) 89(6):927–32. doi: 10.3171/jns.1998.89.6.0927

16. Walker TLJ, Bamford R, Finch-Jones M. Intraoperative ultrasound for the colorectal surgeon: Current trends and barriers. *ANZ J Surg* (2017) 87(9):671–6. doi: 10.1111/ans.14124

17. Kaale AJ, Rutabasibwa N, Mchome LL, Lillehei KO, Honce JM, Kahamba J, et al. The use of intraoperative neurosurgical ultrasound for surgical navigation in low- and middle-income countries: The initial experience in Tanzania. *J Neurosurg* (2020) 134 (2):630–7. doi: 10.3171/2019.12.JNS192851

18. Alshareef M, Lowe S, Park Y, Frankel B. Utility of intraoperative ultrasonography for resection of pituitary adenomas: A comparative retrospective study. *Acta Neurochirurgica* (2021) 163(6):1725–34. doi: 10.1007/s00701-020-04674-2

19. Domino JS, Gattozzi DA, Jack M, Carroll M, Harn N, Beahm DD, et al. Outcomes of intraoperative ultrasound for endoscopic endonasal transsphenoidal pituitary surgery in adenomas with parasellar extension. *Interdiscip Neurosurg* (2021) 25:101225. doi: 10.1016/j.inat.2021.101225

frontiers | Frontiers in Oncology

TYPE Original Research
PUBLISHED 02 March 2023
DOI 10.3389/fonc.2023.1133074

OPEN ACCESS

EDITED BY
Sergio García,
Hospital Universitario Río Hortega, Spain

REVIEWED BY
Jose Juan Gonzalez,
Barcelona Clinic, Spain
Wolfgang Draxinger,
University of Lübeck, Germany

*CORRESPONDENCE
Ksenia A. Achkasova
achkasova.k@bk.ru

SPECIALTY SECTION
This article was submitted to Neuro-Oncology and Neurosurgical Oncology, a section of the journal Frontiers in Oncology

RECEIVED 28 December 2022
ACCEPTED 27 January 2023
PUBLISHED 02 March 2023

CITATION
Achkasova KA, Moiseev AA, Yashin KS, Kiseleva EB, Bederina EL, Loginova MM, Medyanik IA, Gelikonov GV, Zagaynova EV and Gladkova ND (2023) Nondestructive label-free detection of peritumoral white matter damage using cross-polarization optical coherence tomography. *Front. Oncol.* 13:1133074. doi: 10.3389/fonc.2023.1133074

Nondestructive label-free detection of peritumoral white matter damage using cross-polarization optical coherence tomography

Ksenia A. Achkasova[1*], Alexander A. Moiseev[2], Konstantin S. Yashin[3], Elena B. Kiseleva[1], Evgenia L. Bederina[4], Maria M. Loginova[1], Igor A. Medyanik[3], Grigory V. Gelikonov[2], Elena V. Zagaynova[1,5] and Natalia D. Gladkova[1]

[1]Research institute of experimental oncology and biomedical technologies, Privolzhsky Research Medical University, Nizhny Novgorod, Russia, [2]Laboratory of Highly Sensitive Optical Measurements, Institute of Applied Physics of Russian Academy of Sciences, Nizhny Novgorod, Russia, [3]Department of oncology and neurosurgery, University clinic, Privolzhsky Research Medical University, Nizhny Novgorod, Russia, [4]Department of pathology, University clinic, Privolzhsky Research Medical University, Nizhny Novgorod, Russia, [5]Lobachevsky State University, Nizhny Novgorod, Russia

Introduction: To improve the quality of brain tumor resections, it is important to differentiate zones with myelinated fibers destruction from tumor tissue and normal white matter. Optical coherence tomography (OCT) is a promising tool for brain tissue visualization and in the present study, we demonstrate the ability of cross-polarization (CP) OCT to detect damaged white matter and differentiate it from normal and tumor tissues.

Materials and methods: The study was performed on 215 samples of brain tissue obtained from 57 patients with brain tumors. The analysis of the obtained OCT data included three stages: 1) visual analysis of structural OCT images; 2) quantitative assessment based on attenuation coefficients estimation in co- and cross-polarizations; 3) building of color-coded maps with subsequent visual analysis. The defining characteristics of structural CP OCT images and color-coded maps were determined for each studied tissue type, and then two classification tests were passed by 8 blinded respondents after a training.

Results: Visual assessment of structural CP OCT images allows detecting white matter areas with damaged myelinated fibers and differentiate them from normal white matter and tumor tissue. Attenuation coefficients also allow distinguishing all studied brain tissue types, while it was found that damage to myelinated fibers leads to a statistically significant decrease in the values of attenuation coefficients compared to normal white matter. Nevertheless, the use of color-coded optical maps looks more promising as it combines the objectivity of optical coefficient

and clarity of the visual assessment, which leads to the increase of the diagnostic accuracy of the method compared to visual analysis of structural OCT images.

Conclusions: Alteration of myelinated fibers causes changes in the scattering properties of the white matter, which gets reflected in the nature of the received CP OCT signal. Visual assessment of structural CP OCT images and color-coded maps allows differentiating studied tissue types from each other, while usage of color-coded maps demonstrates higher diagnostic accuracy values in comparison with structural images (F-score = 0.85-0.86 and 0.81, respectively). Thus, the results of the study confirm the potential of using OCT as a neuronavigation tool during resections of brain tumors.

KEYWORDS

optical coherence tomography, peritumoral white matter, myelin, brain tumor, neurosurgery, attenuation coefficient

1 Introduction

Malignant tumors are recognized to be the second leading cause of human deaths around the world with more than 250 000 deaths caused by brain tumors annually (1). The most common neoplasms of the brain are malignant gliomas developing from neuroglial cells (astrocytes, oligodendrocytes) (2). The main paradigm for treating patients with brain gliomas remains achieving the maximum possible life expectancy while at the same time maintaining its high quality.

Despite the improvements in the diagnosis and treatment of brain neoplasms, however, tumor development often leads to the onset of neurological deficit, which is primarily associated with its infiltrative growth into the surrounding white matter. The invasion of tumor cells into the white matter leads to morphological and functional changes in myelinated fibers in the peritumoral region, resulting in a violation of the nerve impulse conduction (3, 4). Moreover, different treatment options may also cause various pathological changes in brain tissues. For example, accidental damage to the healthy white matter pathways may occur during tumor resection due to the absence of a method allowing performing intraoperative assessment of white matter morphological features in the peritumoral area (5).

In view of the leading role of the white matter in organizing the integral functionality of the brain and its low degree of plasticity (that is, the low ability to recover) in comparison with the cerebral cortex, the study of its morphological and functional changes in glial brain tumors and their treatment is an important scientific and practical task. The ability to intraoperatively determine and predict the degree of damage to the white matter can increase the quality of tumor resections, allow more accurate choice of chemo- and radiotherapy treatment regimens and development of drugs to protect the brain during combined treatment.

Diffusion-tensor MRI (DT-MRI) is currently the only method for *in vivo* evaluation of the state of the brain pathways, which can qualitatively assess the relative position of the tumor and fiber tracts and quantitatively evaluate orientation and preservation of the nerve pathways (6, 7). In case of the glial tumor surgery, DT-MRI imaging allows the surgeon to select a surgical approach to the tumor focus, bypassing healthy pathways (8). However, the limitation of this method is its insufficient resolution and the impossibility of intraoperative use for analyzing the white matter structure in the exact region of interest due to possible discrepancies between MRI images and real situation caused by displacement of brain structures as a result of intracranial pressure during tumor resection (known as “brain shift”) (9).

Several intraoperative imaging techniques are available at present to visualize tumor tissue by detecting its typical features (10, 11), however they do not make it possible to intraoperatively detect the damage of the white matter in the peritumoral region. Carrying out neurosurgical intervention using only these methods may lead, on the one side, to damage of the healthy brain tissues and on the other side, to leaving areas with destroyed nerve fibers. The persistence of these non-viable areas, abundantly infiltrated with tumor cells, is likely to lead to early tumor recurrence. Therefore, all the abovementioned emphasizes the need for developing new methods of intraoperative imaging of brain tissues being able to address current demands.

Optical coherence tomography (OCT) is a rapidly developing, minimally invasive, label-free method for real time visualizing the structure of biological tissues with a resolution up to a few micrometers at a depth up to 1.5 mm (12). Currently, OCT occupies a leading place in the clinical practice among optical diagnostic methods due to its high resolution, high speed of obtaining and evaluating images, as well as the availability of several modalities. Several studies have shown the promise of using OCT to differentiate between normal and tumorous white matter with high diagnostic accuracy (13, 14). Targeted visualization of white matter, including individual myelinated fibers, is possible with the use of special functional extensions of OCT - polarization-sensitive OCT (PS OCT) (15) and cross-polarization OCT (CP OCT) (13), sensitive to the phenomenon of light birefringence in tissues which allows obtaining high-quality information about the presence of elongated structures (myelinated fibers).

Identifying scattering, and, accordingly, morphological, features of biological tissues using the OCT method is based on two main approaches to the analysis of OCT images: qualitative (visual) and quantitative (16–18). Qualitative approach is based on visual analysis of structural two-dimensional OCT images, which is considered subjective. However, this method is still the only one available for use in clinical practice in several countries (19). The quantitative approach to the analysis of OCT images is based on the calculation of optical coefficients, where the attenuation coefficient is frequently used for this purpose (14, 16, 20). This method allows objectifying the obtained data, which leads to a decrease in the influence of the "human factor" on the interpretation of the results. The use of color-coded maps that display the distribution of coefficient values throughout the image allows one to combine the advantages of both approaches, namely, the clarity of the visual method and the objectivity of the quantitative one.

In the present work, for the first time we study the scattering properties of peritumoral white matter, characterized by the destruction of myelinated fibers, and determine the diagnostic ability of CP OCT to differentiate three brain tissue types in the peritumoral area (white matter, damaged white matter and tumor) based on the qualitative and quantitative processing of OCT images.

2 Materials and methods

2.1 Ex vivo studies of the human brain specimens

The study was carried out on *ex vivo* samples of brain tissue obtained during tumor resection from 57 patients with brain neoplasms aged from 36 to 60 including 52 patients with gliomas of different degrees of malignancy (astrocytoma Grade I-II (n = 18), astrocytoma Grade III (n = 15), glioblastoma Grade IV (n = 19)) and 5 patients with brain metastasis of extracerebral tumors (see Table 1). A surgical approach to tumor node was carried out in accordance with the plan of surgical intervention without any changes due to sample collection. During access to the tumor node, white matter that is usually exposed to resection or coagulation during surgery was removed. Tissue sampling included two main stages: at the first stage, samples of normal white matter were obtained, as far as possible from the tumor; at the second stage, white matter sampling was carried out at the direct adjacency to the tumor node. In addition, samples from tumor core were collected. In several cases it was possible to obtain samples that included both tumor and peritumoral white matter.

TABLE 1 The characteristics of patients included in the study.

Number of patients	57
Sex (male/female)	35/22
Age (average (min – max))	47 (36 – 60)
Tumor Grade (I-II/III/IV/metastasis)	18/15/19/5
Tumor localization (frontal lobe/parietal lobe/temporal lobe/occipital lobe)	31/14/27/6

Each sample was immediately placed in Petri dish, covered with cotton cloth moistened with saline solution, closed to prevent dehydration, put on ice and delivered to the location of CP OCT study, which took several minutes. To create a fresh flat surface, each sample was cut proximately before the CP OCT study. The CP OCT study was performed in a contactless mode when the sample was placed on a special motorized table under the OCT probe, which took 10-15 minutes for each sample. In total, 158 samples of normal and peritumoral white matter and 98 tumor samples were scanned; 930 CP OCT images of white matter and 400 images of tumor were obtained. One can consider each patient as a separate data point from the sample and sampling several images from each patient's data can be considered as a Kernel Density Estimation (KDE) which can provide an estimate of the density distribution of the attenuation coefficient from the limited number of measured data points (21). It is necessary to mention that during subsequent analysis of morphological features and CP OCT images of tumors we did not divide them into subgroups according to the Grade or "glioma/metastasis". All kinds of tumors were included into one group and analyzed altogether.

The study was approved by Institutional Review Board of Privolzhsky Research Medical University and informed consent was obtained from all patients. All the methods were performed in accordance with the relevant guidelines and regulations.

2.2 Histological analysis

After imaging, all of the samples were forwarded to histological study. The scanning area of each sample was marked with histological ink; the sample was fixed in 10% formalin for 48 hours. The ink mark was used as a guide for the subsequent match of the histological sections and en-face CP OCT images. Histological sections of tumors and white matter were stained with hematoxylin & eosin (H&E) to obtain general information about the sample. White matter samples were selected for further study, samples containing tumor or gray matter areas were excluded from this stage of the study. For targeted study of samples of white matter, sections were stained using Luxol fast blue with crezyl violet to identify myelinated fibers structure. With this staining, the preserved myelin sheath is stained bright blue, which makes it possible to assess the morphology of the fibers. Violation of the structure of myelin, which occurs due to various reasons, leads to the absence of staining of the fibers. All sections were studied by the pathologist using light microscopy and classified into three main tissue types: 1) normal white matter (numerous preserved densely packed myelinated fibers are visualized), n=41; 2) damaged white matter (loss of fiber staining is observed, ≥20% of fibers are damaged and infiltration of tumor cells is observed), n=76; 3) tumor, n=98.

2.3 CP OCT device

The study was performed with a spectral-domain CP OCT device (Institute of Applied Physics of Russian Academy of

Sciences, Nizhny Novgorod, Russia). The system has a common-path interferometric layout operating on 1310 nm central wavelength. CP characterizes the change in polarization state due to propagation in anisotropic media. The active polarization control system is based on the analysis of the polarization state of the light returned from the tip of the optical probe. The axial resolution is 10 μm and transverse resolution is 15 μm in air. The utilized device has a 20000 A-scans/s scanning rate and performs lateral scanning of 2,4x2,4 mm^2 (256x256 A-scans) area to obtain a backscattered light distribution in the polarization with the same and reversed rotations of the electric-field vector (22).

2.4 CP OCT data evaluation

Before analyzing the obtained OCT data, we selected artifact-free images (cropped and damaged images were excluded). As a result, the study included 576 white matter OCT images and 297 tumor OCT images.

The analysis of the obtained CP OCT data was carried out in three stages (Figure 1). At the first stage, a visual analysis of structural CP OCT images was performed to identify signal parameters distinctive for each studied tissue type. After that, a test was compiled, consisting of a training presentation and a set of 100 CP OCT images, offered to respondents for evaluation. The test was offered to 8 blinded researchers, including 4 researchers from the laboratory of optical coherence tomography who work daily with OCT images (Group 1) and 4 biomedical researchers with no previous experience in "reading" OCT images (Group 2). Based on the analyzed signal parameters, the respondents had to classify the images into one of three types of tissue and assign a number to each image based on the intended tissue type, where: 1 – normal white matter, 2 – damaged white matter, 3 – tumor. The first stage is described in detail in section 2.4.1. At the second stage, described in section 2.4.2.1, for each CP OCT image, the attenuation coefficients in co- and cross-polarizations were calculated with obtaining the median values of the coefficients for each image, followed by comparison between tissue types and correlation analysis of tissue types and attenuation coefficients values. The third stage described in section 2.4.2.2 included building color-coded maps of the distribution of attenuation coefficients values with subsequent visual analysis. This stage was carried out on the same arrays of CP OCT data as the first one. For each type of tissue, characteristic visual features of optical maps were identified in co- and cross polarizations. A second classification test was then compiled containing a training presentation, a set of 100 Att(co) maps and 100 Att(cross) maps. This test was also offered to the same groups of respondents. Based on the results of two tests, the level of inter-rater agreement in each group was identified using the Fleiss' kappa, and the level of diagnostic accuracy was calculated using the F-score

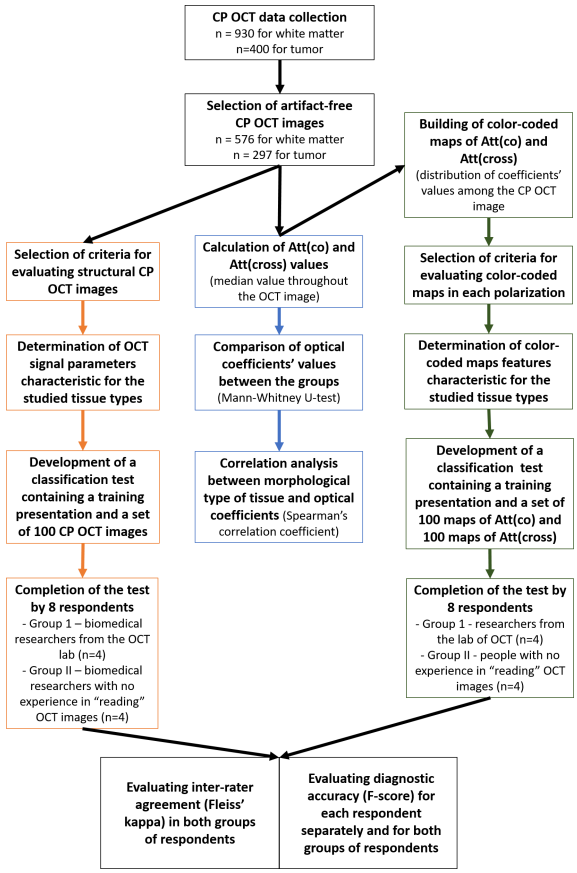

FIGURE 1
CP OCT study design.

parameter (for each respondent separately, as well as for both groups of respondents).

2.4.1 Qualitative analysis

A qualitative (visual) analysis of two-dimensional CP OCT images was carried out to study the nature of the OCT signal received from different types of tissue and to develop criteria for their differentiation. A structural CP OCT image consists of B-scans in co- (upper part of the image) and cross-polarizations (lower part of the image) stitched together. During visual assessment, we performed a complex analysis of OCT signal in both polarizations.

Based on the results of previous studies (23), we chose the following parameters for evaluating structural images and their subsequent classification:

1) OCT signal intensity (intense/non-intense) – characterizes OCT signal level throughout the image

2) OCT signal attenuation rate (low/high) - characterizes the degree of penetration of the probing radiation over the depth of the object

3) Uniformity of OCT signal attenuation (uniform/non-uniform) - characterizes the variability of the penetration depth of the probing radiation in different parts of the OCT image.

For each studied tissue type, distinctive OCT signal features were evaluated. Then, to determine the diagnostic ability of visual analysis of CP OCT images to differentiate between three types of tissue (normal white matter, damaged white matter and tumor), a special test was developed containing a training set of images demonstrating classification criteria (Supplementary Figure 1), typical images of each tissue type (Supplementary Figure 2) and the test itself of 100 images (30 images of normal white matter, 40 images of damaged white matter and 30 tumor images). For each image included in the test, three response options were indicated: “normal white matter”, “damaged white matter” and “tumor”. As it was mentioned above, the test was offered to 8 blinded researchers, divided into two groups.

2.4.2 Quantitative analysis

2.4.2.1 Calculation of the attenuation coefficient

To quantify the optical properties of brain tissue relying on OCT data, we used attenuation coefficients in co- (Att(co)) and cross-polarization (Att(cross)) modes. We expect that the additional usage of Att(cross) may provide us with more information about the morphological features of the white matter.

Depth-resolved approach was applied for the quantitative assessment of the OCT data in co-polarization. Such an approach was proposed in (24) under the assumption that the backscattering coefficient is proportional to the attenuation coefficient with the constant ratio between the two in the OCT depth range:

$$I_i \sim \alpha \cdot \mu_{att}(z_i) \cdot \exp[-2 \cdot \sum_{j=0}^{i} \mu_{att}(z_i) \cdot \Delta] \quad (1)$$

where I_i is the sum of OCT signal intensities in both polarization channels, μ_{att} is the specimen attenuation coefficient, $z_i$is the depth coordinate, Δ is the pixel size along the axial dimension.

In the present study, the method from (25) was adopted since it accounts for the noise with the non-zero mean, present in the distributions of the measured absolute values of the OCT images and allows to avoid systemic attenuation coefficient estimation bias, characteristic for the (24). According to (25), the depth-resolved attenuation coefficient can be written as:

$$\begin{aligned} \mu_i &= \frac{H_i \cdot SNR_i^{\mu}}{|H_i|^2 \cdot SNR_i^{\mu}+1} \cdot \mu_i^{est} \\ H_i &= 1 - \frac{\sum_{i+1}^{\infty} N_j}{\sum_{i+1}^{\infty} I_j + \sum_{i+1}^{i_{max}} N_j} = 1 - \frac{\langle N \rangle \cdot (i_{max} - i)}{\sum_{i+1}^{\infty} I_j + \sum_{i+1}^{i_{max}} N_j} \\ SNR_i^{\mu} &= \sum_{x_i, z_i \in W} \frac{|\mu_i^{est}|^2 - |N_i^{\mu}|^2}{|N_i^{\mu}|^2} \\ N_i^{\mu} &= \frac{N_i}{2\Delta \sum_{i+1}^{i_{max}} (I_j + N_j)} = \frac{\langle N \rangle}{2\Delta \sum_{i+1}^{i_{max}} (I_j + N_j)} \end{aligned} \quad (2)$$

where <N > is the amplitude of the noise floor, which can be estimated before the measurements, SNR_i^{μ} is the local signal-to-noise ratio (SNR) for the attenuation coefficient distribution, which is estimated by the averaging in the rectangular window with the side of W pixels. The W value should be sufficiently large (≥32 pixels) to provide sufficient statistics inside each window. The value (I_j+N_j) is simply the measured signal at the depth *j*. Thus, all the values from Eq. (2) can be measured from the cross-sectional OCT intensity distributions. According to (25), the confocality and the spectral roll-off for the OCT system used in the study will lead to the attenuation coefficient estimation error which will not exceed 10%, thus these factors were not considered in the present study.

To calculate Att(cross) values, the method of linear fitting of the logarithmic signal described in (14) was used because the differential equations describing signal propagation in co-polarization are not valid for the signal in cross-polarization, and, consequently, the method based on their solution cannot be directly applied to a signal in cross-polarization.

Both attenuation coefficients were estimated in the depth range of 120–300 μm. The choice of depths was determined by the construction of the most contrasting color-coded maps in this range, providing the best information about the morphology of brain tissue.

2.4.2.2 En-face color-coded map building

En-face color-coded maps were constructed based on the distribution of coefficients values for each OCT image in co- and cross-polarizations. Based on the range of the numerical values of the optical coefficients for the studied tissue types, a universal color scale was selected for maps in co- and cross-polarization, which allows differentiating brain tissues in the specified color range. Visual criteria for color-coded maps in both polarizations corresponding to the studied three types of tissue were determined, namely, the predominance of one or another color, the color variation in maps (Supplementary Figure 3). Then a special test was developed containing a training set and a set of 100 color-coded maps of each attenuation coefficient (30 maps of

normal white matter, 40 maps of damaged white matter and 30 maps of tumor). This test was also offered to two groups of blinded researchers mentioned above.

Although the selected rainbow colormap 'jet' is widely criticized for its poor performance, since small variations in the color green are not perceived as green is a common natural color, while small variations in the colors red and blue are perceived (26, 27), the difference between the attenuation coefficient values for the tumorous and normal tissues allows assigning colors of maximal contrast (i.e. red and blue) for the two classes of interest, which lead to the easy visual differentiation of these classes for the user.

2.4.3 Statistical analysis

Statistical analysis was performed using GraphPad Prism 8 and SPSS Statistics 26. According to the results of the test aimed at classifying OCT images according to visual criteria of B-scans and color-coded maps, we calculated the inter-rater agreement level and F-score. Inter-rater agreement was calculated using the Fleiss' kappa (k) coefficient: $k \geq 0.8$ – perfect agreement; $0.7 \geq k < 0.8$ – substantial agreement; $k<0.7$ – poor agreement. F-score represents the measure of a test's accuracy in case of a multiclass classification. Its values were interpreted in the following way: $f>0.9$ – excellent diagnostic accuracy, $0.8< f \leq 0.9$ – good, $0.5< f \leq 0.8$ – fair, $f<0.5$ – poor. To evaluate the results of quantitative image processing, we used the median value among all values of every optical coefficient calculated for each A-scan of 3D CP OCT image. The results are expressed as Me [Q1;Q3], where Me – is the median value of optical coefficient; Q1, Q3 – are the values of 25th and 75th percentiles, respectively. To compare optical coefficient values of different tissue types, we used the Mann-Whitney U-test with the hypothesis that there was no difference between the compared groups. To establish correlation level between optical coefficients values and studied brain tissue types we calculated the Spearman's correlation coefficient.

3 Results

3.1 Visual assessment of CP OCT images of normal white matter, damaged white matter and tumor tissue

This part of the study was devoted to the analysis of structural CP OCT images and determination of OCT signal parameters specific for studied tissue types. We found that the white matter on ex vivo CP OCT images is characterized by the following features: 1) high intensity of the OCT signal in both polarizations; 2) high attenuation rate of the OCT signal in both polarizations; 3) homogeneity of the attenuation of the OCT signal in both polarizations. The features of the OCT signal received from the tumor tissue are opposite, namely: 1) low intensity of the OCT signal in both polarizations; 2) low attenuation rate of the OCT signal in both polarizations; 3) inhomogeneity of the attenuation of the OCT signal in both polarizations. The variation in the scattering properties of normal and tumorous white matter tissues are due to differences in the structural characteristics of these types of tissues. The white matter contains a large number of myelinated fibers with highly scattering properties (Figure 2A). The tumor, on the other hand, contains mainly cellular elements, which results in a low attenuation of the probing radiation (Figure 2C). In the case of damaged white matter, the nature of the received OCT signal changes: there is a decrease in the signal intensity in both polarizations (while the signal in cross-polarization decreases more significantly) in comparison with healthy white matter (however, it remains higher than in the tumor), as well as a decrease in the signal attenuation rate in both polarizations (Figure 2D). In rare cases, signal attenuation inhomogeneity may be observed, however, such cases are an exception, and it is not clear which morphological features cause these changes of OCT signal. Histologically, damaged white matter is characterized by destruction of myelinated fibers while only individual preserved fibers can be visualized as well as infiltration of tumor cells (Figure 2C).

Thus, each of the three types of tissue has a unique combination of OCT signal characteristics, which indicates the validity of using visual analysis of CP OCT images to differentiate the studied tissues.

3.2 Quantitative assessment of CP OCT images of normal white matter, damaged white matter and tumor tissue

Quantitative processing of the OCT signal using attenuation coefficients further confirms differences between all the studied types of tissues with high accuracy (Tables 2, 3). Normal white matter is characterized by highest values of the coefficients in co- and cross-polarizations, while the scattering properties of the tumor tissue are significantly reduced. It was found that the destruction of myelinated fibers in the region of interest leads to deterioration in scattering properties, which is reflected in a decrease in the attenuation coefficients values in both polarizations compared to normal white matter. Thus, the white matter, characterized by the destruction of myelinated fibers in the study area, occupies an intermediate position between normal white matter and tumor tissue (Figure 3). At the same time, it is worth mentioning that, in contrast to normal white matter and a tumor, there is a greater variability of the values of both attenuation coefficients for damaged white matter, which is associated with morphological heterogeneity of samples, in particular, with a different amount of altered myelinated fibers in the studied area (Figure 4).

Correlation analysis performed using Spearman's rank correlation coefficient demonstrated statistically significant negative correlation between both attenuation coefficients and morphological types of brain tissue that were encoded as "1" – normal white matter, "2" – damaged white matter, "3" – tumor (Table 4). Thus, the lower values of attenuation coefficient correspond to more pathologically altered tissue state.

However, in view of the morphological heterogeneity of the studied samples, the usage of individual numerical value obtained from CP OCT image may be insufficient. Thereby, we decided to carry out visual analysis of color-coded maps, representing the optical coefficients' values distribution throughout the OCT image.

10.3389/fonc.2023.1133074

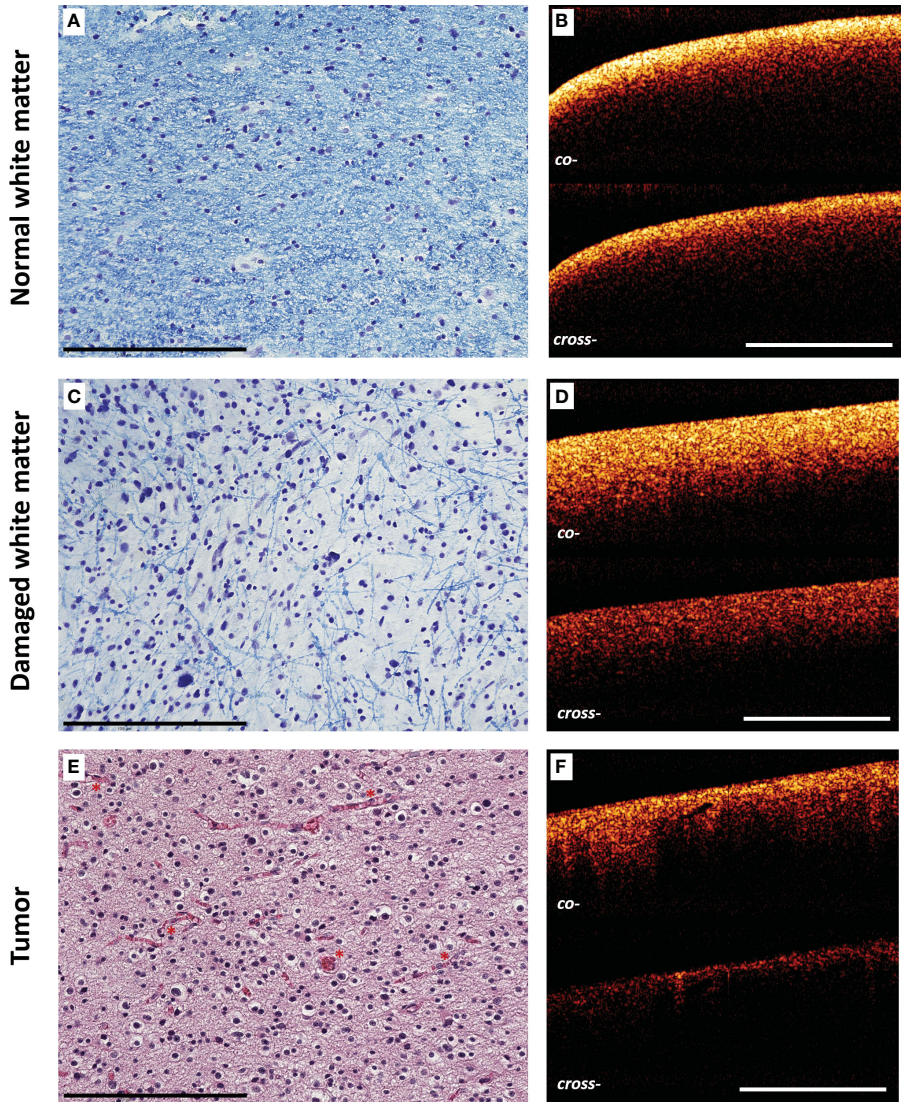

FIGURE 2
Comparison of morphological features of brain tissues and CP OCT signal. Histological images of normal **(A)** and damaged **(B)** white matter stained by Luxol fast blue, tumor tissue **(C)** (astrocytoma Grade III) stained by H&E and corresponding CP OCT images **(D–F)**, respectively. The destruction of myelinated fibers in peritumoral area is reflected in histological images (only individual preserved fibers are visualized in comparison with normal white matter) **(B)** and leads to the changes in CP OCT signal: slight reduction of the signal intensity and decrease in the attenuation rate in both polarizations **(E)**. Fundamentally different structural characteristics of the tumor, expressed in the predominance of cellular elements, the presence of a large number of blood vessels (marked by red asterisks), are reflected in a decrease in the intensity of the OCT signal in both polarizations and its heterogeneity **(F)**. Scale bar = 200 μm on histological image and 1 mm on OCT image.

TABLE 2 Comparison of the studied tissue types using Att(co) coefficient.

	Normal white matter (n=169) 10.3 [9.6; 10.9][a]	Damaged white matter (n=407) 9.2 [6.4; 10.7][a]	Tumor (n=297) 5.8 [4.6; 6.8][a]
Normal white matter	–	<0.0001	<0.0001
Damaged white matter	<0.0001	–	<0.0001
Tumor	<0.0001	<0.0001	–

p-values for the alternative hypothesis of the Mann-Whitney U-test about the presence of differences between the compared groups are indicated.
[a]Me [Q1;Q3] – where Me – median, Q1, Q3 – values of 25th and 75th percentiles, respectively.

TABLE 3 Comparison of the studied tissue types using Att(cross) coefficient.

	Normal white matter (n=169) 12.2 [11.6; 13.0][a]	Damaged white matter (n=407) 9.2 [6.0; 12.3][a]	Tumor (n=297) 5.3 [4.2; 6.8][a]
Normal white matter	–	<0.0001	<0.0001
Damaged white matter	<0.0001	–	<0.0001
Tumor	<0.0001	<0.0001	–

p-values for the alternative hypothesis of the Mann-Whitney U-test about the presence of differences between the compared groups are indicated.
[a]Me [Q1;Q3] – where Me – median, Q1, Q3 – values of 25th and 75th percentiles, respectively.

3.3 Application of color-coded optical maps for brain tissue type differentiation

Third stage of the study included visual analysis of color-coded maps representative for three studied tissue types. Optical maps allow to present data in a customizable color palette. In previous studies, optical maps were used to distinguish white matter and tumor where areas with high attenuation coefficients (normal white matter) were presented dominantly by bright hues (orange to deep red), while low optical coefficients (tumor) were rendered in cyan and blue (13). In the present work, for the first time we developed optical maps also representing damaged white matter. As Figures 5b2, b3 demonstrates, the destruction of myelinated fibers leads to the predominance of intermediate colors on optical maps, in particular, green and yellow. In addition, these maps are more heterogeneous, characterized by the presence of areas with high attenuation coefficients (areas with preserved myelin fibers) and zones with low values of these coefficients (total fiber destruction).

Thus, we distinguished the following characteristics of optical maps representing the distributions of co- and cross-polarization attenuation coefficients for three studied tissue types:

A) normal white matter (Figures 5a1–a3)

- Att(co): Total prevalence of dark red and orange. In rare cases: presence of yellow

- Att(cross): Total prevalence of dark red color

B) damaged white matter (Figures 5b1–b3)

- Att(co): The most heterogeneous group; prevalence of azure, green and yellow colors; possible presence of blue and red areas

- Att(cross): Multicolored maps; possible presence of all colors: red, yellow, green, azure, blue

C) tumor (Figures 5c1–c3)

- Att(co): Total prevalence of blue; in rare cases: presence of areas with higher values of Att(co): azure, green, yellow

- Att(cross): Total prevalence of blue color; in rare cases: presence of areas with higher values of Att(cross): azure, yellow, red

Importantly, in certain cases differentiation of areas of damaged white matter from both tumor and normal white matter is complicated due to overlap of attenuation coefficient values for differentiable tissue types. In particular, with a small amount of damaged myelin fibers in the study area, the values of the coefficients decrease moderately and are represented in yellow. At the same time, areas of normal white matter are also characterized by presence of yellow color in rare cases. Areas of total fiber destruction are characterized by the appearance of azure-blue hues, which can be confused with a tumor (Figures 5d1–d6).

3.4 The diagnostic ability of visual assessment of structural CP OCT images and color-coded maps to differentiate various tissue types in the peritumoral area

To assess the possibility of using CP OCT as a neuronavigation method during brain tumors resections we evaluated the level of diagnostic accuracy of visual analysis of structural CP OCT images and optical maps.

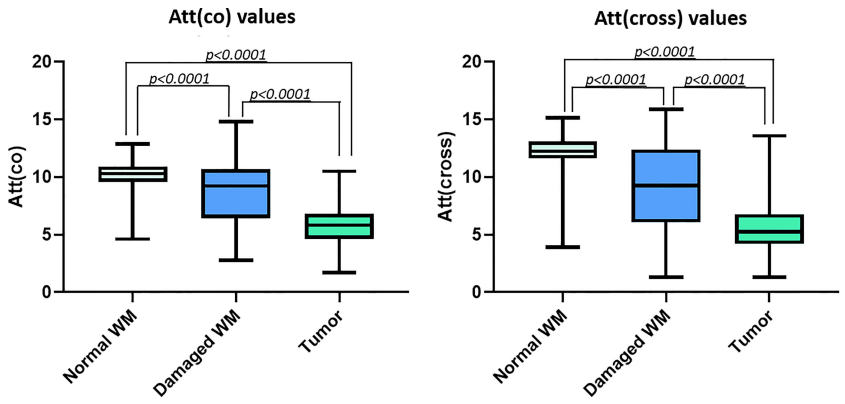

FIGURE 3
Distributions of Att(co) and Att(cross) values for the studied tissue types.

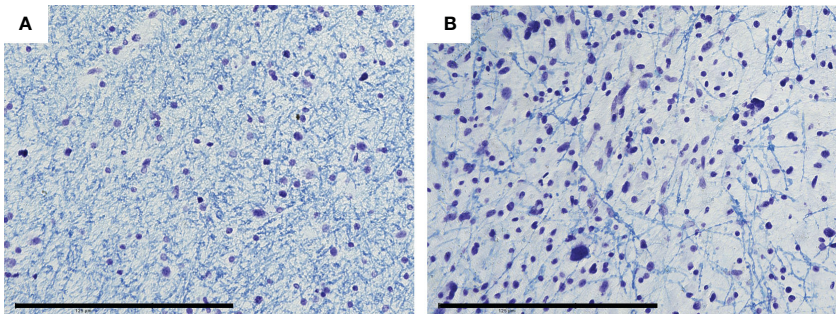

FIGURE 4
Morphological heterogeneity of damaged white matter is predominantly based on different amount of preserved myelinated fibers that varies from formed grid, which is sparser compared to areas of normal white matter **(A)** to areas with individual preserved fibers **(B)**. Scale bar = 200 μm.

Our study demonstrates that both approaches, visual assessment of CP OCT images as well as use of color-coded maps, allow researchers to differentiate three types of studied brain tissue from each other. The assessed inter-rater agreement revealed a higher level of agreement between all the respondents in the case of evaluation of color-coded maps (k = 0.79 and k = 0.77 for Att(co) and Att(cross) maps, respectively) compared to the analysis of B-scans (k=0.64). We suggest it is caused by greater clarity of the data presented in optical maps. In this case, the respondents had to analyze only presence and predominance of different colors (blue, azure, green, yellow, orange and red) in contrast to structural CP OCT images, where three parameters were needed to be assessed.

As mentioned above, the diagnostic accuracy of the image interpretation test was assessed using the F-score parameter due to three answer options being available in the test. Importantly, the F-score values obtained in the two groups of respondents did not differ significantly from each other (Figure 6A). This could be explained by high-quality training of the second group of respondents (biomedical researchers with no experience in working with OCT data) before passing the test. In this way, we suppose that with an adequate training visual analysis of structural CP OCT images and optical maps may be carried out by a researcher or a doctor without the additional help of an OCT specialist. In light of us not finding differences between the groups of respondents, further experiment in identifying differences in the diagnostic accuracy of the visual assessment of B-scans and optical maps was conducted on a combined group of respondents, which included all the specialist participants.

F-score values were initially calculated for each respondent separately, resulting in three values for each respondent, corresponding to the analysis of B-scans, Att(co) maps, and Att (cross) maps. Subsequently, all the values were presented in one table with the F-score values for each respondent in the rows and the type of images being evaluated in the corresponding columns. Afterwards, we analyzed the diagnostic accuracy level of used approaches to OCT data analysis. It has been demonstrated that the use of color-coded maps improves the diagnostic accuracy of the method (0.85-0.86 compared to 0.81) and provides objective information about the scattering properties of brain tissue (Figure 6B).

As it was mentioned above, we expected that the additional use usage of cross-polarization coefficient would provide us with more information about the morphological features of studied brain tissues. However, we have not discovered any additional advantages in using Att(cross) coefficient. Therefore, in future studies and clinical practice it could be sufficient to use Att(co) coefficient for visualization and differentiation brain tissue types in the peritumoral zone.

TABLE 4 The results of correlation analysis of optical coefficients and brain tissue types.

	Spearman's rank correlation coefficient	p-value
Att(co)	-0,5909	<0,0001
Att(cross)	-0,6047	<0,0001

4 Discussion

In recent decades, studies on brain tissue imaging using OCT have mainly focused on the differentiation between normal and tumor tissues. There are several studies demonstrating the possibility of distinguishing normal white matter from tumor based on visual analysis of structural OCT images and quantitative signal processing using the attenuation coefficient and optical maps (14, 16, 17, 28). In addition, some studies go further to apply machine learning and artificial intelligence for the purpose of tissue differentiation (18, 29). However, none of the studies have paid close attention to the peritumoral area in general, and the issue of white matter morphological features in particular, which is important for improving the quality of tumor resections.

In the present work, for the first time we carried out a targeted assessment of the scattering properties of peritumoral white matter, characterized by damage to myelinated fibers using CP OCT. In addition, we evaluated the diagnostic ability of visual assessment of structural CP OCT images and color-coded maps of Att(co) and Att (cross) to differentiate normal white matter, damaged white matter and tumor.

We determined the visual features of structural CP OCT images, as well as color-coded optical maps, characteristic of each

10.3389/fonc.2023.1133074

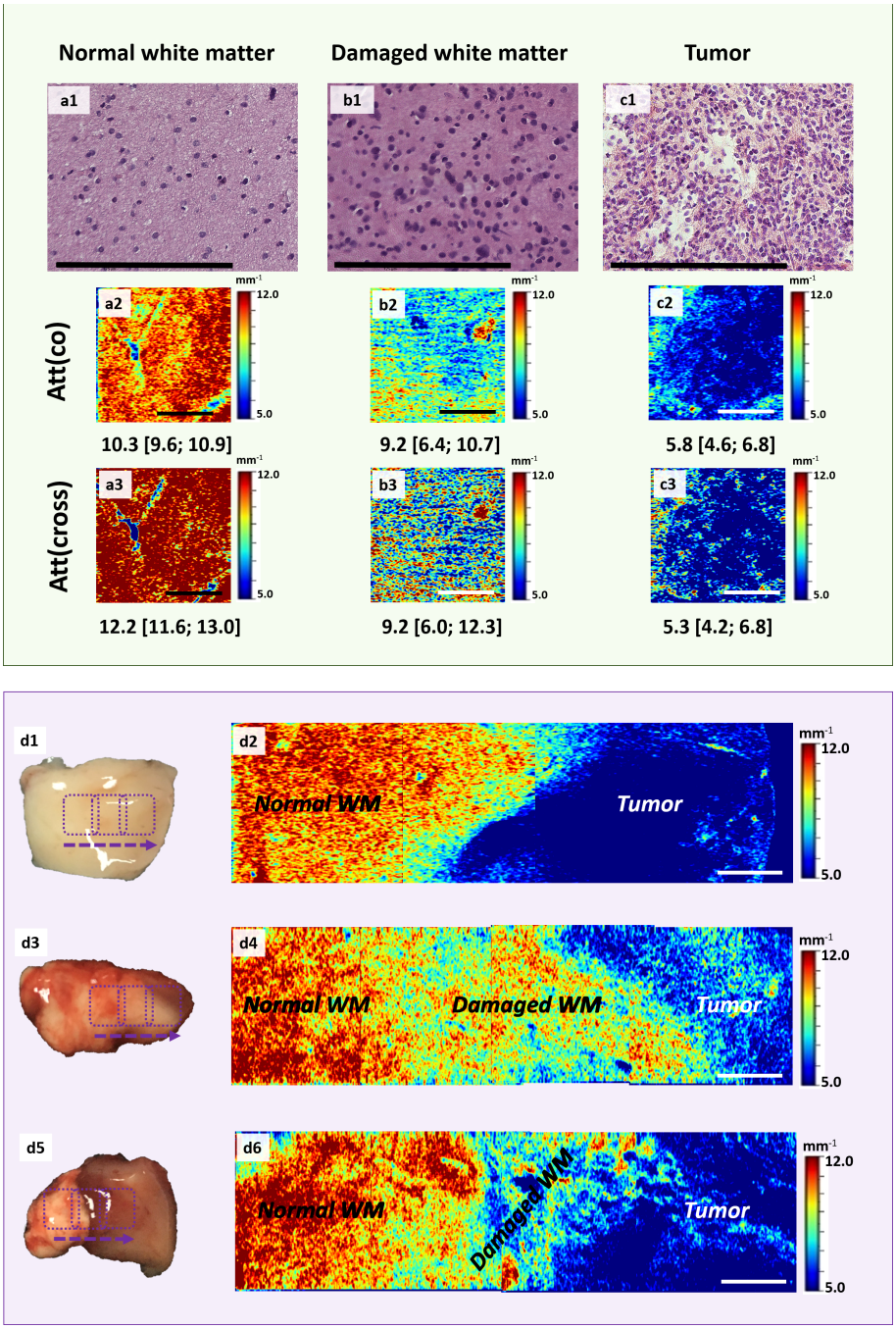

FIGURE 5
Application of color-coded maps for brain tissue visualization. Examples of en-face color-coded maps built based on the Att(co) **(a2, b2, c2)** and Att (cross) **(a3, b3, c3)** values distributions for all the studied tissue types with corresponding histology in H&E staining **(a1, b1, c1)**. **(d2, d4, d6)** – color-coded map of Att(co) representing different examples of tumor border where the areas of damaged and normal white matter can be visualized. The border between normal white matter and tumor may vary from a narrow strip of damaged white matter **(d2)** to a broad zone with smaller **(d4)** or bigger **(d6)** amount of altered myelinated fibers. The area of scanning is marked on the sample **(d1, d3, d5)** using purple rectangles. Scale bar = 200 μm on histological image and 1 mm on OCT image.

of the studied tissue types. Additionally, the median values of the attenuation coefficients in co- and cross-polarizations were calculated. Subsequently, two groups of respondents were offered to pass two classification tests (containing sets of B-scans and optical maps), the results of which determined the level of diagnostic accuracy of the method.

During the study, it was found that areas of damaged white matter are characterized by a decrease in scattering properties in both polarizations compared to the tissue of normal pathways. This phenomenon can be detected both by visual analysis of structural OCT images and by applying quantitative data processing followed by analysis of color-coded optical maps.

10.3389/fonc.2023.1133074

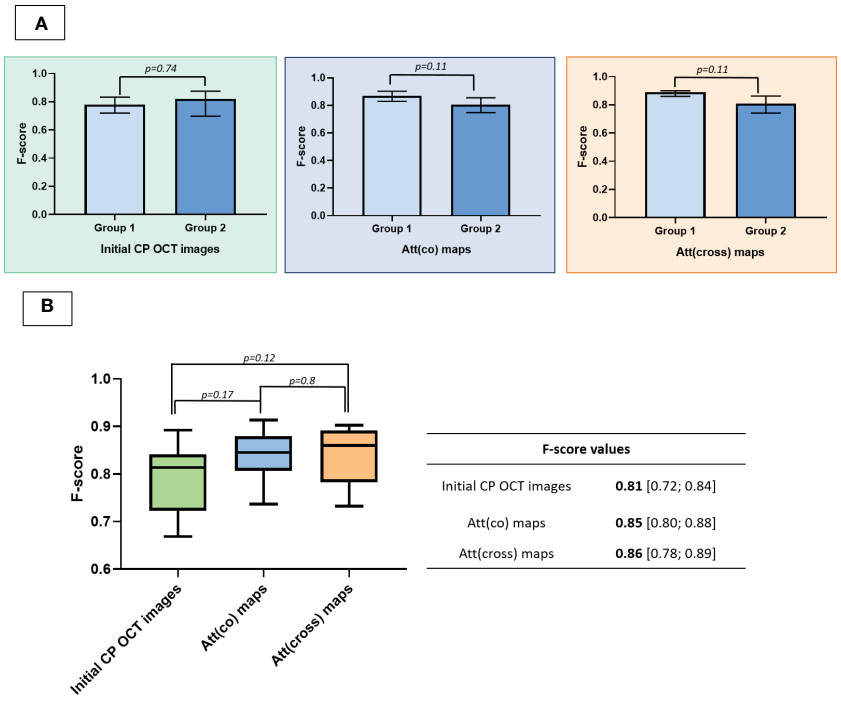

FIGURE 6
Diagnostic ability of different approaches to OCT data assessment for delineation of brain tissue types in the peritumoral area. **A–F**-score values of using different approaches to the evaluation of CP OCT images to differentiate normal white matter, damaged white matter and tumor. **B–F**-score values calculated in 2 subgroups of respondents where "Group 1" includes researchers experienced in working with OCT data and "Group 2" consists of researchers without previous experience in the analysis of OCT data. Data is presented as Me [Q1; Q3].

It should be noted that areas of damaged white matter are structurally heterogeneous because the tumor has a complex effect on the tissue of the pathways (4). On the one hand, there is a destruction of myelinated nerve fibers, the exact mechanism of which has not yet been established (30). In our previous work (31), we carried out a quantitative assessment of the relationship between the morphological and optical properties of normal white matter, and it was shown that myelinated fibers make the main contribution to its scattering properties. In the present work, we found that differences in the amount of damaged myelinated fibers in the studied samples result in a large variability of the attenuation coefficients values compared with areas of normal white matter. Color-coded optical maps of these samples are also heterogeneous due to the content of areas with a large number of preserved myelin fibers, as well as areas with their complete destruction. However, the destruction of myelinated fibers is not the only consequence of the influence of the tumor on the tissue of the white matter. At the same time, areas of damaged white matter are characterized by infiltration by tumor cells, as well as the occurrence of vasogenic edema (32). Thus, in each patient diagnosed with a brain neoplasm, complex changes in the structural characteristics of the white matter occur in comparison with the normal state. At the same time, in each specific case, a unique combination is observed, consisting in a different degree of edema and in a different amount of damaged myelinated fibers. In this regard, scattering properties only cannot precisely reflect the percentage of damaged myelin fibers in each particular case.

In addition, we analyzed the diagnostic ability of the method to differentiate three types of tissue in the peritumoral zone. It should be noted that the introduction of a third type of tissue, characterized by an intermediate position between normal white matter and a tumor, leads to a decrease in the diagnostic accuracy of the method, compared with the distinction between tumor and normal tissues only. For example, in the work of Yashin et al. (33), the diagnostic accuracy of visual analysis of structural OCT images for the differentiation of normal white matter and glial tumors was 87-88%. The need to detect areas with destroyed myelinated fibers complicates the study, which is reported to be due to the greater heterogeneity of OCT images obtained from this type of tissue. The use of quantitative processing of OCT data with threshold values of optical coefficients makes it possible to objectify the data and increase the diagnostic accuracy of the method, which was demonstrated by several groups (13, 14). However, during surgery, the assessment of a single numerical value obtained from an OCT image may not be sufficient, in particular, if several types of tissue are included in the field of view. In this regard, the use of color-coded optical maps looks more promising for distinguishing between normal and pathological brain tissues. This approach combines both the clarity of the visual assessment of structural OCT images and the objectivity of quantitative data processing. We demonstrate that the analysis of optical maps allows a slight increase in the diagnostic accuracy of the method, compared with the evaluation of structural OCT images (F-score = 0.85-0.86 and 0.81 for the assessment of optical maps and structural OCT images, respectively). In addition, it has been shown that optical maps allow presenting the data in a more accessible form for respondents in comparison with B-scans, which is reflected in the level of inter-

rater agreement. Moreover, it is interesting that we did not find a significant advantage in respondents who work daily with OCT images and, accordingly, have significant experience in "reading" them. This fact demonstrates the prospects for the use of visual analysis of CP OCT data intraoperatively by the neurosurgeon without additional specialists.

The use of numerical values of the attenuation coefficients also makes it possible to distinguish three types of tissue from each other with high accuracy ($p<0.0001$). In this regard, the additional use of median values of the attenuation coefficients in the OCT image can be useful in cases where predominated colors on the optical maps, reflect the cross values of the coefficients between adjacent tissue types (normal white matter/damaged white matter or damaged white matter/tumor). Thus, for intraoperative determination of tissue type, it looks promising to build optical maps with simultaneous calculation of the median value of the optical coefficient (clinical example demonstrated in Supplementary Figure 4).

In view of applying our results in clinical practice, it is worth noting that this study was carried out on ex vivo samples of brain tissue. We assume that transportation of samples in closed Petri dishes on ice preserves the structural characteristics and, consequently, the optical properties of the object and the results of the experiment demonstrated (34). However, to confirm the obtained results, it is necessary to carry out *in vivo* studies during surgical intervention.

Moreover, study limitations connected with several aspects are needed to be marked. On the one hand, we need to mention the limitations of OCT method, in particular, low penetration depth of the probing light. Therefore, it is possible to obtain the information about the tissue structure only of the depth up to 1.5 mm. This aspect also includes the small size of the OCT image and, accordingly, the small volume of tissue scanning. On the other hand, during the evaluation of myelinated fibers preservation in the study area we cannot exclude the influence of edema on the features of the obtained OCT signal. It is known, that brain tissue edema causes differences in its scattering properties (35, 36). Consequently, the severe edema may significantly decrease the scattering properties of white matter, which may be confusing in the case of low amount of destructed myelinated fibers. In addition, the areas of coagulation, hemorrhages and necrosis may also lead to changes in the nature of the received OCT signal, which is important especially if we are speaking about in vivo studied during surgery.

To summarize, OCT is a promising tool for neuronavigation during resection of malignant neoplasms of the brain or stereotaxic biopsies. Currently, various options for intraoperative OCT systems are known (integration into an operating microscope or the use of optical probes) (20, 37), which indicates the possibility of intraoperative application of this method to obtain precise information about the brain tissue type in a specific region of interest.

5 Conclusions

We discovered that alteration of myelinated fibers causes changes in the scattering properties of the white matter and OCT is a promising tool for studying the state of the white matter for the subsequent differentiation of tissue types in the perifocal zone of the tumor. To accomplish this task, it is possible to use both visual analysis of structural OCT images and the use of optical maps. The construction of color-coded maps makes it possible to objectify the information, maintaining the visibility of the visual assessment, while there is an increase in diagnostic accuracy (F-score = 0.85-0.86 and 0.81 for the assessment of optical maps and structural OCT images, respectively). At the same time, the presence of prior experience with OCT images does not provide an advantage in the image classification process. Thus, data analysis will not require the participation of a specially trained person and can be carried out directly by a neurosurgeon after the adequate training. In addition, we have not discovered any advantages of additional usage of cross-polarization, which demonstrates the ability to determine type of tissue in the peritumoral area using non-polarization OCT devices.

Data availability statement

The raw data supporting the conclusions of this article will be made available by the authors, without undue reservation.

Ethics statement

The studies involving human participants were reviewed and approved by Institutional Review Board of Privolzhsky Research Medical University. The patients/participants provided their written informed consent to participate in this study. Written informed consent was obtained from the individual(s) for the publication of any potentially identifiable images or data included in this article.

Author contributions

KA: study concept and design, data acquisition and quality control of data, data analysis and interpretation, manuscript preparation. KY, EK, EB, ML, IM: data acquisition and quality control of data. AM: data analysis, manuscript preparation. EK, GG, EZ and NG: manuscript review. All authors contributed to the article and approved the submitted version.

Funding

The work was carried out as part of the "Priority - 2030" implementation.

Acknowledgments

The authors thank Dr. Anna Gladkova (Australian National University/Higher School of Economics (Nizhny Novgorod)) for the proofreading of the manuscript.

Conflict of interest

The authors declare that the research was conducted in the absence of any commercial or financial relationships that could be construed as a potential conflict of interest.

Publisher's note

All claims expressed in this article are solely those of the authors and do not necessarily represent those of their affiliated organizations, or those of the publisher, the editors and the reviewers. Any product that may be evaluated in this article, or claim that may be made by its manufacturer, is not guaranteed or endorsed by the publisher.

Supplementary material

The Supplementary Material for this article can be found online at: https://www.frontiersin.org/articles/10.3389/fonc.2023.1133074/full#supplementary-material

References

1. Sung H, Ferlay J, Siegel RL, Laversanne M, Soerjomataram I, Jemal A, et al. Global cancer statistics 2020: GLOBOCAN estimates of incidence and mortality worldwide for 36 cancers in 185 countries. *CA Cancer J Clin* (2021) 71:209–49. doi: 10.3322/caac.21660

2. Leece R, Xu J, Ostrom QT, Chen Y, Kruchko C, Barnholtz-Sloan JS. Global incidence of malignant brain and other central nervous system tumors by histology, 2003-2007. *Neuro Oncol* (2017) 19(11):1553–64. doi: 10.1093/neuonc/nox091

3. Witwer BP, Moftakhar R, Hasan KM, Deshmukh P, Haughton V, Field A, et al. Diffusion-tensor imaging of white matter tracts in patients with cerebral neoplasm. *J Neurosurg* (2002) 97(3):568–75. doi: 10.3171/jns.2002.97.3.0568

4. Yen PS, Teo BT, Chiu CH, Chen SC, Chiu TL, Su CF. White matter tract involvement in brain tumors: a diffusion tensor imaging analysis. *Surg Neurol* (2009) 72 (5):464–9. doi: 10.1016/j.surneu.2009.05.008

5. Jackson C, Westphal M, Quiñones-Hinojosa A. Complications of glioma surgery. *Handb Clin Neurol* (2016) 134:201–18. doi: 10.1016/B978-0-12-802997-8.00012-8

6. Romano A, Fasoli F, Ferrante M, Ferrante L, Fantozzi LM, Bozzao A. Fiber density index, fractional anisotropy, adc and clinical motor findings in the white matter of patients with glioblastoma. *Eur Radiol* (2008) 18(2):331–6. doi: 10.1007/s00330-007-0740-9

7. Szmuda T, Kierońska S, Ali S, Słoniewski P, Pacholski M, Dzierżanowski J, et al. Tractography-guided surgery of brain tumours: what is the best method to outline the corticospinal tract? . *Folia Morphol (Warsz)* (2021) 80(1):40–6. doi: 10.5603/FM.a2020.0016

8. Henderson F, Abdullah KG, Verma R, Brem S. Tractography and the connectome in neurosurgical treatment of gliomas: the premise, the progress, and the potential. *Neurosurg Focus* (2020) 48(2):E6. doi: 10.3171/2019.11.FOCUS19785

9. Gerard IJ, Kersten-Oertel M, Hall JA, Sirhan D, Collins DL. Brain shift in neuronavigation of brain tumors: An updated review of intra-operative ultrasound applications. *Front Oncol* (2021) 10:618837. doi: 10.3389/fonc.2020.618837

10. Roberts DW, Valdes PA, Harris BT, Fontaine KM, Hartov A, Fan X, et al. Coregistered fluorescence-enhanced tumor resection of malignant glioma: Relationships between delta-aminolevulinic acid-induced protoporphyrin IX fluorescence, magnetic resonance imaging enhancement, and neuropathological parameters. *J Neurosurg* (2011) 114:595–603. doi: 10.3171/2010.2.JNS091322

11. Sastry R, Bi WL, Pieper S, Frisken S, Kapur T, Wells W, et al. Applications of ultrasound in the resection of brain tumors. *Neuroimaging* (2017) 27(1):5–15. doi: 10.1111/jon.12382

12. Leitgeb R, Placzek F, Rank E, Krainz L, Haindl R, Li Q, et al. Enhanced medical diagnosis for dOCTors: a perspective of optical coherence tomography. *J BioMed Opt* (2021) 26(10):100601. doi: 10.1117/1.JBO.26.10.100601

13. Yashin KS, Kiseleva EB, Moiseev AA, Kuznetsov SS, Timofeeva LB, Pavlova NP, et al. Quantitative nontumorous and tumorous human brain tissue assessment using microstructural co- and cross-polarized optical coherence tomography. *Sci Rep* (2019) 9:2024. doi: 10.1038/s41598-019-38493-y

14. Kut C, Chaichana KL, Xi J, Raza SM, Ye X, McVeigh ER, et al. Detection of human brain cancer infiltration ex vivo and in vivo using quantitative optical coherence tomography. *Sci Transl Med* (2015) 7:292ra100. doi: 10.1126/scitranslmed.3010611

15. Wang H, Akkin T, Magnain C, Wang R, Dubb J, Kostis WJ, et al. Polarization sensitive optical coherence microscopy for brain imaging. *Opt Lett* (2016) 41(10):2213–6. doi: 10.1364/OL.41.002213

16. Yuan W, Kut C, Liang W, Li. X. Robust and fast characterization of OCT-based optical attenuation using a novel frequency-domain algorithm for brain cancer detection. *Sci Rep* (2017) 7:44909. doi: 10.1038/srep44909

17. Bizheva K, Unterhuber A, Hermann B, Povazay B, Sattmann H, Fercher AF, et al. Imaging ex vivo healthy and pathological human brain tissue with ultra-high-resolution optical coherence tomography. *J BioMed Opt* (2005) 10:11006. doi: 10.1117/1.1851513

18. Juarez-Chambi RM, Kut C, Rico-Jimenez JJ, Chaichana KL, Xi J, Campos-Delgado DU, et al. AI-Assisted *In situ* detection of human glioma infiltration using a novel computational method for optical coherence tomography. *Clin Cancer Res* (2019) 25:6329–38. doi: 10.1158/1078-0432.CCR-19-0854

19. Yashin K, Bonsanto MM, Achkasova K, Zolotova A, Wael AM, Kiseleva E, et al. OCT-guided surgery for gliomas: Current concept and future perspectives. *Diagnostics* (2022) 12:335. doi: 10.3390/diagnostics12020335

20. Böhringer HJ, Lankenau E, Stellmacher F, Reusche E, Hüttmann G, Giese A. Imaging of human brain tumor tissue by near-infrared laser coherence tomography. *Acta Neurochir* (2009) 151(5):507–17. doi: 10.1007/s00701-009-0248-y

21. Węglarczyk S. Kernel density estimation and its application. *ITM Web Conferences* (2018) 23:37. doi: 10.1051/itmconf/20182300037

22. Gelikonov VM, Romashov VN, Shabanov DV, Ksenofontov S, Terpelov DA, Shilyagin PA, et al. Cross-polarization optical coherence tomography with active maintenance of the circular polarization of a sounding wave in a common path system. *Radiophys Quant El* (2018) 60:897–911. doi: 10.1007/s11141-018-9856-9

23. Kiseleva EB, Moiseev AA, Kuyarov AS, Molvi MA, Gelikonov GV, Maslennikova AV, et al. *In vivo* assessment of structural changes of the urethra in lower urinary tract disease using cross-polarization optical coherence tomography. *J Innov Opt Health Sci* (2020) 13:2050024. doi: 10.1142/S1793545820500248

24. Vermeer KA, Mo J, Weda JJ, Lemij HG, de Boer JF. Depth-resolved model-based reconstruction of attenuation coefficients in optical coherence tomography. *BioMed Opt Express* (2013) 5(1):322–37. doi: 10.1364/BOE.5.000322

25. Gubarkova EV, Moiseev AA, Kiseleva EB, Vorontsov DA, Kuznetsov SS, Vorontsov AY, et al. Tissue optical properties estimation from cross-polarization OCT data for breast cancer margin assessment. *Laser Phys Lett* (2020) 17(7):075602. doi: 10.1088/1612-202X/ab9091

26. van der Velden E. CMasher: Scientific colormaps for making accessible, informative and'cmashing'plots. *arXiv preprint arXiv* (2020). 2003.01069. doi: 10.21105/joss.02004

27. Liu Y, Heer J. Somewhere over the rainbow: An empirical assessment of quantitative colormaps. *Conf Hum Factors Comput Syst - Proc* (2018), 1–12. doi: 10.1145/3173574.3174172

28. Almasian M, Wilk LS, Bloemen PR, van Leeuwen TG, Ter Laan M, Aalders MCG. Pilot feasibility study of *in vivo* intraoperative quantitative optical coherence tomography of human brain tissue during glioma resection. *J Biophotonics* (2019) 12 (10):e201900037. doi: 10.1002/jbio.201900037

29. Möller J, Bartsch A, Lenz M, Tischoff I, Krug R, Welp H, et al. Applying machine learning to optical coherence tomography images for automated tissue classification in brain metastases. *Int J Comput Assist Radiol Surg* (2021) 16(9):1517–26. doi: 10.1007/s11548-021-02412-2

30. Brooks LJ, Clements MP, Burden JJ, Kocher D, Richards L, Devesa SC, et al. The white matter is a pro-differentiative niche for glioblastoma. *Nat Commun* (2021) 12:2184. doi: 10.1038/s41467-021-22225-w

31. Moiseev AA, Achkasova KA, Kiseleva EB, Yashin KS, Potapov AL, Bederina EL, et al. Brain white matter morphological structure correlation with its optical properties estimated from optical coherence tomography (OCT) data. *BioMed Opt Express* (2022) 13(4):2393–413. doi: 10.1364/BOE.457467

32. Cuddapah VA, Robel S, Watkins S, Sontheimer H. A neurocentric perspective on glioma invasion. *Nat Rev Neurosci* (2014) 15(7):455–65. doi: 10.1038/nrn3765

33. Yashin KS, Kiseleva EB, Gubarkova EV, Moiseev AA, Kuznetsov SS, Shilyagin PA, et al. Cross-polarization optical coherence tomography for brain tumor imaging. *Front Oncol* (2019) 9:201. doi: 10.3389/fonc.2019.00201

34. Kiseleva EB, Yashin KS, Moiseev AA, Sirotkina MA, Timofeeva LB, Fedoseeva VV, et al. Cross-polarization optical coherence tomography in comparative *in vivo* and

ex vivo studies of the optical properties of normal and tumorous brain tissues. *Sovrem Tehnol v Med* (2017) 9(4):177. doi: 10.17691/stm2017.9.4.22

35. Liu J, Li Y, Yu Y, Yuan X, Lv H, Zhao Y, et al. Cerebral edema detection *in vivo* after middle cerebral artery occlusion using swept-source optical coherence tomography. *Neurophotonics* (2019) 6(4):45007. doi: 10.1117/1.NPh.6.4.045007

36. Rodriguez CL, Szu JI, Eberle MM, Wang Y, Hsu MS, Binder DK, et al. Decreased light attenuation in cerebral cortex during cerebral edema detected using optical coherence tomography. *Neurophotonics* (2014) 1(2):25004. doi: 10.1117/1.NPh.1.2.025004

37. Lankenau E, Klinger D, Winter C, Malik A, Müller HH, Oelckers S, et al. Combining optical coherence tomography (OCT) with an operating microscope. In: Buzug TM, Holz D, Bongartz J, Kohl-Bareis M, Hartmann U, Weber S, editors. *Advances in medical engineering*. Springer, Berlin: Springer Proceedings in Physics (2007).

frontiers | Frontiers in Oncology

TYPE Original Research
PUBLISHED 23 March 2023
DOI 10.3389/fonc.2023.1161496

OPEN ACCESS

EDITED BY
Santiago Cepeda,
Hospital Universitario Río Hortega, Spain

REVIEWED BY
Giuseppe Roberto Giammalva,
University of Palermo, Italy
Volker Tronnier,
Universitärtsklinikum Schleswig-Holstein,
Germany,

*CORRESPONDENCE
Jincao Chen
chenjincao2012@163.com

SPECIALTY SECTION
This article was submitted to Neuro-Oncology and Neurosurgical Oncology, a section of the journal Frontiers in Oncology

RECEIVED 08 February 2023
ACCEPTED 10 March 2023
PUBLISHED 23 March 2023

CITATION
Wang M, Yu J, Zhang J, Pan Z and Chen J (2023) Intraoperative ultrasound in recurrent gliomas surgery: Impact on residual tumor volume and patient outcomes. *Front. Oncol.* 13:1161496. doi: 10.3389/fonc.2023.1161496

Intraoperative ultrasound in recurrent gliomas surgery: Impact on residual tumor volume and patient outcomes

Meiyao Wang[1,2], Jin Yu[1], Jibo Zhang[1], Zhiyong Pan[1] and Jincao Chen[1]*

[1]Department of Neurosurgery, Zhongnan Hospital of Wuhan University, Wuhan, China, [2]Department of Neurology, University Hospital Zurich, Zurich, Switzerland

Background: Reoperation may be beneficial for patients with recurrent gliomas. Minimizing the residual tumor volume (RTV) while ensuring the functionality of relevant structures is the goal of the reoperation of recurrent gliomas. Intraoperative ultrasound (IoUS) may be helpful for intraoperative tumor localization, intraoperative real-time imaging to guide surgical resection, and postoperative evaluation of the RTV in the reoperation for recurrent gliomas.

Objective: To assess the effect of real-time ioUS on minimizing RTV in recurrent glioma surgery compared to Non-ioUS.

Methods: We retrospectively analyzed the data from 92 patients who had recurrent glioma surgical resection: 45 were resected with ioUS guidance and 47 were resected without ioUS guidance. RTV, Karnofsky Performance Status (KPS) at 6 months after the operation, the number of recurrent patients, and the time to recurrence were evaluated.

Results: The average RTV in the ioUS group was significantly less than the Non-ioUS group (0.27 cm^3 vs. 1.33 cm^3, p = 0.0004). Patients in the ioUS group tended to have higher KPS scores at 6 months of follow-up after the operation than those in the Non-ioUS group (70.00 vs. 60.00, p = 0.0185). More patients in the Non-ioUS group experienced a recurrence than in the ioUS group (43 (91.49%) vs. 32 (71.11%), p = 0.0118). The ioUS group had a longer mean time to recurrence than the Non-ioUS group (7.9 vs. 6.3 months, p = 0.0013).

Conclusion: The use of ioUS-based real-time for resection of recurrent gliomas has been beneficial in terms of both RTV and postoperative outcomes, compared to the Non-ioUS group.

KEYWORDS

recurrent gliomas, surgical resection, intraoperative ultrasound, localization, guidance, postoperative residual, patient outcomes

Abbreviations: ioUS, intraoperative Ultrasound; US, Ultrasound; MRI, Magnetic Resonance Imaging; KPS, Karnofsky Performance Status; PFS, Progression-Free Survival; CT, Computed Tomography; RTV, Residual Tumor Volume; WHO, World Health Organization; IQR, Interquartile Range.

Introduction

In the case of glioma treatment, recurrence is a question of time (1–4). There is currently no agreement on the protocol for treating recurrent gliomas, reoperation may be beneficial for the development of the disease (5–7). Reoperation of recurrent gliomas is more challenging for surgeons because of scar tissue, distorted anatomical markers, more diffuse tumor boundaries, and scattered multifocal lesions left by previous surgery and adjuvant treatment. However, the goal of reoperation remains to remove the recurrent tumor as completely as possible to minimize the residual tumor volume (RTV) while trying to preserve the functionality of relevant structures, which is known to improve patient survival and surgical outcomes (8–10).

In recent years, intraoperative ultrasound (ioUS) in neurosurgical brain tumor surgery is helpful for intraoperative tumor localization, intraoperative real-time imaging to guide surgical resection, and postoperative evaluation of the RTV (11–13), which is not affected by brain shift due to a reduction in cerebrospinal fluid after craniotomy and the change of tumor location during surgical operation (14, 15). Meanwhile, ioUS demonstrates several important advantages, such as low cost, rapid repeatability, real-time scanning of the surgical field, portability, and user-friendliness (16–19).

Although the advantages of ioUS in the first surgery for gliomas have been widely researched and reported (18, 20), not much is known regarding reoperation for recurrent gliomas. Therefore, we assessed the patients who had undergone recurrent glioma reoperation using ioUS to find out if the application of ioUS has an impact on the RTV, and understand how ioUS-guided surgery can impact RTV and early postoperative neurological outcomes in patients with recurrent glioma.

Methods

Patients' characteristics

We searched the computerized medical records at our institution for appropriate individuals. Inclusion criteria were age < 80 years, a KPS score > 60, a histopathological diagnosis of Astrocytoma, IDH-mutant, WHO grades 3–4, Glioblastoma, IDH-wildtype, WHO grade 4, or oligodendroglioma, IDH-mutant and 1p/19q-codeleted, WHO grades 2–3 that after a first surgery (The pathology was determined by a senior neuropathologist in all cases, and the grading criteria were based on the gliomas in the 2021 edition of the World Health Organization (WHO) classification of central nervous system tumors), and a feasible gross-total resection of recurrent tumor according to preoperative MRI. Exclusion criteria were age > 80 years, a low KPS score (≤ 60), and poor health in general. A total of 92 patients with recurrent glioma underwent surgical resection, and their data were assessed retrospectively. Surgeries were performed, between January 2016 and October 2022, by neurosurgeons with at least ten years of surgical experience who are board-certified, at the Department of Neurosurgery, Zhongnan Hospital of Wuhan University, Wuhan, Hubei, China. The glioma's grade was determined *via* a histopathological diagnostic. Patients were subgrouped according to the use of intraoperative ultrasound (ioUS): of those patients, a total of 45 underwent surgery with the assistance of real-time intraoperative ultrasound (ioUS group); the remaining 47 underwent surgery without such assistance (Non-ioUS group). Patients with tumors in eloquent areas, such as the Broca or Wernicke area, motor cortex, thalamus, and basal ganglia, underwent surgery while awake using techniques such as motor evoked potentials, cortical and subcortical stimulation, and sensory evoked potentials. Patients with non-eloquent tumors underwent surgery while under general anesthesia. Preoperative tumor volume was evaluated by preoperative magnetic resonance imaging (MRI) scans and preoperative Karnofsky Performance Status (KPS) was evaluated. In accordance with the Response Assessment in Neuro-Oncology criteria, progression-free survival (PFS) following a first operation was determined from the date of the first surgery to the date of documented evidence of disease progression. The ioUS group and the Non-ioUS group were compared in parallel. The study was approved by the institutional review board, all patients were fully informed about the surgical technique, and signed consent was collected.

MRI and CT assessment

All patients performed preoperative MRI and computed tomography (CT) for surgical planning and the determination of preoperative tumor volume. The postoperative MRI and CT for the evaluation of tumor residual. MRI scans were conducted on a 3.0 T MRI scanner uMR790 (United Imaging Healthcare). A GE discovery 750HD scanner (GE Medical Systems, Milwaukee, WI, USA) was used for CT scans. Tumor volumes were evaluated by manual segmentation using the ITK-SNAP software. After case discussion among the neurosurgeons, neurooncologists, and radiation oncologists, patients were typically recommended a second operation for recurrent tumors. Typically, recurrent tumors were discovered on routine postoperative MRI scans that were carried out three months after the first surgery or if symptoms like worsening headaches, muscle weakness, or other deficiencies appeared. Likewise, the surgeon, radiation oncologist, medical oncologist, and patients themselves decided on the specific adjuvant radiation and chemotherapy treatments to utilize.

IoUS assessment

All patients (ioUS and non-ioUS control groups) were operated on using preoperative MRI and CT. In the Non-ioUS control group, microsurgical tumor resections were completed according to preoperative MRI and CT, the eloquent or non-eloquent tumor location, and the surgeon's experience. In the ioUS group, except for the preoperative MRI and CT, we used a US system (GE LOGIQ E, USA) to obtain the US images. IoUS was performed by doctors with expertise and training in the US. The probe utilized is a variable band linear transducer with a bandwidth of 4.5 to 14.0 MHz (GE

L8-18i-RS, USA), a sterile cover is used for the execution of the ioUS scan and after the bone flap is removed, the first ioUS is performed before accessing the dura to correctly identify the lesion and surrounding structures (Figures 1A–E). A second ioUS was carried out after the dura was opened to find the tumor on the surface of the brain (Figures 1B–F). IoUS can be used numerous times during surgery to provide real-time guidance in locating the lesion for excision. (Figure 1C). To determine whether there was any remaining tumor tissue after the microsurgical removal of all visible tumor tissue, ioUS was used. If there was no residual tumor (Figure 1D), the resection was completed. Further excision was carried out when a tumor remnant was seen on ioUS images (Figure 1G). Repeated ioUS was performed to confirm complete resection (Figure 1H). Surgery was completed according to the preoperative MRI and CT, the ioUS observations, the eloquent or non-eloquent tumor area, and the surgeon's assessment.

Postoperative patients' outcomes

All patients underwent an early postoperative MRI 48 hours following surgery, which was compared to preoperative MRI images. When comparing the postoperative MRI scans to the preoperative MRI images, complete resection was defined as the absence of solid tumor remains. Utilizing a specific instrument from the operating station, residual tumor volume was assessed using manual segmentation and a volume rendering approach. A third-year neurosurgery resident assessed tumor volumes, which were then confirmed by a board-certified neurosurgeon. Preoperative and postoperative KPS scores were assessed. Postoperative patients were followed up for one year. The KPS at 6 months after the operation, whether relapse, and time to recurrence were recorded.

Statistical analysis

The Student t-test, Mann-Whitney U test, Chi-square test, and Fisher's exact test were used in the statistical analysis. GraphPad Prism 8.0 (GraphPad Software, San Diego, California) was used to conduct the statistical analysis. $P<0.05$ was regarded as statistically significant.

Results

Patients' characteristics

A total of 92 patients were involved in the study (mean age of 38.71 years, 45 males and 47 females). All patients were diagnosed with recurrent gliomas, 8 of them were WHO grade 2, 21 were WHO grade 3 and 63 were WHO grade 4. 45 patients were operated on with the use of a real-time ioUS, and 47 of them were operated on without the use of a real-time ioUS. There were 25 patients with tumors in eloquent regions and 67 individuals with tumors in non-eloquent areas. The mean preoperative tumor volume is 4.00cm^3 and the median preoperative KPS is 80 (interquartile range (IQR) is 70-80). The mean PFS after 1st surgery was 26.28 (range from 1 to 108). The cohort's detailed clinical characteristics are summarized in Table 1.

The 2 patient groups (ioUS and Non-ioUS) were comparable for sex, age, grade of recurrent gliomas, tumor localization, preoperative tumor volume, and preoperative KPS and PFS after 1st surgery (no significant difference, $p > 0.05$, Table 2).

Postoperative patients' outcomes

A postsurgical residual tumor volume (RTV) is a significant indicator of poor patient outcomes in glioma. RTV was discovered

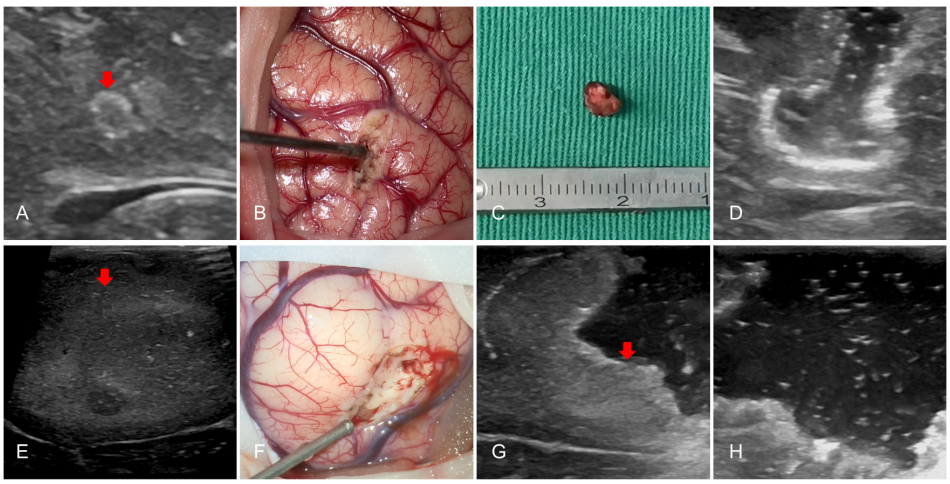

FIGURE 1
IoUS done prior to opening the dura revealed one little hyperechoic signal in the surgical area (**A, E**, red arrow). A second ioUS was carried out after the dura was opened to locate the tumor on the surface of the brain **(B, F)**. The tumor was resected with the real-time repeated ioUS guidance **(C)**. A hyperechogenic lesion presumed to be a tumor remnant was discernible when the doctor used the US to evaluate the surgical field near the anticipated end of the resection (**G**, red arrow). The doctor used the US to evaluate the surgical field after the excision and found no tumor remnants **(D, H)**.

TABLE 1 Preoperative overall characteristics of patients with recurrent gliomas.

Patients' characteristics	Overall (n = 92)
Age (Mean ± SD)	38.71 ± 13.28
Gender	
Male (%)	45 (48.9)
Female (%)	47 (51.09)
Grade of recurrent gliomas	
WHO grade 2 (%)	8 (8.69)
WHO grade 3 (%)	21 (22.83)
WHO grade 4 (%)	63 (68.48)
ioUS (%)	45 (48.91)
Non-ioUS (%)	47 (51.09)
Localization	
Eloquent (%)	25 (27.17)
Non-eloquent (%)	67 (72.83)
Tumor volume cm^3 (Mean ± SD)	4.00 ± 2.22
Preoperative KPS (median [IQR])	80.00 [70.00, 80.00]
PFS after 1st surgery (months, (Mean [Range]))	26.28 [1 – 108]

SD, standard deviation; WHO, World Health Organization; ioUS, intraoperative Ultrasound; KPS, Karnofsky Performance Status; IQR, Interquartile Range; PFS, Progression-Free Survival.

at the end of surgery with the US in 35/45 (77.78%) of the ioUS group. Surgeons continued the procedure in 20 of the 35 patients until full resection was established by the US. The discovered residual tumor could not be completely resected in the remaining 15 individuals due to its proximity to important structures. After surgery, MRI in all 45 individuals revealed the existence of a residual tumor, with an average postoperative volume of 0.27 cm^3 (range 0.00 - 1.00 cm^3). The postoperative MRI revealed the full eradication of the tumor mass in 10 of the 47 (21.28%) patients in the Non-ioUS control group. In all of these 47 cases, the mean residual volume was 1.33 cm^3 on average (range 0.00 – 4.88 cm^3). There was a significant difference between the ioUS and the non-ioUS groups concerning residual tumor volume. Resection tended to be more complete in the ioUS group (ioUS vs. Non-ioUS, mean RTV 0.27 vs. 1.33, p = 0.0004). In the ioUS group, the KPS score decreased from a preoperative median of 80 (IQR: 70 - 90) to a postoperative median of 70 (IQR: 65 - 80). At the follow-up 6 months after the operation, the mean KPS score was 70 (IQR: 60 - 70). In the Non-ioUS control group, the median preoperative KPS score was 80 (IQR: 70 - 80), whereas the median postoperative KPS score was 70 (IQR: 70 - 80). But at the follow-up 6 months after the operation, the mean KPS score was 60 (IQR: 60 - 70). Although there was no difference in postoperative KPS between the ioUS and Non-ioUS groups, there was a significant difference between ioUS and Non-ioUS groups concerning the KPS scores at 6 months after the operation. Those in the ioUS group tended to have higher KPS scores at 6 months of follow-up after the operation than patients in the Non-ioUS group (p = 0.0185). More patients had a recurrence in the Non-ioUS group than patients in the ioUS group ((ioUS vs. Non-ioUS, 43 (91.49%) vs. 32 (71.11%), p = 0.0118). The ioUS group had a longer mean time to recurrence than the Non-ioUS group (7.9 months (range 4 – 12 months) vs. 6.3 months (range 2 – 11 months, p = 0.0013) (Table 3).

To analyze the reason why intraoperative ultrasound can reduce RTV, we carefully compared the preoperative and postoperative CT, MRI, US, and pathological results of the patients, number of tumors in three patients is listed in Table 4. Details are as follows.

Patient 1

M.X.Y, a 57-year-old male patient, preoperative MRI sequences showed one tumor located at the right temporal (Figure 2A, red arrow). Three hyperechoic signals (three tumors) were detected by ioUS before the dura was opened in the operative field (Figure 2B, red arrow). Surgeons removed the three lesions separately according to intraoperative ultrasound guidance. The three lesions were loaded into specimen bags for pathological examination. Histopathology revealed that all three lesions were recurrent glioblastoma WHO grade 4. When the surgeon used ioUS to check the operative field after the resection, no tumor remnants were seen (Figure 2C). The postoperative CT scan reveals no signs of the tumor (Figure 2D).

Patient 2

Z.K.Y, a 50-year-old male patient, preoperative CT scan that showed four high density (four tumors) located at the right frontal lobe (Figure 3A, red arrow). preoperative MRI sequences showed only one tumor (Figure 3B). Before opening the dura, ioUS revealed four hyperechoic signals (four tumors) in the operative field (Figure 3C, red arrow). Surgeons removed the four lesions separately according to intraoperative ultrasound guidance. Histopathology revealed recurrent oligodendroglioma WHO grade 2. When the surgeon used ioUS to check the operative field after the resection, no tumor remnants were seen (Figure 3D). The postoperative CT scan reveals no signs of the tumor (Figure 3E). No tumor remains are visible on the postoperative MRI scan (Figure 3F).

Patient 3

J.L.X, a 7-year-old girl, preoperative MRI sequences showed one tumor located at the right periventricular (Figure 4A, red arrow). Prior to opening the dura, ioUS revealed two tumors (two hyperechoic signals) in the operative field (Figure 4B, red arrow). Surgeons removed the two lesions separately according to intraoperative ultrasound guidance. Histopathology revealed that all two lesions were recurrent glioma WHO grade 3. The doctor used ioUS to evaluate the surgical field after the excision and found no tumor remnants (Figure 4C). The postoperative CT scan reveals no signs of the tumor (Figure 4D). No tumor remains are visible on the postoperative MRI scan (Figure 4E).

TABLE 2 Comparison between patients undergoing ioUS and patients not undergoing ioUS localization and guided surgical resection of recurrent gliomas.

Patients' characteristics	ioUS (n = 45)	Non-ioUS (n = 47)	P	Test
Age (years, Mean ± SD)	34.78 ± 14.95	39.19 ± 11.19	0.1113	Student t
Gender			0.4139	Fisher's exact
Male (%)	20 (44.44)	25 (53.19)		
Female (%)	25 (55.56)	22 (46.81)		
Grade of recurrent gliomas			0.7235	Chi-square
WHO grade 2 (%)	5 (11.11)	3 (6.38)		
WHO grade 3 (%)	10 (22.22)	11 (23.40)		
WHO grade 4 (%)	30 (66.67)	33 (70.21)		
Localization			0.2435	Fisher's exact
Eloquent (%)	15 (33.33)	10 (21.28)		
Non-eloquent (%)	30 (66.67)	37 (78.72)		
Tumor volume (cm^3, Mean ± SD)	4.10 ± 2.44	3.90 ± 2.01	0.6627	Student t
Preoperative KPS (median [IQR])	80.00 [70.00, 90.00]	80.00 [70.00, 80.00]	0.6450	Non-norm (Mann Whitney)
PFS after 1st surgery (months, (Mean [Range]))	24.04 [1 – 96]	26.28 [3 – 108]	0.1052	Non-norm (Mann Whitney)

SD, standard deviation; WHO, World Health Organization; ioUS, intraoperative Ultrasound; KPS, Karnofsky Performance Status; IQR, Interquartile Range; PFS, Progression-Free Survival.

Discussion

There is no universal agreement on the optimal treatment strategy for glioma recurrence. Even though the consistent effect was unclear, Kirkpatrick and Sampson investigated several therapy strategies and identified re-operation as a beneficial treatment choice (21). The survival rate after two resections has increased, according to recent surgical experience. According to Montemurro et al., patients who underwent their first and second gross-total resections for recurrent glioblastoma experienced an improvement in overall survival (HR = 0.195, 95% CI 0.091-0.419; p < 0.0001) (22). Another study found that the reoperation group outlived the non-reoperation group by 16.4 and 10.5 months in overall survival and 3.5 and 2.7 months in PFS (P < 0.001 and 0.01, respectively) (23).

In recurrent glioma, the initial recurrence site is frequently a few millimeters from or inside the original surgical area, infiltrates and expands around the sinus tract of the previous surgery, and is mostly distributed to satellite and multifocal lesions (24, 25), which are not easily detected under the microscope during surgery. These characteristics pose a challenge for the surgical localization of satellite and multiple tumors and complete resection. A growing number of studies have demonstrated the value of the US in locating brain tumors and assisting with their removal. Between January 2021 and September 2021, 17 patients with various brain malignancies underwent ioUS guidance, according to Giammalva et al. (20), they thought the use of ultrasound is crucial to improve surgical effectiveness and patient safety. However, few studies have reported the application of ioUS in recurrent glioma and analyzed patient outcomes. In our research, we reported ioUS localization, guided surgical resection of recurrent glioma, and detection of postoperative residual and analyzed its impact on RTV and patient outcomes.

Generally, preoperative CT and MRI will be done in the recurrent glioma surgery, but it is difficult to locate tumor tissues

TABLE 3 Outcomes of patients who underwent a second surgery for recurrent gliomas according to ioUS versus non-ioUS.

Results	ioUS (n = 45)	Non-ioUS (n = 47)	P	Test
RTV (cm^3, Mean [Range])	0.27 [0.00 – 1.00]	1.33 [0.00 – 4.88]	**0.0004**	Non-norm (Mann Whitney)
Postoperative KPS (median [IQR])	70.00 [65.00, 80.00]	70.00 [70.00, 80.00]	0.3759	Non-norm (Mann Whitney)
KPS at 6 months after the operation (median [IQR])	70.00 [60.00, 70.00]	60.00 [60.00, 70.00]	**0.0185**	Non-norm (Mann Whitney)
Number of patients			**0.0118**	Chi-square
Recurrence	32 (71.11%)	43 (91.49%)		
No recurrence	13 (28.89%)	4 (8.51%)		
Time to recurrence (months, (Mean [Range]))	7.91 [4-12]	6.30 [2-11]	**0.0013**	Non-norm (Mann Whitney)

RTV, Residual Tumor Volume; KPS, Karnofsky Performance Status; IQR, Interquartile Range.
Statistically significant differences (*p*-value <0 .05) are highlighted in bold.

TABLE 4 Number of tumors in representing patients on preoperative CT, MRI, ioUS, postoperative US, postoperative CT and MRI.

Patients	preoperative CT	preoperative MRI	ioUS	postoperative US	postoperative CT	Postoperative MRI
M.X.Y.	–	1	3	0	0	–
Z.K.Y.	4	1	4	0	0	0
J.L.X	–	1	2	0	0	0

CT, Computed Tomography; MRI, Magnetic Resonance Imaging; ioUS, intraoperative Ultrasound; US, Ultrasound.

under the microscope because of brain shift due to the release of cerebrospinal fluid or swelling of brain tissue after opening the dura and brain shift due to tumor resection (26). In addition, the characteristics of recurrent gliomas are scattered and multiple, making it more difficult to find the tumor tissue under the microscope completely according to the surgeons' impression. However, ioUS is not affected by brain shift (14, 27), and after opening the dura, it can still be performed to locate the tumor and guide it in real-time to find all the scattered tumor tissue, which could have assisted in achieving lesser RTV throughout. In our research, ioUS decreased the RTV (mean RTV 0.27 vs. 1.33 cm^3, p = 0.0004) compared to patients without the guidance of ioUS. Lesser RTV was associated with a trend towards higher KPS at 6 months after the operation, lower recurrence rates, and longer recurrence intervals (median KPS 70 vs. 60, p = 0.0185; recurrence rates 71.11 vs. 91.49%, p = 0.0118; time to recurrence 7.9 vs. 6.3 months, p = 0.0013). Under previous studies (28), the outcome of patients with recurrent glioblastoma who underwent reoperations improved with decreasing postoperative RTV.

To analyze the possible reasons why intraoperative ultrasound can reduce RTV, we carefully compared the preoperative and postoperative CT, MRI, US, and pathological results of the patients, the possible reasons are as follows.

Firstly, MRI is effective in detecting intracranial lesions, but it is often incapable of differentiating between tumors, gliosis, or edema (29). Patient 1 (M.X.Y.)'s peritumoral edema may contribute to the missed diagnosis of the tumor tissue on MRI. Meanwhile, MRI is very reliable in visualizing brain tumors and residual tumors during primary surgery. However, owing to artifacts from earlier surgical therapy, its specificity is limited in recurring patients (30). MRI artifacts may also be the main cause of missed diagnosis of lesions. However, high-frequency ioUS overcomes these shortcomings and can well identify multiple lesions, thereby reducing RTV in our study.

Secondly, in term of patient 2 (Z.K.Y.), due to recurrent oligodendroglioma, which has the characteristics of scattered calcification, MRI is superior to CT in assessing tumor extent, whereas CT is most sensitive to calcification (31). MRI is not sensitive to identify calcification, and it is difficult to based on MRI to complete the resection of lesions, CT can though in preoperative identification of calcification, but can't guide for scattered lesions during operation, and ioUS can not only locate calcifications, after removal of part of lesions in operation, under the condition of brain shift occurred, it can still guide to find other scattered lesions and achieve complete resection of multiple lesions, thereby reducing RTV in our research.

Last but not least, In the case of patient 3 (J.L.X.), the small lesion missed by MRI was only 3*3mm, recurrent gliomas with complex per cerebral structures may obscure or interfere with MRI identification of small lesions (30). On the other hand, MRI is a tomography scan, and ultrasound is a continuous, multi-directional scan, which may lead to small lesions not detected by MRI, but detected by US (32).

In our study, patients with tumors in eloquent areas in the ioUS group have less RTV and higher KPS, which might be attributed to the following factors: Firstly, we can more precisely locate the tumor using ioUS and remove it with a surgical corridor without considerably damaging the healthy functioning brain tissue around it. As a result, there is less remaining tumor and less harm. On the contrary, detecting and pinpointing the tumor without ioUS guidance may cause more harm to normal brain tissue and the boundary between the tumor and normal brain tissue cannot be properly recognized, and the doctor will decide to remove

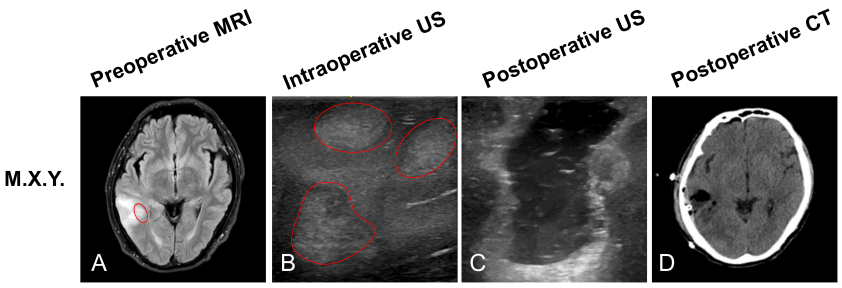

FIGURE 2
Illustrating case 1: M.X.Y, a 57-year-old male patient, MRI sequences showed one tumor located at the right temporal (**A**, red circle). Prior to opening the dura, ioUS revealed three tumors (three hyperechoic signals) in the operative field (**B**, red circles). The doctor used the ioUS to evaluate the surgical field at the ending of the resection and found no tumor remnants **(C)**. The postoperative CT scan reveals no signs of the tumor **(D)**. Histopathology indicated that the patient had recurrent Glioblastoma WHO grade 4.

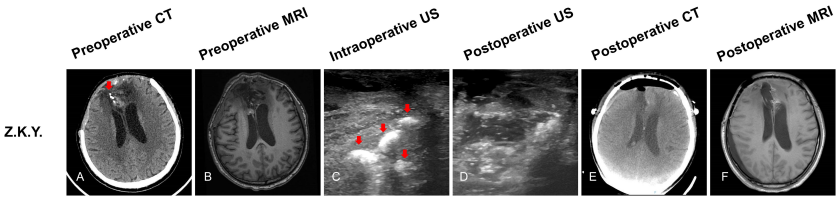

FIGURE 3
Illustrating case 2: Z.K.Y, a 50-year-old male patient, CT scan showed four high density (four tumors) located at the right frontal lobe (**A**, red arrow). MRI (T1WI) sequences showed only one tumor **(B)**. Before opening the dura, ioUS revealed four hyperechoic signals (four tumors) in the operative field (**C**, red arrow). When the doctor used the ioUS to check the surgical field after the resection, no tumor remnants were found **(D)**. The postoperative CT scan shows no tumor remnant **(E)**. The postoperative MRI (T1WI) scan reveals no signs of the tumor **(F)**. Recurrent WHO grade 2 oligodendroglioma was discovered by histopathology.

as little as possible to avoid hurting the functioning brain tissue, leaving more tumor remains. Secondly, we can enter through a surgical corridor from the surrounding non-functional cortex and utilize real-time ultrasound guidance to remove cancers below the functional cortex without harming the functional cortex while removing tumors below the functional cortex. When excision from the bypass is performed without ioUS guidance, it is difficult to detect the tumor directly, which may result in brain tissue injury during the procedure. Last but not least, the color doppler aspect of ioUS enables us to recognize blood vessels and guard against damaging the blood vessels that innervate the functioning region during tumor removal, if there is no color doppler cues, it is hard to have a solid grasp of the vascular status, and injury to arteries innervating the cortex.

According to certain research, the RTV for primary glioma surgery is decreased when using ultrasound (33). However, some studies have reported that ioUS cannot evaluate the RTV of recurrent glioma with a previous surgical cavity that hindered good contact between the brain surface and the US probe (34). To solve this problem, our experience is that during US scanning, normal saline is continuously and slowly injected into the surgical cavity, so that the probe completely fits the normal saline, without any gaps and bubbles, and the lesions can be observed.

Nonetheless, the density of a mass and the mass differential between two neighboring tissue sections are what determine the echogenicity of the US (35). The main disadvantage is that acquiring and interpreting the US picture is doctor-dependent and subjective (36). In our study, the acquisition and interpretation of ultrasound images were done by doctors with ultrasound qualifications, which well overcame this shortcoming. Some artifacts, such as blood, air bubbles, or postoperative radiotherapy-associated alterations, confuse picture interpretation and can decrease ioUS sensitivity to detect tumor remains (37). The hyperechoic areas covered by the hemostatic gauze might have been misinterpreted as tumor infiltration and covered the underlying parenchyma, lowering the sensitivity to scan for tumor remains (Figure 5A). In our study, when performing a US examination of tumor residual, we achieved high-quality US images by fully hemostatic, removing all the hemostatic materials (hemostatic gauze, brain cotton, etc.) from the surgical cavity, and slowly and continuously filling the surgical cavity with normal saline to make the US probe fit perfectly with normal saline (Figure 5B).

IoUS was performed to identify the lesion before to dural opening and during tumor removal, as well as to detect any remaining tumor at the termination of surgery. The cerebral cortex and dura mater are extensively adherent during surgery for recurrent glioma. An wide separation, particularly in motor regions or close to significant blood vessels, can be avoided by intraoperative ultrasound localization by separating just the dura mater corresponding to the tumor from the cerebral cortex. We desire to contribute to the research of future perspectives on technology developments and potential in recurrence glioma surgery. We'd like to demonstrate how ioUS may assist surgeons in better finding tumor tissue, reducing damage to important brain tissue and blood vessels and resecting multifocal tumors properly and completely.

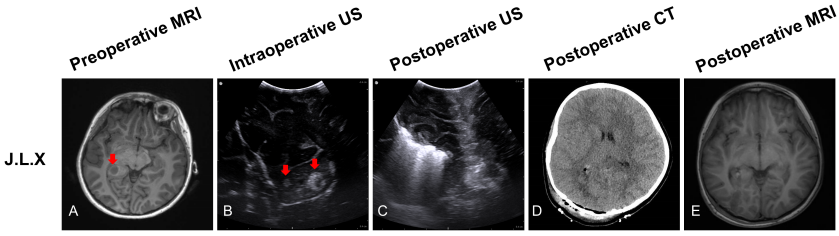

FIGURE 4
Illustrating case 3: J.L.X, a 7-year-old girl, MRI (T1WI) sequences showed one tumor located at the right periventricular (**A**, red arrow). Before opening the dura, IoUS found two hyperechoic signals (two tumors) in the operative field (**B**, red arrow). After the resection, the doctor used the ioUS to check the surgical field, and no tumor remnants were found **(C)**. The postoperative CT scan reveals no tumor remnants **(D)**. No tumor remains are visible on the postoperative MRI (T1WI) scan **(E)**. Histopathology indicated recurrent WHO grade 3 glioma.

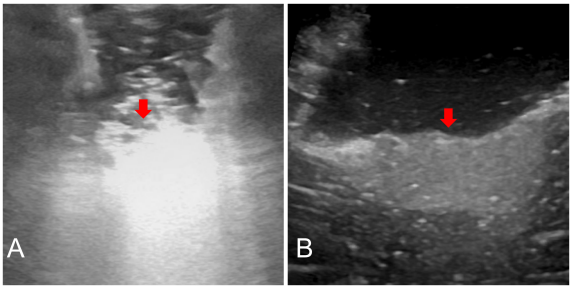

FIGURE 5
Postoperative US: Surgical cavity was covered by the hemostatic gauze (**A**, red arrow). Fully hemostatic, taking out all hemostatic materials and normal saline fills the surgical cavity, and the residual tumor can be seen (**B**, red arrow).

The limitation of our work is that it is retrospective research, and we only investigated a small number of surgeries retrospectively. We attempted to minimize retrospective bias by verifying RTV with pre- and postoperative MRI, eliminating selection bias, and avoiding grouping patients into groups based on age, tumor location, and size, or preoperative conditions. Further prospective studies such as a larger number of patients in multiple centers are required.

Conclusion

The use of ioUS in repeat glioma surgery is feasible and worthy of being widely used clinically. It aids in achieving a lesser RTV, which improves the KPS, reduces the recurrence rate, and prolongs the time to recurrence. Despite the study's limitations, ioUS has shown promise in terms of RTV and postoperative outcomes for the surgery of recurrent gliomas.

Data availability statement

The original contributions presented in the study are included in the article/supplementary material. Further inquiries can be directed to the corresponding author.

Ethics statement

The studies involving human participants were reviewed and approved by the Ethics Committee at Zhongnan Hospital of Wuhan University. Written informed consent to participate in this study was provided by the participants' legal guardian/next of kin.

Author contributions

Conceptualization and Supervision, JCC. Methodology, MYW, JBZ and ZYP. Data curation, JY. Writing-original draft preparation, MYW. Writing-review and editing, JY and JCC. All authors contributed to the article and approved the submitted version.

Funding

This work was supported by the National Natural Science Foundation of China (No. 81771280) and China Scholarship Council.

Conflict of interest

The authors declare that the research was conducted in the absence of any commercial or financial relationships that could be construed as a potential conflict of interest.

Publisher's note

References

1. Barthel FP, Johnson KC, Varn FS, Moskalik AD, Tanner G, Kocakavuk E, et al. Longitudinal molecular trajectories of diffuse glioma in adults. *Nature* (2019) 576 (7785):112–20. doi: 10.1038/s41586-019-1775-1

2. Chen W, Lei C, Liu P, Liu Y, Guo X, Kong Z, et al. Progress and prospects of recurrent glioma: A recent scientometric analysis of the web of science in 2019. *World Neurosurg* (2020) 134:e387–e99. doi: 10.1016/j.wneu.2019.10.078

3. Hervey-Jumper SL, Berger MS. Reoperation for recurrent high-grade glioma: A current perspective of the literature. *Neurosurgery* (2014) 75(5):491-9. doi: 10.1227/NEU.0000000000000486

4. Mellinghoff IK, Penas-Prado M, Peters KB, Burris HA3rd, Maher EA, Janku F, et al. Vorasidenib, a dual inhibitor of mutant Idh1/2, in recurrent or progressive glioma; results of a first-in-Human phase I trial. *Clin Cancer Res* (2021) 27(16):4491–9. doi: 10.1158/1078-0432.CCR-21-0611

5. McBain C, Lawrie TA, Rogozinska E, Kernohan A, Robinson T, Jefferies S. Treatment options for progression or recurrence of glioblastoma: A network meta-analysis. *Cochrane Database Syst Rev* (2021) 5:CD013579. doi: 10.1002/14651858.CD013579.pub2

6. Woodroffe RW, Zanaty M, Soni N, Mott SL, Helland LC, Pasha A, et al. Survival after reoperation for recurrent glioblastoma. *J Clin Neurosci* (2020) 73:118–24. doi: 10.1016/j.jocn.2020.01.009

7. Capo G, Skrap M, Guarracino I, Isola M, Battistella C, Ius T, et al. Cognitive functions in repeated glioma surgery. *Cancers (Basel)* (2020) 12(5):1077. doi: 10.3390/cancers12051077

8. Wann A, Tully PA, Barnes EH, Lwin Z, Jeffree R, Drummond KJ, et al. Outcomes after second surgery for recurrent glioblastoma: A retrospective case-control study. *J Neurooncol* (2018) 137(2):409–15. doi: 10.1007/s11060-017-2731-2

9. Barbagallo GMV, Certo F, Di Gregorio S, Maione M, Garozzo M, Peschillo S, et al. Recurrent high-grade glioma surgery: A multimodal intraoperative protocol to safely increase extent of tumor resection and analysis of its impact on patient outcome. *Neurosurg Focus* (2021) 50(1):E20. doi: 10.3171/2020.10.FOCUS20744

10. Yamaguchi S, Motegi H, Ishi Y, Okamoto M, Sawaya R, Kobayashi H, et al. Clinical outcome of cytoreductive surgery prior to bevacizumab for patients with recurrent glioblastoma: A single-center retrospective analysis. *Neurol Med Chir (Tokyo)* (2021) 61(4):245–52. doi: 10.2176/nmc.oa.2020-0308

11. Shi J, Zhang Y, Yao B, Sun P, Hao Y, Piao H, et al. Application of multiparametric intraoperative ultrasound in glioma surgery. *BioMed Res Int* (2021) 2021:6651726. doi: 10.1155/2021/6651726

12. Petridis AK, Anokhin M, Vavruska J, Mahvash M, Scholz M. The value of intraoperative sonography in low grade glioma surgery. *Clin Neurol Neurosurg* (2015) 131:64–8. doi: 10.1016/j.clineuro.2015.02.004

13. Bal J, Camp SJ, Nandi D. The use of ultrasound in intracranial tumor surgery. *Acta Neurochir (Wien)* (2016) 158(6):1179–85. doi: 10.1007/s00701-016-2803-7

14. Gerard IJ, Kersten-Oertel M, Hall JA, Sirhan D, Collins DL. Brain shift in neuronavigation of brain tumors: An updated review of intra-operative ultrasound applications. *Front Oncol* (2020) 10:618837. doi: 10.3389/fonc.2020.618837

15. Gerard IJ, Kersten-Oertel M, Drouin S, Hall JA, Petrecca K, De Nigris D, et al. Combining intraoperative ultrasound brain shift correction and augmented reality visualizations: A pilot study of eight cases. *J Med Imaging (Bellingham)* (2018) 5 (2):21210. doi: 10.1117/1.JMI.5.2.021210

16. Kaale AJ, Rutabasibwa N, McHome LL, Lillehei KO, Honce JM, Kahamba J, et al. The use of intraoperative neurosurgical ultrasound for surgical navigation in low- and middle-income countries: The initial experience in Tanzania. *J Neurosurg* (2020) 1-8. doi: 10.3171/2019.12.JNS192851

17. Singh V, Shaikh S, Shetty P, Moiyadi A. Customized low-cost model for hands-on training in intraoperative ultrasound for neurosurgeons: Our experience and review of literature. *World Neurosurg* (2020) 143:564–71 e2. doi: 10.1016/j.wneu.2020.07.044

18. Trevisi G, Barbone P, Treglia G, Mattoli MV, Mangiola A. Reliability of intraoperative ultrasound in detecting tumor residual after brain diffuse glioma surgery: A systematic review and meta-analysis. *Neurosurg Rev* (2020) 43(5):1221–33. doi: 10.1007/s10143-019-01160-x

19. de Quintana-Schmidt C, Salgado-Lopez L, Aibar-Duran JA, Alvarez Holzapfel MJ, Cortes CA, Alvarado JDP, et al. Neuronavigated ultrasound in neuro-oncology: A true real-time intraoperative image. *World Neurosurg* (2022) 157:e316–e26. doi: 10.1016/j.wneu.2021.10.082

20. Giammalva GR, Ferini G, Musso S, Salvaggio G, Pino MA, Gerardi RM, et al. Intraoperative ultrasound: Emerging technology and novel applications in brain tumor surgery. *Front Oncol* (2022) 12:818446. doi: 10.3389/fonc.2022.818446

21. Kirkpatrick JP, Sampson JH. Recurrent malignant gliomas. *Semin Radiat Oncol* (2014) 24(4):289–98. doi: 10.1016/j.semradonc.2014.06.006

22. Montemurro N, Fanelli GN, Scatena C, Ortenzi V, Pasqualetti F, Mazzanti CM, et al. Surgical outcome and molecular pattern characterization of recurrent glioblastoma multiforme: A single-center retrospective series. *Clin Neurol Neurosurg* (2021) 207:106735. doi: 10.1016/j.clineuro.2021.106735

23. Delgado-Fernandez J, Garcia-Pallero MÁ, Blasco G, Penanes JR, Gil-Simoes R, Pulido P, et al. Usefulness of reintervention in recurrent glioblastoma: An indispensable weapon for increasing survival. *World Neurosurg* (2017) 108:610–7. doi: 10.1016/j.wneu.2017.09.062

24. Georgescu MM, Olar A. Genetic and histologic spatiotemporal evolution of recurrent, multifocal, multicentric and metastatic glioblastoma. *Acta Neuropathol Commun* (2020) 8(1):10. doi: 10.1186/s40478-020-0889-x

25. Ene CI, Macomber MW, Barber JK, Ferreira MJ, Ellenbogen RG, Holland EC, et al. Patterns of failure after stereotactic radiosurgery for recurrent high-grade glioma: A single institution experience of 10 years. *Neurosurgery* (2019) 85(2):E322–E31. doi: 10.1093/neuros/nyy520

26. Yang JY, Beare R, Seal ML, Harvey AS, Anderson VA, Maixner WJ. A systematic evaluation of intraoperative white matter tract shift in pediatric epilepsy surgery using high-field mri and probabilistic high angular resolution diffusion imaging tractography. *J Neurosurg Pediatr* (2017) 19(5):592–605. doi: 10.3171/2016.11.PEDS16312

27. Prada F, Del Bene M, Mattei L, Lodigiani L, DeBeni S, Kolev V, et al. Preoperative magnetic resonance and intraoperative ultrasound fusion imaging for real-time neuronavigation in brain tumor surgery. *Ultraschall Med* (2015) 36(2):174-86. doi: 10.1055/s-0034-1385347

28. Yong RL, Wu T, Mihatov N, Shen MJ, Brown MA, Zaghloul KA, et al. Residual tumor volume and patient survival following reoperation for recurrent glioblastoma. *J Neurosurg* (2014) 121(4):802–9. doi: 10.3171/2014.6.JNS132038

29. Braun V, Dempf S, Weller R, Reske SN, Schachenmayr W, Richter HP. Cranial neuronavigation with direct integration of (11)C methionine positron emission tomography (Pet) data – results of a pilot study in 32 surgical cases. *Acta Neurochir (Wien)* (2002) 144(8):777–82. doi: 10.1007/s00701-002-0942-5

30. Hesselmann V, Mager AK, Goetz C, Detsch O, Theisgen HK, Friese M, et al. Accuracy of high-field intraoperative mri in the detectability of residual tumor in glioma grade iv resections. *Rofo* (2017) 189(6):519–26. doi: 10.1055/s-0043-106189

31. Weller M, van den Bent M, Preusser M, Le Rhun E, Tonn JC, Minniti G, et al. Eano guidelines on the diagnosis and treatment of diffuse gliomas of adulthood. *Nat Rev Clin Oncol* (2021) 18(3):170–86. doi: 10.1038/s41571-020-00447-z

32. Smith-Bindman R, Kwan ML, Marlow EC, Theis MK, Bolch W, Cheng SY, et al. Trends in use of medical imaging in us health care systems and in Ontario, Canada, 2000-2016. *JAMA* (2019) 322(9):843–56. doi: 10.1001/jama.2019.11456

33. Moiraghi A, Prada F, Delaidelli A, Guatta R, May A, Bartoli A, et al. Navigated intraoperative 2-dimensional ultrasound in high-grade glioma surgery: Impact on extent of resection and patient outcome. *Oper Neurosurg (Hagerstown)* (2020) 18 (4):363–73. doi: 10.1093/ons/opz203

34. Bastos DCA, Juvekar P, Tie Y, Jowkar N, Pieper S, Wells WM, et al. Challenges and opportunities of intraoperative 3d ultrasound with neuronavigation in relation to intraoperative mri. *Front Oncol* (2021) 11:656519. doi: 10.3389/fonc.2021.656519

35. Aldrich JE. Basic physics of ultrasound imaging. *Crit Care Med* (2007) 35(5 Suppl):S131–7. doi: 10.1097/01.CCM.0000260624.99430.22

36. Steno A, Buvala J, Babkova V, Kiss A, Toma D, Lysak A. Current limitations of intraoperative ultrasound in brain tumor surgery. *Front Oncol* (2021) 11:659048. doi: 10.3389/fonc.2021.659048

37. Solheim O, Selbekk T, Jakola AS, Unsgard G. Ultrasound-guided operations in unselected high-grade gliomas–overall results, impact of image quality and patient selection. *Acta Neurochir (Wien)* (2010) 152(11):1873–86. doi: 10.1007/s00701-010-0731-5

frontiers | Frontiers in Oncology

TYPE Original Research
PUBLISHED 13 April 2023
DOI 10.3389/fonc.2023.1151149

OPEN ACCESS

EDITED BY
Sergio García,
Hospital Universitario Río Hortega, Spain

REVIEWED BY
Natalia D. Gladkova,
Privolzhsky Research Medical University (PIMU), Russia
Nathan Simmons,
Dartmouth Hitchcock Medical Center, United States
Julius Höhne,
University Medical Center Regensburg, Germany

*CORRESPONDENCE
Patrick Kuppler
Patrick.Kuppler@uksh.de

SPECIALTY SECTION
This article was submitted to Neuro-Oncology and Neurosurgical Oncology, a section of the journal Frontiers in Oncology

RECEIVED 25 January 2023
ACCEPTED 13 March 2023
PUBLISHED 13 April 2023

CITATION
Kuppler P, Strenge P, Lange B, Spahr-Hess S, Draxinger W, Hagel C, Theisen-Kunde D, Brinkmann R, Huber R, Tronnier V and Bonsanto MM (2023) The neurosurgical benefit of contactless *in vivo* optical coherence tomography regarding residual tumor detection: A clinical study. *Front. Oncol.* 13:1151149. doi: 10.3389/fonc.2023.1151149

The neurosurgical benefit of contactless *in vivo* optical coherence tomography regarding residual tumor detection: A clinical study

Patrick Kuppler[1]*, Paul Strenge[2], Birgit Lange[2], Sonja Spahr-Hess[1], Wolfgang Draxinger[3], Christian Hagel[4], Dirk Theisen-Kunde[2], Ralf Brinkmann[2,3], Robert Huber[3], Volker Tronnier[1] and Matteo Mario Bonsanto[1]

[1]Department of Neurosurgery, University Medical Center Schleswig-Holstein, Luebeck, Germany, [2]Medical Laser Center Luebeck, Luebeck, Germany, [3]Institute of Biomedical Optics, University of Luebeck, Luebeck, Germany, [4]Institute of Neuropathology, University Medical Center Hamburg-Eppendorf, Hamburg, Germany

Purpose: In brain tumor surgery, it is crucial to achieve complete tumor resection while conserving adjacent noncancerous brain tissue. Several groups have demonstrated that optical coherence tomography (OCT) has the potential of identifying tumorous brain tissue. However, there is little evidence on human *in vivo* application of this technology, especially regarding applicability and accuracy of residual tumor detection (RTD). In this study, we execute a systematic analysis of a microscope integrated OCT-system for this purpose.

Experimental design: Multiple 3-dimensional *in vivo* OCT-scans were taken at protocol-defined sites at the resection edge in 21 brain tumor patients. The system was evaluated for its intraoperative applicability. Tissue biopsies were obtained at these locations, labeled by a neuropathologist and used as ground truth for further analysis. OCT-scans were visually assessed with a qualitative classifier, optical OCT-properties were obtained and two artificial intelligence (AI)-assisted methods were used for automated scan classification. All approaches were investigated for accuracy of RTD and compared to common techniques.

Results: Visual OCT-scan classification correlated well with histopathological findings. Classification with measured OCT image-properties achieved a balanced accuracy of 85%. A neuronal network approach for scan feature recognition achieved 82% and an auto-encoder approach 85% balanced accuracy. Overall applicability showed need for improvement.

Conclusion: Contactless *in vivo* OCT scanning has shown to achieve high values of accuracy for RTD, supporting what has well been described for ex vivo OCT brain tumor scanning, complementing current intraoperative techniques and even exceeding them in accuracy, while not yet in applicability.

KEYWORDS

optical coherance tomography, brain tumor imaging, residual tumor detection, tumor border detection, tissue classification, visual image analysis, artificial intelligence, automated tissue characterization

1 Introduction

Neurosurgical tumor resection is a crucial part of neurooncological treatment concepts of brain tumor patients and maximizing the extent of tumor resection has shown to have beneficial prognostic impact on overall and disease free survival (1–3). Gross total resection (GTR) of the tumor depends on the surgeon's experience and skill, as much as the use of intraoperative tools that help differentiate tumorous from healthy brain tissue. Fluorescence-guided surgery after preoperative administration of fluorescent dye, such as 5-aminolevulinic acid (5-ALA) or fluorescein sodium (FNa), has shown to increase the extent of tumor resection and subsequently the progression free survival in glioma patients (4). However, photosensitivity reactions are acknowledged side effects of 5-ALA and adverse reactions, though rare, have been reported for FNa guided surgery. Intraoperative magnetic resonance imaging (MRI) has shown great potential for this purpose, but poses economic challenges to any department, requires specific conditions in the operating room and has shown to significantly increase operative time in comparison to traditional operating rooms (5). Due to factors like intraoperative brain shift, the use of neuronavigation for the detection of tumor borders should always be critically questioned by the operating surgeon and intraoperative ultrasound has not yet shown to increase the extent of tumor resection (6). Improving intraoperative RTD is therefore a crucial part of neurosurgical research and a variety of *in vivo* imaging techniques, such as Raman spectroscopy (RS), confocal laser endomicroscopy (CLE) or multiphoton laser microscopy (MPLM), are emerging for this purpose with the goal of gaining real-time histopathological information. Optical coherence tomography (OCT) has first been introduced for the detection of brain tumor tissue in 1998 by Boppart et al. (7) and has since gained increasing interest with promising potential. By measuring light interference of backscattered light from a target tissue with a reference light signal, OCT can provide real-time three-dimensional (3D) images of tissue microstructures at a spatial resolution of 5–15 µm with an imaging depth up to 3 mm in solid tissues. Low cost and non-invasiveness are further advantages of this technology. OCT provides intraoperative image impressions that are comparable to those of intraoperative ultrasound images, with the difference of an almost microscopic resolution, for the generation of these images is based on backscattered light instead of reflected sound. However, interpretation of these images is a complex undertaking. Several authors have described both qualitative (8, 9) and quantitative (10) image properties that differ in healthy and diseased brain tissue. Thus, image interpretation requires high levels of viewer expertise and its accuracy has only been reported for ex vivo imaging on small patient cohorts, varying in sensitivity and specificity in the range of 90-100% and 76-96%, respectively (9–12). Research on neurosurgical *in vivo* application, in contrast, is still mostly focused on feasibility (8, 9, 13–15). A variety of different OCT systems, e.g. time domain (TD) OCT, spectral domain (SD) OCT, etc. with different set ups, e.g. hand-held imaging probes, stationary systems, etc. have been introduced for intraoperative application. Each system in turn operates on fixed basic settings, such as specific wavelength of probing light, imaging rate and dimensions of field of view, with influence on axial and lateral image resolution. The resulting lack of comparability combined with varying data regarding accuracy of RTD and complex image interpretation are among a few of the reasons why OCT imaging of the central nervous system (CNS), in contrast to ophthalmology, has only limited acceptance in intraoperative application. Therefore, in order to assess the benefit of such a system, we propose a systematic analysis of the respective applicability and accuracy in the detection of tumorous tissue in comparison to techniques that are currently applied in clinical practice.

2 Material and methods

2.1 Optical coherence tomography

A microscope-integrated SD OCT System by Haag-Streit (OptMedt iOCT, Wedel, Germany) was used with a central imaging wavelength of 830nm at an A-scan rate of 35000/s, achieving an axial and lateral resolution of 8µm (full width half maximum (FWHM) in air) and 23µm (FWHM in air), respectively. In all scans, the working distance was set to 300 mm at zoom level 9 to achieve high resolution with sufficient relative back scattered signal intensity. The field of view was limited to a frame of 5.7x15.7, as described before (15). On average, 5 distinct locations at protocol-defined sites for representative coverage of the entire resection area were imaged after tumor tissue extraction by an

experienced neurosurgeon. An additional image was taken from the surface of the tumor. Each scanning process took approximately 30 seconds to complete. By moving the microscope manually, it was aimed to achieve a 90° angle from the light source onto the underlying tissue. Thereby, an *in vivo* OCT dataset was created that consists of a total of 108 OCT volume scans of *in vivo* brain and brain tumor.

2.2 Specimens and histology

After imaging, MRI navigated tissue biopsies were obtained at these locations within the resection cavity in a clinical study under protocol #18-204 granted by the ethics committee of the University of Lübeck. Every tissue sample underwent histological preparation and was analyzed for validation of tissue type, residual tumor burden and cancer grade by a neuropathologist. In addition, classification and grading of the main tumor mass was performed routinely in a separate analysis. The average sample size was 4x4x2 mm. 10 sections were cut from each sample, stained with hematoxylin and eosin and segmented within a tissue labeling system. Labels consist of healthy white matter, edematous tissue, gray matter or different grades of tumorous infiltration. The distribution of the main tumor types is displayed in Table 1. Neuropathology found residual tumor in at least one tissue sample in 12 of the patients, where tissue samples in the remaining 9 patients were free of tumor infiltration.

2.3 Image processing

In order to achieve exact correlation between tissue sample and OCT image, the field of view within the OCT volume had to be reduced to a specific region of interest (ROI), that was defined after locating the area of tissue acquisition within white light images and reproducing it within their matched OCT generated en-face images as displayed in Figure S1 (Supplemental Material). The corresponding en-face OCT images were created from the original OCT volumes by using a custom-written code (Matlab 9.10.0 R2021a; The Mathworks Inc., Natick, Massachusetts). In a second step, a subvolume from within the ROI was generated that could then be used for further analysis where a comparison to the histopathological findings was possible. Each subvolume contains 40 sequential B-scans on average.

Each A-scan in a subvolume is still influenced by the roll-off and the focus function, for depth dependent signal effects have to be taken into account. Therefore, these effects need to be compensated in order to allow a sufficient analysis as has been described before by our group (16). Exemplarily, Figure S2 shows the results of that compensation (Supplemental Material).

For qualitative analysis, the surface was also normalized for each OCT B-scan (Figure S3; Supplemental Material). This step simplifies visual assessment for the neurosurgeon. For quantitative and neural network analysis, patches were manually extracted from the surface normalized OCT B-scans. These patches only contain valid OCT data and no artifacts or empty information. 914 patches were extracted in total at a size of 144x56 pixel.

2.4 Qualitative OCT scan analysis

2.4.1 Image properties

In analogy to qualitative OCT image properties for visual assessment of tumorous tissue vs. healthy brain tissue, as has been suggested by Yashin et al. (9), Böhringer et al. (8) and Yu et al. (17), five image properties that evidently indicate the underlying tissue type after tumor excision were defined. These parameters aimed to reflect common knowledge on what has been described as indicators for cancerous brain tissue alteration by using OCT imaging. In short, the idea is that myelin degradation within white matter of the brain, caused by cancerous infiltration, results in a decreased optical light attenuation in the target tissue. Also, an increase of microstructures, such as cysts, calcifications and hypervascularization within tumor tissue, that OCT imaging has

TABLE 1 List of tumor entities for 21 brain tumor patients.

Patient ID	Entity	Patient ID	Entity
001	Glioblastoma	012	Metastasis (Renal cell carcinoma)
002	Anaplastic Oligodendroglioma (WHO III)	013	Metastasis (Adenocarcinoma)
003	Glioblastoma	014	Anaplastic Oligodendroglioma (WHO III)
004	Metastasis (Lymphoma)	015	Metastasis (Ovarian cancer)
005	Glioblastoma	016	Glioblastoma
006	Neuroendocrine Carcinoma (WHO III)	017	Glioblastoma
007	Glioblastoma	018	Metastasis (Melanoma)
008	Anaplastic Astrocytoma (WHO III)	019	Glioblastoma
009	Glioblastoma	020	Anaplastic Oligodendroglioma (WHO III)
010	Glioblastoma	021	Glioblastoma
011	Metastasis (Non-small-cell-lung-cancer)		

shown to illustrate (17), has been described as an indicator for tumor detection. In accordance with these propositions, the mentioned parameters were combined into a visual classifier containing the following image criteria:

(1) Signal intensity ("high"/"low") – intensity value [dB] displayed through color code, deep red signal (70 dB) with abrupt fading vs. deep blue signal (40 dB) with steady fading, average throughout the OCT subvolume
(2) Homogeneity of intensity (homogeneous/heterogeneous) – variation of the signal within the ROI OCT subvolume
(3) Penetration depth of the signal (high/low) – signal depth >500µm = high, signal depth<500µm = low
(4) Uniformity of the penetration depth (uniform/non-uniform) – varying signal depth throughout the OCT subvolume
(5) Increase in microstructures – signal shadowing within OCT image that indicates calcifications, cysts or hypervascularization

Analyzing OCT scans in that way aimed to take structural differences within the tissue scans into account. In analogy to surgical assessment of intraoperative ultrasound, it was thereby intended to reenact the baseline in the use of OCT imaging during tumor resection in a surgical setting. Figure 1 exemplarily displays these image properties within OCT B-scans that were taken from the described subvolumes.

2.4.2 Visual classifier

In correlation with our findings from ex-vivo OCT imaging and literature (9), the intensity of the signal (1) was defined as the major criterion for the differentiation between white matter and tumorous tissue. High signal intensity was therefore representative for white matter and called "*white matter*". The additional criteria (2) – (5) were only considered when signal intensity was graded low. In this case, [(2) = homogeneous] + [(3) = low] + [(4) = uniform] + [(5) = no microstructures] was defined as "*rather not tumorous/white matter/edema*". Whenever one or more of the additional criteria were graded otherwise, the visual classifier was set to export "*rather tumorous*", with the exception of [(1) = low] + [(2) = homogeneous] + [(3) = high] + [(4) = uniform] + [(5) = no microstructures] which was set to export "*rather tumorous/gray matter*". Whenever signal intensity was graded low [(1) = low] + [(2) = heterogeneous] + [(3) = high] + [(4) = non-uniform] + [(5) = microstructures], the visual classifier was set to export "*tumorous*". For further illustration see Figure 2.

Visual analysis of OCT subvolumes was performed by two neurosurgeons, one surgical attending and one surgical resident, in consecutive turns and later compared regarding the concordance of the results. Both observers were shown respective OCT scans blinded to location of sample acquisition and histopathological finding and merely evaluated main and additional scan criteria. No training sets were provided. An open-source software (ImageJ, 1.53a, Wayne Rasband, National Institute of health, USA) was used for OCT image visualization and filemaker (Claris Filemaker Pro 19) for data storage and classification. It was recorded whether the used OCT scans were eligible for analysis, for some subvolumes lacked image quality, and visually evaluated the degree of concordance between white light image and OCT generated en-face image after matching. Scans with no correlation were also excluded from further analysis.

2.5 Quantitative OCT scan analysis

2.5.1 Tumor classification using optical properties

Quantitative analysis included the determination of optical properties, which can be extracted from an OCT A-scan $A^2(z)$'

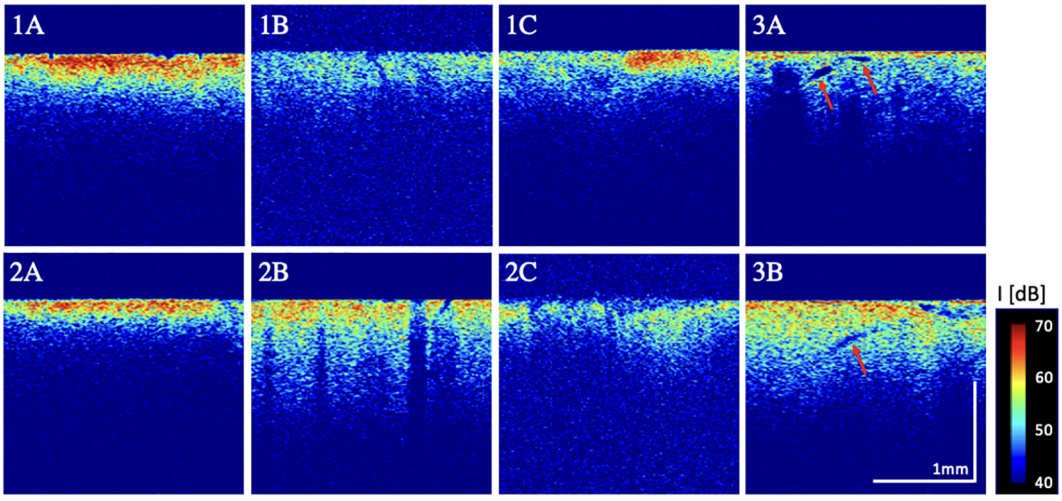

FIGURE 1
Examples of qualitative image properties. 1A: high + homogenous signal intensity, 1B: low signal intensity 1C: heterogenous intensity; 2A: low + uniform penetration depth, 2B: high penetration depth and 2C: non-uniform penetration depths; 3A/3B: increase in microstructures (here, presumably hypervascularization, pointed out through red arrows).

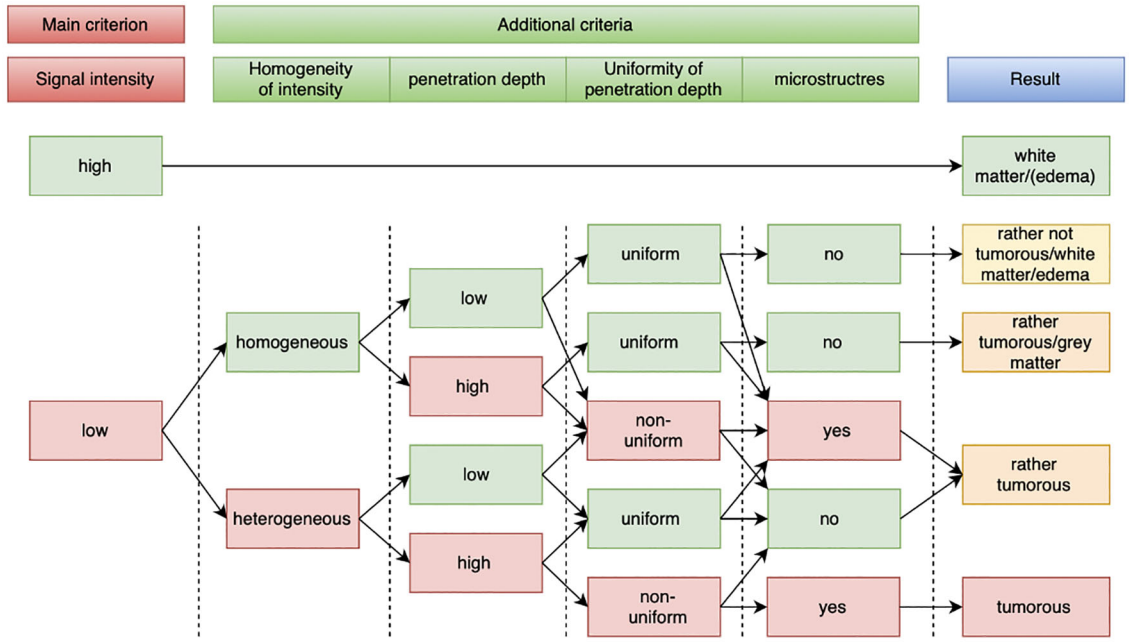

FIGURE 2
Flowchart for visual classifier. OCT signal intensity was set as main criterion. Homogeneity of signal, penetration depth, uniformity of penetration depth and the appearance of micro structures were set as additional criteria. Image properties that indicate healthy tissue are highlighted in green rectangles; image properties that indicate tumorous tissue are highlighted in red rectangles.

(18–21). The resulting signal $A^2(z)'$ contained only the information of the medium, which the incident light hit:

$$A^2(z)' = I{\star}\exp(-2\mu z) \quad \text{Eq. 1}$$

μ is the attenuation coefficient, which describes how strong the signal decreases along the depth axis. I is the maximum backscattered intensity, which was detected by the OCT system. Both parameters are influenced by the scattering anisotropy of the imaged medium, which changes due to different tissue compositions (e.g. increasing tumor infiltration) (22, 23). In order to extract the two optical parameters from an OCT A-scan, a linear least-squares fit was applied to the logarithmized OCT A-scan. The quality of each fit was determined with the coefficient of determination $r^2 \in [0, 1]$, which was defined as:

$$r^2 = 1 - \frac{\sum_{i=1}^{N}(y_i - f_i)^2}{\sum_{i=1}^{N}(y_i - \bar{y})^2} \quad \text{Eq. 2}$$

y defines the measured logarithmized OCT A-scan values and f (μ, I) the signal values for the specified I and μ. r^2 correlates with the homogeneity of the OCT A-scan. The higher r^2, the closer are the measured A-scan values to the determined function f (μ, I). Meaning the A-scan is more homogeneous, than an A-scan, which was fitted with and smaller r^2. Therefore, r^2 was used to evaluate structural information on signal homogeneity, while I and μ resemble optical properties of the tissue.

For the quantitative analysis all extracted OCT B-scan patches were averaged to one A-scan each. The fit was applied to a region of interest, which was 300 μm long and started 20 μm after the maximum measured intensity of the A-scan. For statistical analysis respective mean values were evaluated regarding normal distribution using the Shapiro-Wilk test. For pairwise comparison of the respective values, the Wilcoxon signed-rank test was used. For the classification based on the optical properties a support vector machine with a linear kernel was used. The training configurations were the same as for the classification using artificial intelligence (2.5.2). The optimal cost parameter for the regularization was empirically determined to be 0.1.

2.5.2 Tumor classification using artificial intelligence

Two different classification approaches were applied to 914 OCT B-scan patches. The images were normalized by subtracting the mean image value and division of the standard deviation before being put into the classification. The first classification approach used the OCT B-scans directly to train a convolutional neural network (CNN) in order to identify healthy tissue from pathological brain tissue. The second approach used an autoencoder network (AE) to extract unsupervised features from the B-scan patches. The found features were then used as the basis for the classification. Figure S4 shows an overview of the architecture used for the classifications (Supplemental Material).

The training of the CNN consisted of a leave-one-out approach. Each patient was once used as the test data, while the remaining patients were used for the training. The training was performed in batches, which contained 32 OCT B-scans for 100 epochs. For each training configuration the specificity, sensitivity and balanced accuracy were calculated and the overall performance of the approach was evaluated by the mean sensitivity and specificity of all training folds.

The AE consisted of an encoder and a decoder network. The output of the encoder was then used to train a fully connected neural network, which classified the data. The training and test data was randomly selected from the pool of all available OCT B-scan patches with a split ratio of 30%. The AE was trained on batches of 32 images. For the classification a fully connected neural network (FC) was used. The training procedure was the same as for the CNN.

2.6 Fluorescence-guided surgery

After induction of general anesthesia and before opening of the dura, 4 mg/kg body weight Fluorescein ALCON® (10% with 100mg/ml; Zul.-Nr.: 6375757.00.00) was used intravenously on every patient for intraoperative fluorescence guidance. Tumor resection was performed >15 minutes after injection of FNa. Fluorescence filters were inserted into the operating microscope which allow excitation with wavelengths of 460nm to 500nm and observation with a cut-on wavelength of 510 nm. Prior to tumor resection, fluorescence imaging was used to confirm localization of the invisible tumor in relation to the brain surface. For the most part, tumor resection was performed with the filter turned off and merely turned on for locating tumor tissue and residual tumor at the resection edge (see Figure S5C; Supplemental Material). Whenever tissue samples were obtained, it was documented whether that tissue showed a fluorescent signal or not. BrainLab VectorVision (Brainlab AG, Munich, Germany) was used for neuronavigation and consulted in all cases for extend of resection. All tissue samples were neuronavigated, as can be seen in Figure S5A and B; Supplemental Material). No intraoperative ultrasound was used.

2.7 Early post-operative MRI

Within 24 hours after surgery, every patient received a 3D gadolinium MRI to view tumor residues. These results were subsequently compared to histopathology and analyzed for accuracy of RTD. Whenever histopathology showed residual tumor and neuroradiology confirmed GTR, that scan was classified as false negative.

2.8 Microscope and scanning applicability

After every surgery, the subjective appreciation of this system was recorded by interviewing each neurosurgeon with a set of questions about usability, convenience and arising issues. In detail, we aimed at documenting the individual applicability of the Haag Streit® (HS Hi-R NEO 900) microscope with its integrated OCT scan technology with regards to mobility of the microscope arm, time-effectiveness of OCT scanning in relation to interruption of the intraoperative workflow and accessibility of the region of interest within the resection cavity.

3 Results

3.1 OCT scan quality

Unprocessed scans did not hold sufficient information for tissue evaluation. For this reason, on-sight analysis of real time tissue imaging was not yet feasible and tissue scans had to be post-processed after surgery as is explained in 2.3. Many artifacts were found in the final volume scans, such as signal fold-over or lack of signal. This is why only 44 volume scans from 18 patients were included in the final analysis, resulting in a 60% drop out of the gathered data.

3.2 Surgical appreciation of the microscope-integrated iOCT system

The overall intraoperative appreciation of this system was rated rather poor. Only in 16% of the cases did the respective surgeons rate the applicability as “good”, whereas 84% rated “rather good” or “bad”. Especially the mobility of the microscope, as well as the scanning time seemed to lead to this unappreciation. The execution of imaging within the resection cavity was also limited to the fact that a 90° angle onto the underlying tissue was not always achievable, which is why only in 43% of the cases surgeons rated “good accessibility” and the rest rated “poor” – or “very poor accessibility”.

3.3 Qualitative OCT scan analysis

Figure 3 shows heatmaps for the correlation of histopathology and visual classification. Both maps show an upward tendency from bottom left to top right, indicating correlation between visual assessment and histopathological finding. By simply regarding the detection of white matter and tumor infiltration, sensitivity and specificity of the applied visual classifier ranged from 75% and 89% (balanced accuracy 82%) in observer 1 to 91% and 83% (balanced accuracy 87%) in observer 2, respectively.

3.4 Quantitative OCT scan analysis

3.4.1 Tumor classification with optical properties

Figure 4 displays the results for the determination of the three optical properties through a linear least-squares fitting approach. The results show that all parameters decrease with increasing grade of tumor infiltration. The measured values suggest that there is a significant difference in the determined optical values of healthy white matter and tumor infiltrated white matter. The measured values for healthy white matter indicate, that the tissue is a smooth

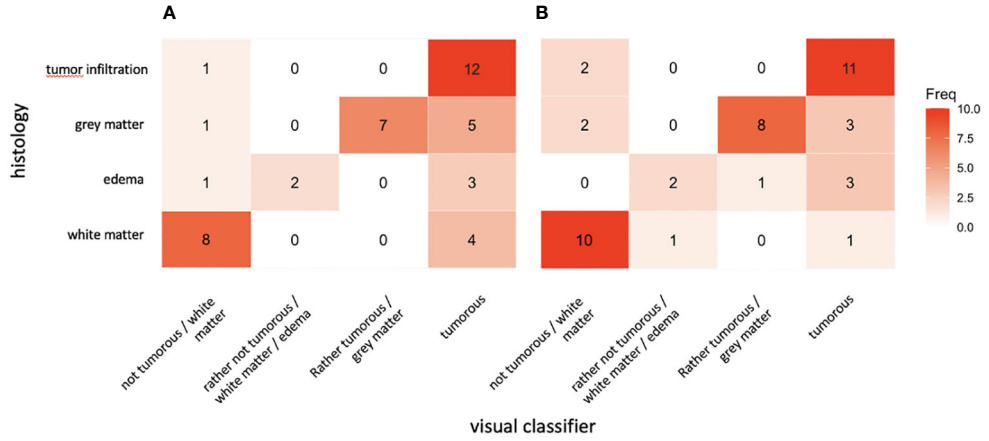

FIGURE 3
Heatmaps for degree of correlation between visual classification and histophatological finding for observer 1 **(A)** and observer 2 **(B)** from 44 subvolume scans.

tissue with high scattering properties, which is why the attenuation and the backscattered intensity are high. Tumor infiltrated white matter on the other hand has the opposite properties. The r^2-value indicates a more heterogeneous structure with lower scattering properties. Gray matter shows similar optical properties to the tumor infiltrated white matter. The edematous tissue shows a more homogeneous tissue structure than tumor infiltrated white matter but is more heterogeneous than healthy white matter. Regarding the attenuation and the backscattered intensity, edema is closer to tumor infiltrated white matter, than healthy white matter.

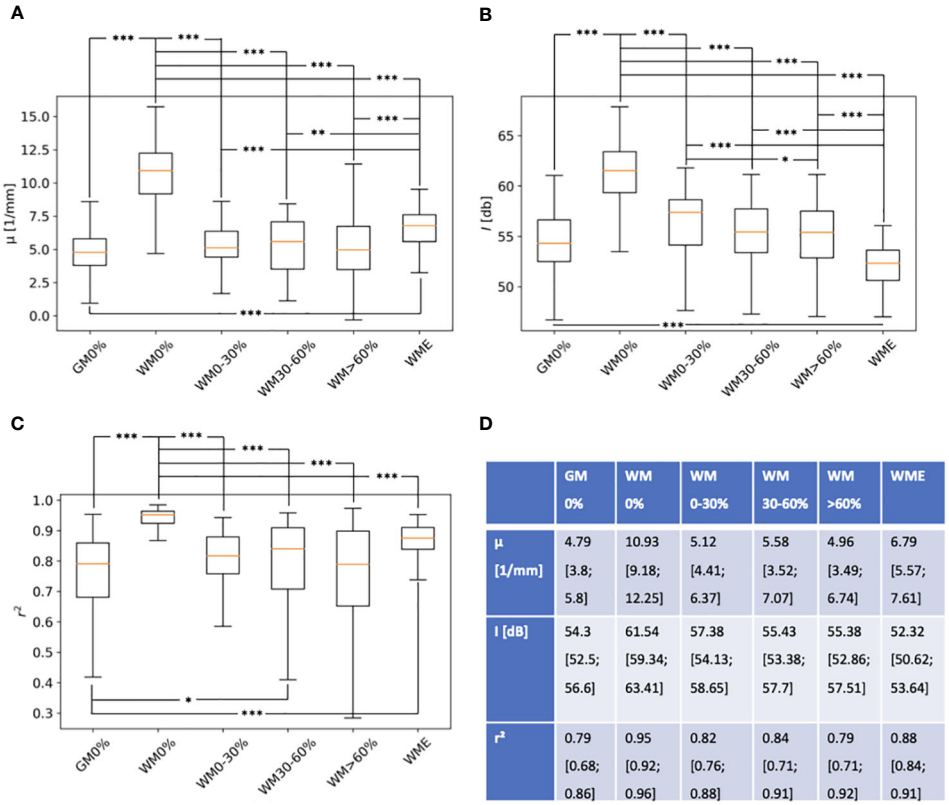

	GM 0%	WM 0%	WM 0-30%	WM 30-60%	WM >60%	WME
μ [1/mm]	4.79 [3.8; 5.8]	10.93 [9.18; 12.25]	5.12 [4.41; 6.37]	5.58 [3.52; 7.07]	4.96 [3.49; 6.74]	6.79 [5.57; 7.61]
I [dB]	54.3 [52.5; 56.6]	61.54 [59.34; 63.41]	57.38 [54.13; 58.65]	55.43 [53.38; 57.7]	55.38 [52.86; 57.51]	52.32 [50.62; 53.64]
r^2	0.79 [0.68; 0.86]	0.95 [0.92; 0.96]	0.82 [0.76; 0.88]	0.84 [0.71; 0.91]	0.79 [0.71; 0.92]	0.88 [0.84; 0.91]

FIGURE 4
Boxplots for three extracted optical properties **(A)** - μ, **(B)** – I and **(C)** – r^2 in regard to different tissue types (GM0%, gray matter with 0 tumor infiltration; WM0%, white matter with 0% tumor infiltration; WMO-30%, white matter with 0-30% tumor infiltration; WM30-60%, white matter with 30-60% tumor infiltration; WM>60%, white matter with > 60% tumor infiltration and WME, white matter with edema). Highly significant differences (p-value <0,001) were marked with ***, significant differences (p-value < 0,01) were marked with **, significant differences (p-value < 0,05) were marked with *. Numerical values of the optical properties are displayed in **(D)**, representing median, 25 and 75 percentiles.

Figure 5 shows relations between optical properties separately by displaying measured optical properties for each OCT B-scan patch. Values for white matter and different grades of tumor infiltration were separated in order to better visualize forming clusters. The measured similarity between tumor infiltration and gray matter creates a big cluster. The measured values for white matter and edematous tissue seem to create a cluster of their own. In order to assess the accuracy of tumor detection through consulting these image property clusters, a support vector machine (SVM) was used in a combined approach to create binary linear categories for the calculation of sensitivity and specificity. For the classification, three different classification tasks were defined. The first task (I) uses the full data available to the classification. Here healthy gray and white matter were assigned to the non-pathological class, while the other tissue labels were assigned to the pathological class. The second task (II) only focuses on the separation of white matter with 0% tumor infiltration and white matter with tumor infiltration. The third task (III) only includes healthy white matter and white matter with >60% tumor infiltration. Figure 5D displays sensitivity, specificity and balanced accuracy values for each task. The data show high accuracy (85%) for the separation of white matter from all degrees of tumor infiltration (tasks II). However, including gray matter and edematous tissue into the non-pathological class compromises accuracy (57%) in that separation task (task I).

3.4.2 Tumor classification with artificial intelligence

The two classification approaches were trained as explained in section 2.5.2, calculating the mean sensitivity and specificity over all test configurations, as explained in 3.2.1. The results for all configurations are displayed in Table 2. The data shows that both approaches achieved good classification results for the classification of white matter from the different grades of tumor infiltration. On the contrary, they struggled to achieve good results for the classification of the healthy tissue from the pathological tissue (task I). Overall, the AE+FC approach showed the better performance.

3.5 Fluorescence guidance

In 16 patients, the operating neurosurgeon agreed on having achieved GTR by assessing the lack of fluorescence signal and consulting neuronavigation. In the 5 remaining patients, the operating surgeon expressed the suspicion of residual tumor. In 9 cases, there was no sign of tumor infiltration within the tissue samples, when the neurosurgeon called for GTR. However, neuropathology showed tumor infiltration in at least one tissue sample in the remaining 7 patients, when the neurosurgeon called

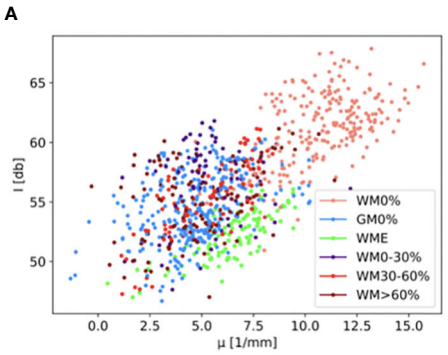

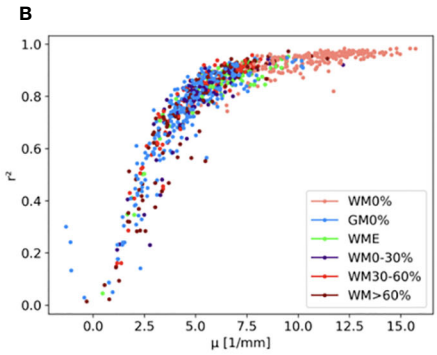

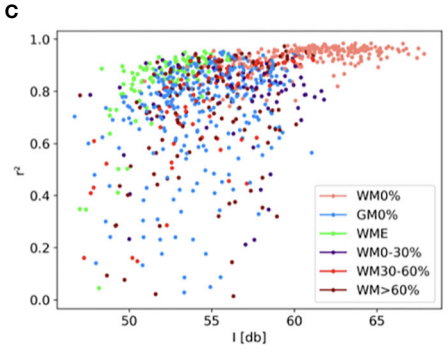

D

	Task I			Task II			Task III		
	Sens (%)	Spec (%)	Acc (%)	Sens (%)	Spec (%)	Acc (%)	Sens (%)	Spec (%)	Acc (%)
SVM	98	16	57	81	89	85	98	63	81

FIGURE 5
Scatter plots of extracted optical properties in regard to tissue labels (GM0%, gray matter with 0 tumor infiltration; WM0%, white matter with 0% tumor infiltration; WM0-30%, white matter with 0-30% tumor infiltration; WM30-60%, white matter with 30-60% tumor infiltration; WM>60%, white matter with >60% tumor infiltration and WME, white matter with edema). **(A)** shows backscatter intensity against attenuation coefficient, **(B)** displays attenuation coefficient against fitted measured r2, **(C)** shows backscatter intensity against fitted measured r2. **(D)** shows results for sensitivity (Sens), specificity (Spec) and balanced accuracy (Acc) for specific classification tasks with support vector machine (SVM) classification. Task I includes full data, Task II includes classification of tumor infiltration in white matter (excluding GM0% and WME) and Task III includes classification of highest tumor infiltration grade in white matter (excluding GM0%, WME, WM0-30% and WM30-60%).

TABLE 2 Sensitivity (Sens), specificity (Spec) and balanced accuracy (ACC) for both CNN and AE + FC classification approaches for specific classification tasks. Task I includes full data, Task II includes classification of tumor infiltration in white matter and Task III includes classification of highest tumor infiltration grade in white matter.

Classification approach	Task I			Task II			Task III		
	Sens (%)	Spec (%)	Acc (%)	Sens (%)	Spec (%)	Acc (%)	Sens (%)	Spec (%)	Acc (%)
CNN	59	77	68	84	79	82	87	79	83
AE + FC	65	66	66	86	83	85	90	84	87

for GTR. All of the 5 patients, where the neurosurgeon expressed concerns for subtotal resection, showed at least one tissue sample with tumor infiltration. Therefore, by merely assessing fluorescence signaling and consulting neuronavigation, only 67% of the expected results where rightfully reflected through histopathological findings, with a sensitivity of just 42%. Table S1 lists the number of cases with true negative/positive and false negative/positive results (Supplemental Material).

3.6 Early post-operative magnetic resonance imaging

In 12 patients, neuroradiology did not show gadolinium enhancement in the early post-operative MRI, while free margins were only histopathologically detected in 9 patients. 3 patients were therefore falsely found tumor-free through neuroradiology, all of which were glioblastoma cases. In the remaining 9 patients, where MRI showed signs of residual tumor, all at least showed one tissue sample with tumor infiltration. The estimated early MRI based sensitivity in this study for the detection of residual tumor was 75%.

4 Discussion

We aimed to analyze a microscope integrated OCT system (iOCT by Haag-Streit) with the intention of gaining insight into intraoperative *in vivo* applicability and accuracy in the detection of residual tumor in a range of approaches and compare these findings to other systems and techniques that are commonly intraoperatively used for this purpose. Miniaturizing large imaging instruments for clinical *in vivo* use is a complicated challenge, where integration into the surgical workflow needs to be feasible without much effort. Therefore, integrating such a system into a surgical microscope appears to be an elegant way of overcoming that obstacle. On-sight interpretation of what is illustrated, however, still remains a difficulty. Hartmann et al. have shown the benefit of *in vivo* OCT for the visualization of distinctive anatomical targets, such as the subarachnoid space (24), vascular anomalies (25) or arachnoid cysts (26), achieving high image quality. In contrast, differentiation of infiltrating tissue, in which a morphological transition is not apparent to the human eye, is a more complex undertaking. Analysis of qualitative and quantitative image properties on ex vivo tissue have well been described as targets for tissue distinction. In this work, it was proven that these approaches were reproduceable in an *in vivo* set up with high values for overall accuracy and demonstrated that machine learning has promising potential for this purpose in a microscope-integrated system.

Introducing new tools in the OR is always a challenge. This might be one of the reasons, why the overall appreciation of this system might not yet be satisfactory. A major challenge is optimal manual adjustment of the microscope for the exploration of the resection cavity where different dimensions of resection cavities led to an inconvenient accessibility. Focusing at a 90° angle on the surface of the tissue was described as particularly difficult. The integration of a robotic system that would automatically traverse resection cavities would simplify this step. Technical developments in this area are on the rise and have well been demonstrated experimentally (27). This, combined with a lack of intraoperative scan quality validation, led to a large number of scans with artifacts that had to be excluded from further analysis. However, finding the right resection edge with current standard techniques is equally challenging in brain tumor surgery today.

Even though authors from the multicentric prospective phase II study (FLUOGLIO) reported a sensitivity and specificity of FNa guidance in identifying tumor tissue with 80.8% and 79.1%, respectively (28), in this study a sensitivity of only 42% was obtained. This might be explained by the different set up of the study design, as well as a more representative cohort size in the phase II study. In this regard, only a 75% sensitivity for early post operative MRI was found in this work, which in analogy and in comparison to other research groups seems rather low. Heßelmann et al. reportet a 95% sensitivity for RTD using intraoperative MRI (29). Nevertheless, these findings show that current techniques for intraoperative RTD are not always easy applicable and far from reliably accurate.

The iOCT system provides real-time dynamic feedback of the underlying tissue, which in its form reminds the viewer of an ultrasound similar signaling. Yashin et al. and Yu et al. proposed a qualitative analysis in regard to specific signal features that could be applied intraoperatively by a trained neurosurgeon. For this reason, a visual classifier was installed that would provide the viewer with a simple step-by-step interpretation tool for a systematic decision-making basis. The respective authors demonstrated qualitative differences in image properties using an ex vivo OCT imaging probe on healthy and diseased brain tissues, whereas in this study a contactless *in vivo* approach was carried out. Yet, through a defined scan distance sufficient relative back scattered signaling was

generated, which in turn made it feasible to achieve comparability throughout the cohort. It is noteworthy to say that real-time image analysis on sight was not feasible, for these images had to undergo post-processing, as is described in 2.3, to make them visually distinctive.

In a blinded retrospective analysis of *in vivo* OCT scans, a sufficient correlation of diagnosed tissue type and histopathology was found. Differentiation of gray matter from tumor infiltrated tissue deemed to be of greater difficulty, for signal intensity is low in both tissues due to less light scattering. Here, additional criteria were not always sufficient to differentiate between the two, which is why values of accuracy for both observers ranged moderately, with a somewhat significant interobserver variability. However, both observers were well able to correctly classify healthy white matter from tumor infiltrated tissue through visual assessment. In this simple approach it was demonstrated that just by visually assessing *in vivo* OCT signaling, one attending neurosurgeon and one resident in neurosurgery were able to differentiate tissue with ranging values for balanced accuracy from 82-87%, which is significantly higher when compared to what could be demonstrated for FNa guidance and neuronavigation in this study and similar to higher from what authors from FLUOGLIO found. Applying real-time image processing onto *in vivo* OCT images, could therefore be a valuable add-on for current intraoperative tissue distinction.

The results for measured optical properties also confirmed findings of other research groups. Highly significant differences in all three properties for the respective tissue labels were found, especially in the comparison between healthy white matter and the different degrees of tumor infiltrated tissue with p values far below a set limit value of 0.05. Looking at the attenuation coefficient, a direct comparison to values from other research groups and the presented values is not sufficient, for light scattering increases with decreasing imaging wavelength (30). Most groups used an imaging wavelength of 1300 nm, whereas the iOCT System functions on 850 nm. However, relative relations of the attenuation coefficient can be compared (8, 10, 14, 18, 31). Furthermore, overall trends match reports from other groups. Yashin et al. explained high light attenuation of healthy white matter with the presence of highly scattering myelin fibers, which for the most part are not present in healthy gray matter. In theory, the higher the degree of tumor infiltration the higher the degradation of myelin fiber, consequently leading to a decrease of light attenuation (18, 32). For edema, Rodriguez et al. reported that edema in gray matter of mice can reduce the attenuation coefficient by up to 8% (31). In this work, the attenuation coefficient of edema in white matter was around 40% smaller than in healthy white matter. These differences may be explained with a different initial set up for both experiments, but the general trend is the same. The relative differences are closer, when comparing the determined values of healthy gray and white matter with other research groups. For Yashin et al., the reported attenuation coefficient of gray matter was 40% smaller than healthy white matter (18). For Kut et al. the difference was 55% and for Almasian et al. 43% (10, 14). For values reported in this work, gray matter was 56% lower than healthy white matter. Unlike other research groups, this work focused on differentiating tissue at the resection edge, where tissue with different degrees of tumor infiltration could be assessed. This complicates comparison to other groups, since most groups do not differentiate various stages of tumor infiltration in the detail this works does. Kut et al. provided a mean attenuation coefficient for tumor infiltrated white matter (3.5 ± 0.8 1/mm) and tumor core (3.9 ± 1.6 1/mm). The relative difference to healthy white matter is similar to the difference, which can be derived from the values from this work. While backscattered intensity showed similar behavior to the attenuation coefficient within different tissue labels, relative differences were much higher. This is a similar observation to findings of Venkata et al., who found that in confocal microscopy, measured reflectivity changed stronger than the scattering coefficient if anisotropy of a medium changes (23). In the case of this work, the anisotropy of brain tissue changes for example with the degree of tumor infiltration.

Structural analysis concerning the r^2-value was very rudimental compared to the analysis of other research groups (14, 33, 34). The value correlated well for white matter and different stages of tumor infiltration. The r^2-value decreased with increasing tumor infiltration, for homogenous structure of white matter is disturbed by upcoming cysts, hemorrhage or vessel proliferations (9). Lenz et al. showed that healthy gray matter is a homogenous tissue, comparable to healthy white matter, which stays in contrast to the presented r^2-values (33). The reasons for the differences could be that in some cases, surface detection in scans from cortex tissue falsely detected arachnoid mater, which led to an unbalanced normalization of the actual tissue and thus to an uneven alignment. This could also be the reason, why it was more difficult to correctly classify gray matter from tumor infiltrated tissue in the qualitative approach, for additional qualitative criteria were less precisely to assess.

When combining all optical properties for classification with the help of a support vector machine, the best results for specificity was assessed for task II in comparison to all of the approaches that are displayed in this work with a value of 89%. The respective sensitivity for this task was 81% with a balanced accuracy of 85%, which is superior in accuracy in comparison to FNa guidance found both in literature and this work.

The classification based on neural networks also achieved superior results for the separation of white matter and tumor infiltrated tissue with the highest sensitivity for the AE + FC approach in task II (Sensitivity and Specificity of 86% and 83%, respectively). These results are comparable to what has been described for 5-ALA guided surgery, where mean sensitivity and specificity in distinguishing tumor from healthy brain tissue at the resection edge ranged between 83 and 87% and 89 and 91%, respectively, in multiple meta-analyses (35). The results on *in vivo* data for this separation task, displayed in this work, even hold up with results achieved on ex vivo data with OCT systems with better resolution. Gesperger et al. achieved a specificity of 100% and a sensitivity of 93% on ex vivo brain data, which was acquired with an

optical coherence microscope system with a lateral resolution of 1.8 µm and an axial resolution of 0.88 µm (36). Juarez-Chambi et al. achieved sensitivity of 99% and a specificity of 86% with an A-scan based approach (11). The data consisted of ex vivo OCT A-scans acquired by an OCT system with a lateral resolution of 16 µm and an axial resolution of 6.4 µm. However, all approaches struggled, when it came to the classification of healthy tissue and pathological tissue. Gray matter provided for extremely similar OCT scans when compared to tumor infiltrated tissue in this work, as has been described in the qualitative analysis approach, which is why task III does not present sufficient results for the classification based on artificial intelligence either.

When assessing the utility of OCT technology, it is evident to consider other laser-based imaging modalities such as RS, MPSM or CLE, that have also been investigated for intraoperative tissue differentiation. Having shown promising results for intraoperative brain tumor detection in multiple study designs with ranging sensitivity and specificity values of 90-96% and 94-100%, respectively (37–39), all share disadvantages of requiring either tissue removal from the surgical site for ex vivo application or requiring a contact-based imaging probe *in vivo*, which is not necessary in the technology presented in this work. In the case of CLE for example, *in vivo* optical biopsies are obtained using fluorescent light reflection of tissue at question by a hand-held probe in a contact-based manner and are simultaneously examined by a neuropathologist, that was specifically trained to interpret CLE images, at a distant cloud-based workstation. OCT, on the other hand, allows for non-contact *in vivo* application without the need of further imaging equipment and the near real-time prospect of automated tissue classification.

5 Conclusion

Due to still inconvenient surgical application and the need of image post-processing, the use of this iOCT system has not yet shown to improve the intraoperative decision-making process concerning the extent of tumor resection. However, qualitative and quantitative *in vivo* OCT data analysis has proven to contain additional information on residual tumor, supporting what has well been described for ex vivo OCT brain tumor scanning. More than half of the scans did not seem fit for further analysis, which for the most part was caused by a missing intraoperative scan quality validation. In the remaining scans, *in vivo* OCT scanning provided for higher values of accuracy in RTD in direct comparison to FNa guidance or early post operative MRI in this study, indicating the possibility of providing complementary information on tissue at question at the resection edge. In particular, the use of artificial intelligence for image feature recognition has shown the most promising results and might be crucial to achieve high accuracy in RTD, expanding current intraoperative methods and even exceeding them in accuracy, while not yet in applicability.

6 Outlook

OCT technology integrated into a surgical microscope is a system in evolution. With further development in user-friendly application and integration of real time tissue analysis, this system has high potential for future intraoperative use for RTD. In an independent development step, the standard Haag Streit® microscope was equipped with a MHz OCT system (40) with the ability of projecting real-time OCT data from underlying tissue as a template into the field of view of the surgeon. Applying classification methods with data that derives from this work could then enhance the extent of brain tumor excision. Currently, we aim to gather more data for the training of neuronal networks to augment classification. Subsequently, this classifier will be used for real time mapping of the operating field in a prospective approach.

Data availability statement

The original contributions presented in the study are included in the article/Supplementary Material. Further inquiries can be directed to the corresponding author.

Ethics statement

The studies involving human participants were reviewed and approved by Universität zu Lübeck. The patients/participants provided their written informed consent to participate in this study.

Author contributions

PK: Conceptualization, formal analysis, investigation, visualization, methodology, data curation, writing original draft. PS: Contributed equally to PK, formal analysis, investigation, software, visualization, methodology, data acquisition, editing. BL: Review and editing, methodology. SS-H: Data acquisition and curation. WD: Software. CH: Histology. DT-K: Review and editing. RB: Review and editing. RH: Supervision. VT: Supervision. MB: Project administration, funding acquisition, review and editing. All authors contributed to the article and approved the submitted version.

Funding

This research is funded by the Federal Ministry of Education and Research Grants No.:13GW0227A, 13GW0227B, 13GW0227C, the European Union Project ENCOMOLE-2i (Horizon 2020, ERC CoGno. 646669), the State of Schleswig-Holstein (Excellence Chair Programme) and Deutsche Forschungsgemeinschaft (EXC 2167-390884018).

Conflict of interest

The authors declare that the research was conducted in the absence of any commercial or financial relationships that could be construed as a potential conflict of interest.

Publisher's note

All claims expressed in this article are solely those of the authors and do not necessarily represent those of their affiliated organizations, or those of the publisher, the editors and the reviewers. Any product that may be evaluated in this article, or claim that may be made by its manufacturer, is not guaranteed or endorsed by the publisher.

Supplementary material

The Supplementary Material for this article can be found online at: https://www.frontiersin.org/articles/10.3389/fonc.2023.1151149/full#supplementary-material

References

1. Smith JS, Chang EF, Lamborn KR, Chang SM, Prados MD, Cha S, et al. Role of extent of resection in the long-term outcome of low-grade hemispheric gliomas. *JCO* (2008) 26:1338–45. doi: 10.1200/JCO.2007.13.9337

2. Brown TJ, Brennan MC, Li M, Church EW, Brandmeir NJ, Rakszawski KL, et al. Association of the extent of resection with survival in glioblastoma: A systematic review and meta-analysis. *JAMA Oncol* (2016) 2:1460–9. doi: 10.1001/jamaoncol.2016.1373

3. Olesrud IC, Schulz MK, Marcovic L, Kristensen BW, Pedersen CB, Kristiansen C, et al. Early postoperative MRI after resection of brain metastases–complete tumour resection associated with prolonged survival. *Acta Neurochir* (2019) 161:555–65. doi: 10.1007/s00701-019-03829-0

4. Stummer W, Pichlmeier U, Meinel T, Wiestler OD, Zanella F, Reulen H-J. Fluorescence-guided surgery with 5-aminolevulinic acid for resection of malignant glioma: a randomised controlled multicentre phase III trial. *Lancet Oncol* (2006) 7:392–401. doi: 10.1016/S1470-2045(06)70665-9

5. Rogers CM, Jones PS, Weinberg JS. Intraoperative MRI for brain tumors. *J Neurooncol* (2021) 151:479–90. doi: 10.1007/s11060-020-03667-6

6. Fountain DM, Bryant A, Barone DG, Waqar M, Hart MG, Bulbeck H, et al. Intraoperative imaging technology to maximise extent of resection for glioma: A network meta-analysis. *Cochrane Database Systematic Rev* (2021). doi: 10.1002/14651858.CD013630.pub2

7. Boppart SA, Brezinski ME, Pitris C, Fujimoto JG. Optical coherence tomography for neurosurgical imaging of human intracortical melanoma. *Neurosurgery* (1998) 43:834–41. doi: 10.1097/00006123-199810000-00068

8. Böhringer HJ, Lankenau E, Stellmacher F, Reusche E, Hüttmann G, Giese A. Imaging of human brain tumor tissue by near-infrared laser coherence tomography. *Acta Neurochir (Wien)* (2009) 151:507–17. doi: 10.1007/s00701-009-0248-y

9. Yashin KS, Kiseleva EB, Gubarkova EV, Moiseev AA, Kuznetsov SS, Shilyagin PA, et al. Cross-polarization optical coherence tomography for brain tumor imaging. *Front Oncol* (2019) 9:201. doi: 10.3389/fonc.2019.00201

10. Kut C, Chaichana KL, Xi J, Raza SM, Ye X, McVeigh ER, et al. Detection of human brain cancer infiltration ex vivo and *in vivo* using quantitative optical coherence tomography. *Sci Transl Med* (2015) 7:292ra100. doi: 10.1126/scitranslmed.3010611

11. Juarez-Chambi RM, Kut C, Rico-Jimenez JJ, Chaichana KL, Xi J, Campos-Delgado DU, et al. AI-Assisted *In situ* detection of human glioma infiltration using a novel computational method for optical coherence tomography. *Clin Cancer Res* (2019) 25:6329–38. doi: 10.1158/1078-0432.CCR-19-0854

12. Strenge P, Lange B, Grill C, Draxinger W, Danicke V, Theisen-Kunde D, et al. Characterization of brain tumor tissue with 1310 nm optical coherence tomography. In: *Optical coherence tomography and coherence domain optical methods in biomedicine XXV*. SPIE (2021). p. 86–92. doi: 10.1117/12.2578409

13. Giese A, Böhringer HJ, Leppert J, Kantelhardt SR, Lankenau E, Koch P, et al. Non-invasive intraoperative optical coherence tomography of the resection cavity during surgery of intrinsic brain tumors. In: *Photonic therapeutics and diagnostics II*. SPIE (2006). p. 495–502. doi: 10.1117/12.674436

14. Almasian M, Wilk LS, Bloemen PR, van Leeuwen TG, Ter Laan M, Aalders MCG. Pilot feasibility study of *in vivo* intraoperative quantitative optical coherence tomography of human brain tissue during glioma resection. *J Biophotonics* (2019) 12:e201900037. doi: 10.1002/jbio.201900037

15. Strenge P, Lange B, Grill C, Draxinger W, Danicke V, Theisen-Kunde D, et al. Ex vivo and in vivo imaging of human brain tissue with different OCT systems. In: *Clinical and preclinical optical diagnostics II (2019)* (2019). p. 11078_49. doi: 10.1117/12.2526932

16. Strenge P, Lange B, Grill C, Draxinger W, Danicke V, Theisen-Kunde D, et al. Registration of histological brain images onto optical coherence tomography images based on shape information. *Phys Med Biol* (2022) 67:135007. doi: 10.1088/1361-6560/ac6d9d

17. Yu X, Hu C, Zhang W, Zhou J, Ding Q, Sadiq MT, et al. Feasibility evaluation of micro-optical coherence tomography (μOCT) for rapid brain tumor type and grade discriminations: μOCT images versus pathology. *BMC Med Imaging* (2019) 19:102. doi: 10.1186/s12880-019-0405-6

18. Yashin KS, Kiseleva EB, Moiseev AA, Kuznetsov SS, Timofeeva LB, Pavlova NP, et al. Quantitative nontumorous and tumorous human brain tissue assessment using microstructural co- and cross-polarized optical coherence tomography. *Sci Rep* (2019) 9:2024. doi: 10.1038/s41598-019-38493-y

19. Gong P, Almasian M, van Soest G, de Bruin DM, van Leeuwen TG, Sampson DD, et al. Parametric imaging of attenuation by optical coherence tomography: review of models, methods, and clinical translation. *J BioMed Opt* (2020) 25:40901. doi: 10.1117/1.JBO.25.4.040901

20. Faber D, van der Meer F, Aalders M, van Leeuwen T. Quantitative measurement of attenuation coefficients of weakly scattering media using optical coherence tomography. *Opt Express* (2004) 12:4353–65. doi: 10.1364/opex.12.004353

21. Schmitt JM, Knüttel A, Bonner RF. Measurement of optical properties of biological tissues by low-coherence reflectometry. *Appl Opt* (1993) 32:6032–42. doi: 10.1364/AO.32.006032

22. Jacques SL. Optical properties of biological tissues: A review. *Phys Med Biol* (2013) 58:R37–61. doi: 10.1088/0031-9155/58/11/R37

23. Venkata RS. *Determination of optical scattering properties of tissues using reflectance-mode confocal microscopy* (2012). Available at: https://www.semanticscholar.org/paper/Determination-of-optical-scattering-properties-of-Venkata/78fa066625818667f3cf6eb77ca31aa74290c4f8 (Accessed May 10, 2022).

24. Hartmann K, Stein K-P, Neyazi B, Sandalcioglu IE. First *in vivo* visualization of the human subarachnoid space and brain cortex *via* optical coherence tomography. *Ther Adv Neurol Disord* (2019) 12:1756286419843040. doi: 10.1177/1756286419843040

25. Hartmann K, Stein K-P, Neyazi B, Sandalcioglu IE. Aneurysm architecture: First *in vivo* imaging of human cerebral aneurysms with extravascular optical coherence tomography. *Cerebrovasc Dis* (2019) 48:26–31. doi: 10.1159/000502450

26. Hartmann K, Stein K-P, Neyazi B, Sandalcioglu IE. Microscope integrated optical coherence tomography of a cerebral arachnoid cyst: A new technique to increase intraoperative security. *J Clin Neurosci* (2020) 82:29–31. doi: 10.1016/j.jocn.2020.10.008

27. Kantelhardt SR, Finke M, Schweikard A, Giese A. Evaluation of a completely robotized neurosurgical operating microscope. *Neurosurgery* (2013) 72 Suppl 1:19–26. doi: 10.1227/NEU.0b013e31827235f8

28. Acerbi F, Broggi M, Schebesch K-M, Höhne J, Cavallo C, De Laurentis C, et al. Fluorescein-guided surgery for resection of high-grade gliomas: A multicentric prospective phase II study (FLUOGLIO). *Clin Cancer Res* (2018) 24:52–61. doi: 10.1158/1078-0432.CCR-17-1184

29. Heßelmann V, Mager A-K, Goetz C, Detsch O, Theisgen H-K, Friese M, et al. Accuracy of high-field intraoperative MRI in the detectability of residual tumor in glioma grade IV resections. *Rofo* (2017) 189:519–26. doi: 10.1055/s-0043-106189

30. Yaroslavsky AN, Schulze PC, Yaroslavsky IV, Schober R, Ulrich F, Schwarzmaier HJ. Optical properties of selected native and coagulated human brain tissues *in vitro* in the visible and near infrared spectral range. *Phys Med Biol* (2002) 47:2059–73. doi: 10.1088/0031-9155/47/12/305

31. Rodriguez CLR, Szu JI, Eberle MM, Wang Y, Hsu MS, Binder DK, et al. Decreased light attenuation in cerebral cortex during cerebral edema detected using optical coherence tomography. *Neurophotonics* (2014) 1:25004. doi: 10.1117/1.NPh.1.2.025004

32. Bevilacqua F, Piguet D, Marquet P, Gross JD, Tromberg BJ, Depeursinge C. *In vivo* local determination of tissue optical properties: applications to human brain. *Appl Opt* (1999) 38:4939–50. doi: 10.1364/ao.38.004939

33. Lenz M, Krug R, Dillmann C, Stroop R, Gerhardt NC, Welp H, et al. Automated differentiation between meningioma and healthy brain tissue based on optical coherence tomography ex vivo images using texture features. *J BioMed Opt* (2018) 23:1–7. doi: 10.1117/1.JBO.23.7.071205

34. Möller J, Bartsch A, Lenz M, Tischoff I, Krug R, Welp H, et al. Applying machine learning to optical coherence tomography images for automated tissue classification in brain metastases. *Int J Comput Assist Radiol Surg* (2021) 16:1517–26. doi: 10.1007/s11548-021-02412-2

35. *Agents for fluorescence-guided glioma surgery: A systematic review of preclinical and clinical results* . PMC. Available at: https://www.ncbi.nlm.nih.gov/pmc/articles/PMC5177668/ (Accessed September 8, 2022).

36. Gesperger J, Lichtenegger A, Roetzer T, Salas M, Eugui P, Harper DJ, et al. Improved diagnostic imaging of brain tumors by multimodal microscopy and deep learning. *Cancers (Basel)* (2020) 12:E1806. doi: 10.3390/cancers12071806

37. Zhang J, Fan Y, He M, Ma X, Song Y, Liu M, et al. Accuracy of raman spectroscopy in differentiating brain tumor from normal brain tissue. *Oncotarget* (2017) 8:36824–31. doi: 10.18632/oncotarget.15975

38. Restelli F, Mathis AM, Höhne J, Mazzapicchi E, Acerbi F, Pollo B, et al. Confocal laser imaging in neurosurgery: A comprehensive review of sodium fluorescein-based CONVIVO preclinical and clinical applications. *Front Oncol* (2022) 12:998384. doi: 10.3389/fonc.2022.998384

39. Uckermann O, Galli R, Mark G, Meinhardt M, Koch E, Schackert G, et al. Label-free multiphoton imaging allows brain tumor recognition based on texture analysis–a study of 382 tumor patients. *Neuro-Oncology Adv* (2020) 2:vdaa035. doi: 10.1093/noajnl/vdaa035

40. Theisen-Kunde D, Draxinger W, Bonsanto MM, Strenge P, Detrez N, Huber R, et al. 1.6 MHz FDML OCT for intraoperative imaging in neurosurgery. In: *Translational biophotonics: Diagnostics and therapeutics*. SPIE (2021). p. 140–2. doi: 10.1117/12.2614855

Frontiers in Oncology

Advances knowledge of carcinogenesis and tumor progression for better treatment and management

The third most-cited oncology journal, which highlights research in carcinogenesis and tumor progression, bridging the gap between basic research and applications to imrpove diagnosis, therapeutics and management strategies.

Discover the latest Research Topics

See more →

Frontiers

Avenue du Tribunal-Fédéral 34
1005 Lausanne, Switzerland
frontiersin.org

Contact us

+41 (0)21 510 17 00
frontiersin.org/about/contact